CHARACTERISTICS AND APPLICATIONS OF HIGH-PERFORMANCE FIBER REINFORCED ASPHALT CONCRETE

by

Philip Park

A dissertation submitted in partial fulfillment
of the requirements for the degree of
Doctor of Philosophy
(Civil Engineering)
in The University of Michigan
2012

Doctoral Committee:

Professor Sherif El-Tawil, Co-Chair
Emeritus Professor Antoine E. Naaman, Co-Chair
Professor Jwo Pan
Assistant Professor Jason P. McCormick
Professor Sang-Yeol Park, Jeju National University, South Korea

DEDICATION

To my beloved wife, Jimi,

to my kids, Sean and Diana,

to my mother, Hang-Ja Hong,

and in memory of my father, Sean-Young Park (1941-2009),
who would have been happier than anyone else...

ACKNOWLEDGMENTS

I received tremendous assistance from numerous people during my graduate study at University of Michigan, and I would like to take this opportunity to express my gratitude toward all these individuals.

Foremost I would like to express my most profound gratitude to my academic advisors, Professor Sherif El-Tawil and Professor Antoine E. Naaman. Professor El-Tawil has provided me with academic knowledge, opportune guidance and encouragement for building a strong career, and financial support throughout my Ph. D. program. He was always willing to take time for me, and helped me resolve my academic and personal problems. Professor El-Tawil is a great mentor and a strong role-model as a scholar and teacher.

Professor Naaman was the one who proposed me to join his and Professor El-Tawil's team. Professor Naaman's last class before his retirement, 'Prestressed Concrete', changed my life in various ways. I was deeply impressed by his beautiful lecture, and it gave me confidence that I indeed was in the right program where I could get exactly what I needed and wanted. In addition, Professor Naaman's steady encouragement was the source of my confidence for continuing my research. I owe both Professor El-Tawil and Professor Naaman for all of the achievements in this dissertation.

I would also like to thank other members of my dissertation committee, Professor Sang-Yeol Park, Professor Jason McCormick, and Professor Jwo Pan, for their time and valuable comments. I especially appreciate Professor Park from Jeju National University for his academic and personal advice during our collaboration on asphalt plug joint.

The University of Michigan has provided a unique opportunity to learn from and work with great leading academic scholars. Professor Alan Wineman and Professor Ellen Arruda introduced me to the world of viscoelasticity. The nonlinear viscoelastic constitutive model for asphaltic materials is developed based on a two-year discussion with Professor Wineman. Professor Jwo Pan, Professor John Shaw, and Professor James Barber taught me the mathematical expressions of mechanical phenomena. In addition, Professor Jerome P. Lynch, Professor Will Hansen, Professor Victor C. Li, and Professor

James K. Wight enriched my days here at the University of Michigan with their plentiful academic background, enthusiastic attitude toward research, respectable personality, and encouragement.

I want to acknowledge Mr. Jan Pantolin and Mr. Robert Fischer for all their help in preparing my experiments, and Ms. Sherry Brueger, Ms. Jessica Taylor, Ms. Janet Lineer, and Ms. Kimberly Smith for their administrative support.

I also feel lucky to have a strong group of supportive and competent colleagues. These include: Simon (Shi-Ho) Chao, Ekin Ekiz, Kapil Khandelwal, Kay Wille, Yasser Alashker, Kittinun Sirijaroonchai, Supat Suwannakarn, Chung-Chan Hung, Dongjoo Kim, Honghao Li, Jieshi Fang, Julie Fogarty, and Sukhoon Pyo. Furthermore, I am happy to have such friendly fellow Ph. D. students including Montian Setkit, Alex DaCosta, Matthew Fadden, Sean O'Conner, Bang-Yeon Lee, Remy D. Lequesne, Jungdae Lim, Junhee Kim, Yongseop Jung, Jongwon Lee, Chul-Goo Lee, Hyun-Dong Kim, and Jongho Kim. In particular, I deeply appreciate Youngjae Kang and his wife for their sincere friendship and help during the settling of my family in Ann Arbor.

The research presented herein was supported in part by the Korea Institute of Construction and Transportation Technology Evaluation and Planning, the Michigan Department of Transportation, the Department of Civil and Environmental Engineering at the University of Michigan, and Jeju National University, South Korea. Any opinions, findings, conclusions, and recommendations expressed in this paper are those of the writers alone and do not necessarily reflect the views of the sponsoring agencies. In addition, Mr. John Nguyen of Ajax Paving Industries Inc. and Mr. Albert Tamashausky of Asbury Carbon are acknowledged for providing the materials used for my tests and the professional advice on mixing asphalt concrete and selecting graphite.

Finally, I owe the greatest thanks to my family. Without the sacrificial support of my wife, Jimi Cho, and without the pleasant cheer of my son and daughter, Sean and Diana, I could not have completed this dissertation. I owe special thanks to my sister and her husband, Phoenix and Bo Kim, for their devoted help and love for my family. Most of my writings including this dissertation were edited by my brother-in-law, Bo. I want to thank my sister, Femme, for her cheering. I am deeply grateful for the help and understanding of my parents-in-law. I would also like to heartily thank my parents for their constant love and support.

TABLE OF CONTENTS

LIST OF FIGURES

LIST OF TABLES

ABSTRACT

Steel fiber reinforced asphalt concrete (SFRAC) is suggested in this research as a multifunctional high performance material that can potentially lead to a breakthrough in developing a sustainable transportation system. The innovative use of steel fibers in asphalt concrete is expected to improve mechanical performance and electrical conductivity of asphalt concrete that is used for paving 94% of U. S. roadways.

In an effort to understand the fiber reinforcing mechanisms in SFRAC, the interaction between a single straight steel fiber and the surrounding asphalt matrix is investigated through single fiber pull-out tests and detailed numerical simulations. It is shown that pull-out failure modes can be classified into three types: matrix, interface, and mixed failure modes and that there is a critical shear stress, independent of temperature and loading rate, beyond which interfacial debonding will occur.

The reinforcing effects of SFRAC with various fiber sizes and shapes are investigated through indirect tension tests at low temperature. Compared to unreinforced specimens, fiber reinforced specimens exhibit up to 62.5% increase in indirect tensile strength and 895% improvements in toughness. The documented improvements are the highest attributed to fiber reinforcement in asphalt concrete to date.

The use of steel fibers and other conductive additives provides an opportunity to make asphalt pavement electrically conductive, which opens up the possibility for multifunctional applications. Various asphalt mixtures and mastics are tested and the results indicate that the electrical resistivity of asphaltic materials can be manipulated over a wide range by replacing a part of traditional fillers with a specific type of graphite powder.

Another important achievement of this study is development and validation of a three dimensional nonlinear viscoelastic constitutive model that is capable of simulating both linear and nonlinear viscoelasticity of asphaltic materials. The developed model is formulated in finite strain for asphalt binder and in infinitesimal strain for asphalt

concrete. Comparisons to published test data show that the model is capable of modeling behavior over a wide range of stress, temperature and strain rate conditions.

The performance of asphalt plug joints (APJ) which are used as expansion joints in bridges is investigated. The study sheds light on the reasons for premature APJ failures observed in the field, based on which improved joint details are proposed.

CHAPTER 1
INTRODUCTION

1.1 BACKGROUND

Highways are the blood vessels of modern society. The U.S. spends $81 billion annually on the construction of highways and streets (U.S. Department of Commerce 2005), and 94 percent of more than 2.6 million miles of paved roads in the U.S. are surfaced with asphalt concrete (NAPA 2009). With weathering and sustained use, asphalt pavements suffer deterioration and require maintenance throughout their typical 26-30 years of designed service life. Rutting and cracking are key failure modes for asphalt pavement that are commonly the target of maintenance programs. These programs tend to be worker- and equipment-intensive and, therefore, expensive. For example, the State of Michigan has 27,345 lane miles of highway network and spends $400 million per year on maintenance (Galehouse 2002). In addition to direct costs, the indirect socioeconomic ripple effects of asphalt pavement construction are substantial. Nationwide traffic congestion results in Americans wasting 4.2 billion hours and $78.2 billion annually (ASCE 2009).

It is well known that the environmental impact of the construction industry is higher than its economic portion. According to Hendrickson and Horvath (2000), the greenhouse gas emissions and toxic release from major U.S. construction sectors are 15% and 9.7% of U.S. totals, while their construction cost is only 6.5% of the U.S. GDP. Therefore, it can be concluded that an extension in the service life of asphalt pavements, which represents a significant portion of the construction industry's efforts, can lead to enormous improvements in the life cycle costs and sustainability of our transportation system.

The concept of a multifunctional high-performance asphaltic composite, comprised of

asphalt concrete, fiber additives and conductive fillers (see Fig. 1.1), is introduced in this dissertation as an innovative technology that could lead to a breakthrough in sustainable pavement systems. The premise is that the addition of a small quantity of steel fibers will: 1) significantly improve the mechanical properties and, therefore, the durability and longevity of asphalt concrete, and 2) along with conductive fillers, make asphalt concrete electrically conductive, paving the way for new opportunities for innovation in asphalt technology as explained below.

Adding short random fibers into asphalt concrete does not require much additional effort in installation of asphaltic pavement, and fiber reinforcement can be combined with other chemical modifiers to maximize the benefits of both types of additives. In addition to improving mechanical properties, imparting electrical conductivity can transform asphalt concrete into a multi-functional material. Multifunctional materials are materials that have at least one other function beyond their basic and traditional attributes (Gibson 2010). Electrically conductive asphalt concrete has potential for several innovative applications such as self-healing, self-monitoring, and snow and ice removal. By providing improved mechanical performance and multifunctional applications, steel fiber reinforced asphalt concrete (SFRAC) is expected to become a candidate for fulfilling demands for improved sustainability and life cycle costs as depicted in Fig. 1.2.

In addition to pavement applications, another possible application of SFRAC is in asphalt plug joints (APJs). An APJ is a type of bridge expansion joint providing quick, easy, and cheap installation along with good surface flatness. However, APJs are known to suffer from premature failure. While materials such as SFRAC could potentially help reduce the propensity for premature failure, APJs also have other deficiencies associated with the way they are constructed that make them prone to failures. These deficiencies are identified and addressed in this work.

1.2 OBJECTIVES

The overarching goals of this research are to: 1) develop a multifunctional high-performance asphalt composite, and 2) study its mechanical and electrical conductivity properties. Fig. 1.3 illustrates the roadmap of the research, including the path towards

future research efforts that stem naturally from the current research effort. Specific objectives are as follows:

- ***Constitutive Modeling***: In pursuing a high performance asphaltic composite, it is necessary to resort to computational modeling with an accurate constitutive model. Therefore, one of the key goals of this work is to develop rigorous constitutive models for asphalt binder and asphalt concrete. Since asphalt binder can undergo large strains, the developed model must be formulated within a finite strain framework. In contrast, asphalt concrete models need only be formulated within a small strain framework since it is expected that pavement behavior will impose small strain demands. It is important that the developed models be capable of simulating both linear and nonlinear viscoelasticity of asphaltic materials with a single set of material parameters and that the models be capable of predicting behavior over a wide range of stress, temperature and strain rate conditions.
- ***Development and Characterization of SFRAC***: In order to successfully develop and optimize SFRAC, it is necessary to develop a fundamental understanding of the interaction between fiber and viscoelastic matrix. To this end, an objective of this work is to conduct single fiber pull out tests and simulations at various temperatures and loading rates. To develop an understanding of composite behavior in tension, indirect tension tests of asphalt concrete specimens reinforced with various types and contents of fibers will be conducted. The tests will be geared towards investigating performance improvements due to fibers and, hence, to determine optimum fiber properties and contents.
- ***Conductivity Properties of Asphalt***: To enable multifunctional properties of the new material, it is necessary to develop an understanding of the electrical conductivity of asphalt. Therefore, one of the objectives of this work is to investigate the use of various types and quantities of fillers and fibers, with the goal of achieving precise control over the electrical conductivity properties of SFRAC.
- ***Asphalt Plug Joints***: Another of the objectives of this work is to investigate the performance of APJs. By resorting to detailed numerical simulations, the research

effort will seek to shed light on the reasons for premature APJ failures observed in the field, and propose improved joint details.

1.3 STRUCTURE OF THE DISSERTATION

This dissertation is composed of eight chapters covering three subjects: constitutive modeling (Chapter 3), SFRAC (Chapter 4, 5, and 6), and asphalt plug joint (Chapter 7). Fig. 1.4 shows the structure of this dissertation, and the details of each chapter are as follows:

Chapter 1: Introduction. This chapter covers the background, objectives, and methodology of the research. A research roadmap including future work is presented.

Chapter 2: Literature Review. A literature survey of the main topics studied in this dissertation is presented. Previous research on fiber reinforced asphalt concrete, electrically conductive asphalt concrete, constitutive modeling for asphaltic materials, and bridge asphalt plug joints are discussed.

Chapter 3: Constitutive Modeling for Asphalt Binder and Mixture. This chapter proposes a three dimensional nonlinear viscoelastic constitutive model that is capable of simulating both linear and nonlinear viscoelasticity of asphaltic materials with a single set of material parameters. The developed model is formulated in finite strain for asphalt binder and in infinitesimal strain for asphalt concrete. Comparisons to published test data show that the model is capable of modeling behavior over a wide range of stress, temperature and strain rate conditions.

Chapter 4: Pull-Out Behavior of Straight Steel Fiber from Asphalt. In an effort to understand the reinforcing mechanism in SFRAC, the interaction between a single straight steel fiber and the surrounding asphalt matrix is investigated through single fiber pull-out tests. The pull-out tests are conducted at various temperatures and loading rates, and the pull-out mechanisms are elucidated with the help of detailed numerical simulations.

Chapter 5: Indirect Tensile Strength and Toughness of Steel Fiber Reinforced Asphalt Concrete at Low Temperature. The reinforcing effects of steel fiber additives for asphalt concrete are investigated through indirect tension tests at low temperature.

Focusing on cracking resistance, indirect tensile strength, fracture energy, and post-cracking energy are obtained from the tests for the specimens reinforced with various diameters, lengths, deformed shapes, and contents of steel fibers.

Chapter 6: Imparting Electrical Conductivity into Asphaltic Composite. The use of steel fibers and other conductive additives provide an opportunity to make asphalt pavement electrically conductive, which opens up the possibility for multifunctional applications. Aiming to manipulate the electrical resistivity of asphalt over a wide range, asphalt mastics with various conductive fillers are tested and reported on in this chapter.

Chapter 7: Improved Geometric Design of Bridge Asphalt Plug Joint. This chapter introduces APJ, which are a kind of bridge expansion joint made from asphalt mixture. The chapter discusses reasons for premature APJ failures observed in the field, based on which improved joint details are proposed.

Chapter 8: Conclusions and Future Research. This chapter provides a summary of the major conclusions that can be drawn from the research and discusses future research efforts that can stem from this work.

1.4 KEY FINDINGS OF THE RESEARCH

Important accomplishments of and findings from this research are as follows:

- A constitutive model that is able to simulate asphalt behavior in both linear and nonlinear viscoelastic ranges with a single set of material parameters is developed. The model is formulated in finite strain for asphalt binder and in infinitesimal strain for asphalt concrete and shows good agreements with experimental data over wide ranges of temperature, stress, and strain rate.
- Fundamental information for understanding the behavior of SFRAC are provided through single fiber pull-out tests. The failure modes are classified based on the failure characteristics. Based on the test data and simulation results, a hypothesis is presented that there is a critical shear stress that controls the pull-out modes that is independent of temperature and loading rate.

- Indirect tension tests at low temperature demonstrate that steel fiber reinforcement can significantly improve cracking resistance. By testing various sizes and shapes of fibers, the effects of diameter, length, deformed shape, and content of steel fibers are clarified. Compared to unreinforced specimens, fiber reinforced specimens saw substantial improvements in indirect tensile strength, fracture energy and toughness. The improvements are the highest documented mechanical improvements attributed to fiber reinforcement in asphalt concrete to date.
- A specific flake type natural graphite that is best for imparting conductivity is identified, and it enables fine control of electrical resistivity of asphaltic composites.
- Detailed finite element analyses provide a thorough understanding of the behavior and vulnerabilities of APJ subjected to thermal and traffic loads. Based on this understanding, an improved geometric design of APJ that can mitigate the risk of premature failure is proposed.

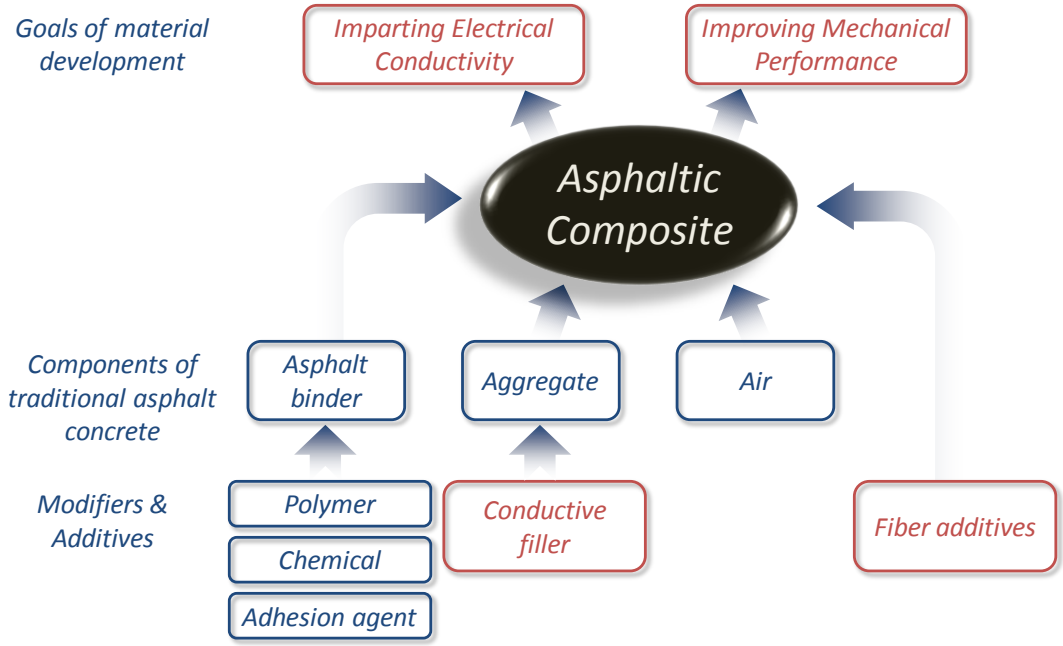

Fig. 1.1 Strategy for developing the multifunctional high performance asphaltic composite

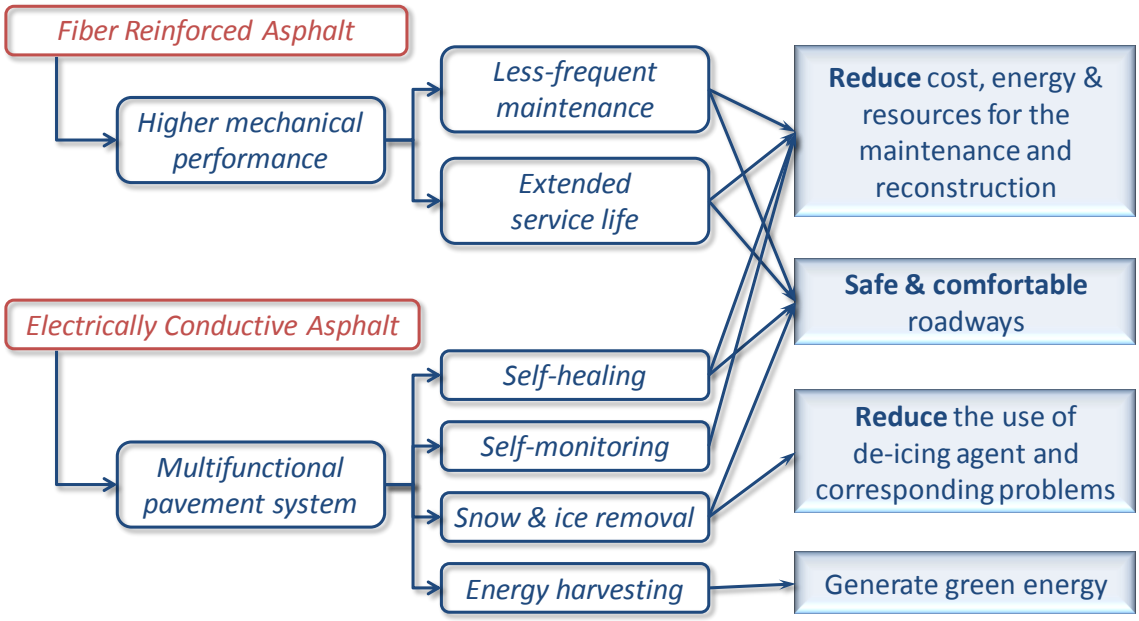

Fig. 1.2 Methodologies and target applications of the research, and relationships to sustainability.

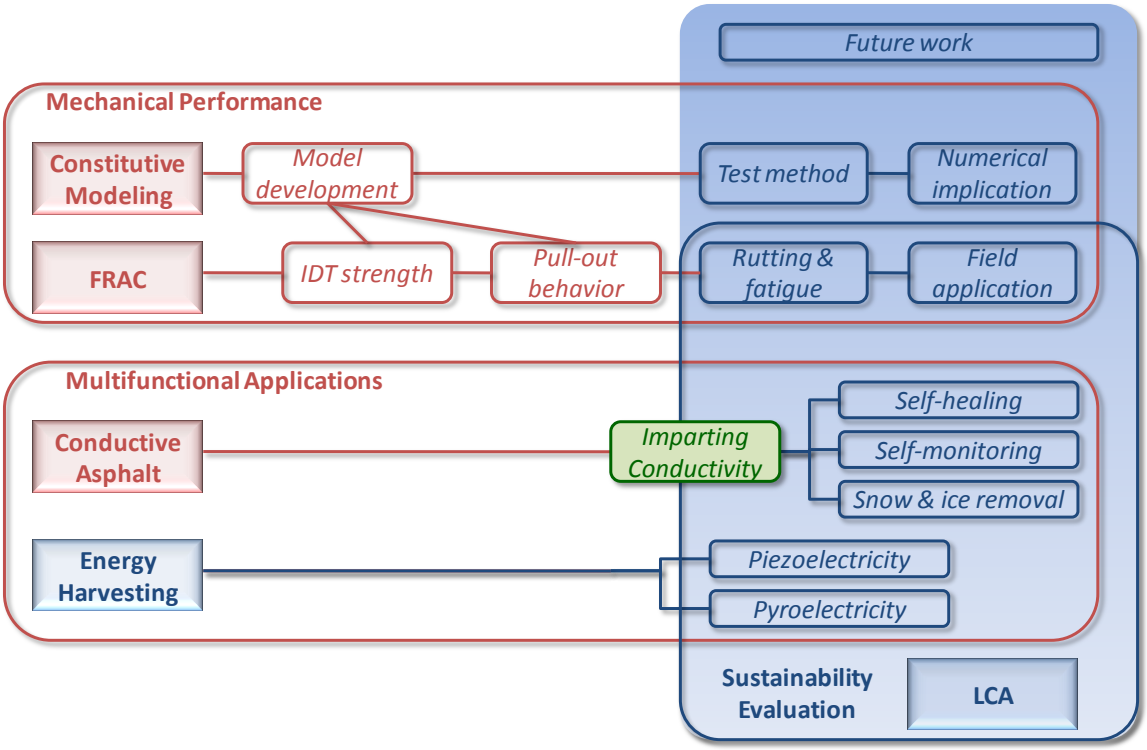

Fig. 1.3 Research roadmap including future work

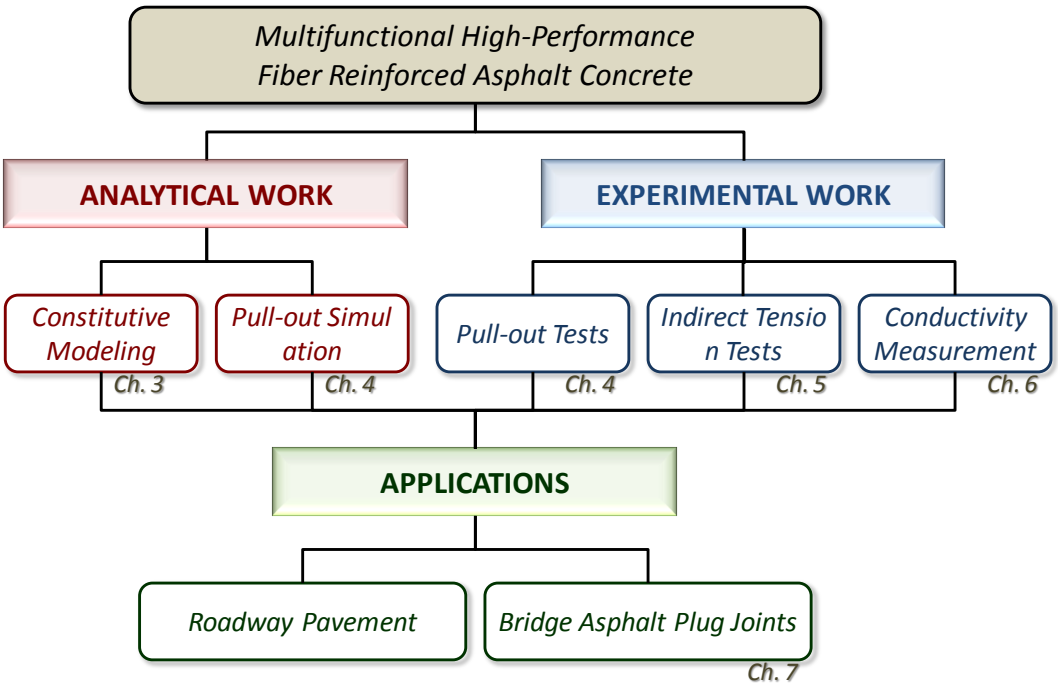

Fig. 1.4 Structure of the dissertation

REFERENCES

ASCE (2009). *2009 Report Card on America's Infrastructure*, American Society of Civil Engineers.

Galehouse, L. (2002). "Strategic planning for pavement preventive maintenance: Michigan Department of Transportation's "Mix Of Fixes" Program." *TR News*, 219, 3-8.

Gibson, R. F. (2010). "A review of recent research on mechanics of multifunctional composite materials and structures." *Composite Structures*, 92, 2793-2810.

Hendrickson, C., and Horvath, A. (2000). "Resource use and environmental emissions of U.S. construction sectors." *Journal of Construction Engineering and Management*, 126(1), 38-44.

NAPA (2009). *Black and Green: Sustainable Asphalt, Now and Tomorrow*, National Asphalt Pavement Association, Lanham, Md.

US Department of Commerce (2005). *Economics and Statistics Administration*, US Census Bureau.

CHAPTER 2
LITERATURE REVIEW

This chapter presents a literature survey of the main topics studied in the dissertation. The first section discusses previous studies that employed fibers for improving mechanical performance or enhancing multifunctional applications of asphalt pavements. The second part summarizes previous constitutive models and efforts undertaken by others to understand the complex behavior of asphaltic materials. The third section introduces the usage, advantages, and recent studies of bridge asphalt plug joints.

2.1 FIBER REINFORCEMENT FOR ASPHALT CONCRETE

Most of the problems in asphalt concrete stem from the poor properties, including thermal sensitivity, of asphalt binder (Roberts et al. 2002). In a historical review of asphalt mixture design technology published in 2002, Roberts et al. (2002) stated that, rather than mixture design, improvement of binder properties using modifiers or additives will lead to a true revolution in paving technology. Bahia (2006) investigated the effect of fifty five modifiers including styrene butadiene polymers, anti-stripping agents, hydrocarbons, fibers, mineral fillers, anti-oxidants, and sulfur extenders. The effects of asphalt modifications were listed as improving performance regarding (1) permanent deformation, (2) fatigue cracking, (3) low temperature cracking, (4) moisture damage, and (5) oxidative aging. The usage, history, and concentration ranges of various modifiers and additives in hot mix asphalt (HMA) based on a recent and extensive survey can be found in Mundt et al. (2009). According to Nicholls (1998), the modifiers and additives are classified into four categories: (1) polymer modifiers, (2) chemical modifiers, (3) adhesion (anti-stripping) agents, and (4) fiber additives.

Currently, the most popular choice for improving mechanical properties of asphalt concrete is to use polymer modifiers. The effects and characteristics of some popular

polymer modifiers explored in recent research are summarized in Yildirim (2007). The basic effect of polymer modifiers is to reduce the temperature susceptibility of the stiffness of asphalt binder within the service temperature range. Low viscosity at high temperature and high brittleness at low temperature are important causes of rutting, cracking, and other deteriorations of asphalt pavement. In general, the stiffness of polymers is less dependent on temperature than asphalt. By blending in polymer modifiers, the temperature susceptibility of asphalt can be reduced, and correspondingly, asphalt performance can be improved. However, achieving appropriate chemical balance between polymers and asphalt is difficult due to the complex chemical nature of both binder and polymers. Polymer modifiers are divided into two types: (1) plastomers (crystalline polymers) including polypropylene, polyethylene, polyvinyl chloride (PVC), polystyrene, ethylene vinyl acetate (EVA), and ethylene methyle acrylate (EMA), and (2) elastomers (thermoplastic rubbers) including natural rubber, styrene-butadiene rubber (SBR), styrene-butadiene-styrene (SBS), styrene-isoprene-styrene (SIS), polybutadiene (PBD), and polyisoprene (Nicholls 1998).

Chemical modifiers such as sulphur, copper sulphate, lignin, and other metallic compounds have been used to improve workability, performances, and resistance to oxidative aging. However, these are less popular choices than polymer modifiers mainly due to toxic emissions at high temperature during construction (Nicholls 1998). Adhesion agents such as fatty amidoamine, polyamine, organo-metallics, acids, amine blends, and lime are used to prevent failure of bond between the binder and aggregates due to the presence of water, which is called 'stripping'. According to a recent survey conducted by Mundt et al. (2009), the most common anti-stripping agent is lime.

Traditionally, fibers have been added to asphalt mixture as a stabilizer that enriches adhesion between binder and aggregates during placement. Open-graded (porous asphalt) or gap-graded (stone mastic asphalt, SMA) friction courses are vulnerable to draindown and raveling. Draindown is the segregation of mixture during transportation and installation and raveling is the loss of pavement materials at the surface while in service. These problems are caused by the drainage of binder, and can be significantly reduced by adding a small amount of fiber (Nicholls, 1998). Mineral fibers including asbestos and rook wool are the most common choices for this purpose in the United States (Mundt et

al. 2009), while cellulose fibers are most widely used in Germany (Nicholls, 1998).

The recent focus on sustainability has heightened interest in using recycled waste materials for asphalt pavement construction. For example, transportation agencies in Arizona and California have studied ways of utilizing crumbed rubber, which is produced from waste tires in asphalt concrete. Their studies verified that blending 20% of crumbed rubber to liquid asphalt increases durability and reduces traffic noise. Pavement material with crumbed rubber is called Rubberized Asphalt Concrete (RAC). The Arizona Department of Transportation (ADOT) has recycled 15 million tires for field application of RAC since 1988 (Hicks 2002). Huang et al. (2007) summarize the required properties and performance of asphalt pavements using waste materials including waste glass, steel slag, scrap tires, and recycled plastics.

2.1.1 Use of Fibers as Stabilizer

Putman and Amirkhanian (2004), Hassan and Al-Jabri (2005), Muniandy and Huat (2006), Wu et al. (2006b), and Alvarez et al. (2009) investigated the stabilizing effects of cellulose, oil palm, date palm, polyester, and some waste fibers for porous asphalt or SMA. Without exception, significant improvements in draindown and raveling resistances were observed when fibers were added. Compared to inorganic fibers that usually have smooth surfaces, organic fibers showed a higher stabilizing effect, which was attributed to their rough surface.

Since the objective of porous asphalt is to facilitate runoff of rain water, moisture susceptibility is a very important factor for pavement performance. Moisture susceptibility of asphalt concrete is represented by TSR (Tensile strength ratio, ASTM D 4867) which is a percentage ratio of wet strength to dry strength. Putman and Amirkhanian (2004) and Hassan and Al-Jabri (2005) evaluated TSR, and concluded that adding fibers does not weaken the wet strength of SMA and porous asphalt. Wu et al. (2006b) noted that adding 0.3% (by weight of the mixture) of cellulose or polyethylene fibers improves the indirect tensile strength, rutting resistance, and moisture susceptibility of porous asphalt.

2.1.2 Mechanical Improvement of Asphalt Pavement

The forms of mechanical distress of general (dense-graded) asphalt pavement are rutting, fatigue, and reflective cracking. Until recently, polymeric or chemical modifiers have been considered as a remedy for these phenomena (Nicholls 1998; Yildirim 2007). On the other hand, installation of fabric reinforced interlayer (geotextile or wire mesh) as an alternative remedial approach was investigated by Elseifi and Al-Qadi (2005), Lee (2008), and Siriwardane (2010).

While fibers have been widely used as a stabilizer for porous asphalt and SMA, their use for improving mechanical performance was not investigated till recently. Some field applications of fibers were tried in the 1980's to improve the mechanical performance of asphalt pavement (Toney 1987; Maurer and Malasheskie 1989; Serfass and Samanos 1996; Huang and White 1996). Although those empirical field applications of fiber reinforced asphalt concrete (FRAC) showed some improvements in rutting and fatigue resistances, the studies concluded that the benefits of FRAC are not enough to overcome its initial installation costs (Maurer and Malasheskie 1989).

Despite the poor reputation that fiber reinforcement received in earlier studies, new interest has arisen in the recent past with a number of studies reported in 2009 and 2010. In the following sections, the field experiences of FRAC pavement are summarized and the recent laboratory investigations are reviewed.

2.1.3 FRAC Field Experience

According to Toney (1987), the City of Tacoma installed FRAC pavement on three major intersections in 1983. Polyester fibers 6.35 mm (1/4 in.) in length were added to the asphalt at 0.25 % by weight through a dry mix process. Toney (1987) concluded that no significant distress was observed at the control and FRAC sections after four years. Due to the lack of qualified evaluation, this experience did not provide any useful information about the reinforcing effect of the added fibers.

Meaningful information about the reinforcing effects of fibers can be found in the field experiments reported by Maurer and Malasheskie (1989). In 1983, Pennsylvania Department of Transportation (DOT) replaced a 1,326m long and 17 m wide interlayer and/or overlay using four types of paving fabrics and two types of discrete fibers

(polypropylene and polyester). After 8, 26, and 44 months, the length of the reflective cracks were compared to the control (no reinforcement) section, and corresponding life-cycle costs (LCC) were evaluated. The highest crack reduction was observed at one of the fabric reinforced pavements (reduced 92.2% and 52.7% of reflective cracks at 8 month and 44 month surveys, respectively). The pavement reinforced with 0.3% (by weight of the mixture) of polyester fibers showed the second highest reduction of reflective cracking (26.8% at 8 month and 50.8% at 44 month). One of the important advantages of fiber reinforcement is that it minimizes construction effort compared to using a fabric reinforced interlayer, which requires an expensive and difficult placing process. According to a simple LCC evaluation considering the costs for installation and repair (crack sealing), the polyester fiber reinforcement turned out to be the least expensive and easiest method to reduce reflective cracking. However, Maurer and Malasheskie (1989) concluded that the economic benefits of crack reduction were less than the additional costs required for initial installation. Although the limited LCC evaluation suggested a negative result for applications of fiber reinforcement, the study by Maurer and Malasheskie (1989) is important because it showed that FRAC is effective in reducing reflective cracking in field application, and can be a superior option to fabric reinforcement.

Another notable field experience was reported by Huang and White (1996). Indiana DOT constructed a fiber reinforced asphalt overlay over a deteriorated concrete slab in 1984. 0.25, 0.30, and 0.38% of polypropylene fibers by weight of the mixture were tested. Monitoring results over a 5-year period showed that FRAC was effective in reducing reflective cracking. Using the samples obtained from the field, Huang and White (1996) measured actual fiber content and volumetric properties, and conducted fatigue and complex modulus tests. The actual fiber content obtained by fiber extraction tests showed large differences in target fiber content (-44 ~ +22%). They concluded that the differences between actual and target fiber content reflect the need for improved fiber blending techniques. Two main reasons may be blamed for the poor fiber distribution. First is the relatively low melting point of the fibers. The fibers used by Indiana DOT were polypropylene fibers of 4±1 denier (thickness ≈ 0.04 mm) and 10±2 mm in length, with a melting point of 146°C, which is lower than the mixing temperature (150°C). Second is

the high aspect ratio (length/diameter = 250) of the used fibers. The clumping of lengthy fibers, called "balling" (Abtahi et al. 2010), impedes good blending of fibers. Moreover, air voids of FRAC measured by Huang and White (1996) were higher than the mixture without fibers. Their fatigue test results showed that 0.22% fiber specimen had two times higher fatigue life. Meanwhile, complex modulus and phase angle (indices for rutting) were observed not to be significantly affected by fiber contents.

The various field application experiences of FRAC in France were summarized by Serfass and Samanos (1996). They concluded that if its design and application are properly controlled, all kinds of fiber modified wearing courses have satisfactory resistance to moisture damage, thermal cracking, raveling, and even aging. On the other hand, some drawbacks were identified. The performance of FRAC is sensitive to fiber-binder ratio, and excessive fiber contents can cause poor workability and compactability. Uniform dispersion of fibers is another critical issue of FRAC. In addition, Serfass and Samanos (1996) noted that FRAC pavement should be sufficiently cooled down before opening to traffic because freshly-laid FRAC is sensitive to early traffic.

2.1.4 Laboratory Investigations of the Reinforcing Effects of Fibers

While the use of fibers in porous asphalt and SMA is intended to prevent draindown, adding fibers to general dense-graded asphalt concrete aims to enhance mechanical performance by exploiting the reinforcement effect attributed to the fibers. One of the earliest laboratory studies of the reinforcing effect was conducted by Freeman et al. (1989). They measured indirect tensile strengths (ITS) of dry and wet asphalt concrete specimens to evaluate moisture susceptibility. The mixture was general dense-graded asphalt concrete with 0.2-0.5% polyester fibers by weight of the mixture. The dimensions of the fibers were 6-12 mm in length, and 15-30 denier (approximately 0.15-0.30 mm in thickness).

The results of the tests, which were conducted at room temperature, show that wet ITS increases and dry ITS decreases (up to 10 %) by adding polyester fibers, and consequently, the tensile strength ratio (TSR, ratio of wet ITS to dry ITS) increases up to 15% when 0.5% of 12 mm and 30 denier fiber is added. This implies that moisture susceptibility can be improved by adding fibers, and using thicker, longer, and larger

amount of fibers are better for moisture damage resistance. Freeman et al. (1989) evaluated toughness as well. Dry and wet toughness of FRAC were higher by up to 25% and 120%, respectively, than that of the control mixture. Optimum asphalt contents evaluated by Marshall mix design procedures increased with the fiber content.

Polyester fibers were combined with various modifiers including styrene-butadien-styrene (SBS), low density polyethylene, and carbon black, and increases in strength and fatigue life were evaluated by Kim et al. (1999). In their tests, Marshall stability (maximum load before failure at 60°C), indirect tensile strength, and fatigue performances significantly increased when fibers were added. Kim et al. (1999) demonstrated that fiber reinforcement can be accompanied by other polymer or chemical modifiers, and synergistic effects can be expected when properly combined. Fatigue life improvements due to these combinations are illustrated in Fig. 2.1.

Bueno et al. (2003) published results that contradicted the above research on fiber reinforcing effects. They investigated the reinforcing effects of fibers for an emulsified cold-mix dense graded asphalt concrete. Marshall stability and resilient modulus were reduced by the addition of 0.1-0.5% (by weight) polypropylene fibers that had lengths of 10, 20, and 40 mm. However, rutting resistance was not affected by addition of fibers.

Lee et al. (2005) examined the influence of carpet fibers on the fatigue cracking resistance of asphalt. Fracture energy was used as a measure of fatigue resistance. They noted up to 85% increase in the fracture energy as a result of adding recycled carpet fibers. To estimate the maximum effective fiber length, Lee et al. (2005) conducted a single fiber pull-out test. With a rate of 5 mm/sec at 20°C, 15 denier (thickness=0.15 mm) nylon ruptured at about 9 mm of embedded depth. This is the only documented pull-out test for FRAC.

Kutay et al. (2008) reported an interesting observation on FRAC in their paper focusing on modeling of various modified asphalt concrete. They stated that "*even though many small (micro) cracks developed on the surface of the fiber lane, they did not coalesce and lead to a large alligator type cracks which was seen in other lanes... Therefore, it was thought that even though the damage occurred earlier in Fiber lane in the form of small cracks, they did not propagate to form large cracks due to the reinforcing effect of the fibers in the mixture.*" The formation of the micro cracks is

frequently observed in fiber reinforced concrete, and is considered to be a positive sign of the proper fiber reinforcement.

Tapkin (2008) examined the effect of polypropylene fibers on asphalt performance. Overall, performance of general dense graded asphalt concrete was improved by adding polypropylene fibers ranging from 0.3% to 1.0% by weight. Marshall stability increased by up to 58%, and fatigue life was slightly extended. In addition, flow decreased by up to 59 % and air voids slightly increased. In a subsequent paper, Tapkin et al. (2009) showed that rutting resistance at high service temperature (50°C) also improved by adding polypropylene fibers. Fig. 2.2 compares the specimens with and without fibers after repeated creep tests.

Li et al. (2008) investigated the reinforcing effects of carbon fiber and graphite filler on the mechanical performance of asphalt. The dimensions of the carbon fiber used was 5 mm in length and 0.010-0.014 mm in diameter, and the particle size of the graphite was smaller than 0.15 mm. The mixture was designed to have 12.5 mm Superpave gradation, and 0.3% of the carbon fibers by weight of aggregate and 12-18% of the graphite by volume of asphalt were added. Up to 20% increase of indirect tensile strength was observed at 20°C. However, improvements in fatigue life were not evident.

A comparative study of the effects of cellulose, polyester, and mineral fibers was conducted by Ye et al. (2009). Based on the dynamic modulus test and indirect tension fatigue test, Ye et al. (2009) concluded that fatigue resistance can be improved by adding fibers. In addition to Li et al. (2008) and Ye et al. (2009), several studies on FRAC conducted in China have been recently presented at international conferences. Those are Fu et al. (2007, glass fiber), Ling et al. (2008, various fibers), Zhou et al. (2009, various fibers), and Yu and Sun (2010, polyester fibers).

Anurag et al. (2009) investigated indirect tensile strength and moisture susceptibility of FRAC using waste polyester fibers. Fig. 2.3 shows the dry and wet strengths and the fiber contents. Fig. 2.3 illustrates the typical trend of indirect tensile strength of FRAC, which is slight decrease in dry strength and increase in wet strength with fiber addition, results that are in accord with the studies reviewed above.

Another comparative study of the effects of polyester fibers, polyacrylonitrile, lignin, and asbestos is Chen et al. (2009). Based on the recommendations of the manufacturers,

0.25-0.40% of fibers were added to general (dense graded) asphalt concrete. Optimum asphalt content, volumetric properties, Marshall stability, and flow value (Marshall flow which is defined as the deformation at failure) were measured. By comparing Marshall stabilities of mixtures with constant asphalt content and optimum asphalt content, Chen et al. (2009) reached a critically important conclusion that was not identified by earlier researchers. As shown in Fig. 2.4c, when the same amount of binder is added, Marshall stabilities of fiber modified specimens are slightly lower than the control mixture, while those with optimum binder contents are higher than the control mixture. As pointed out by other investigators (Freeman et al. 1989; Huang and White 1996; Kim et al. 1999; Tapkin et al. 2009), adding fibers causes an increase in optimum asphalt content due to the additional surface area of fibers that need to be coated by the binder. Therefore, as illustrated in Fig. 2.4b, when the same amount of binder is used, air voids of FRAC will increase due to insufficient binder, resulting in strength reduction. As compared in Fig. 2.4c, when the optimum asphalt contents are added to the FRAC, the problem vanishes and the reinforcing effect becomes obvious. Fig. 2.4d shows improvement in Marshall flow due to fiber addition implying an increase in toughness.

Xu et al. (2010) measured indirect tensile strength and rut depth of FRACs with the optimum asphalt contents as identified in Chen et al. (2009). Fig. 2.5a compares stress strain curves obtained from indirect tension tests (at 25°C), and Fig. 2.5b shows the influence of fiber contents on rut depth (at 60°C) when polyester fibers are added. Fig. 2.5 shows slight improvements in strength and rutting resistance due to the fiber additives.

The most significant improvement in FRAC mechanical behavior is reported by Kaloush et al. (2010). By adding 0.045% (by weight of mixture) of commercial fibers, named FORTA-FI, Kaloush et al. (2010) observed 25-50% increase in indirect tensile strength, 50-75% increase in fracture energy, and improvement in rutting and fatigue resistances (Fig. 2.6). FORTA-FI is a blend of polypropylene and aramid fibers 19 mm in length, produced by FORTA Corp. The tested mixtures were prepared by the fiber manufacturer, and the blending ratio of polypropylene and aramid was not specified. Another observation from this study is that the increase in strength due to fibers is more significant at lower temperature than at higher temperature (Fig. 2.6a), which implies a high resistance to thermal cracking.

2.1.5 Tests for Asphalt Binder - Fiber Mastics

Serfass and Samanos (1996) suggested that tests of mastics (asphalt + fibers) and mortars (asphalt + fiber + fine aggregates) can help researchers understand the behavior of FRAC. To compare the stabilizing effects of various (Cellulose, Mineral, Glass, and polyester) fibers, Peltonen (1991) conducted elongation tests for the fiber-bitumen mastics, and found that polyester fiber is particularly promising for improving strength and elastic recovery as illustrated in Fig. 2.7. Such a significant difference was not observed in tests of asphalt concrete. Of the fibers considered, cellulose fibers showed best improvement in stability. Another study for binder-fiber mastics was conducted by Chen and Lin (2005). They measured viscosity, toughness, tenacity, and complex modulus of asphalt binders containing mineral (basalt), cellulose, and polyester fibers. Fig. 2.8a shows the force-elongation curves for various contents of mineral fibers at 25°C. With the increase of fiber content, strength increases while the elongation at rupture decreases. As a result, the toughness of binder-fiber mastics varied as shown in Fig. 2.8b. In addition, they observed that complex modulus, which is an indicator for rutting resistance, was improved by adding fibers. Recommended optimum fiber content for improving rutting resistance was 0.3-0.4% by weight. Based on their experiments, Chen and Lin (2005) concluded that proper use of fibers can satisfy both requirements of stabilization and reinforcement.

One of the important findings of SHRP (Strategic Highway Research Program) is the relationship between rheological measurements of binder and end performance of the asphalt mixture. According to SHRP-A-409 (1994), the number of cycles to failure and rut depth decrease with increase of $G^*\sin\delta$ and $G^*/\sin\delta$, respectively. Where, G^* is complex shear modulus and δ is phase angle that can be evaluated by the dynamic shear rheometer (DSR) test. $G^*\sin\delta$ and $G^*/\sin\delta$ are called fatigue and rutting parameters, respectively. Wu et al. (2006a), Wu et al. (2008), and Ye and Wu (2010) evaluated the fatigue and rutting parameters for mastics with various fibers including cellulose, polyester, and mineral fibers, and reported improvements in fatigue and rutting parameters. Fig. 2.9 is a comparison of creep strain curves of fiber modified mastics to that of binder without fibers.

Chen and Xu (2010) investigated the stabilizing and reinforcing effects of fibers for

mastics modified by five types of fibers, and reported that polyester and polyacrylonitrile fibers have a better reinforcing effect while lignin and asbestos are better for stabilizing.

2.1.6 Multifunctional Applications of FRAC

Multifunctional materials are materials that have at least one other function beyond its basic and traditional attribute. According to Gibson (2010), functions of interest can be divided into structural properties including strength, stiffness, fracture toughness, and damping, and non-structural functions such as electrical and/or thermal conductivity, sensing and actuation, energy harvesting/storage, self-healing capability, electromagnetic interference (EMI) shielding, recyclability and biodegradability. Fiber reinforced polymers as well as nanomaterials are the currently most actively studied multifunctional materials.

Several studies on the electro-mechanical applications of asphalt concrete using conductive fibers and fillers were published recently. Asphalt binder and asphalt concrete are insulating materials, but their conductive property can be remarkably improved by adding conductive fillers or fibers. The first idea of using electrical conductivity for asphalt concrete was suggested in the 1960s. Minsk (1968) tried to make electrically conductive asphalt concrete by adding graphite for the purpose of controlling snow and ice accumulation on roadway surfaces. However, use of electrical conductivity in asphalt concrete was not studied further until Wu et al. (2003), who investigated the reduction of electrical resistance of asphalt associated with using graphite, carbon black, carbon fiber, and their combinations (Wu et al. 2005). Liu and Wu (2009) studied the piezoresistivity (variation of electrical resistance with stress level) of asphalt for the purpose of structural health self-monitoring. In addition, mechanical improvements due to the conductive additives were investigated by Wu et al. (2010).

Similar studies were conducted by a research team at Changsha University in China. Huang et al. (2006) evaluated improvement in conductivity of asphalt concrete by adding steel fiber, aluminum chips, and graphite, and concluded that micron-scale steel fibers are most efficient for introducing conductivity. Subsequently, Huang et al. (2009) published a paper on the influence of the conductive additives on the mechanical performance of asphalt. Fig. 2.10 shows the variation of electrical and mechanical properties versus

conductive additives. In Huang et al.'s (2009) tests, steel fibers significantly improved rutting resistance, but did not improve strength and fracture energy.

Comprehensive information on the electrical conductivity of asphalt concrete was provided by a research team in Delft University in Netherlands. Garcia et al. (2009) investigated the variation in electric conductivity of asphalt mortar (binder + sand + conductive fillers) with the contents of conductive additives including steel wool (diameter ranged 0.00635-0.00889 mm) and graphite (particle size of less than 0.02 mm). Fig. 2.11 summarizes the findings of Garcia et al. (2009). Fig. 2.11a illustrates that there is a critical threshold in the contents of conductive additives that makes the mixture conductive or non-conductive. Similar to Huang et al. (2009), they concluded that steel fibers are more effective for inducing conductivity than graphite. One of the new findings in Garcia et al. (2009) is that the conductivity is dependent not only on the contents of conductive additives but also on the sand-asphalt ratio, and that those factors cannot be considered separately. As shown in Fig. 2.11b, when the optimum conductivity (least electrical resistance) is reached, a small increase in the sand-asphalt ratio causes an increase in electric resistance. On the other hand, a small decrease of sand content can make the mixture nonconductive. Fig. 2.11d illustrates the relationships between the sand-asphalt ratio, conductive additive content, and electric resistance. The purpose of the study by Garcia et al. (2009) is to generate heat for self healing and de-icing. They verified the feasibility of this application by showing that the temperature of the samples can be heated up to 200°C.

Liu et al. (2010) prepared conductive porous asphalt concrete samples and conducted indirect tension tests to evaluate the reinforcing effects. Thicker steel fibers (diameter ranged 0.0296-0.1911 mm) are compared to steel wool, and showed a better reinforcing effect than steel wool. The test data in Liu et al. (2010) showed positive reinforcing effects due to the addition of steel fibers.

2.1.7 Types of Fibers Added to Asphalt Concrete

The types of fibers added to asphalt concrete are polyester, polypropylene, polyacrylonitrile, cellulose, mineral, glass, carbon, and waste fibers. Physical properties of those fibers are listed in Table 2.1, and Scanning Electron Microscope (SEM) images

of some fibers are shown in Fig. 2.12. Characteristics of the fibers can be summarized as follows.

(1) Polyester fibers

The most popular choice for reinforcing asphalt concrete is polyester fibers (Toney 1987; Maurer and Malasheskie 1989; Freeman et al. 1989; Kim et al. 1999; Putman and Amirkhanian 2004; Wu et al. 2006b; Kutay et al. 2008; Ling et al. 2008; Anurag et al. 2009; Chen et al. 2009; Ye et al. 2009; Zhou et al. 2009; Yu and Sun 2010). Its outstanding reinforcing effect was demonstrated by Peltonen (1991) through the tests for fiber-binder mastics. In the comparative studies reviewed above, polyester fibers consistently showed better resistance to rutting and fatigue that other types of fibers. Polyester is a kind of polymeric fiber produced from crude oil, and has a smooth surface when it is observed using a microscope (Fig. 2.12b and 2.12c).

(2) Polypropylene fibers

Polypropylene fibers are another popular fiber used for the purpose of reinforcing asphalt concrete (Maurer and Malasheskie 1989; Huang and White 1996; Bueno et al. 2003; Tapkin 2008; Tapkin et al. 2009; Zhou et al. 2009). Polypropylene fibers are a kind of synthetic fiber made from alkenes. As shown in Table 2.1, the low melting point (about 160°C) of polypropylene fibers requires tight control of mixing temperature (Maurer and Malasheskie 1989; Abtahi et al. 2010).

(3) Polyacrylonitrile fibers

Polyacrylonitrile (PAN) is a kind of copolymers (or heteropolymer, derived from two ro more monomic species) having acrylonitrile as a main component. PAN is the chemical precursor of high quality carbon fiber (Abtahi et al. 2010). A commercial fiber (Dolanit$^{@}$AC) produced by Lenzing Plastic GmbH have been tested by Ling et al. (2008) and Chen et al. (2009). The comparative test results of Ling et al. (2008) and Chen et al. (2009) show that the reinforcing effect and volumetric changes due to PAN fibers are similar to those of polyester fibers.

(4) Organic fibers: Cellulose, lignin, date-palm, and oil-palm fibers

The primary purpose of adding organic fibers is to prevent draindown in open-graded or gap graded asphalt mixtures. Organic fibers have higher surface area than the same volume of synthetic fibers because of its rough surfaces, which is considered to be the cause of more increase in optimum asphalt content and better stabilizing effect than synthetic fibers. However, the research surveyed above shows that the improvement in mechanical performance of asphalt due to organic fibers are less than the synthetic fibers such as polyester or polypropylene. The most frequently used organic fibers are cellulose fibers (Putman and Amirkhanian 2004; Wu et al. 2006b; Ling et al. 2008; Ye et al. 2009; Zhou et al. 2009), while other fibers (Date-palm, Hassan and Al-Jabri 2005; Cellulose oil palm fibers, Minuandy and Huat 2006; Lignin, Chen et al. 2009) showed similar stabilizing effects. Usually cellulose fibers are manufactured from dissolving pulp.

(5) Mineral fibers: asbestos and rock wool

According to Mundt et al. (2009), the most common choice for stabilizing porous asphalt in the United States is mineral fibers including asbestos and rock wools. The effects of adding mineral fibers to asphalt concrete is similar to cellulose fibers, i.e. high stabilizing effect and low reinforcing effect (Ling et al. 2008; Chen et al. 2009; Ye et al. 2009). However, the use of asbestos is diminishing because of its health hazard (Abtahi et al. 2010)

(6) Glass fibers

The reinforcing effect of glass fibers is examined by Fu et al. (2007). By adding 0.1-0.3% of glass fibers, Fu et al. (2007) obtained improvements in strength, fatigue, and rutting performances.

(7) Conductive Fibers and Fillers: carbon and steel fibers

The addition of conductive fibers provides for multifunctional applications in asphalt concrete such as structural health self-monitoring, self-healing, and removal of snow and ice on the pavement surface. Combinations of carbon fibers, graphite, and carbon black (Wu et al. 2005; Li et al. 2008; Liu and Wu 2009; Wu et al. 2010), combinations of micro

steel fibers, aluminum chips, and graphite (Huang et al. 2006; Huang et al. 2009), and combinations of steel wool, steel fibers, and graphite (Garcia et al. 2009; Liu et al. 2010) have been tried for this purpose. In addition to conductivity, a reinforcing effect attributed to those fibers was observed as well. Since asphalt binder is a hydrocarbon, carbon fiber is presumed to be a chemically compatible additive (Abtahi et al. 2010). The electrical resistivity of carbon fiber is 10^{-3} Ω cm. The dimension of micro fiber made of stainless steel used by Huang et al. (2006; 2009) are 0.008 mm in diameter and 6 mm in length (aspect ratio = 750). Liu et al. (2010) tested three types of steel fibers: steel fiber (diameter = 0.03-0.19 mm and length < 1mm), steel wool 00 (diameter = 0.009-0.013 mm and length = 3.2-9.5 mm), and steel wool 000 (diameter = 0.006-0.009 mm and length = 6 mm). The electric resistivity of steel is 7×10^{-7} Ω cm.

(8) Waste fibers: Nylon, scrap tire, and textile fibers

Waste fibers include scrap tire fibers (Putman and Amirkhanian 2004), waste carpet fibers (Nylon, Putman and Amirkhanian 2004; Lee et al. 2005), and waste textile fibers (Hassan and Al-Jabri 2005). The stabilizing effect of waste fibers showed no significant difference compared to other fibers (Putman and Amirkhanian 2004), but they were observed to slightly improve toughness (Putman and Amirkhanian 2004; Lee et al. 2005).

(9) Other fibers: blend of polypropylene and aramid fibers

The reinforcing effect of a blend of polypropylene and aramid fibers produced by FORTA Corp. was investigated by two different groups, but conflicting results were reported. Kaloush et al. (2010) reported a 25-50% improvement in strength (which is most superior improvement reported) by adding 0.045% of the blended fibers by weight, while Ling et al. (2008) observed that the reinforcing effects of the blend produced by the same company is similar or slightly lower than polyester fibers. Therefore, the reinforcing effect of this blend should be verified by further research. On the other hand, this blend contains polypropylene fibers (the content was not specified by the investigator), and polypropylene has a low melting point as mentioned above, which makes its use problematic.

2.1.8 Summary of the Review

Important findings from the above literature review on FRAC can be summarized as follows.

1. Many studies comparing the effects of various fibers agree that inorganic fibers are better for reinforcing asphalt concrete, while organic fibers have better stabilizing effect. Polyester fiber is the most common choice for reinforcement. The effective stabilization of organic fibers is presumed to be attributed to rough surface. On the other hand, the reinforcing effect seems to be influenced by fiber length. Usual length of organic fibers was 1 mm, while the lengths of inorganic fibers were 6 mm or longer. According to Abtahi et al. (2010), fibers that are too short may not provide a reinforcing effect. However, none of studies surveyed the effect of fiber length or geometry, topics that are considered in this work.
2. There are conflicting results pertaining to the reinforcing effect of fibers. Some investigators (Kim et al. 1999; Tapkin 2008; Li et al. 2008; Xu et al. 2010; Liu et al. 2010) obtained improved Marshall strength or indirect tensile strength from FRAC specimens, while others (Bueno et al. 2003; Lee et al. 2005; Huang et al. 2009) observed negative effects. The source of these contradictory results is attributed to the changes in optimum asphalt content that occur when fibers are added. The role of the binder is to coat the surface area of all mix components, and hence adding fibers requires more binder than would be necessary to just accommodate the aggregate in an asphalt mix. The slight increase in the optimum content of asphalt binder was observed by various investigators (Freeman et al. 1989; Huang and White 1996; Kim et al. 1999; Tapkin et al. 2009; Chen et al. 2009). Correspondingly, when the amount of binder is not increased to accommodate the added fibers, FRACs will have more air voids than the control mixture, leading to a decrease in strength. Chen et al. (2009) clearly demonstrated this effect by comparing the indirect tensile strengths of FRAC specimens with optimum asphalt content (adjusted for fiber addition) and less than optimum asphalt contents (not adjusted for fiber addition). The former showed higher strength than the latter.

3. Although FRACs with optimum asphalt contents show improvement in strength and toughness (Kim et al. 1999; Tapkin 2008; Li et al. 2008; Chen et al. 2009; Xu et al. 2010; Liu et al. 2010), the strength improvements are not substantial when evaluated by Marshall stability tests (conducted at 60°C) or indirect tension tests (conducted at 25°C). On the other hand, more substantial improvements in cracking and rutting resistances were observed from fatigue and rutting tests (Huang and White 1996; Kim et al. 1999; Tapkin 2008; Kytay et al. 2008; Ye et al. 2009) and field studies (Maurer and Malasheskie 1989; Huang and White 1996). These contradictory observations can be explained by the tests in Kaloush et al. (2010). They showed that the reinforcing effect of fibers increases with a decrease in test temperature. This implies that strength measurements at room temperature can underestimate the reinforcing effect of fibers. Therefore, to evaluate cracking resistance of FRAC, the effect of temperature should be taken into consideration.
4. Substantial improvements in moisture susceptibility due to fiber additives was observed by various studies, i.e. improvement in the indirect tensile strength of wet specimens is higher than that of dry specimens (Freeman et al. 1989; Putman and Amirkhanian 2004; Wu et al. 2006; Fu et al. 2007; Anurag et al. 2009).
5. Several studies tried to combine fiber additives and polymeric modifiers and observed synergistic effects in improving rutting and fatigue resistances (Kim et al. 1999; Hassan and Al-Jabri 2005; Wu et al. 2006; Ling et al. 2008).
6. Some field applications reported a problem of fiber clumping while mixing that hinders uniform distribution of fibers. This problem was attributed to the high aspect ratio of the fibers (Huang and White 1996; Abtahi et al. 2010).
7. Previous studies on FRAC simply compared the effects of various fiber types. None of the studies investigated the reinforcing mechanism associated with the fibers. A more systematic approach considering temperature, loading rate, fiber dimensions, and fiber content is required to develop more effective fiber reinforcement as is done in this dissertation. In addition, a mechanical model for the reinforcing effect considering temperature dependent rheology of asphalt binders should be developed, as is also done in this work.

8. Multifunctional application of FRAC with conductive additives have been investigated (Wu et al. 2003; 2005; 2010; Liu et Wu 2009; Huang et al. 2006; 2009; Garcia et al. 2009; Liu et al. 2010). In theory, if the electrical conductivity of asphalt concrete can be controlled, various multifunctional applications such as health monitoring, self-healing, and deicing of pavement surface could be possible. However, work in this area is still preliminary and the relationship between the amount of conductive materials and electric resistance is being explored by various researchers and also in this work.

2.2 CONSTITUTIVE MODELS FOR ASPHALT BINDER AND MIXTURES

2.2.1 Characteristics of Asphalt Behavior

The modeling of asphalt behavior is complicated because its response varies greatly with loading rate, temperature, and asphalt type. Various experimental investigations have been conducted to understand asphalt behavior (Lethersich 1942; Van der Poel 1954; Corbett 1954; Saal 1955; Gaskins et al. 1960; Brodnyan et al. 1960; Majidzadeh and Schweyer 1965; Khong et al. 1978; Attane et al. 1984; Storm et al. 1996; Cheung and Cebon 1997a and 1997b; Airey et al. 2003). One of the general conclusions of those studies is that the phase of asphalt varies with increasing temperature as follows: glassy solid → viscoelastic solid → viscoelastic fluid → Newtonian fluid (Krishnan and Rajagopal 2005). However, the transition temperatures between the phases are difficult to specify because they vary not only with asphalt type, but also with the loading and heating history. For example, in the experimental investigation conducted by Khong et al. (1978), the glass transition temperatures of asphalts from four different sources vary from -45.2 to -18.3 °C depending on source and heating rate (Table 2.2). Above the glass transition temperature, the variations of the transition temperatures are quite complex and this complexity is thought to arise from the coexistence of amorphous and crystalline phases and their inter-conversion (Krishnan and Rajagopal 2005)

This literature survey focuses on asphalt behavior at the field service temperature, and correspondingly, viscoelasticity, which governs behavior above the glass transition temperature. This restriction is reasonable because the field service temperatures are

generally higher than the glass transition temperatures given by Khong et al. (1978) except for in extreme climates.

When strain responses of creep tests or stress responses of relaxation tests are proportional to the applied stresses or strains, respectively, the material is considered to be a linear viscous material. It implies that the material has constant viscosity and follows the Newtonian flow rule. On the other hand, the viscosity of nonlinear viscous material varies with stress or rate of deformation. In nonlinear viscous materials, the relaxation modulus and creep compliance cannot be used for material characterization because those vary with loading condition. The nonlinear viscous nature of asphalt in the range of typical service temperatures (phases between the glassy solid and Newtonian fluid) are well known since Trouton (1906). It is also widely accepted that asphalt at these phases exhibits linear viscosity in the small strain range and that the effect of nonlinearity becomes significant beyond this range (Van der Poel 1954; Cheung and Cebon 1997b; Airey et al. 2003; Krishnan and Rajagopal 2005).

One of the comprehensive studies into the mechanical behavior of asphalt above the glass transition temperature is the experimental investigation by Cheung and Cebon (1997a and 1997b). They conducted constant strain rate tests and creep tests for asphalt covering a wide range of strain rates, stress levels, and temperatures. Cheung and Cebon (1997b) used their experimental data to identify the relationship between steady state strain rate and the corresponding stress. Some of their key results are: 1) the mechanical behavior of asphalt above the glass transition temperature varies from linear to nonlinear viscous with increasing stress, and 2) a power law relationship between strain rate and stress holds in the nonlinear viscous region.

An important characteristic of asphalt behavior within linear viscoelastic range is the existence of multiple relaxation times. It means that the relaxation function of asphalt is broadly distributed over a logarithmic time scale, so that it cannot be represented by a single exponential function. This was observed by Lethersich (1942), and its detailed explanation can be found in Park and Kim (2001). Such broadband relaxation functions can be represented by power-law functions (Kim and Little 1990) or Prony series (Park and Kim 2001). The generalized Maxwell model is one of the mechanical analogs representing the multiple relaxation characteristic, and employed by Stastna et al. (1997)

for asphalt and Gibson et al. (2003) and many others for asphalt concrete.

The time-temperature superposition principle (Leadermann 1943; Ferry 1950) is a useful way of describing the temperature dependency. Many researchers have agreed that the time-temperature superposition principle is applicable to asphalt (Brodnyan et al. 1960; Anderson et al. 1994; Cheung and Cebon 1997b; Andriescu and Hesp 2009) and to asphalt concrete (Goodrich 1991; Kim and Lee 1995; Schwartz et al. 2002). In an experimental study focusing on steady state behavior that can be observed under large deformation, Cheung and Cebon (1997b) concluded that asphalt follows the Arrhenius equation in the vicinity of the glass transition temperature and the Williams, Landal, and Ferry (WLF) equation (Williams et al. 1955) at higher temperatures. By introducing this principle, the loading rate becomes the only matter of concern in considering asphalt behavior.

2.2.2 Models for Asphaltic Materials

Based on the assumption that the deformation range of asphalt in practical applications remains small, Van der Poel (1954) developed a nomograph on the basis of linear viscoelastic theory. Because of its simplicity, the nomograph has found wide acceptance in many pavement design codes. Ever since Van der Poel (1954), most of the studies on modeling asphalt (Jongepier and Kuilman 1969; Dobson 1969; Dickinson 1974; Stastna et al. 1997) and the current design manuals for asphalt concrete (Anderson et al. 1994) characterize asphalt as a linear viscoelastic material with the restriction of their applicable range to small deformation. The most important advantage of this approach is that it permits the use of the concept of superposition as well as simple-to-apply linear viscous parameters such as the relaxation modulus and creep compliance.

However, the assumption that the deformation range of asphalt binder in practice is small enough to be described by linear viscoelasticity, is not an accurate one (Kirshnan and Rajagopal 2003). Recent studies combining computer-aided image analysis techniques and microscopic finite element analysis proved that, even if the macroscopic strain of asphalt concrete is small, the strain magnitudes of asphalt binder between aggregates are high enough to reach into nonlinear viscoelastic range (Masad et al. 2001; Masad and Somadevan 2002). Although this nonlinear viscoelasticity of asphalt binder

should be included as one of the important sources of mechanical nonlinearity observed in asphalt concrete, recent constitutive models for asphalt concrete (Kim and Little 1990; Neifar and Di Benedetto 2001; Desai 2001; Chehab et al. 2002) assume linearity of viscosity, and add damage mechanics and/or plasticity theory to explain nonlinear responses. These standpoints are based on an assumption that all nonlinearity of particle reinforced viscoelastic materials is due to microcracking (Schapery 2000). However, while there is no doubt that damage evolution must be considered in describing the behavior of asphalt concrete, it may be a more realistic assumption to assign some portion of the nonlinearity in the mechanical response to the nonlinear nature of asphalt viscosity.

Modeling attempts for asphalt focusing on its non-Newtonian behavior are relatively few. Those can be found in Majidzadeh and Schweyer (1965; 1966), Schweyer and Busot (1969), Attane et al. (1984), and Cheung and Cebon (1997b). In the case of asphalt concrete, Vakili (1983) tried to apply a multiple-integral constitutive equation. However, none of these models have achieved wide recognition as rigorous constitutive models.

Another recent constitutive model for asphaltic material (both pure asphalt and asphalt concrete) is Krishnan and Rajagopal's model based on finite strain theory (Krishnan and Rajagopal 2004; 2005; Krishnan et al. 2006). One of the implications of using finite strain theory is that large deformation is itself a source of nonlinearity (Oldroyd 1950). However, the nonlinearity due to large deformation is not sufficient to capture the time-dependent nonlinear behavior of asphaltic materials. Krishnan and Rajagopal (2004; 2005) divided the deformation state into reference, natural, and current configurations. The natural configuration indicates the state of deformation where tractions are removed from the current configuration. Therefore, the deformation gradient relating reference and natural configurations represents viscous flow and damage evolution. To describe evolution of the natural configuration, they assumed various energy dissipation rate equations including linear (Krishnan and Rajagopal 2004; 2005) and nonlinear forms (Krishnan et al. 2006). Their models are based on Burgers' model with four elements, but a combination of linear and nonlinear models has not been tried, as is done in this paper. Filograna et al. (2009) tried to simulate the behavior of pure asphalt using a model similar to Krishnan and Rajagopal's. However, they indicated that

the model could not describe various test data associated with different strain rates with a single set of material parameters.

The above discussion suggests that in spite of the nonlinear viscosity exhibited by asphalt, many researchers have approximated its behavior based on the theory of linear viscoelasticity, and a comprehensive constitutive model has not yet been proposed that accounts for both linear and nonlinear viscoelastic responses over various temperatures and loading conditions. Part of this dissertation is dedicated to addressing this deficiency.

2.3 BRIDGE ASPHALT PLUG JOINT

2.3.1 Usage, Advantages, and Disadvantages of Asphalt Plug Joint

An asphalt plug joint (APJ) is a type of bridge expansion joint that is becoming popular with some State Departments of Transportation in the United States (Transportation Research Board 2003). It is made of flexible asphalt concrete usually comprising 20% asphalt and 80% aggregates by weight. As shown in Fig. 2.13, the APJ material is placed into a prepared space between pavements permitting a smooth ride across the joint while accommodating thermal movements of the bridge deck at the same time. The Bridge Joint Association of the United Kingdom (2003) indicates that the typical size of an APJ is 500 mm wide and 100 mm deep and its allowable movement without cracking at the lowest operating design temperature is ±20 mm. ASTM D6297-01 specifies that the standard minimum blockout dimensions for an APJ are 50×500 mm, and the maximum allowable movement is 25 mm.

APJs have been developed by trial and error and are widely used without a good understanding of their behavior (Bramel et al. 1999). Partl et al. (2002) stated that APJ was introduced in the 1980's in Switzerland, and have successfully substituted traditional joints. In fact, to date, very few research projects have actually investigated the performance and behavior of APJs. Comprehensive studies on APJ were conducted by Bramel et al. (1999) in the United States and Partl et al. (2002) in the EU. Both studies aimed to establish a practical guideline for installation and design of APJs.

By providing a smooth transition across an expansion joint, an APJ offers better bridge surface flatness than other types of joints. Simplicity and low cost of its

installation are additional important advantages of APJs (Qian et al., 2000). According to a survey by Bramel et al. (1999), 41 states in the US have installed APJs. Of those, 23 states still use APJs for either new construction or retrofit, without geographic preference. The benefits of APJs, as collected through the survey, were categorized into three areas: functionality, serviceability, and cost. For functionality, a smooth transition from pavement to bridge deck (9 states), asphalt compatibility (5 states), reduced leakage (5 states), and ease of installation (6 states) were mentioned. For serviceability, reduced snow plow snagging (4 states), reduced maintenance (4 states), timeliness of installation (3 states), ease of placement over existing joints (1 states), and convenience in making temporary fixes (1 states) were mentioned. Two states responded that the reduced cost was a major benefit.

On the other hand, APJs frequently suffer from premature failure, sometimes as early as 6 months after installation, even though they are generally expected to have a life of about 6-7 years. Barnard and Cuninghame (1998) pointed out the overall cost of replacing a damaged APJ can exceed the cost of a new APJ installation in the United Kingdom. According to Reid et al. (1998), in the United Kingdom, £20 million is spent for APJ maintenance per year. Bramel et al. (1999) also reported that premature failure was one of the important problems hindering the widespread use of APJs in the US. The various failure modes in APJs can be categorized into two classes: cracking related failures and rutting. According to Bramel et al. (1999), two locations within an APJ are especially vulnerable to cracking as a result of bridge movement: 1) the interface between the pavement and joint, and 2) the edges of the steel gap plates. The possible failure modes in APJ are demonstrated in Fig. 2.13.

2.3.2 Research on Asphalt Plug Joint

An effort to prevent premature failure of APJ by modifying the standard geometric design was made by a University of Aberdeen team. Reid et al. (1998) suggested two alternative geometries and compared their stress distributions to conventional APJ's using of finite element analyses. They focused on the debonding that commonly occurs at the plug/pavement interface due to traffic loads, and suggested that increasing the contact area between the plug and pavement would reduce the stress concentration thought to

lead to early failures. Fig. 2.14 shows the conventional APJ and two proposed alternatives having larger contact area. The first alternative, which was called ‘trapezoidal’ type had an inclination of 45°, while the other alternative, which was called ‘sinusoidal’, had a 400 mm wavelength and 200 mm amplitude.

The finite element analyses were carried out using the commercial code ANSYS v5.1, and the mechanical properties of APJ were obtained by a compressive test (ASTM D1074-96). All plug types were modeled with 3-D elements. For modeling vehicular loads, a static 38 kN vertical load and 6 kN horizontal shear force were applied across an area 300 mm × 210 mm to simulate a heavy truck moving over an APJ at the speed of 100 km/h. A longitudinal contraction deformation of 20 mm was applied separately to simulate thermal movement. Analysis results indicate that increasing the area of the interface reduces the maximum internal stresses, which could help reduce or postpone premature failures of APJs. The location of the highest stress was the top edges of the plug/pavement interfaces for all geometric types.

A complementary study to Reid et al. (1998) was published by Qian et al. (2000). In this paper, only the trapezoidal APJ under traffic load was considered. A parameter study to obtain the optimum angle of the trapezoid was carried out and the effect of the base plate was discussed. Another advance made in this study is that a simplified model for considering viscoelasticity and temperature was applied. Based on their analysis results Qian et al. (2000) suggested that the optimum joint angle should be more than 30 degree to prevent stress reversal and to minimize stress intensity. The results strongly imply that the risk of debonding failure could be reduced by providing proper angles to the interfaces of APJ.

Although Reid et al. (1998) and Qian et al. (2000) suggested practical ideas on improving APJ durability, their studies have some limitations. One of the limitations is that they did not adequately consider the effect of the gap plate. Reid et al. (1998) did mention that the gap plates could increase stresses, but they did their study in a qualitative manner and the gap plate was not included in their model. When an APJ is subjected to thermal movement, the boundary conditions around the gap plate cannot be fully described without simulating the debonding of plug material that occurs as a result of relative movement between the gap plate and concrete deck. As described in Bramel et

al.'s (1999) near full scale test and Partl et al.'s (2002) field investigation, the edge of the gap plate is a location that is vulnerable to crack initiation. Another limitation of their studies was the simplified material model they employed. Reid et al. (1998) applied an elastic material model. In case of Qian et al. (2000), the effect of viscosity was investigated by a set of analyses for various elastic modulus. As a result, they concluded that the model with smaller elastic modulus due to slower traffic load causes higher stress concentration. Strictly speaking, it is hard to say that Qian et al.'s (2000) simulation is viscoelastic, because each of the analysis employed a linear elastic model. In an actual viscous material, even under constant loading speed, if the strain distribution is not constant, the material constants would vary with strain distribution. Such simplifications are valid in case of high strain rate and small deformation problem, i.e. the strains are in the elastic range. Since they were concerned with traffic load only, their simplifications were reasonable. However, when thermal movement is of interest, their simplified models are not valid. Under slow strain rate and large deformation, viscosity will be more important than elasticity. In addition, effect of temperature will be significant because asphalt behavior is highly sensitive to temperature. Therefore, a thorough understanding of the effect of thermal and traffic loading on APJ is needed and is the focus of part of this dissertation.

2.4 SUMMARY

This chapter surveyed previous research related to the topics of this dissertation. Traditional use, potential benefits, and the current state-of-the-art of fiber additives for asphalt concrete are investigated through a comprehensive literature review. The types of fibers used for asphalt and their characteristics are summarized. The temperature dependent viscoelastic behavior of asphaltic materials and previous efforts for developing their constitutive models are introduced. Finally, a research overview of bridge asphalt plug joint is presented.

Table 2.1 Physical properties of fibers

Types of fibers	Tensile strength (MPa)	Specific gravity	Melting point (°C)	Fiber size, in general	References
Polyester	> 500	≈ 1.36	> 240	ϕ 0.02 – 0.30 mm l = 6-13 mm	
Polypropylene	≈ 276	≈ 0.91	≈ 160	ϕ 0.04 ± 0.01 mm l = 10 ± 2 mm	Huang and White (1996); Tapkin (2008)
Polyacrylonitrile (PAN)	> 910	≈ 1.15	> 240	ϕ 0.013 mm l = 4 – 6 mm	Chen et al. (2009)
Organic (cellulose, lignin, date-palm, oil-palm)		0.025-0.030	> 200	ϕ 0.045 mm l = 1.1 mm	Ye et al. (2009)
Mineral (asbestos, rock wool)	> 910	≈ 2.7	≈ 1500	ϕ 0.005 mm l = 6 mm	Ye et al. (2009)
Glass	≈ 3000	≈ 2.5	≈ 1500	ϕ 0.010 mm l = 6 mm	Fu et al. (2007)
Carbon	≈ 1680	-	-	ϕ 0.010 mm l = 5 mm Resistivity = 10^{-3} Ω cm	Wu et al. (2005)
Steel	-	≈ 7.8	-	- Resistivity = 7×10^{-7} Ω cm	Huang et al. (2006; 2009); Liu et al. (2010)
Waste (Nylon, scrap tire, textile)					Putman and Amirkhanian (2004); Lee et al. (2005); Hassan and Al-Jabri (2005)

Table 2.2 Characteristics of asphalt samples including glass transition temperature (T_g) investigated by Khong et al. (1978)

No	Source and grade	a Penetration			b Viscosity at 60°C (poises)	c Softening point °C	e Molecular weights		f Tg (°C) at different heating rates q (°C.min-1)				g
		at 4°C	at 25°C	at 60°C			$\overline{Mw}$	$\overline{Mn}$	q = 80	q = 40	q = 20	q = 10	q = 1
	A												
1	85-100	20	90	260	1479	46.7	1230	845	-18.3	-20.7	-24.5	-26.3	-35.0
2	150-200	29	148	300+	703	40.0	1180	820	-25.8	-28.7	-32.3	-34.5	-43.4
	B												
3	85-100	15	90	275+	1570	47.2	1300	880	-26.3	-29.7	-32.5	-34.5	-44.7
4	150-200	28	170	275+	615	40.0	1250	865	-26.6	-29.7	-32.8	-35.2	-45.2
5	300-400	48	293	275+	286	33.3	1160	835	-27.8	-31.0	-33.6	-35.0	-45.0
	C												
6	85-100	19	83	250	1977	47.8	1210	875	-20.3	-23.2	-25.5	-26.6	-36.0
7	150-200	34	164	300+	511	38.3	1130	835	-25.3	-27.7	-30.8	-32.0	-40.0
	D												
8	85-100	-	-	-	-	-	1160	845	-22.0	-24.7	-26.6	-29.8	-37.7

a – ASTM D 5-71, b – ASTM D 2171-66, c – ASTM D 2398-68, e – GPC (Waters Model A 200), f – Perkin-Elmer DSC-2 and g – extrapolated value using the equation $\log q = a - b/T_g$

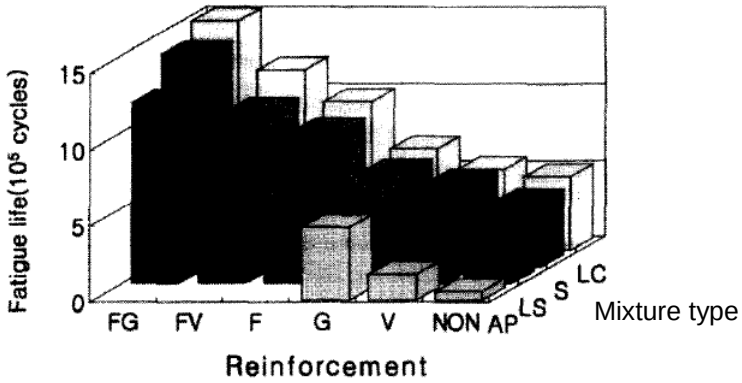

Fig. 2.1 Comparison of fatigue life for various mixtures tested by Kim et al. (1999); F=polyester fiber, G=glass fiber grid, V=polypropylene vinyl, AP=plain asphalt mixture, L=low density polypropylene modified mixture, S=SBS modified mixture, C=carbon black modified mixture

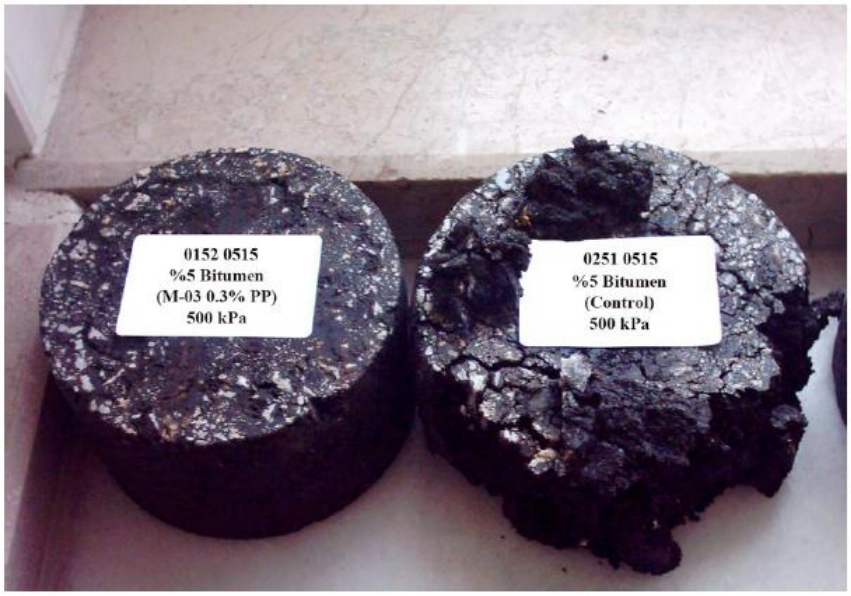

Fig. 2.2 Picture representing final conditions of control and polypropylene fiber reinforced specimens (Tapkin et al. 2009)

Fiber type	Name	Length (cm)	% Fiber by total weight of mix
0.635 cm and 0.35%	A	0.635	0.35
0.635 cm and 0.50%	B	0.635	0.50
1.270 cm and 0.35%	C	1.270	0.35
1.270 cm and 0.50%	D	1.270	0.50
Control	Control	No fiber	

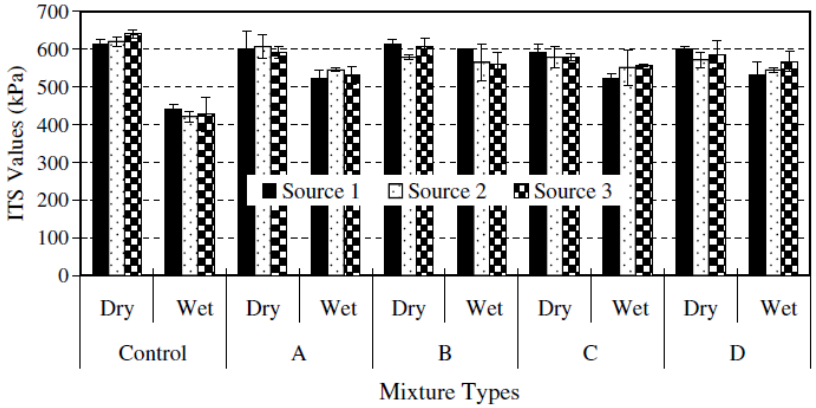

Fig. 2.3 Lengths and contents of waste polyester fiber additives and indirect tensile strengths of the mixtures (Anurag et al. 2009)

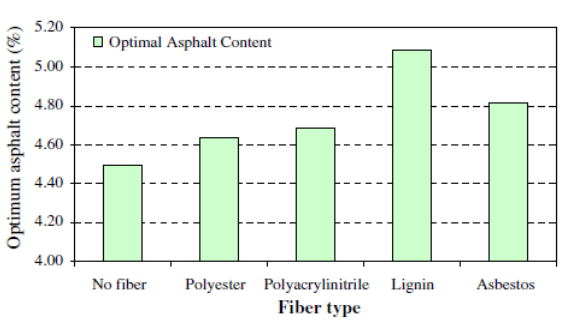

(a) optimum asphalt content

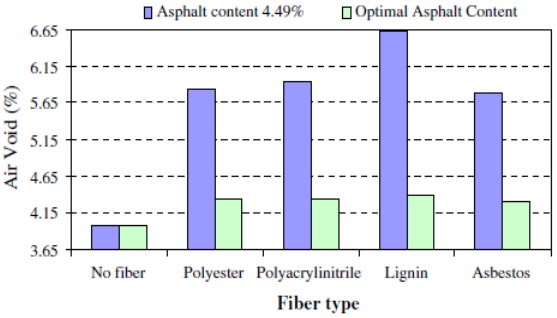

(b) air voids

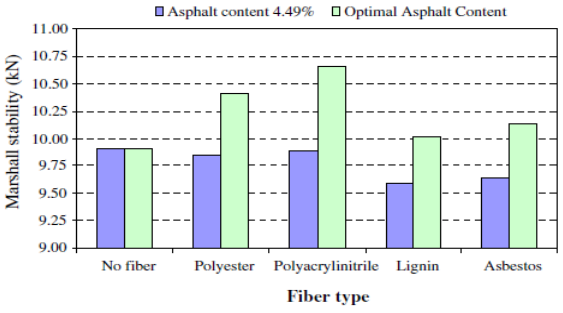

(c) Marshall stability

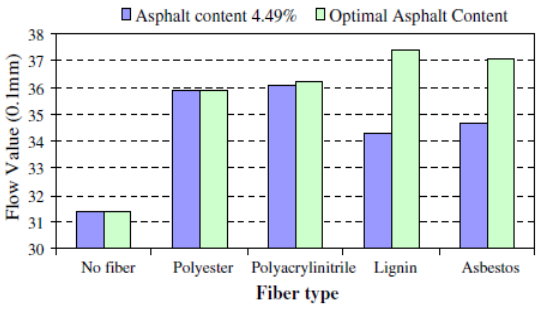

(d) Marshall flow

Fig. 2.4 Relations between asphalt content, air voids, Mashall stability, and Marshall flow of FRAC (Chen et al. 2009)

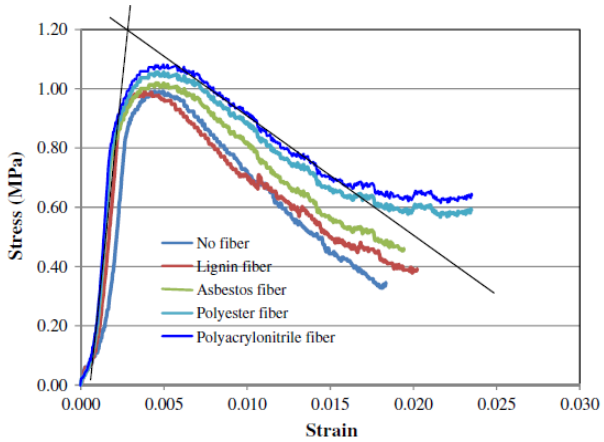

(a) stress-strain curves of FRAC and control specimens obtained from indirect tension tests

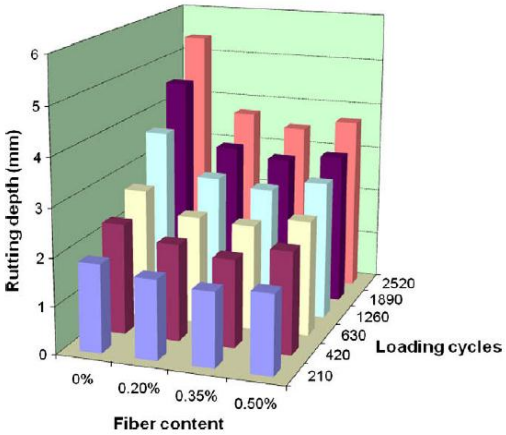

(b) variation of rut depth with the contents of polyester fibers

Fig. 2.5 Effects of fibers on indirect tensile strength and rut depth (Xu et al. 2010)

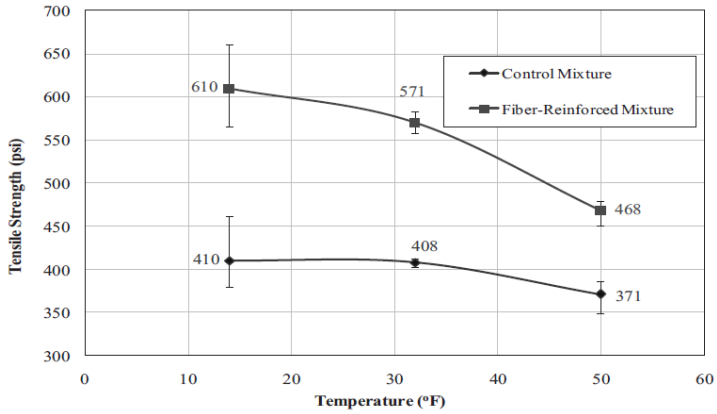

(a) indirect tensile strength

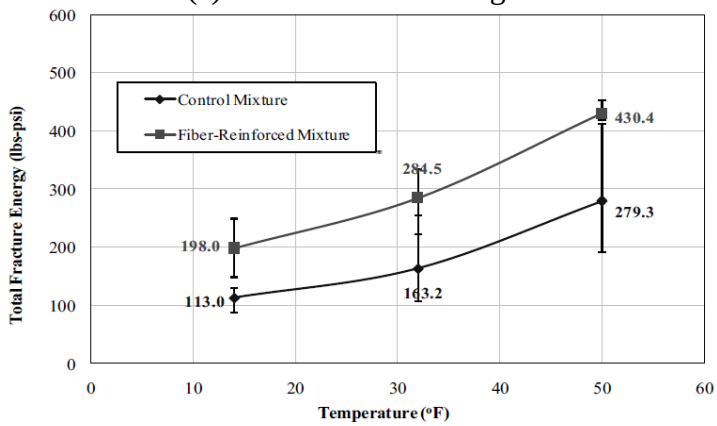

(b) fracture energy

Fig. 2.6 Strength and fracture energy improvement due to fiber additives (Kaloush et al. 2010)

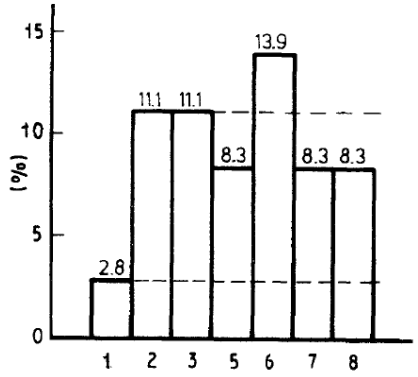

(a) Elastic recoveries at 25°C

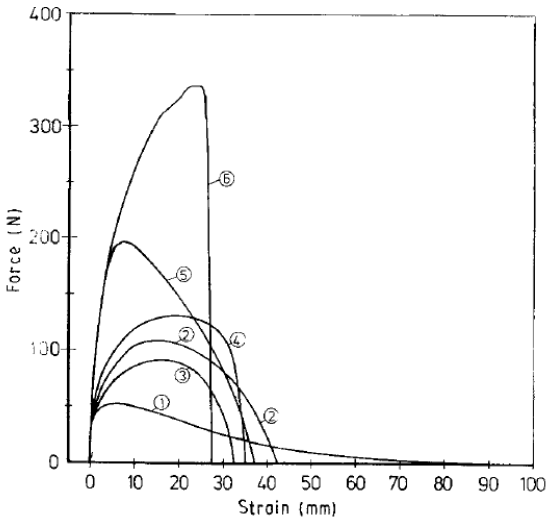

(b) Elongation test curves at 7°C

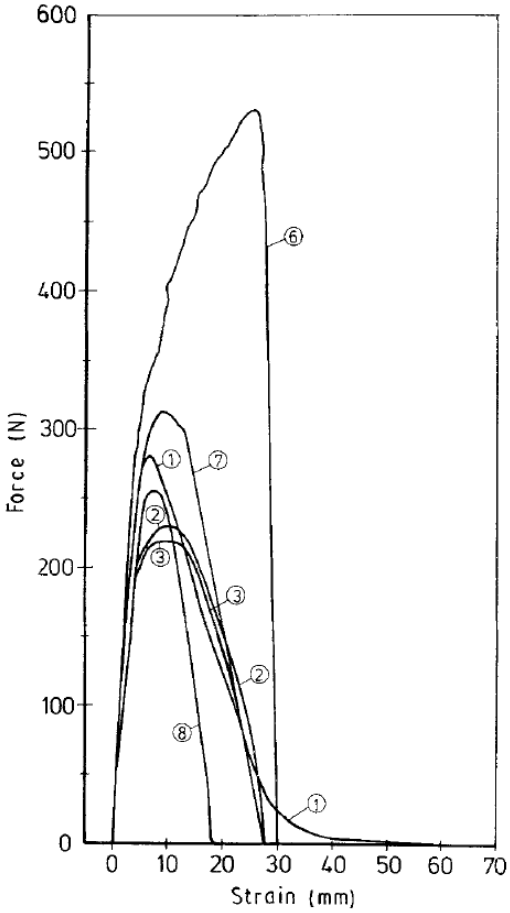

(c) Elongation test curves at -10°C

Fig. 2.7 Elastic recoveries and force-displacement curves of different fiber bitumen blends: ① bitumen without fiber; ② cellulose 1; ③ cellulose 2; ④ cellulose 3; ⑤ mineral fiber M-P; ⑥ polyester fiber; ⑦ mineral fiber M-D2; ⑧ glass fiber (Peltonen, 1991)

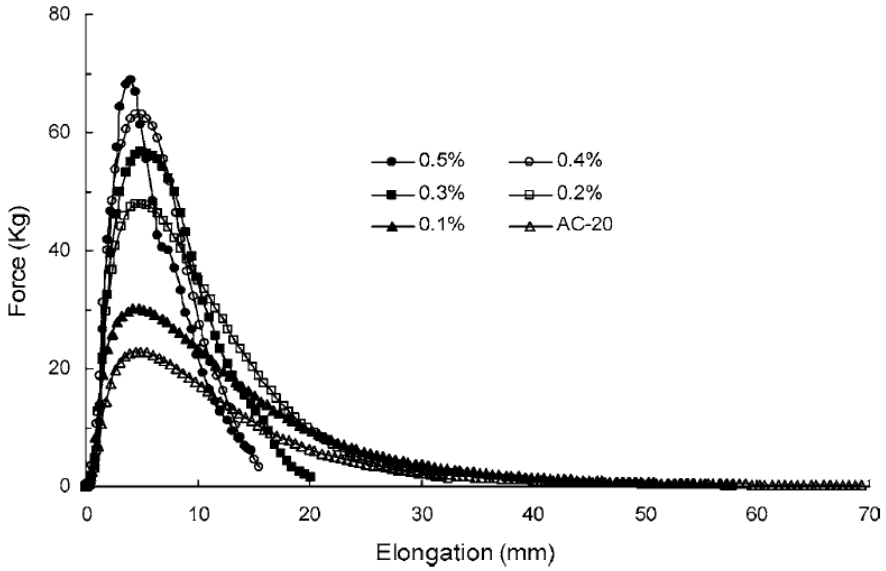

(a) tensile force versus elongation curves of asphalt mastics with various concentrations of mineral fibers

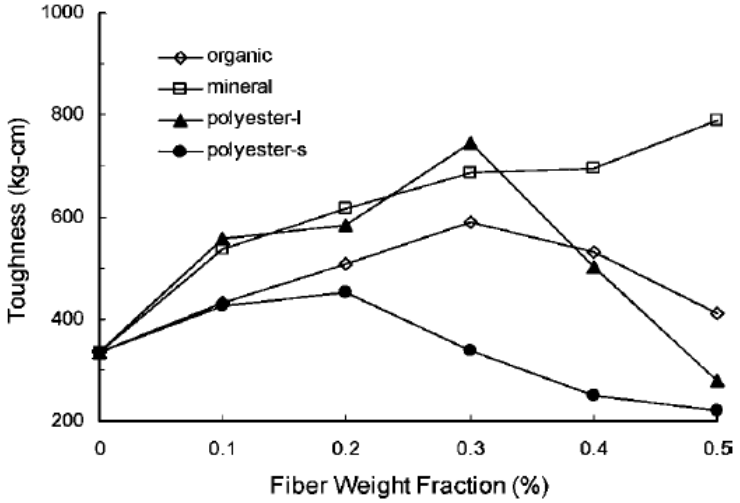

(b) toughness of asphalt mastics with various fibers

Fig. 2.8 Toughness and tenacity test (ASTM D 5801) results for asphalt mastics conducted by Chen and Lin (2005); fiber contents are percent by weight of mixture, and the test temperature was 25°C

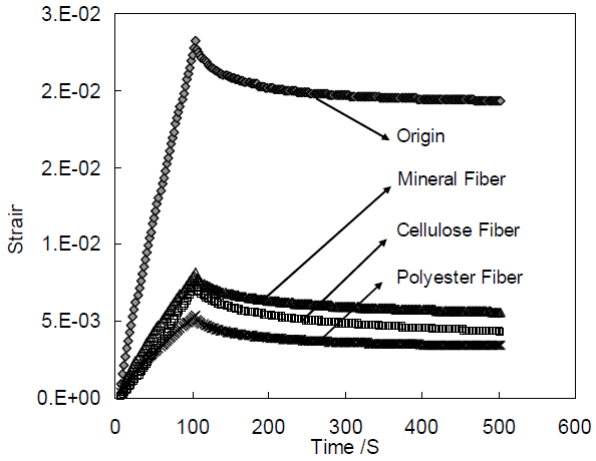

Fig. 2.9 Comparison of creep strains of fiber modified mastics to the binder without fibers (Ye and Wu 2010)

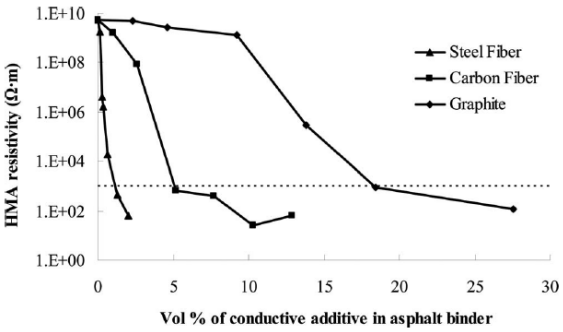

(a) variation of electrical resistance with the contents of additives

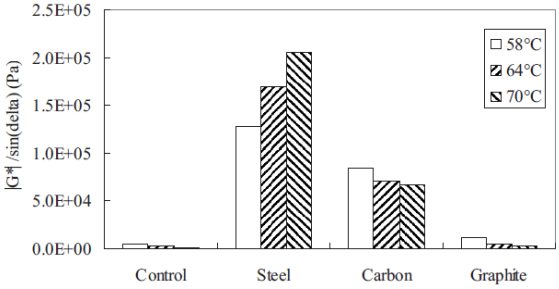

(b) rutting parameters of mastics with various additives

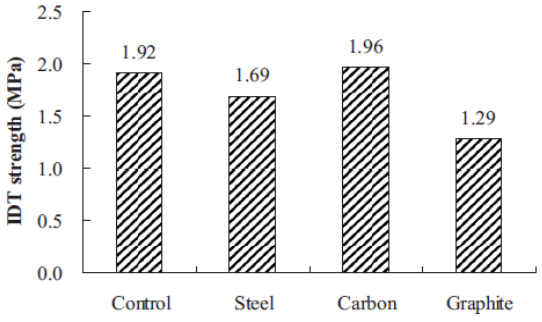

(c) indirect tensile strength of asphalt concretes with various additives

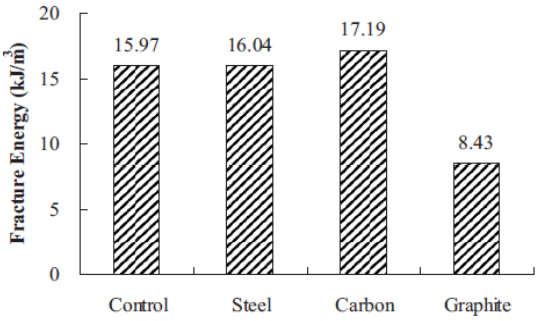

(d) fracture energy of asphalt concretes with various additives

Fig. 2.10 Changes in electrical and mechanical properties due to conductive additives (Huang et al. 2009)

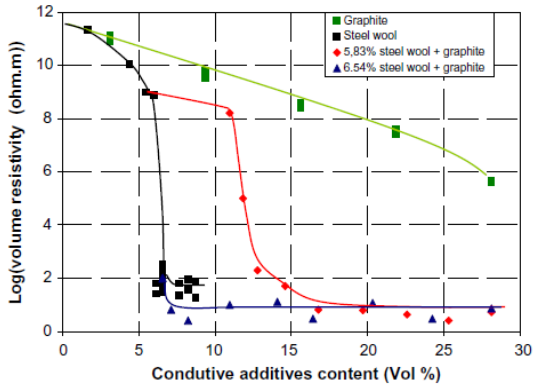

(a) variation of electric resistance with the contents of conductive additives

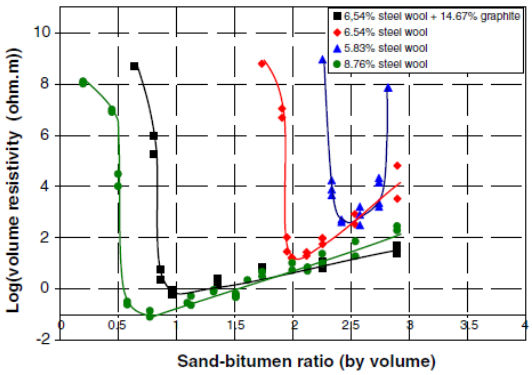

(b) effect of sand-bitumen ratio on the electrical resistance

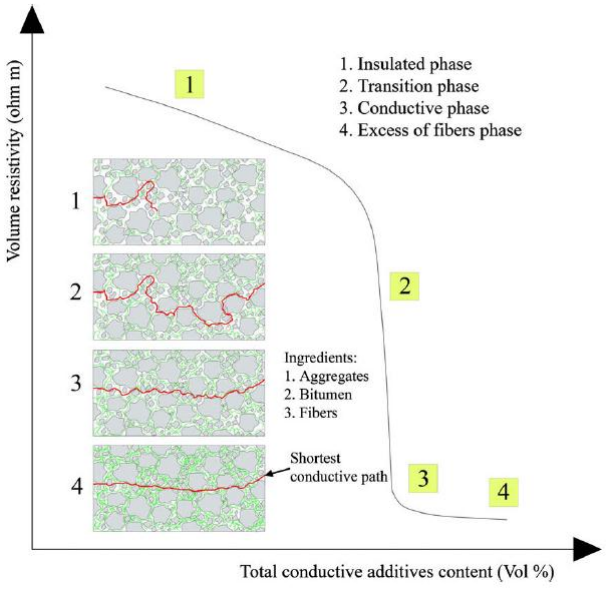

(c) scheme of volume resistivity versus conductive additives content

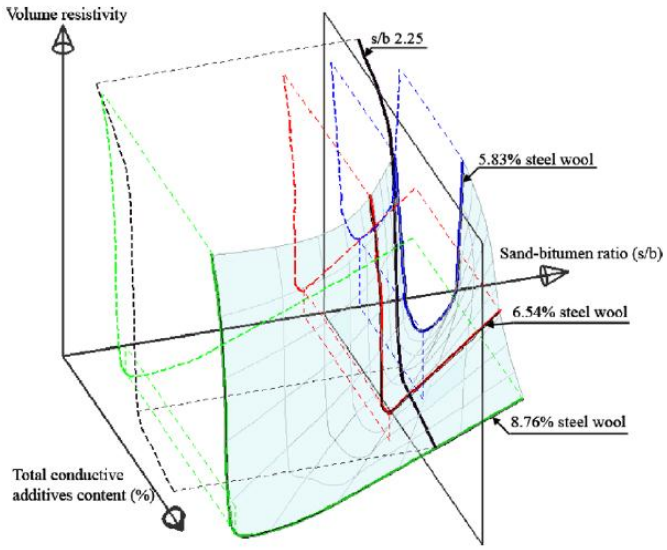

(d) electrical conductivity surface of asphalt mortar against the sand-asphalt ratio and the total volume of conductive additives

Fig. 2.11 Electric conductivity of asphalt mortar with conductive additives (Garcia et al. 2009)

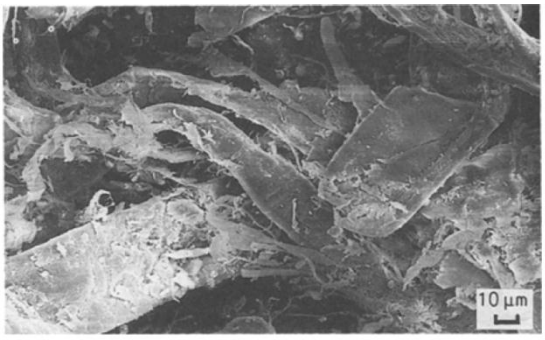

(a) cellulose fibers (Peltonen 1991)

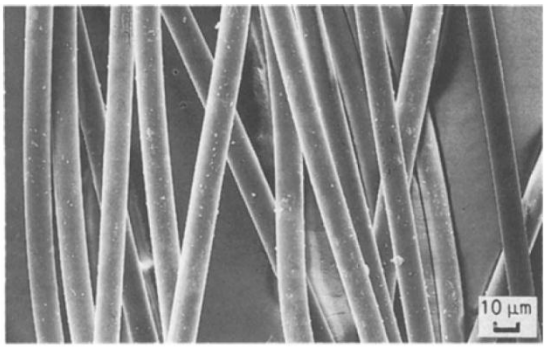

(b) polyester fibers (Peltonen 1991)

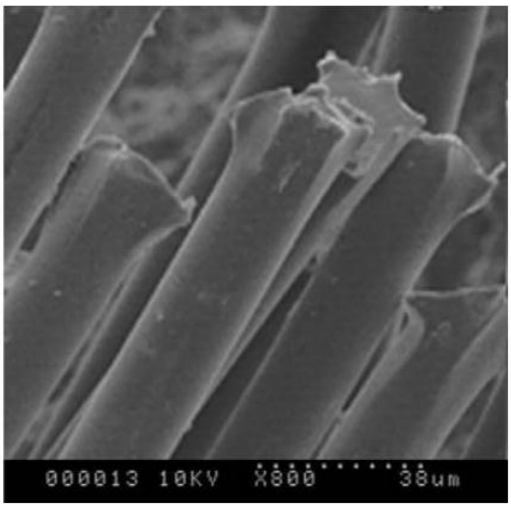

(c) polyester fibers (Xu et al. 2010)

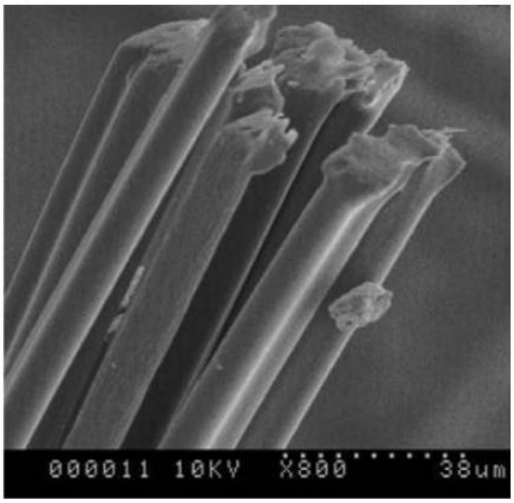

(d) polyacrylonitrile fibers (Xu et al. 2010)

Fig. 2.12 Scanning Electron Microscope (SEM) images of various fibers

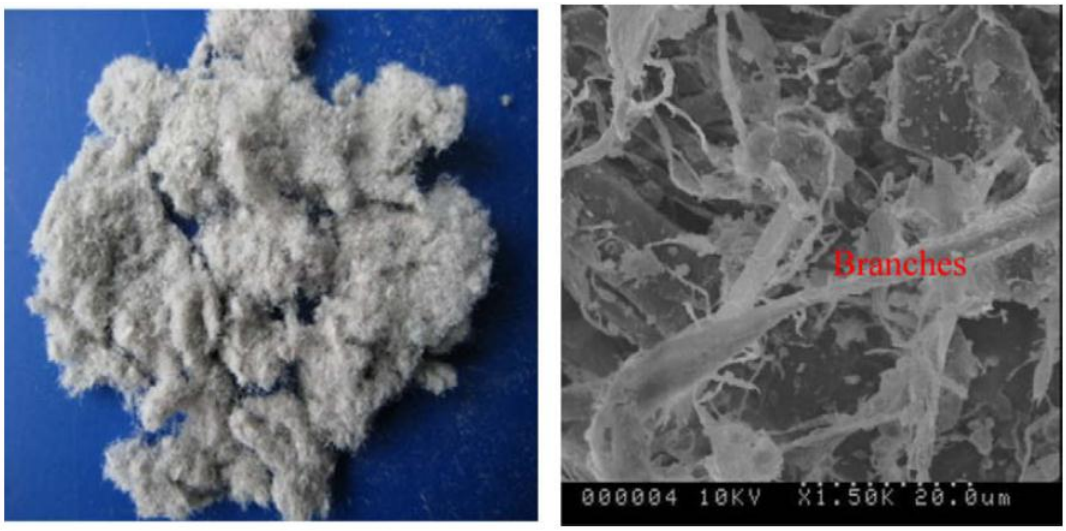

(e) organic fibers: lignin (Xu et al. 2010)

(f) mineral fibers: asbestos (Xu et al. 2010)

Fig. 2.12 continued

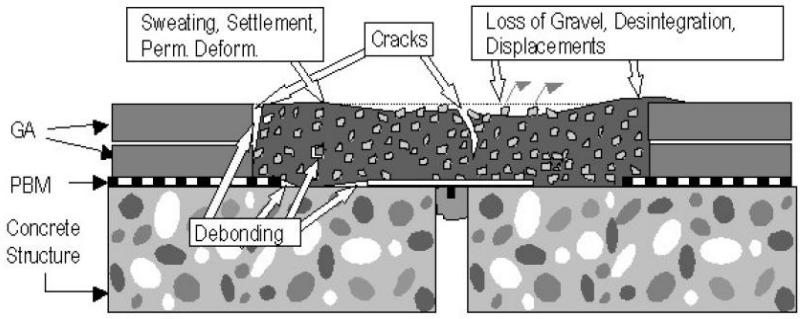

Fig. 2.13 Typical damage observed in APJ (Partl et al. 2002)

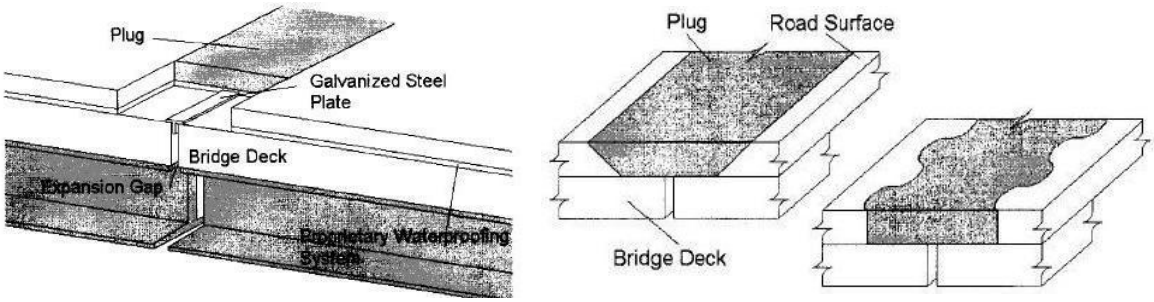

(a) standard APJ system (b) alternative APJs

Fig. 2.14 Alternative APJs proposed by Reid et al. (1998)

REFERENCES

Abtahi, S. M., Sheikhzadeh, M., and Hejazi, S. M. (2010). "Fiber-reinforced asphalt-concrete - A review." *Construction and Building Materials*, 24(6), 871-877.

Airey, G. D., Rahimzadeh, B., and Collop, A. C. (2003). "Viscoelastic linearity limits for bituminous materials." *Materials and Structures*, 36, 643-647.

Alvarez, A. E., Martin, A. E., Estakhri, C., and Izzo, R. (2009). "Determination of volumetric properties for permeable friction course mixtures." *Journal of Testing and Evaluation*, 37(1), 1-10.

Anderson, D. A., Christensen, D. W., Bahia, H. U., Dongre, R., Sharma, M. G., Antle, C. E., and Button, J. (1994). *Binder characterization and evaluation, Volume 3: Physical Characterization. Report SHRP-A-369*, Strategic Highway Research Program, National Research Council, Washington, DC.

Andriescu, A., and Hesp, S. A. (2009). "Time-temperature superposition in rheology and ductile fracture of asphalt binders." *International Journal of Pavement Engineering*, 10(4), 229-240.

Anurag, K., Feipeng X., and Amirkhanian, S. N. (2009). "Laboratory investigation of indirect tensile strength using roofing polyester waste fibers in hot mix asphalt." *Construction and Building Materials*, 23(5), 2035-2040.

ASTM. (1996). *Standard Test Method for Compressive Strength of Bituminous Mixtures*, ASTM D 1074, West Conshohocken, Pa.

ASTM. (2001). *Standard specification for asphaltic plug joints for bridges*, ASTM D 6297, West Conshohocken, Pa.

ASTM. (2007). "Standard Test Method for Effect of Moisture on Asphalt Concrete Paving Mixtures." *ASTM D4867/D4867M-09*, West Conshohocken, PA.

Attane, P., Soucemarianadin, A., Turrel, G., and Prud'homme, J. B. (1984). "Non-linear behavior of asphalts in steady and transient shear flow." *Rheol. Acta*, 23, 297–310.

Bahia, H. (2006). "Modified Asphalt Binders for Paving Applications." *Asphalt Mix Design and Construction – Past, Present, and Future: A special publication of the 150th anniversary of ASCE*, ASCE, 84-154.

Barnard, C. P. and Cuninghame, J. R. (1998). *Improving the Performance of Bridge Expansion Joints: Bridge Deck Expansion Joint Working Group Final Report*, TRL Report 236.

Bramel, B. K., Dolan, C. W., Puckett, J. A., and Ksaibati, K. (1999). *Asphalt plug joints: Characterization and specifications*, Ph.D. dissertation, Univ. of Wyoming, Laramie,

Wyo.

Bridge Joint Association. (2003). *Standard for asphaltic plug joints*, Concrete Bridge Development Group, U.K.

Brodnyan, J.G., Gaskins, F.H., Philippoff, W., and Thelen, E. (1960). "The Rheology of asphalt, III Dynamic Mechanical properties of asphalt." *Trans. Soc. Rheol*., 4, 279–296.

Bueno, B. S., Silva, W. R., Lima, D. C., and Minete, E. (2003). "Engineering Properties of Fiber Reinforced Cold Asphalt Mixes." *Journal of Environmental Engineering*, 129(10), 952-955.

Chehab, G. R., Kim, Y. R., Schapery, R. A., Witczak, M. W., and Bonaquist, R. (2002). "Time-temperature superposition principle for asphalt concrete with growing damage in tension state." *Proc. of Assoc. of Asphalt Paving Technologists,* 71, 559-593.

Chen, H., Xu, Q., Chen, S., and Zhang, Z. (2009). "Evaluation and design of fiber-reinforced asphalt mixtures." *Materials and Design*, 30(7), 2595-2603.

Chen, H., and Xu, Q. (2010). "Experimental study of fibers in stabilizing and reinforcing asphalt binder." *Fuel*, 89(7), 1616-1622.

Chen, J. S. and Lin, K. Y. (2005). "Mechanism and Behavior of Bitumen Strength Reinforcement Using Fibers." *Journal of Materials Science*, 40, 87-95.

Cheung, C. Y., and Cebon, D. (1997a). "Deformation mechanisms of pure bitumen." *J. Mater. Civ. Eng*., 9(3), 117-129.

Cheung, C. Y., and Cebon, D. (1997b). "Experimental study of pure bitumens in tension, compression, and shear." *J. Rheol*., 41(1), 45-73.

Corbett, L. W. (1954). "A comparative study of straight run, thermal and blown asphalts." *Proc. of Assoc. of Asphalt Paving Technologists*, 23, 14–27.

Desai, C. S. (2001). *Mechanics of Materials and Interfaces: The Disturbed State Concept*, CRC Press, Boca Raton, Fl.

Dickinson, E. J., Witt, H. P., (1974). "The dynamic shear modulus of paving asphalts as a function of frequency." *Transactions of the Society of Rheology*, 18 (4), 591–606.

Dobson, G. R. (1969). "The dynamic mechanical properties of bitumen." *Proc. of Assoc. of Asphalt Paving Technologists*, 38, 123–139.

Elseifi, M. A., and Al-Qadi, I. L. (2005). "Effectiveness of Steel Reinforcing Nettings in Combating Fatigue Cracking in New Flexible Pavement Systems." *Journal of Transportation Engineering*, 131(1), 37-45.

Ferry, J. D. (1950). "Mechanical properties of substance of high molecular weight; VI. Dispersion in concentrated polymer solutions and its dependence on temperature and

concentration.” *Journal of the American Chemical Society*, 72(8), 3746-3752.

Filograna, L., Racioppi, M., Saccomandi, G., and Sgura, I. (2009). “A simple model of nonlinear viscoelasticity taking into account stress relaxation.” *Acta Mech*., 204, 21-36.

Freeman, R. B., Burati, J. L., Amirkhanian, S. N., and Bridges, W. C. (1989). “Polyester fibers in asphalt paving mixtures.” *Journal of the Association of Asphalt Paving Technologists*, 58, 387-409.

Fu, J., Liu, H.B., and Cheng, Y.C. (2007). “Mechanical parameter measuring and contrastive analysis on pavement performance of glass fiber reinforced bituminous mixtures.” *Proceedings of International Conference on Transportation Engineering 2007; ICTE 2007*, ASCE, 425-430.

García, Á., Schlangen, E., Van de Ven, M., and Liu, Q. (2009). "Electrical conductivity of asphalt mortar containing conductive fibers and fillers." *Construction and Building Materials*, 23(10), 3175-3181.

Gaskins, F. H., Brodnyan, J. G., Philippoff, W., and Thelen, E. (1960). "The rheology of asphalt, II: Flow characteristics of asphalt." *Trans. Soc. Rheol*., 4, 265–278.

Gibson, N. H., Schwartz, C. W., Schapery, R. A., and Witczak, M. W. (2003). “Viscoelastic, viscoplastic, and damage modeling of asphalt concrete in unconfined compression.” *Transportation Research Record*, 1860, 3-15.

Gibson, R. F. (2010). "A review of recent research on mechanics of multifunctional composite materials and structures." *Composite Structures*, 92, 2793-2810.

Goodrich, J. L. (1991). “Asphalt binder rheology, asphalt concrete rheology and asphalt concrete mix properties.” *Asphalt Paving Technology: Association of Asphalt Paving Technologists-Proceedings of the Technical Sessions*, 60, 80-120.

Hassan, H. F., and Al-Jabri, K. S. (2005). "Effect of organic fibers on open-graded friction course mixture properties." *The International Journal of Pavement Engineering*, 6(1), 67-75.

Hicks, R. G. (2002). *Asphalt Rubber Design and Construction Guidelines: Volume I - Design Guidelines*, Northern California Rubberized Asphalt Concrete Technology Center (NCRACTC) and California Integrated Waste Management Board (CIWMB), Sacramento, CA.

Huang, B., Cao, J., Chen, X., Shu, X., and He, W. (2006). "Laboratory Investigation into Electrically Conductive HMA Mixtures." *Journal of the Association of Asphalt Paving Technologists*, 75, 1235-1253.

Huang, B., Chen, X., and Shu, X. (2009). "Effects of electrically conductive additives on laboratory-measured properties of asphalt mixtures." *Journal of Materials in Civil*

Engineering, 21(10), 612-617.

Huang, H., and White, T. D. (1996). "Dynamic Properties of Fiber-Modified Overlay Mixture." *Transportation Research Record*, 1545, 98-104.

Huang, Y., Bird, R. N., and Heidrich, O. (2007). "A review of the use of recycled solid waste materials in asphalt pavements." *Resources Conservation and Recycling*, 52, 58-73.

Jongepier, R., and Kuilman, B. (1969). "Characteristics of the rheology of bitumens." *Proc. of Assoc. of Asphalt Paving Technologists*, 38, 98–122.

Kaloush, K. E., Biligiri, K. P., Zeiada, W. A., Rodezno, M. C., and Reed, J. X. (2010). "Evaluation of fiber-reinforced asphalt mixtures using advanced material characterization tests." *Journal of Testing and Evaluation*, 38(4), DOI: 10.1520/ JTE102442.

Khong, T. D., Malhotra, S. L., and Blanchard, L. P. (1978). ‘‘A study of the glass transition temperature of asphalts and their viscosity.’’ *Rheologica Acta*, 17(6), 654–662.

Kim K. W., Doh, Y. S., and Lim, S. (1999). "Mode I reflective cracking resistance of strengthened asphalt concrete." *Construction and Building Materials*, 13, 243-251.

Kim, Y. R., and Lee, Y. C. (1995). “Interrelationships among stiffnesses of asphalt aggregate mixtures.” *Asphalt Paving Technology: Association of Asphalt Paving Technologists-Proceedings of the Technical Sessions*, 64, 575-609.

Kim, Y. R., and Little, D. N. (1990). “One-dimensional constitutive modeling of asphalt concrete.” *Journal of Engineering Mechanics*, 116(4), 751-772.

Krishnan, J. M., and Rajagopal, K. R. (2003). “Review of the uses and modeling of bitumen from ancient to modern times.” *Appl. Mech. Rev.*, 56(2), 149-214.

Krishnan, J. M., and Rajagopal, K. R. (2004). “Thermodynamic framework for the constitutive modeling of asphalt concrete: theory and applications.” *Journal of Materials in Civil Engineering*, 16(2), 155-166.

Krishnan, J. M., and Rajagopal, K. R. (2005). “On the mechanical behavior of asphalt.” *Mechanics of Materials*, 37, 1085-1100.

Krishnan, J. M., Rajagopal, K. R., Masad, E., and Little, D. N. (2006). “Thermomechanical framework for the constitutive modeling of asphalt concrete.” *International Journal of Geomechanics*, 6(1), 36-45.

Kutay, M. E., Gibson, N., Youtcheff, J. (2008). "Conventional and Viscoelastic Continuum Damage (VECD) - Based Fatigue Analysis of Polymer Modified Asphalt Pavements." *Journal of the Association of Asphalt Paving Technologists*, 77, 395-434.

Leadermann, H. (1943). *Elastic and Creep Properties of Filamentous Materials and Other High Polymers*, Textile Foundation, Washington, D. C.

Lee, S. J. (2008). " Mechanical performance and crack retardation study of a fiberglass-grid-reinforced asphalt concrete system." *Canadian Journal of Civil Engineering*, 35, 1042-1049.

Lee, S. J., Rust, J. P., Hamouda, H., Kim, Y. R., and Borden, R. H. (2005). "Fatigue Cracking Resistance of Fiber-Reinforced Asphalt Concrete." *Textile Research Journal*, 75(2), 123-128.

Lethersich, W. (1942). "The mechanical behavior of bitumen." *Journal of the Society of Chemical Industry*, 61, 101–108.

Ling, T., Xia, W., Dong, Q., and He, D. (2008). "Study on the influence of the fiber and modified asphalt upon the performance of asphalt mixture." *Proceedings of Symposium on Pavement Mechanics and Materials at the 18th ASCE Engineering Mechanics Division EMD Conference 2007 - Pavements and Materials: Characterization, Modeling, and Simulation: Geotechnical Special Publication*, 182, 45-54.

Li, N., Wu, S., and Liu, C. (2008). "Investigation of static and dynamic response of graphite and carbon fiber modified conductive asphalt-based composite." *Key Engineering Materials*, 385-387, 469-472.

Liu, Q., Schlangen, E., García, Á., and Van de Ven, M. (2010). "Induction heating of electrically conductive porous asphalt concrete." *Construction and Building Materials*, 24(7), 1207-1213.

Liu, X., and Wu, S. (2009). "Research on the conductive asphalt concrete's piezoresistivity effect and its mechanism." *Construction and Building Materials*, 23(8), 2752-2756.

Majidzadeh, K., and Schweyer, H. E. (1965). "Non-newtonian behavior of asphalt cements." *Proc. of Assoc. of Asphalt Paving Technologists*, 34, 20–44.

Majidzadeh, K., and Schweyer, H. E. (1966). "Free-space concepts and rheology of asphalt cements." *Mater. Res. Stand*., 6, 617–624.

Masad, E., Somadevan, N., Bahia, H. U., and Kose, S. (2001). "Modeling and experimental measurements of strain distribution in asphalt mixes." *Journal of Transportation Engineering*, 127(6), 477-485.

Masad, E., and Somadevan, N. (2002). "Microstructural finite-element analysis of influence of localized strain distribution on asphalt mix properties." *Journal of Engineering Mechanics*, 128(10), 1105-1114.

Maurer, D. A., and Malasheskie, G. J. (1989). "Field performance of fabrics and fibers to

retard reflective cracking." *Geotextiles and Geomembranes*, 8, 239-267.

Minsk, L. D. (1968). "Electrically conductive asphalt for control of snow and ice accumulation." *Highway Research Record*, 227, 57-63.

Mundt, D. J., Marano, K. M., Nunes, A. P., and Adams, R. C. (2009). "A Review of Changes in Composition of Hot Mix Asphalt in the United States", *Journal of Occupational and Environmental Hygiene*, 6(11), 714-725.

Muniandy, R. and Huat, B.B.K. (2006). "Laboratory diameteral fatigue performance of stone matrix asphalt with cellulose oil palm fiber." *American Journal of Applied Sciences*, 3(9), 2005-2010.

Neifar, M., and Di Benedetto, H. (2001). "Thermo-viscoplastic law for bituminous mixes." *International Journal Road Materials and Pavement Design*, 2(1), 71-95.

Nicholls, C. (1998). *Asphalt Surfacings*, E & FN Spon, New York, NY.

Oldroyd, J. G. (1950). "On the formulation of rheological equations of state." *Proceedings of the Royal Society of London. Series A*, Mathematical and Physical Sciences, 200(1063), 523-541.

Park, S. W., and Kim, Y. R. (2001). "Fitting Prony-series viscoelastic models with power-law presmoothing." *Journal of Materials in Civil Engineering*, 13(1), 26-32.

Partl, M. N., Hean, S., and Poulikakos, L. (2002). "Asphaltic plug joint characterization and performance evaluation." *Proc., 9th Int. Conf. on Asphalt Pavements*, International Society for Asphalt Pavements, Copenhagen.

Peltonen, P.V. (1991). "Characterization and testing of fibre-modified bitumen composites." *Journal of Materials Science*, 26(20), 5618-22.

Putman, B. J., and Amirkhanian, S. N. (2004). "Utilization of waste fibers in stone matrix asphalt mixtures." *Resources, Conservation and Recycling*, 42, 265–274.

Qian, Z., Akisanya, A. R., and Imbabi, M. S. (2000). "Effects of geometry on the deformation of asphaltic plug joints subjected to surface tractions." *J. Strain Anal.*, 35(5), 403–413.

Reid, M. D., Imbabi, M. S., and Coutellier, D. (1998). "Effects of joint geometry on response of asphaltic plug joints." *J. Transp. Eng.*, 124(4), 311–318.

Roberts, F. L., Mohammad, L. N., and Wang, L. B. (2002). " History of hot mix asphalt mixture design in the United States." *Journal of Materials in Civil Engineering*, 14(4), 279-293.

Saal, R. N. J. (1955). "Mechanical testing of bitumen." *Proc of 4th World Petroleum Congress, Section VI*, 29–46, Rome.

Schapery, R. A. (2000). "Nonlinear viscoelastic solids." *International Journal of Solids*

and Structures, 37, 359-366.

Schwartz, C. W., Gibson, N. H., and Schapery, R. A. (2002). "Time-temperature superposition for asphalt concrete at large compressive strains." *Transportation Research Record*, 1789, 101-112.

Schweyer, H. E., and Busot, J. C. (1969). "A new approach in asphalt rheology." *Highw. Res. Rec*., 273, 1–11.

Serfass, J. P., and Samanos, J. (1996). "Fiber-modified asphalt concrete characteristics, application and behavior." *Journal of the Association of Asphalt Paving Technologists*, 65, 193-230.

Siriwardane, H., Gondle, R., and Kutuk, B. (2010). "Analysis of flexible pavements reinforced with geogrids." *Geotechnical and Geological Engineering*, 28(3), 287-297.

Stastna, J., Zanzotto, L., and Berti, J. (1997). "How good are some rheological models of dynamic material functions of asphalt." *Proc. of Assoc. of Asphalt Paving Technologists*, 66, 458–485.

Storm, D. A., Barresi, R. J., and Sheu, E. Y. (1996). "Development of solid properties and thermochemistry of asphalt binders in the 25–65 °C temperature range." *Energy and Fuels*, 10, 855–864.

Strategic Highway Research Program (1994). *Validation of Relationships Between Specification Properties and Performance*, SHRP-A-409, National Research Council, Washington D.C.

Tapkin, S. (2008). "The effect of polypropylene fibers on asphalt performance." *Building and Environment*, 43, 1065-1071.

Tapkin, S., Usar, U., Tuncan, A., and Tuncan, M. (2009). "Repeated creep behavior of polypropylene fiber-reinforced bituminous mixtures." *Journal of Transportation Engineering*, 135(4), 240-249.

Toney, C. A. (1987). *Fiber Reinforced Asphalt Concrete Pavements - City of Tacoma Fina Report - WA-RD 133.1*, Washington State Transportation Commission, Department of Transportation, Olympia, WA.

Transportation Research Board. (2003). *Bridge deck joint performance—A synthesis of highway practice*, Rep. No. NCHRP Synthesis 319, Washington, D.C.

Trouton, F. T. (1906). "On the coefficient of viscous traction and its relation to that of viscosity." *Proc. R. Soc. London, Ser. A*, 57(519), 426–440.

Vakili, J. (1983). "An experimental study of asphalt concrete based on a multiple-integral representation of constitutive equation of a nonlinear viscoelastic solid" *J. Rheol*., 27(3), 211-222.

Van der Poel, C. (1954). "A general system describing the visco-elastic properties of bitumens and its relation to routine test data", *J. Appl. Chem*., 4, 221–236.

Williams, M. L., Landal, R. F., and Ferry, J. D. (1955). "The temperature dependence of relaxation mechanisms in armorphous polymers and other glass forming liquid." *The Journal of the American Chemical Society*, 77, 3701-3707.

Wu, S., Mo, L., and Shui, Z. (2003). "Piezoresistivity of graphite modified asphalt-based composites." *Key Engineering Materials*, 249, 391-396.

Wu, S., Mo, L., Shui, Z., and Chen, Z. (2005). "Investigation of the conductivity of asphalt concrete containing conductive fillers." *Carbon*, 43, 1358-1363.

Wu, S., Chen, Z., Ye, Q., and Liao, W. (2006a). "Effects of fibre additive on the high temperature property of asphalt binder." *Journal of Wuhan University of Technology - Materials Science Edition*, 21(1), 118-120.

Wu, S., Liu, G., Mo, L., Chen, Z., and Ye, Q. (2006b). "Effect of Fiber Types on Relevant Properties of Porous Asphalt." *Transactions of Nonferrous Metals Society of China*, 16, s791-s795.

Wu, S., Ye, Q., and Li, N. (2008). " Investigation of rheological and fatigue properties of asphalt mixtures containing polyester fibers." *Construction and Building Materials*, 22, 2111-2115.

Wu, S., Zhang, Y., and Chen, M. (2010). "Research on mechanical characteristics of conductive asphalt concrete by indirect tensile test." *Proceedings of the SPIE - The International Society for Optical Engineering*, 7522, 752265, doi: 10.1117/12.851473.

Xu, Q., Chen, H., and Prozzi, J. A. (2010). "Performance of fiber reinforced asphalt concrete under environmental temperature and water effects." *Construction and Building Materials*, 24(10), 2003-2010.

Ye, Q., Wu, S., and Li, N. (2009). "Investigation of the dynamic and fatigue properties of fiber-modifiedasphalt mixtures." *International Journal of Fatigue*, 31, 1598–1602.

Ye, Q., and Wu, S. (2010). "Dynamic properties of asphalt binders containing fiber modifiers." *Advanced Materials Research*, 97-101, 724-727.

Yildirim, Y. (2007). " Polymer modified asphalt binders." *Construction and Building Materials*, 21, 66-72.

Yu, X., and Sun, L. (2010). "Anti-cracking ability of asphalt mixture added with polyester fiber." *Proceedings of the 7th International Conference on Traffic and Transportation Studies*, Kunming, China, 383, 1399-1406.

Zhou, L., Li, P., and Zhang, Z. (2009). "Investigation of high temperature properties of asphalt mixture containing fibers." *Geotechnical Special Publication, No. 193: Proceedings of 2009 GeoHunan International Conference - Material, Design,*

Construction, Maintenance, and Testing of Pavemen, Changsha, Hunan, China, 139-144.

CHAPTER 3
CONSTITUTIVE MODELING FOR ASPHALT BINDER AND MIXTURE

A nonlinear viscoelastic constitutive model that can simulate both linear and nonlinear viscoelasticity of asphaltic materials is proposed. The model is constructed by combining a nonlinear damper with a generalized Maxwell or Kelvin-Voigt model, and because of the manner it is formulated, the behavior of asphalt in both linear and nonlinear ranges can be simulated over a wide range of time, temperature, and stress/strain levels. Numerical integration algorithms for displacement and force controlled deformation and a calibration method employing the constant strain rate test are also proposed. The time-temperature superposition principle is adopted to consider temperature dependency. Two different versions of the model, which are distinguished by the deformable range, are presented in separate sections of this chapter: finite strain version for asphalt binder and infinitesimal strain version for asphalt concrete. The model for asphalt binder is fully three dimensional and described in finite strain kinematics for simulating large deformation. For asphalt concrete, a uniaxial model is formulated in infinitesimal strain theory. In addition, damage mechanics is employed to account for damage evolution of asphalt concrete, which was not necessary for asphalt binder. Calibration and validation of the two versions of the model are demonstrated using previously published experimental data for asphalt binder and asphalt concrete, respectively. It is shown that the proposed constitutive model is capable of successfully simulating creep and constant strain rate tension and shear tests at various temperatures with a single set of material parameters.

3.1. INTRODUCTION

Asphalt is regarded as "a colloidal system consisting of high molecular weight asphaltene micells dispersed or dissolved in a lower molecular weight oily medium"

(Read and Whiteoak 2003). Utilizing its damp-proofing and water-proofing properties, asphalt is widely used as dampers for buildings, agricultural structures, bridge asphalt plug joints, base or stabilizer of aggregate ballast in railway construction, and linings and sealants for canals, reservoirs, and dams (Krishnan and Rajagopal 2003). Additionally, because of its low electrical conductivity, asphalt is used as an insulator for battery and junction boxes and underwater cables (Mathes 1991). However, the primary application of asphalt is to produce asphalt concrete in road construction. Asphalt concrete is a mixture of asphalt and aggregate. When used for paving applications, asphalt concrete is comprised of 4-6% by weight of asphalt to bind the aggregate. In some European countries, the term 'asphalt' refers to asphalt concrete whereas pure asphalt is denoted as 'bitumen'. In this dissertation, following the custom in North America, the term 'asphalt' indicates pure asphalt without aggregate and 'asphalt concrete' implies a composite of asphalt and aggregate. Since the mechanical properties, especially viscoelastcity, of asphalt concrete are largely dependent on the asphalt binder, developing a rigorous mechanical model of asphalt is fundamental for understanding and improving the mechanical properties of asphalt concrete.

The literature survey for asphalt constitutive modeling presented in Chapter 2 can be summarized that: (1) asphalt exhibits linear viscoelasticity in the small strain range and that the effect of nonlinearity becomes significant as the deformation increase (Van der Poel 1954; Cheung and Cebon 1997b; Airey et al. 2003; Krishnan and Rajagopal 2005), (2) even if the macroscopic strain of asphalt concrete is small, the strain magnitudes of asphalt binder between aggregates are high enough to reach into nonlinear viscoelastic range (Masad et al. 2001; Masad and Somadevan 2002), (3) nevertheless, many researchers have approximated its behavior based on the theory of linear viscoelasticity (Jongepier and Kuilman 1969; Dobson 1969; Dickinson 1974; Stastna et al. 1997; Kim and Little 1990; Neifar and Di Benedetto 2001; Desai 2001; Chehab et al. 2002), and a comprehensive constitutive model has not yet been proposed that accounts for both linear and nonlinear viscoelastic responses over various temperatures and loading conditions.

According to the literature survey in Chapter 2, the characteristics of viscoelastic behavior of asphalt can be summarized that: (1) the nonlinear viscosity dominating the asphalt behavior under large deformation can be described by a power law relationship

between strain rate and stress (Cheung and Cebon 1997b), and (2) the linear viscoelasticity of asphalt in small strain region has multiple relaxation times, and hence, its relaxation function can be represented best by Prony series. Based on these perceptions, a new viscoelastic constitutive model that is capable of simulating the characteristics of both linear and nonlinear range is proposed in this Chapter. As illustrated in Fig. 3.1, the proposed model has four different appearances. Deformable range of asphalt binder is so large as to exceed infinitesimal strain while that of asphalt concrete is not. Therefore, the model for asphalt is described in finite strain kinematics to simulate the large deformation rigorously, and the model for asphalt concrete is expressed using infinitesimal strain. The former is explained in Section 3.2, and the latter in Section 3.3. Further classification of the model appearances according to loading condition will be described in those sections.

3.2. NON-LINEAR VISCOELASTIC CONSTITUTIVE MODEL FOR PURE ASPHALT IN FINITE STRAIN KINEMATICS

The nonlinear viscoelastic constitutive model for asphalt is described by a three dimensional finite strain theory to include the effects of large deformation. The model starts off with defining the elemental constitutive equations for elastic spring, linear damper, and nonlinear damper. Then the numerical integration processes originated from Boyce et al. (1989) and Weber et al. (1990) are presented for displacement and force controlled deformations, respectively. Since the linear viscoelastic part of the model has two appearances (Maxwell model and Kelvin-Voigt model) according to loading condition, interconversion between relaxation and creep functions suggested by Park and Schapery (1999) is introduced. Additionally, the time-temperature superposition principle is employed to consider temperature dependency of asphalt.

The proposed model has a number of material parameters that need to be calibrated. This calibration is especially challenging since the model entails a combination of linear and nonlinear viscoelastic components. Therefore, a new calibration method tailored to the proposed model is developed and is demonstrated herein. The experimental data published by Cheung and Cebon (1997b) are used for the demonstration and the

validation of the proposed model.

3.2.1 Model Description

(1) Characteristics of Asphalt Behavior

According to Cheung and Cebon (1997a; 1997b), nonlinear viscosity dominates the behavior of asphalt at stresses above 0.1 MPa. Below this level, asphalt exhibits linear viscoelasticity. As discussed above, others have used strain-based criteria to make that distinction (Van der Poel 1954; Airey et al. 2003). The transition between linear and nonlinear viscosity can be seen in Fig. 3.2, which compares the behavior of asphalt to purely linear and nonlinear viscoelastic models. The solid lines in Fig. 3.2 indicate actual behavior of asphalt (taken from data in Cheung and Cebon 1997b) subjected to uniaxial constant strain rate deformation. Fig. 3.2a shows how a single Maxwell model with nonlinear (power law) damper compares to actual asphalt behavior. The spring constant of the model is determined from the instantaneous response and the parameters for the power law damper are set to capture the steady state response as suggested by Cheung and Cebon (1997b). While the model successfully predicts the peak stresses, it fails to simulate the initial behavior. The decrease of nominal stress after the peak response is caused by large deformation effects, which will be discussed later on. Fig. 3.2a demonstrates the necessity of including an additional model to capture the initial behavior.

The fact that the initial behavior of asphaltic materials varies widely with applied strain rate in the bottom left corner of Fig. 3.2 implies an important characteristic of linear viscoelasticity dominating the small strain region: the existence of multiple relaxation times. In this study, a Prony series which can represent both the generalized Maxwell model and the generalized Kelvin-Voigt model is used for the linear part of the model. Fig. 3.2b compares the response of a generalized Maxwell model to typical asphalt behavior. Clearly, the variation of the initial responses with strain rates are captured well, but the behavior in the nonlinear dominant range including the peak stress cannot be captured by the generalized Maxwell model. Together, Fig. 3.2a and 3.2b demonstrate the advantages and limits of the two models and demonstrate the necessity of combining them to capture the response over the entire range of behavior.

(2) Modeling Strategy

Mechanical analog is a useful tool to understand and formulate constitutive models for viscoelastic materials. Maxwell model, Kelvin-Voigt model, Standard linear solid model, and Burgers' model are the most popular mechanical analogs for viscoelastic materials (Findley 1976). Previously published mechanical analogs for asphaltic materials are composed of a set of elastic springs, viscous dampers, and sometimes plastic dampers. Although many existing constitutive models use plastic and viscous models separately, the separation of viscous and plastic deformation is controversial. The differences between typical plastic and viscous dampers are: 1) the behavior of plastic damper is not a function of time, and 2) the plastic damper does not activate below a certain stress level. The similarity between both is that deformations lead to non-recoverable energy dissipation. Phenomenological distinction of plastic and viscous flow is often considered to be impossible in viscoelastic materials. Therefore, only viscous dampers are used in this study.

Fig. 3.3 illustrates the two mechanical analogs proposed for asphalt. The model consists of a nonlinear system (a nonlinear damper) and linear system. Consequently, the total deformation gradient can be divided into nonlinear and linear parts. Nonlinear deformation is purely viscous, and linear deformation is viscoelastic. The behavior of the nonlinear system is assumed to have power law viscosity based on Cheung and Cebon's data (1997b). The driving force of the nonlinear damper is the force generated in the linear system.

As shown in Fig. 3.3a and Fig. 3.3b, the linear system of the proposed model varies with the loading condition to facilitate numerical integration. In the case of displacement controlled deformation, the deformation gradient of the linear system at a specific time can be determined from total and nonlinear deformation gradients. When a fixed deformation is given, the generalized Maxwell model illustrated in Fig. 3.3a is more convenient than the generalized Kelvin-Voigt model to calculate the resultant stress because each Maxwell element can be considered separately. On the other hand, when the deformation is controlled by force, total stress history is given as the loading condition. To calculate the resultant strain from the mechanical analog in Fig. 3.3a, the given total stress should be properly distributed into each Maxwell element so as to satisfy

equilibrium and compatibility conditions of all Maxwell elements at the same time. This is possible in theory, but involves complex calculation processes, especially in hyperelasticity. If the same loading condition is applied to the mechanical analog shown in Fig. 3.3b, the situation becomes much simpler. The resultant deformation gradient of each Kelvin-Voigt element can be obtained independently for the same applied stress, and the total resultant deformation gradient can be calculated by multiplying the deformation gradients of all elements.

Although the appearances of the generalized Maxwell model and the generalized Kelvin-Voigt model are different, those models are mathematically identical (Wineman and Rajagopal 2000). In other words, those are two different appearances of one linear viscoelastic model, and they share the same viscoelastic functions. When the spring constants and the damper viscosities of the generalized Maxwell model are known, its viscoelastic function can be easily expressed by relaxation modulus in the form of a Prony series. On the other hand, Prony form creep compliance is more convenient to describe the generalized Kelvin-Voigt model. The interconversion between creep compliance and relaxation modulus is possible to achieve using the method suggested by Park and Schapery (1999). Therefore, when a set of material parameters are calibrated for any one of the two linear models, the parameters of the other model that is mathematically equivalent can be obtained through the interconversion.

To simulate the mechanical response of the proposed model which is a combination of elastic, linear viscous, and nonlinear viscous components, numerical integration processes are introduced for both displacement and force controlled deformations. The method of numerical integration is based upon techniques proposed by Weber et al. (1990) and Boyce et al. (1989). This numerical integration has been applied to various polymeric materials with viscoelasticity (Bergstrom and Boyce 2000; Lion 2000; Miehe and Keck 2000). The numerical integration presented in this work shares their logic, but is modified to fit the proposed mechanical analogs.

The deformable range of asphalt is large. The constant strain rate uniaxial tension tests of asphalt by Cheung and Cebon (1997b) were conducted up to a nominal strain of 0.5. The resulting stress - strain curves reached the peak nominal stress at a nominal strain that ranged from 0.2 to 0.4. Harvey and Cebon (2003) reported the fracture strain

of asphalt in the ductile region to be approximately 2.6. There is common consensus that infinitesimal strain theory applies for strains below 0.01, and for the large strain over 0.01, finite strain theory should be used, as is done herein.

While the proposed model uses the Neo-Hookean model which is one of the simplest models for hyperelasticity, the elastic parameters of the springs in Fig. 3.3 are characterized by the elastic moduli (E_{M_i} and E_{K_i}) of Hooke's law for reasons described and justified later on in the chapter. Another aspect of this study is that asphalt is assumed to be an incompressible material because asphalt is considered as a continuous fluid in general.

(3) Stress Measure

The stress measure used in the proposed model is the Cauchy (true) stress ($\boldsymbol{\sigma}$) that considers the deformed configuration. Eq. (3.1) and (3.2) are the relationship between the Cauchy stress tensor ($\boldsymbol{\sigma}$) and the nominal (first Piola-Kirchoff) stress tensor ($\mathbf{S}$).

$$\boldsymbol{\sigma} = J^{-1}\mathbf{S}\mathbf{F}^{\mathbf{T}} \tag{3.1}$$

$$\mathbf{S} = J\boldsymbol{\sigma}\mathbf{F}^{-\mathbf{T}} \tag{3.2}$$

where, J is the Jacobian representing volumetric change, and $\mathbf{F}$ is the deformation gradient. For an incompressible material, the Jacobian $J = \det \mathbf{F} = 1$.

(4) Finite Strain Kinematics

When a position vector of a material point at a current configuration, $\mathbf{x} = \mathbf{x}(\mathbf{X}, t)$, is given as a function of time, t, and its position vector at the reference configuration, $\mathbf{X}$, the deformation gradient $\mathbf{F}$ is defined as;

$$\mathbf{F} = \frac{\partial \mathbf{x}}{\partial \mathbf{X}} = \mathbf{R}\mathbf{U} = \mathbf{V}\mathbf{R} \tag{3.3}$$

where, $\mathbf{U}$ and $\mathbf{V}$ are the symmetric stretch tensors, and $\mathbf{R}$ is the orthogonal rotation tensor.

The velocity gradient $\mathbf{L}$ and the left Cauchy-Green strain tensor $\mathbf{B}$ are;

$$\mathbf{L} = \dot{\mathbf{F}}\mathbf{F}^{-1} = \mathbf{D} + \mathbf{W} \tag{3.4}$$

$$\mathbf{B} = \mathbf{F}\mathbf{F}^{\mathbf{T}} = \mathbf{V}\mathbf{V}^{\mathbf{T}} \tag{3.5}$$

where, $\mathbf{D}$ and $\mathbf{W}$ are the symmetric and the skew-symmetric parts of $\mathbf{L}$, and are defined as Eq. (3.6) and (3.7), respectively. Physically, $\mathbf{D}$ represents the rate of stretching, and $\mathbf{W}$ represents the spin.

$$\mathbf{D} = \tfrac{1}{2}\left(\mathbf{L} + \mathbf{L}^{\mathrm{T}}\right) \tag{3.6}$$

$$\mathbf{W} = \tfrac{1}{2}\left(\mathbf{L} - \mathbf{L}^{\mathrm{T}}\right) \tag{3.7}$$

(5) Kinematics for Uniaxial Deformation

Fig. 3.4a illustrates a uniaxial tensile deformation. When the material is incompressible, the relationship between the reference ($\mathbf{X}$) and the current ($\mathbf{x}$) configurations is described as follows;

$$\begin{aligned} x_1 &= \Lambda X_1 \\ x_2 &= \frac{1}{\sqrt{\Lambda}} X_2 \\ x_3 &= \frac{1}{\sqrt{\Lambda}} X_3 \end{aligned} \tag{3.8}$$

where, Λ is the stretch. When the displacement vector ($\mathbf{u}$) and the linearized (nominal) strain ($\mathbf{e}$) are defined as Eq. (3.9) and (3.10), the relationship between Λ and e_{11} for uniaxial deformation can be written as Eq. (3.11).

$$\mathbf{u}(\mathbf{X}, t) = \mathbf{x}(\mathbf{X}, t) - \mathbf{X} \tag{3.9}$$

$$\mathbf{e} = \frac{1}{2}\left[\nabla_{\mathbf{X}}\mathbf{u} + \left(\nabla_{\mathbf{X}}\mathbf{u}\right)^{\mathrm{T}}\right] \tag{3.10}$$

$$\Lambda = e_{11} + 1 \tag{3.11}$$

From Eq. (3.3), the deformation gradient ($\mathbf{F}$) for uniaxial deformation is;

$$\mathbf{F} = \begin{bmatrix} \Lambda & 0 & 0 \\ 0 & 1/\sqrt{\Lambda} & 0 \\ 0 & 0 & 1/\sqrt{\Lambda} \end{bmatrix} \tag{3.12}$$

The velocity gradient ($\mathbf{L}$) for uniaxial deformation can be obtained from Eq. (3.4);

$$\mathbf{L} = \dot{\mathbf{F}}\mathbf{F}^{-1} = \begin{bmatrix} \dot{\Lambda} & 0 & 0 \\ 0 & -\dot{\Lambda}/2\sqrt{\Lambda^3} & 0 \\ 0 & 0 & -\dot{\Lambda}/2\sqrt{\Lambda^3} \end{bmatrix} \begin{bmatrix} 1/\Lambda & 0 & 0 \\ 0 & \sqrt{\Lambda} & 0 \\ 0 & 0 & \sqrt{\Lambda} \end{bmatrix}$$
$$= \begin{bmatrix} \dot{\Lambda}/\Lambda & 0 & 0 \\ 0 & -\dot{\Lambda}/2\Lambda & 0 \\ 0 & 0 & -\dot{\Lambda}/2\Lambda \end{bmatrix} \tag{3.13}$$

Since the velocity gradient is a diagonal matrix, the skew-symmetric part $\mathbf{W} = \mathbf{0}$ and the symmetric part $\mathbf{D} = \mathbf{L}$.

From Eq. (3.5), the left Cauchy-Green strain tensor ($\mathbf{B}$) is;

$$\mathbf{B} = \mathbf{F}\mathbf{F}^{\mathbf{T}} = \begin{bmatrix} \Lambda^2 & 0 & 0 \\ 0 & 1/\Lambda & 0 \\ 0 & 0 & 1/\Lambda \end{bmatrix} \tag{3.14}$$

To solve the hyperelastic constitutive equation for incompressible materials shown in Eq. (3.41), the hydrostatic pressure (p) should be determined from the boundary condition. Applying the uniaxial boundary condition that $\sigma_{22} = \sigma_{33} = 0$ to Eq. (3.41);

$$p = 2C_{NH}\frac{1}{\Lambda} \tag{3.15}$$

It should be noted that Eq. (3.41) is the constitutive equation for each spring in the model, and the total stress is the sum of the stresses of each component connected in parallel as shown in Eq. (3.51) and (3.72). Therefore, the hydrostatic pressure for each spring element (p_{ME_i} or p_{KE_i}) should be determined using the stretch (Λ_{ME_i} or Λ_{KE_i}) and the Neo-Hookean constant ($C_{NH\_M\_i}$ or $C_{NH\_K\_i}$) for each spring.

In uniaxial deformation, the only non-zero component in the Cauchy stress tensor ($\boldsymbol{\sigma}$) is σ_{11};

$$\boldsymbol{\sigma} = \begin{bmatrix} \sigma_{11} & 0 & 0 \\ 0 & 0 & 0 \\ 0 & 0 & 0 \end{bmatrix} \tag{3.16}$$

From Eq. (3.2) and the incompressibility, the nominal stress tensor ($\mathbf{S}$) is;

$$\mathbf{S} = \begin{bmatrix} \sigma_{11}/\Lambda & 0 & 0 \\ 0 & 0 & 0 \\ 0 & 0 & 0 \end{bmatrix} \tag{3.17}$$

In this study, Hooke's law is temporarily used to calibrate the linear system dominating infinitesimal strain range while the elasticity of the model is represented by the Neo-Hookean model. Therefore, the relationship between the elastic modulus (E) and the Neo-Hookean constant (C_{NH}) need to be derived. Consider a spring with the Neo-Hookean constant C_{NH_S} and the elastic modulus E_S subjected to uniaxial deformation. Then, the uniaxial component of the Cauchy stress tensor is;

$$\sigma_{11} = 2C_{NH\_S}\left(\Lambda^2 - \frac{1}{\Lambda}\right) \tag{3.18}$$

The uniaxial Hooke's law in terms of nominal stress (S_{11}) and nominal strain (e_{11}) is;

$$S_{11} = E_S e_{11} = E_S(\Lambda - 1) \tag{3.19}$$

At small strain ($\Lambda \to 1$), $S_{11} \approx \sigma_{11}$. The relationship between E_S and C_{NH_S} can be obtained as follows;

$$\begin{aligned}\lim_{\Lambda\to 1}\sigma_{11} &= \lim_{\Lambda\to 1} 2C_{NH\_S}\left(\frac{\Lambda^3 - 1}{\Lambda}\right) = \lim_{\Lambda\to 1} 2C_{NH\_S}(\Lambda - 1)\frac{\left(\Lambda^2 + \Lambda + 1\right)}{\Lambda} \\ &= \lim_{\Lambda\to 1} 6C_{NH\_S}(\Lambda - 1) = 6C_{NH\_S}e_{11} = S_{11} = E_S e_{11}\end{aligned} \tag{3.20}$$

Therefore,

$$C_{NH\_S} = \frac{E_S}{6} \tag{3.21}$$

In the mechanical analog shown in Fig. 3.3b, the deformation gradient of the single spring ($\mathbf{F}_E$) is calculated at the component level. The stretch of the single spring can be determined by Eq. (3.22).

$$\Lambda_E = e_{11\_E} + 1 = \frac{S_{11}}{E_{K\_0}} + 1 = \frac{S_{11}}{6C_{NH\_K\_0}} + 1 \tag{3.22}$$

Then, $\mathbf{F}_E$ for uniaxial loading is;

$$\mathbf{F}_E = \begin{bmatrix} \Lambda_E & 0 & 0 \\ 0 & 1/\sqrt{\Lambda_E} & 0 \\ 0 & 0 & 1/\sqrt{\Lambda_E} \end{bmatrix} \tag{3.23}$$

(6) Kinematics for Simple Shear Deformation

The relationship between the reference ($\mathbf{X}$) and the current ($\mathbf{x}$) configurations in the simple shear deformation illustrated in Fig. 3.4b can be described as follows;

$$\begin{aligned} x_1 &= X_1 + KX_2 \\ x_2 &= X_2 \\ x_3 &= X_3 \end{aligned} \tag{3.24}$$

With the definition of the engineering shear strain (γ_{ij}) shown in Eq. (3.25), the relationships between γ_{12}, e_{12} (defined in Eq. (3.10)), and a constant K can be written as Eq. (3.26);

$$\gamma_{ij} = \frac{\partial u_i}{\partial X_j} + \frac{\partial u_j}{\partial X_i} \qquad \text{for} \quad i \neq j \tag{3.25}$$

$$K = \gamma_{12} = \frac{1}{2} e_{12} \tag{3.26}$$

From Eq. (3.3) and (3.24), the deformation gradient ($\mathbf{F}$) for the simple shear is;

$$\mathbf{F} = \begin{bmatrix} 1 & K & 0 \\ 0 & 1 & 0 \\ 0 & 0 & 1 \end{bmatrix} \tag{3.27}$$

From Eq. (3.4) and (3.27), the velocity gradient ($\mathbf{L}$) for the simple shear is;

$$\mathbf{L} = \dot{\mathbf{F}}\mathbf{F}^{-1} = \begin{bmatrix} 0 & \dot{K} & 0 \\ 0 & 0 & 0 \\ 0 & 0 & 0 \end{bmatrix} \begin{bmatrix} 1 & -K & 0 \\ 0 & 1 & 0 \\ 0 & 0 & 1 \end{bmatrix} = \begin{bmatrix} 0 & \dot{K} & 0 \\ 0 & 0 & 0 \\ 0 & 0 & 0 \end{bmatrix} \tag{3.28}$$

In the numerical integration procedure, the skew-symmetric part of velocity gradient ($\mathbf{W}$) should be determined by applying a proper constraint. From Eq. (3.28), the symmetric ($\mathbf{D}$) and the skew-symmetric ($\mathbf{W}$) parts of the velocity gradient for the simple shear deformation can be determined as follows.

$$\mathbf{D} = \frac{1}{2}\left(\mathbf{L} + \mathbf{L}^{\mathrm{T}}\right) = \begin{bmatrix} 0 & \dot{K}/2 & 0 \\ \dot{K}/2 & 0 & 0 \\ 0 & 0 & 0 \end{bmatrix} \tag{3.29}$$

$$\mathbf{W} = \frac{1}{2}\left(\mathbf{L} - \mathbf{L}^{\mathrm{T}}\right) = \begin{bmatrix} 0 & \dot{K}/2 & 0 \\ -\dot{K}/2 & 0 & 0 \\ 0 & 0 & 0 \end{bmatrix} \tag{3.30}$$

As shown in Eq. (3.30), $W_{12} = D_{12}$, $W_{21} = -D_{21}$, and other components of $\mathbf{W}$ are zero for simple shear deformation.

From Eq. (3.5) and (3.27), the left Cauchy-Green strain tensor ($\mathbf{B}$) is;

$$\mathbf{B} = \mathbf{F}\mathbf{F}^{\mathbf{T}} = \begin{bmatrix} 1+K^2 & K & 0 \\ K & 1 & 0 \\ 0 & 0 & 1 \end{bmatrix} \tag{3.31}$$

Applying the boundary condition that $\sigma_{33} = 0$ to Eq. (3.41), the hydrostatic pressure (p) is;

$$p = 2C_{NH} \tag{3.32}$$

In the mechanical analogs illustrated in Fig. 3.3, each element has the same form of the left Cauchy-Green strain tensor with corresponding K. Therefore, the Cauchy stress tensor ($\boldsymbol{\sigma}$) calculated from Eq. (3.41) of each spring and Eq. (3.51) or Eq. (3.72) has three non-zero components as shown in Eq. (3.33).

$$\boldsymbol{\sigma} = \begin{bmatrix} \sigma_{11} & \sigma_{12} & 0 \\ \sigma_{21} & 0 & 0 \\ 0 & 0 & 0 \end{bmatrix} \tag{3.33}$$

Since, the left Cauchy-Green strain tensor is symmetric, $\sigma_{21} = \sigma_{12}$.

From Eq. (3.2) with $J = 1$ and Eq. (3.33), the nominal stress tensor ($\mathbf{S}$) is;

$$\mathbf{S} = \begin{bmatrix} \sigma_{11} - K\sigma_{12} & \sigma_{12} & 0 \\ \sigma_{12} & 0 & 0 \\ 0 & 0 & 0 \end{bmatrix} \tag{3.34}$$

The relationship between the elastic modulus (E) and the Neo-Hookean constant (C_{NH}) can be derived in simple shear as well. Considering a spring with C_{NH_S} and E_S subjected to simple shear deformation, the shear component of the Cauchy stress tensor is;

$$\sigma_{12} = 2C_{NH}\gamma_{12} \tag{3.35}$$

Hooke's law for the simple shear is;

$$S_{12} = \frac{E}{2(1+\nu)}\gamma_{12} = \frac{E}{3}\gamma_{12} \tag{3.36}$$

where, Poisson's ratio, $\nu = 1/2$ for incompressible materials. As shown in Eq. (3.34), $\sigma_{12} = S_{12}$. Therefore;

$$C_{NH} = \frac{E}{6} \tag{3.37}$$

As the same manner to uniaxial loading, the deformation gradient of the single spring ($\mathbf{F}_E$) in Fig. 3.3b subjected to simple shear can be determined by Eq. (3.38) and (3.39).

$$K_E = \gamma_{12\_E} = \frac{3S_{12}}{E_{K\_0}} \tag{3.38}$$

$$\mathbf{F}_E = \begin{bmatrix} 1 & K_E & 0 \\ 0 & 1 & 0 \\ 0 & 0 & 1 \end{bmatrix} \tag{3.39}$$

(7) Elemental Constitutive Equations

In the numerical integration, the mechanical response of the proposed model is obtained by computing the response of each element (springs, linear dampers, and nonlinear damper) by applying the compatibility and equilibrium conditions. In the case of the elastic spring, a general form of the hyperelastic constitutive equation for incompressible materials is expressed in Eq. (3.40).

$$\boldsymbol{\sigma} = 2\left[\left(\frac{\partial \mathcal{U}}{\partial I_1} + I_1 \frac{\partial \mathcal{U}}{\partial I_2}\right)\mathbf{B} - \frac{\partial \mathcal{U}}{\partial I_2}\mathbf{B}\mathbf{B}^{\mathbf{T}}\right] - p\mathbf{I} \tag{3.40}$$

where, $\boldsymbol{\sigma}$, $\mathcal{U}$, p, I_1, I_2, and $\mathbf{I}$ are the Cauchy stress tensor, the strain energy density, the hydrostatic pressure, the first and the second invariants of $\mathbf{B}$, and the identity tensor, respectively. The value of p can be determined from the boundary condition. In this study, the classical Neo-Hookean strain energy density function ($\mathcal{U}_{NH} = C_{NH}(I_1 - 3)$) is selected to describe the elastic property of the proposed model because of its simplicity. Then, Eq. (3.40) becomes Eq. (3.41) by substituting $\partial \mathcal{U}_{NH} / \partial I_1 = C_{NH}$ and $\partial \mathcal{U}_{NH} / \partial I_2 = 0$.

$$\boldsymbol{\sigma} = 2C_{NH}\mathbf{B} - p\mathbf{I} \tag{3.41}$$

where, C_{NH} is a constant. The stress-strain relationship of the Neo-Hookean model is approximately linear in the small deformation range. If the elastic modulus (E) is calibrated in the infinitesimal strain range, then C_{NH} will be one sixth of the elastic modulus ($C_{NH} = E/6$).

In the proposed model, Eq. (3.41) is the constitutive equation for each spring in the linear system. Therefore, the stress of each spring ($\boldsymbol{\sigma}_{M\_i}$ or $\boldsymbol{\sigma}_{KE\_i}$) should be calculated from the corresponding elastic strain tensor ($\mathbf{B}_{ME\_i} = \mathbf{F}_{ME\_i}\mathbf{F}_{ME\_i}^{\mathbf{T}}$ or $\mathbf{B}_{K\_i} = \mathbf{F}_{K\_i}\mathbf{F}_{K\_i}^{\mathbf{T}}$).

Weber et al. (1990) proposed a finite strain plastic flow rule for rate dependent materials that does not depend on a yield function and where plastic flow occurs at all nonzero stress levels. This approach was adopted by other researchers, e.g. Reese and Govindjee (1998), Bergstrom and Boyce (1998), and Miehe and Keck (2000), and is applied herein. According to Weber et al. (1990), the rate of shape change of the viscous damper, $\mathbf{D}_V$, can be written as Eq. (3.42).

$$\mathbf{D}_V = \sqrt{3/2}\dot{\bar{\varepsilon}}_V \mathbf{N} \tag{3.42}$$

where, the equivalent tensile viscous strain rate ($\dot{\bar{\varepsilon}}_V$) and the direction of viscous flow ($\mathbf{N}$) are;

$$\dot{\bar{\varepsilon}}_V = \sqrt{(2/3)\mathbf{D}_V : \mathbf{D}_V} \geq 0 \tag{3.43}$$

$$\mathbf{N} = \sqrt{3/2}\,\frac{\boldsymbol{\sigma}'}{\bar{\sigma}} \tag{3.44}$$

and the equivalent tensile stress ($\bar{\sigma}$) is;

$$\bar{\sigma} = \sqrt{(3/2)\boldsymbol{\sigma}' : \boldsymbol{\sigma}'} \tag{3.45}$$

$\boldsymbol{\sigma}'$ is the deviator of the Cauchy stress tensor.

In Eq. (3.42), $\dot{\bar{\varepsilon}}_V$ is prescribed by the elemental constitutive function of the viscous damper. When the material constants are calibrated for the uniaxial loading condition, the uniaxial viscous strain rate and corresponding stress will be the same for $\dot{\bar{\varepsilon}}_V$ and $\bar{\sigma}$. Then, $\dot{\bar{\varepsilon}}_V$ for the linear dampers in Fig. 3.3 is;

$$\dot{\bar{\varepsilon}}_V = \frac{\bar{\sigma}}{\mu} \tag{3.46}$$

where, μ is the axial viscosity of the damper.

The $\dot{\bar{\varepsilon}}_V$ for a nonlinear damper can be expressed by power form (Cheung and Cebon 1997b).

$$\dot{\bar{\varepsilon}}_V = A\bar{\sigma}^m \tag{3.47}$$

where, A and m are the material parameters.

Substituting Eq. (3.44), (3.46), and (3.47) into Eq. (3.42), the rates of shape change for the linear and the nonlinear dampers can be written as follows.

$$\mathbf{D}_{LV} = \frac{3}{2\mu}\boldsymbol{\sigma}'_{LV} \tag{3.48}$$

$$\mathbf{D}_{NL} = \left(\frac{3}{2}A\bar{\sigma}_{NL}^{m-1}\right)\boldsymbol{\sigma}'_{NL} \tag{3.49}$$

where, the subscripts '*LV*' and '*NL*' indicate linear damper and nonlinear damper, respectively.

(8) Numerical Integration for Displacement Controlled Deformation

Fully three-dimensional constitutive models in finite strain for viscoelastic materials have been proposed by various researchers (Boyce et al. 1989; Bergstrom and Boyce 2000; Lion 2000; Reese and Govindjee 1998). Their works include development of mechanical analogs for standard linear (or nonlinear) solids and their various modifications. The finite strain version of the numerical integration is a common technique used in their simulations. The theoretical background and applications to viscoelastic materials of the finite strain based numerical integration can be found in Weber et al. (1990); Boyce et al. (1989), and Miehe and Keck (2000). The numerical integration presented here is based on their procedures, modified to fit the proposed model.

The basic idea of the numerical integration is to partition time into small time steps and to calculate the displacement and its rate for each damper separately using the elemental constitutive equations. The rate of deformation gradient ($\dot{\mathbf{F}}$) of each damper at each time step is used to calculate the deformation gradient ($\mathbf{F}$) of the dampers at the next time step, i.e. the scheme is essentially explicit. The time interval (Δt) between each

step determines the accuracy and the stability of the numerical integration. For example, at step *k*, if an increment of deformation gradient of any linear damper ($\left(\dot{\mathbf{F}}_{MV\_i}\right)_{k-1}\Delta t$) is larger than the increment of deformation gradient of the linear system ($\left(\mathbf{F}_L\right)_k$), the result will diverge. Extensive simulation studies showed that stability problems can be eliminated if the time interval is smaller than the smallest characteristic time ($\tau_{R\_i} = \mu_{M\_i}/E_{M\_i}$) of the linear dampers.

The numerical integration process depends upon whether loading is controlled by displacement or force. In displacement controlled deformation, displacement or strain are given as a function of time, and force or stress are the resultant. In that case, the mechanical analog with the generalized Maxwell model shown in Fig. 3.3a is used to calculate the resultant force or stress.

In the proposed nonlinear model, the total deformation gradient, $\mathbf{F}$, is divided into the nonlinear viscous flow gradient, $\mathbf{F}_{NL}$, and the linear viscoelastic deformation gradient, $\mathbf{F}_L$. In the mechanical analog shown in Fig. 3.3a, $\mathbf{F}_L$ is divided into the linear viscous flow gradient, $\mathbf{F}_{MV\_i}$, and the elastic deformation gradient, $\mathbf{F}_{ME\_i}$, at each Maxwell element. Therefore, the compatibility and equilibrium equations for the displacement controlled deformation can be expressed as Eq. (3.50) and (3.51), respectively.

$$\mathbf{F} = \mathbf{F}_L\mathbf{F}_{NL} = \mathbf{F}_{ME\_i}\mathbf{F}_{MV\_i}\mathbf{F}_{NL} \tag{3.50}$$

$$\boldsymbol{\sigma} = \boldsymbol{\sigma}_{NL} = \boldsymbol{\sigma}_L = \sum_{i=1}^{n}\boldsymbol{\sigma}_{M\_i} \tag{3.51}$$

where, $\boldsymbol{\sigma}_{NL}$, $\boldsymbol{\sigma}_L$, and $\boldsymbol{\sigma}_{M\_i}$ are the Cauchy stress tensors for the nonlinear system, the linear system, and the i^{th} Maxwell element, respectively.

To apply the damper constitutive model shown in Eq. (3.48) and (3.49) to the numerical integration, the relationship between $\dot{\mathbf{F}}$ and $\mathbf{D}$ of each damper should be derived. From Eq. (3.4) and (3.50), the total velocity gradient, $\mathbf{L}$ can be decomposed into $\mathbf{L}_L$ and $\tilde{\mathbf{L}}_{NL}$ as Eq. (3.52).

$$\begin{aligned}\mathbf{L} = \dot{\mathbf{F}}\mathbf{F}^{-1} &= \left[\frac{\partial}{\partial t}\left(\mathbf{F}_L\mathbf{F}_{NL}\right)\right]\left(\mathbf{F}_L\mathbf{F}_{NL}\right)^{-1} = \dot{\mathbf{F}}_L\mathbf{F}_{NL}\mathbf{F}_{NL}^{-1}\mathbf{F}_L^{-1} + \mathbf{F}_L\dot{\mathbf{F}}_{NL}\mathbf{F}_{NL}^{-1}\mathbf{F}_L^{-1} \\ &= \dot{\mathbf{F}}_L\mathbf{F}_L^{-1} + \mathbf{F}_L\dot{\mathbf{F}}_{NL}\mathbf{F}^{-1} = \mathbf{L}_L + \tilde{\mathbf{L}}_{NL}\end{aligned} \tag{3.52}$$

Again, the velocity gradient of the linear system, $\mathbf{L}_L$, is decomposed into $\mathbf{L}_{ME\_i}$ and $\tilde{\mathbf{L}}_{MV\_i}$ at the i^{th} Maxwell element.

$$\begin{aligned}\mathbf{L}_L = \dot{\mathbf{F}}_L\mathbf{F}_L^{-1} &= \left[\frac{\partial}{\partial t}\left(\mathbf{F}_{ME\_i}\mathbf{F}_{MV\_i}\right)\right]\left(\mathbf{F}_{ME\_i}\mathbf{F}_{MV\_i}\right)^{-1} \\ &= \dot{\mathbf{F}}_{ME\_i}\mathbf{F}_{ME\_i}^{-1} + \mathbf{F}_{ME\_i}\dot{\mathbf{F}}_{MV\_i}\mathbf{F}_L^{-1} = \mathbf{L}_{ME\_i} + \tilde{\mathbf{L}}_{MV\_i}\end{aligned} \tag{3.53}$$

From Eq. (3.4), (3.52), and (3.53), $\tilde{\mathbf{L}}_{NL}$ and $\tilde{\mathbf{L}}_{MV\_i}$ can be written as Eq. (3.54) and (3.55).

$$\tilde{\mathbf{L}}_{NL} = \mathbf{F}_L\dot{\mathbf{F}}_{NL}\mathbf{F}^{-1} = \tilde{\mathbf{D}}_{NL} + \tilde{\mathbf{W}}_{NL} \tag{3.54}$$

$$\tilde{\mathbf{L}}_{MV\_i} = \mathbf{F}_{ME\_i}\dot{\mathbf{F}}_{MV\_i}\mathbf{F}_L^{-1} = \tilde{\mathbf{D}}_{MV\_i} + \tilde{\mathbf{W}}_{MV\_i} \tag{3.55}$$

At the right side of Eq. (3.54) and (3.55), the rates of stretching $\tilde{\mathbf{D}}_{NL}$ and $\tilde{\mathbf{D}}_{MV\_i}$ can be calculated from the corresponding stresses using Eq. (3.48) and (3.49). Boyce et al. (1989) suggested two choices for dealing with $\mathbf{W}$ of the inelastic part and recommended imposing a constraint on inelastic $\mathbf{W}$. For instance, Bergstrom and Boyce (1998; 2000) used a constraint of $\mathbf{W} = \mathbf{0}$. This constraint is useful when $\mathbf{F}$ is symmetric, in other words, the deformation is a pure stretch condition without any shear component. When $\mathbf{F}$ is non-symmetric, the values of each element of anti-symmetric matrix $\mathbf{W}$ can be determined from the prescribed $\mathbf{F}$ and $\mathbf{D}$. An example of determining $\mathbf{W}$ is demonstrated for a simple shear case earlier. Once, $\tilde{\mathbf{W}}_{NL}$, $\tilde{\mathbf{W}}_{MV\_i}$, $\tilde{\mathbf{D}}_{NL}$, and $\tilde{\mathbf{D}}_{MV\_i}$ are determined, the rates of deformation gradients $\dot{\mathbf{F}}_{NL}$ and $\dot{\mathbf{F}}_{MV\_i}$ can be obtained by Eq. (3.56) and (3.57).

$$\dot{\mathbf{F}}_{NL} = \mathbf{F}_L^{-1}\tilde{\mathbf{L}}_{NL}\mathbf{F} \tag{3.56}$$

$$\dot{\mathbf{F}}_{MV\_i} = \mathbf{F}_{ME\_i}^{-1}\tilde{\mathbf{L}}_{MV\_i}\mathbf{F}_L \tag{3.57}$$

In the numerical integration process, the rates of shape change of dampers ($\dot{\mathbf{F}}_{NL}$ and $\dot{\mathbf{F}}_{MV\_i}$) at certain time step are used to calculate the deformation gradients of each damper at the next time step. Once the deformation gradient of each damper is known, overall deformation and corresponding stress at the time step can be obtained by the compatibility, the equilibrium, and the elemental constitutive equations. A complete calculation process for an arbitrary time step *k* with time interval $\Delta t = t_k - t_{k-1}$ is demonstrated in Eq. (3.58)-(3.70).

The deformation gradient of each damper at step *k* can be calculated cumulatively using $\dot{\mathbf{F}}_{NL}$ and $\dot{\mathbf{F}}_{MV\_i}$ of the previous step.

$$\left(\mathbf{F}_{NL}\right)_k = \left(\mathbf{F}_{NL}\right)_{k-1} + \left(\dot{\mathbf{F}}_{NL}\right)_{k-1}\Delta t \tag{3.58}$$

$$\left(\mathbf{F}_{MV\_i}\right)_k = \left(\mathbf{F}_{MV\_i}\right)_{k-1} + \left(\dot{\mathbf{F}}_{MV\_i}\right)_{k-1}\Delta t \tag{3.59}$$

where, the subscript outside of the parentheses indicates the number of the step. Since the total deformation gradient at step *k* is given, the deformation gradient of the linear system can be obtained from the compatibility condition of Eq. (3.50).

$$\left(\mathbf{F}_L\right)_k = \left(\mathbf{F}\right)_k \left(\mathbf{F}_{NL}^{-1}\right)_k \tag{3.60}$$

Then, the deformation gradient of each spring is;

$$\left(\mathbf{F}_{ME\_i}\right)_k = \left(\mathbf{F}_L\right)_k \left(\mathbf{F}_{MV\_i}^{-1}\right)_k \tag{3.61}$$

The stress of each spring can be calculated from $\left(\mathbf{B}_{ME\_i}\right)_k$ and Eq. (3.41), as follows.

$$\left(\mathbf{B}_{ME\_i}\right)_k = \left(\mathbf{F}_{ME\_i}\right)_k \left(\mathbf{F}_{ME\_i}^{\mathbf{T}}\right)_k \tag{3.62}$$

$$\left(\boldsymbol{\sigma}_{M\_i}\right)_k = 2C_{NH\_M\_i}\left(\mathbf{B}_{ME\_i}\right)_k - \left(p_{M\_i}\right)_k \mathbf{I} \tag{3.63}$$

In Eq. (3.63), the value of hydrostatic pressure p_{M_i} is determined from the boundary conditions. Examples of the hydrostatic pressure for uniaxial and simple shear deformations are demonstrated earlier.

Then, the total stress is;

$$\left(\boldsymbol{\sigma}\right)_k = \sum_{i=1}^{n}\left(\boldsymbol{\sigma}_{M\_i}\right)_k \tag{3.64}$$

To determine the rate of shape change, $\tilde{\mathbf{D}}_{NL}$ and $\tilde{\mathbf{D}}_{MV\_i}$, the deviatoric stress tensor applied to each damper should be calculated.

$$(\boldsymbol{\sigma}')_k = (\boldsymbol{\sigma})_k - \frac{1}{3} tr[(\boldsymbol{\sigma})_k]\mathbf{I} \tag{3.65}$$

$$(\boldsymbol{\sigma}'_{M\_i})_k = (\boldsymbol{\sigma}_{M\_i})_k - \frac{1}{3} tr[(\boldsymbol{\sigma}_{M\_i})_k]\mathbf{I} \tag{3.66}$$

Then, from Eq. (3.48) and (3.49);

$$(\tilde{\mathbf{D}}_{MV\_i})_k = \frac{3}{2\mu_{M\_i}} (\boldsymbol{\sigma}'_{M\_i})_k \tag{3.67}$$

$$(\tilde{\mathbf{D}}_{NL})_k = \left(\frac{3}{2} A \bar{\sigma}^{m-1}\right)(\boldsymbol{\sigma}')_k \tag{3.68}$$

The spins $(\tilde{\mathbf{W}}_{NL})_k$ and $(\tilde{\mathbf{W}}_{MV\_i})_k$ can be determined from the prescribed constraints as explained above. Then, $(\tilde{\mathbf{L}}_{NL})_k$ and $(\tilde{\mathbf{L}}_{MV\_i})_k$ are obtained from Eq. (3.54) and (3.55).

The rates of deformation gradient of each damper for the next time step k+1 are;

$$(\dot{\mathbf{F}}_{MV\_i})_k = (\mathbf{F}^{-1}_{ME\_i})_k (\tilde{\mathbf{L}}_{MV\_i})_k (\mathbf{F}_L)_k \tag{3.69}$$

$$(\dot{\mathbf{F}}_{NL})_k = (\mathbf{F}^{-1}_{L})_k (\tilde{\mathbf{L}}_{NL})_k (\mathbf{F})_k \tag{3.70}$$

(9) Numerical Integration for Force Controlled Deformation

In force controlled deformation, force or stress are given as a function of time and displacement or deformation gradient are the result. In that case, the mechanical analog with the generalized Kelvin-Voigt model shown in Fig. 3.3b is convenient to calculate the response to the force.

The compatibility and the equilibrium equations for the mechanical analog in Fig. 3.3b can be expressed as Eq. (3.71) and (3.72), respectively.

$$\mathbf{F} = \mathbf{F}_L \mathbf{F}_{NL} = \mathbf{F}_E \mathbf{F}_{K\_1} \mathbf{F}_{K\_2} \cdots \mathbf{F}_{K\_n} \mathbf{F}_{NL} \tag{3.71}$$

$$\boldsymbol{\sigma} = \boldsymbol{\sigma}_{NL} = \boldsymbol{\sigma}_L = \boldsymbol{\sigma}_E = \boldsymbol{\sigma}_{KE\_i} + \boldsymbol{\sigma}_{KV\_i} \tag{3.72}$$

where, $\mathbf{F}_E$ and $\mathbf{F}_{K\_i}$ are the deformation gradients for the elastic spring and the i^{th} Kelvin-Voigt element, $\boldsymbol{\sigma}_E$ is the Cauchy stress tensor for the spring of E_{K_0} in Fig.

3.3b, and $\boldsymbol{\sigma}_{KE\_i}$ and $\boldsymbol{\sigma}_{KV\_i}$ are the Cauchy stress tensors for the spring and the damper of the i^{th} Kelvin-Voigt element, respectively.

In contrast to the displacement controlled deformation, the displacement of each Kelvin-Voigt element does not have a predefined constraint and can each have different displacements. Hence, the rate kinematics expressed in Eq. (3.52) and (3.53) are not necessary. The overall flow of the numerical integration for the force controlled deformation is similar to that for the displacement controlled deformation, but its detail needs some modification. A complete calculation process for the mechanical analog of Fig. 3.3b at an arbitrary time step *k* is presented in Eq. (3.73)-(3.87).

The deformation gradient of the nonlinear damper at step *k* is;

$$\left(\mathbf{F}_{NL}\right)_k = \left(\mathbf{F}_{NL}\right)_{k-1} + \left(\dot{\mathbf{F}}_{NL}\right)_{k-1}\Delta t \tag{3.73}$$

As shown in Fig. 3.3b, the deformation gradient of the spring and the damper in each Kelvin-Voigt element must be the same, and it is determined by the damper as expressed in Eq. (3.74).

$$\left(\mathbf{F}_{K\_i}\right)_k = \left(\mathbf{F}_{K\_i}\right)_{k-1} + \left(\dot{\mathbf{F}}_{K\_i}\right)_{k-1}\Delta t \tag{3.74}$$

The deformation gradient of the single spring without damper ($\mathbf{F}_E$) is another component of total deformation gradient. The single spring is necessary because the Kelvin-Voigt element cannot simulate instantaneous response to the applied force. Hence, the stiffness of the single spring (E_{K_0}) represents the instantaneous stiffness and its value is the sum of all spring constants of the generalized Maxwell model of Fig. 3.3a. The calculation of $\mathbf{F}_E$ from the applied stress requires consideration of each component of $\mathbf{F}_E$ as well as the loading and the boundary condition because Eq. (3.41) defines the relationship between the stress tensor ($\boldsymbol{\sigma}$) and the Cauchy-Green strain tensor ($\mathbf{B}_E$), and a general equation of calculating $\mathbf{F}_E$ from $\mathbf{B}_E$ does not exist. In addition, determination of $\mathbf{F}_E$ for uniaxial deformation using Eq. (3.41) involves a solution of a cubic equation. However, these issues are unimportant because $\mathbf{F}_E$ is so small as to remain in the infinitesimal strain range. In order to reduce the calculation effort, Hooke's law is used instead of Eq. (3.41) to calculate $\mathbf{F}_E$. Determinations of $\mathbf{F}_E$ for uniaxial and simple shear deformations are shown previously.

Using the compatibility condition expressed in Eq. (3.71), the total deformation gradient at step *k* can be calculated by Eq. (3.75).

$$\left(\mathbf{F}\right)_k = \left(\mathbf{F}_E\right)_k \left(\mathbf{F}_{K\_1}\right)_k \left(\mathbf{F}_{K\_2}\right)_k \cdots \left(\mathbf{F}_{K\_n}\right)_k \left(\mathbf{F}_{NL}\right)_k \tag{3.75}$$

The Cauchy stress tensor generated by the spring of each Kelvin-Voigt element is;

$$\left(\mathbf{B}_{K\_i}\right)_k = \left(\mathbf{F}_{K\_i}\right)_k \left(\mathbf{F}_{K\_i}^{\mathbf{T}}\right)_k \tag{3.76}$$

$$\left(\boldsymbol{\sigma}_{KE\_i}\right)_k = 2C_{NH\_K\_i}\left(\mathbf{B}_{K\_i}\right)_k - \left(p_{K\_i}\right)_k \mathbf{I} \tag{3.77}$$

The total Cauchy stress tensor for the current configuration can be determined from the given nominal stress tensor ($\mathbf{S}$) and the total deformation gradient.

$$\left(\boldsymbol{\sigma}\right)_k = \left(\mathbf{S}\right)_k \left(\mathbf{F}^{\mathbf{T}}\right)_k \tag{3.78}$$

Then, the Cauchy stress tensors applied to the linear dampers are calculated using the equilibrium condition expressed in Eq. (3.72).

$$\left(\boldsymbol{\sigma}_{KV\_i}\right)_k = \left(\boldsymbol{\sigma}\right)_k - \left(\boldsymbol{\sigma}_{KE\_i}\right)_k \tag{3.79}$$

The deviatoric stress tensors for $\boldsymbol{\sigma}$ and $\boldsymbol{\sigma}_{KV\_i}$ are;

$$\left(\boldsymbol{\sigma}'\right)_k = \left(\boldsymbol{\sigma}\right)_k - \frac{1}{3} tr\left[\left(\boldsymbol{\sigma}\right)_k\right]\mathbf{I}$$

(3.80)

$$\left(\boldsymbol{\sigma}'_{KV\_i}\right)_k = \left(\boldsymbol{\sigma}_{KV\_i}\right)_k - \frac{1}{3} tr\left[\left(\boldsymbol{\sigma}_{KV\_i}\right)_k\right]\mathbf{I} \tag{3.81}$$

The rates of stretching for the nonlinear and the linear dampers are;

$$\left(\mathbf{D}_{NL}\right)_k = \left(\frac{3}{2} A \bar{\sigma}^{m-1}\right)\left(\boldsymbol{\sigma}'\right)_k \tag{3.82}$$

$$\left(\mathbf{D}_{K\_i}\right)_k = \frac{3}{2\mu_{K\_i}}\left(\boldsymbol{\sigma}'_{KV\_i}\right)_k \tag{3.83}$$

As mentioned before, the spins $\left(\mathbf{W}_{NL}\right)_k$ and $\left(\mathbf{W}_{K\_i}\right)_k$ can be determined from the prescribed constraints on the deformation. Then, the velocity gradients of the nonlinear and the linear dampers are;

$$\left(\mathbf{L}_{NL}\right)_k = \left(\mathbf{D}_{NL}\right)_k + \left(\mathbf{W}_{NL}\right)_k \tag{3.84}$$

$$\left(\mathbf{L}_{K\_i}\right)_k = \left(\mathbf{D}_{K\_i}\right)_k + \left(\mathbf{W}_{K\_i}\right)_k \tag{3.85}$$

The rates of deformation for the nonlinear and the linear dampers that will be used for the next time step can be obtained using Eq. (3.4).

$$\left(\dot{\mathbf{F}}_{NL}\right)_k = \left(\mathbf{L}_{NL}\right)_k \left(\mathbf{F}_{NL}\right)_k \tag{3.86}$$

$$\left(\dot{\mathbf{F}}_{K\_i}\right)_k = \left(\mathbf{L}_{K\_i}\right)_k \left(\mathbf{F}_{K\_i}\right)_k \tag{3.87}$$

3.2.2 Calibration of Model Parameters

The proposed nonlinear viscoelastic constitutive model is comprised of a set of linear and nonlinear systems in series. As shown in Eq. (3.50), (3.71), and Fig. 3.3, total deformation is composed of both linear and nonlinear deformations. This means that conventional calibration methods for linear models or nonlinear models are not appropriate for this model. Therefore, it is necessary to develop a proper calibration method tailored to the proposed model. The proposed technique is composed of three steps:

(1) Linear system calibration including;
   - Calibration of modified power law (MPL) relaxation function (Williams 1964)
   - Conversion of the relaxation function from MPL to a Prony series
   - Conversion of the generalized Maxwell parameters to generalized Kelvin-Voigt parameters

(2) Nonlinear system calibration through an iterative technique

(3) Calibration of the temperature shift factor

Cheung and Cebon (1997b) used two different batches of asphalt (designated B1 and B2 in their paper) for their experimental investigation. The uniaxial tension test data for B1 (solid lines in Fig. 3.2) is used for the calibration exercise herein. The data contains six stress-strain curves obtained from uniaxial constant strain rate tests. Using the calibrated material parameters, uniaxial creep tests for the same material performed by Cheung and Cebon (1997b) are simulated to show that the proposed model is capable of yielding reasonable results.

(1) Linear System Calibration

The final goal of the linear system calibration is to determine the elastic constants (E_{M_i} and E_{K_i}) and the viscosities (μ_{M_i} and μ_{K_i}) of each element of the generalized Maxwell model and the generalized Kelvin-Voigt model in Fig. 3.3. Although the proposed model is described in finite strain, the viscoelastic functions for linear system calibration are expressed in terms of infinitesimal strain. This is acceptable because the linear system calibration utilizes the data within small strain range. Once the parameters of the linear system are obtained in infinitesimal strain framework, those will be converted into the parameters for the finite strain framework. This conversion is simple because the linear viscosities (μ_{M_i} and μ_{K_i}) are identical for both frameworks, and the elastic constants of the Neo-Hookean model ($C_{NH\_M\_i}$ and $C_{NH\_K\_i}$) are one sixth of the elastic moduli (E_{M_i} and E_{K_i}) as shown earlier.

Linear viscoelastic materials can be characterized by relaxation modulus or creep compliance. Properties of the relaxation modulus of asphaltic material within the linear range were identified experimentally by Lethersich (1942), Stastna et al. (1997), Kim et al. (1995), Gibson et al. (2003), and Park and Kim (2001). To capture the broadband nature of asphalt concrete relaxation function over time, a Prony series or power-law based function is used.

Since the experimental data for the calibration are obtained from the displacement controlled deformation test (constant nominal strain rate test), the parameters of the generalized Maxwell model (Fig. 3.3a) are calibrated first. The parameters of the generalized Kelvin-Voigt model can be determined through the interconversion method suggested by Park and Schapery (1999). The relaxation function ($G(t)$) of the generalized Maxwell model is represented by a Prony series shown in Eq. (3.88).

$$G(t) = E_{M\_0} + \sum_{i=1}^{n} E_{M\_i} \exp\left(-\frac{t}{\tau_{R\_i}} \right) \tag{3.88}$$

where, $\tau_{R\_i} = \mu_{M\_i} / E_{M\_i}$ is the characteristic time of relaxation. E_{M_0} is the remaining stiffness at infinite time of relaxation, and is described as a single spring in the generalized Maxwell model as shown in Fig. 3.3a.

Since each Maxwell element has two material parameters (E_{M_i} and μ_{M_i}), the total number of material parameters to be calibrated for all Maxwell elements is 2*n*, where *n* is the number of the Maxwell element. The calibration process in this study entails selecting an alternative function among the power-law based relaxation functions in order to reduce the number of material parameters. Once the material parameters of the power law relaxation function are determined, the power law function can be easily translated into a Prony series. This translation technique is called power-law presmoothing, and its details are provided by Park and Kim (2001).

Calibration of modified power law relaxation function

One of the popular choices for the relaxation modulus of asphalt is the MPL function suggested by Williams (1964). Eq. (3.89) shows the MPL function including four material parameters (E_{ins}, E_{∞}, τ_0, and r).

$$G(t) = E_{\infty} + \frac{E_{ins} - E_{\infty}}{\left(1 + \frac{t}{\tau_0}\right)^r} \tag{3.89}$$

where, E_{ins} and E_{∞} are instantaneous and long-term moduli of elasticity, and represent short- and long-time asymptotes of the relaxation function. τ_0 determines a stating time of transition in the relaxation function from E_{ins}, and r is the negative value of the slope of the relaxation function in log-log graph.

From the experimental data shown in Fig. 3.2 (solid lines), the instantaneous elastic modulus, E_{ins}, can be estimated using the initial stiffness of the fastest strain rate test. E_{∞} is assumed to be zero for asphalt because pure asphalt is considered as liquid in general. To determine τ_0 and r, the constant strain rate tests should be simulated. In linear viscoelasticity, the nominal stress history, $S(t)$, can be expressed in terms of relaxation modulus and strain rate by the integral equation as shown in Eq. (3.90).

$$S(t) = e(0)G(t) + \int_0^t G(t-s)\dot{e}(s)ds \tag{3.90}$$

From the test condition of Fig. 3.2, the initial strain, $e(0) = 0$, and the nominal strain

rate, $\dot{e}$, is a constant. Then, by substituting Eq. (3.89), Eq. (3.90) becomes:

$$S(t) = \dot{e}\left[E_\infty \tau_0 t + (E_{ins} - E_\infty)\frac{\tau_0}{1-r}\left\{\left(1+\frac{t}{\tau_0}\right)^{1-r} - 1\right\}\right] \tag{3.91}$$

The curve $S(t)$ associated with each strain rate can be easily plotted and compared with experimental data. Since, E_{ins} and E_∞ are already known, there are only two unknowns (τ_0 and r) for the relaxation function. The values of τ_0 and r for fitting the initial behavior of test data is then determined by trial and error through comparison of the curves of Eq. (3.91) to the test data. The dotted lines in Fig. 3.2b are curves obtained from Eq. (3.91). The calibrated MPL parameters of Fig. 3.2b are listed in Table 3.1.

Conversion of the relaxation function from MPL to a Prony series

The conversion of the relaxation function from MPL to a Prony series can be accomplished by the least square method, and is explained in Park and Kim (2001). The values of the Prony series parameters converted from the MPL model are listed in Table 3.1. Fig. 3.5 compares the relaxation functions in MPL form, Prony series form, and exponential functions of each Maxwell elements comprising the Prony series. The same logarithmic interval of 1 (=log 10) between the characteristic times (τ_{R_i}) is selected for the Prony series, and consequently, the number of the series (n) is determined from the width of MPL function in the logarithmic time scale. Then, the stiffness of each spring (E_{M_i}) is determined to match the MPL function. The viscosities of the linear dampers can be calculated as $\mu_{M\_i} = \tau_{R\_i} E_{M\_i}$.

Interconversion of the generalized Maxwell parameters to generalized Kelvin-Voigt parameters

Since the generalized Maxwell model and the generalized Kelvin-Voigt model, illustrated in Fig. 3.3a and 3.3b are two different appearances of a single model, the material parameters of two models should be chosen so that the models are mathematically equivalent to each other. The linear parameters of the generalized

Maxwell model determined above should be converted into the parameters of the generalized Kelvin-Voigt model.

Park and Schapery (1999) suggested three methods of interconversion between linear viscoelastic material functions expressed using a Prony series. In this study, a method of interconversion using the relationship between relaxation and creep functions is selected to determine the linear parameters of the generalized Kelvin-Voigt model from the generalized Maxwell parameters.

The Prony series form of the creep function ($J(t)$) is expressed easier when it is written in terms of the material parameters of generalized Kelvin-Voigt model, E_{K_0}, E_{K_1}, $\cdots$ E_{K_n}, and μ_{K_1}, μ_{K_2}, $\cdots$ μ_{K_n}. Defining the characteristic time of creep as $\tau_{C\_i} = \mu_{K\_i} / E_{K\_i}$ and the coefficients of Prony series as $J_{K\_i} = 1/E_{K\_i}$, $J(t)$ can be expressed as Eq. (3.92).

$$J(t) = J_{K\_0} + \sum_{i=1}^{n} J_{K\_i} \left(1 - \exp\left(-\frac{t}{\tau_{C\_i}} \right) \right) \tag{3.92}$$

The mathematical relation between $G(t)$ and $J(t)$ is shown in Eq. (3.93) (Wineman and Rajagopal 2000).

$$1 = J(0)G(t) + \int_0^t G(t-s)\frac{dJ(s)}{ds} ds \tag{3.93}$$

By substituting Eq. (3.88) and (3.92) into Eq. (3.93), Park and Schapery (1999) derived a system of equations for unknown constants J_{K_i} expressed as Eq. (3.94).

$$A_{kj} J_j = B_k \qquad (k = 1, 2, \cdots, m \text{ and } j = 1, 2, \cdots, n) \tag{3.94}$$

where,

$$A_{kj} = \begin{cases} E_\infty \left[1 - \exp(-t_k / \tau_{C\_j}) \right] + \sum_{i=1}^{n} \frac{\tau_{R\_i} E_{M\_i}}{\tau_{R\_i} - \tau_{C\_j}} \left[\exp(-t_k / \tau_{R\_i}) - \exp(-t_k / \tau_{C\_j}) \right] & \text{when} \quad \tau_{R\_i} \neq \tau_{C\_j} \\ or & \\ E_\infty \left[1 - \exp(-t_k / \tau_{C\_j}) \right] + \sum_{i=1}^{n} \frac{t_k E_{M\_i}}{\tau_{C\_j}} \exp(-t_k / \tau_{R\_i}) & \text{when} \quad \tau_{R\_i} = \tau_{C\_j} \end{cases} \tag{3.95}$$

and

$$B_k = 1 - \left(E_\infty + \sum_{i=1}^{n} E_{M\_i} \exp(-t_k / \tau_{R\_i}) \right) \Big/ \left(E_\infty + \sum_{i=1}^{n} E_{M\_i} \right) \tag{3.96}$$

In Eq. (3.95) and (3.96), t_k is a sampling point which is a discrete time corresponding to the upper limit of integration in Eq. (3.93), and the number of the sampling point, *m*, indicates the number of equations. Therefore, *m* should be equal or greater than the number of unknowns (*n* for *n*-Kelvin-Voigt model) to solve Eq. (3.94). In general, the number of the Maxwell element of Fig. 3.3a and the number of the Kelvin-Voigt element of Fig. 3.3b are not necessarily the same to each other, but it is convenient to select them to be the same. When the numbers of the Maxwell and Kelvin-Voigt elements are the same, Park and Schapery (1999) recommends setting the sampling points to be $t_k = a\tau_{C\_k}$ where a = 1 or a = 1/2. Eq. (3.94) does not include J_{K_0}, the instantaneous creep compliance that is represented by the single spring in Fig. 3.3b. J_{K_0} can be obtained from Eq. (3.97).

$$J_{K\_0} = \frac{1}{E_{K\_0}} = \frac{1}{E_\infty + \sum_{i=1}^{n} E_{M\_i}} \tag{3.97}$$

In this study, the parameters of the generalized Maxwell model are converted into the parameters of the generalized Kelvin-Voigt model using Eq. (3.94)-(3.97). t_k and τ_{C_i} are selected to be the same to τ_{R_i}. The converted parameters for the generalized Kelvin-Voigt mode are listed in Table 3.1. Fig. 3.6 compares the creep curve plotted using the converted Kelvin-Voigt parameters to the relaxation curve using the calibrated Maxwell parameters. It should be noted that the curves in Fig. 3.6 represent the properties of the linear system only (not the whole model).

(2) Nonlinear System Calibration

The power law viscous damper of the nonlinear system illustrated in Fig. 3.3 has two material parameters that need to be calibrated, *A* and *m* of Eq. (3.47). Cheung and Cebon (1997b) suggested a power form viscous constitutive equation similar to Eq. (3.47), and evaluated its parameters based on the steady state behavior defined in terms of nominal stress (*S*) and nominal strain rate ($\dot{e}$). However, Cheung and Cebon's (1997b)

constants are not applicable to the proposed model because of the following reasons. Cheung and Cebon (1997b) considered that once the nominal stress reaches the steady state, additional strain is fully carried by nonlinear viscous flow. However, in the model proposed in this study, the viscous strain is decomposed into linear and nonlinear portions as shown in Fig. 3.3 and Eq. (3.50). Therefore, the nonlinear damper of the proposed model carries only a part of the viscous flow. In addition, the concept of steady state in nominal stress and nominal strain is inappropriate for uniaxial large deformation. As shown in Fig. 3.2, the strain in Cheung and Cebon's (1997b) experiments reaches 0.5, i.e. deformations are large. Under such conditions, the axial Cauchy stress (σ_{11}) is significantly larger than the nominal stress (S_{11}) because the cross sectional area has decreased. In addition, while the nominal strain rate is constant, the true strain rate is no longer constant because of the current configuration is continuously changing. More details about uniaxial large deformation will be presented later on.

As explained in Fig. 3.2, the assumption behind the linear system calibration is that the contribution of the nonlinear damper to total deformation is negligible in the small strain regime. On the other hand, at large deformation, both the linear and the nonlinear portion in total deformation cannot be neglected. To calibrate the two parameters, *A* and *m* of the nonlinear system using Eq. (3.47), the velocity gradient of the nonlinear damper (L_{11_NL}) and the Cauchy stress (σ_{11}) should be known, but it is difficult to separate the nonlinear portion out of the total deformation in the displacement controlled deformation. Therefore, an iterative method is introduced to calibrate *A* and *m*.

As the first step, a control point for the iteration is selected within the nonlinear dominant region. As marked in Fig. 3.7, $e_{11} = 0.35$ where the strain at peak stress is selected to calibrate to Cheung and Cebon's (1997b) data. For the first iteration, any value of *A* and *m* can be selected in general. To reduce the number of iterations, it is recommended to evaluate *A* and *m* using Eq. (3.47) with the velocity gradient ($L_{11} = \dot{e}_{11}/\Lambda$) and the Cauchy stress ($\sigma_{11} = \Lambda S_{11}$) at the control point. With these *A* and *m* values, the contribution of nonlinear damper in total deformation is overestimated because *A* and *m* are selected so that the velocity gradient of the nonlinear damper is the same as the total velocity gradient ($L_{11\_NL} = L_{11}$) under the stress at the control point while

the linear system of the model shares some portion of the total velocity gradient ($L_{11} = L_{11\_NL} + L_{11\_L}$). In other words, the nonlinear damper is more flexible than the target. As a result, the resultant stresses of the first simulation are lower than the experiments as shown in Fig. 3.7.

In the first simulation, the velocity gradient of the nonlinear damper at the control point must be somewhere between the target velocity gradient and the total velocity gradient. If A and m values are re-evaluated with L_{11_NL} of the first simulation, the stiffness of the damper will become closer to the target stiffness. By repeating these processes, the stiffness of the nonlinear damper will converge to the target stiffness, and the simulation results will converge to the experimental data.

Fig. 3.8 demonstrates the convergence of A and m through the iteration process for the data of Cheung and Cebon (1997b). From each iteration, L_{11_NL} at the control point for six applied strain rates are plotted on the L_{11_NL} versus σ_{11} plot in log-log scale, and a power law function for each iteration is obtained through regression. Since, the regressed power law function has an identical form to Eq. (3.47), A and m are the coefficient and the index of the function, respectively. Then, the values of A and m are used for the next iteration. In Fig. 3.8, the stresses at the control point for L_{11_NL} versus σ plot (the horizontal axis) are determined from experimental curves, and kept constant, because those are the targets of the iterative process. Fig. 3.9 compares the simulation results after the 5th iteration to the test data. The simulated stress-strain curves with the 5th iteration parameters (A=1.925×10^{-5} /s MPa$^{-3.294}$, m=3.294) show good agreement with the experimental data. In addition to the data for the six strain rates that are used for the calibration, the data for the strain rates of 1/s and 2/s that are not used for the calibration show good agreement with the simulations. This good agreement beyond the calibrated strain rate range show the expandability of the model to other test conditions.

An important advantage of the proposed calibration method is that all of the viscoelastic material parameters in the proposed model can be calibrated using only a set of constant strain rate tests with several different strain rates. The proposed calibration procedure greatly reduces the effort for material characterization compared to the large number of tests required by traditional calibration methods.

(3) Calibration of Temperature Shift Factor

According to time-temperature superposition or time-temperature correspondence principle (Leadermann 1943; Ferry 1950), the actual time (t) at a specific temperature can be translated into reduced time (t_R), which is an equivalent time at the reference temperature through Eq. (3.98).

$$t_R = \frac{t}{a_T} \tag{3.98}$$

where, a_T is temperature shift factor which is a function of temperature. a_T can be calculated from Arrhenius or WLF equation if their parameters are known. By replacing actual time with reduced time, the mechanical behavior of asphaltic materials at any temperature above the glass transition temperature can be translated into behavior at the reference temperature. In other words, the material parameters of the model calibrated at the reference temperature can be used to predict behavior at other temperatures, which significantly reduces the number of tests required for material characterization.

Cheung and Cebon (1997b) suggested to use the Arrhenius equation for their asphalt at temperature below 30ºC, and provided its constants. Dividing the Arrhenius equation for an actual time (t) by that for the reduced time (t_R), Eq. (3.99) can be obtained.

$$\frac{dt_R}{dt} = \exp\left(-\frac{Q_p}{RT} + \frac{Q_p}{RT_R}\right) \tag{3.99}$$

where, Q_p, R, T, and T_R are activation energy, gas constant, temperature, and reference temperature in Kelvin scale, respectively. Integrating and rearranging Eq. (3.99), an equation similar to Eq. (3.98) can be obtained as shown in Eq. (3.100).

$$t_R = \frac{t}{\exp\left(\frac{Q_p}{R}\left(\frac{1}{T} - \frac{1}{T_R}\right)\right)} = \frac{t}{a_T} \tag{3.100}$$

Therefore, the exponential term of Eq. (3.100) is the shift factor, a_T. The values of the Arrhenius constants provided by Cheung and Cebon (1997b) are $Q_p = 228\times10^3$ (J mol^{-1}) and $R = 8.314$ (J mol^{-1} K^{-1}). Fig. 3.10 shows the variation of $\log a_T$ with temperature. The reference temperature (T_R) is 10°C because the material parameters of

the proposed model are calibrated at 10°C.

3.2.3 Model Validation and Discussion

To show that the model yields reasonable results, simulations using the proposed constitutive model are compared to test data obtained for conditions different than what the model was calibrated for. First, the uniaxial creep tests in Cheung and Cebon (1997b) are simulated and the results compared to the available test data for B1. Then, the three dimensional capability of the developed model is examined by simulating shear test data for material B2. The effects of large deformation and the limit of linear viscoelasticity are also discussed in this section.

(1) Simulation of Uniaxial Creep Test

In a creep test, a fixed load is applied to the specimen and the variation of displacement with time is measured. During a uniaxial creep test, the applied nominal stress is constant, while the Cauchy stress varies with the increase in deformation because of the change in cross sectional area of the specimen. This is taken into account in the simulation by applying a fixed nominal stress and calculating the corresponding Cauchy stress using the computed deformation gradient via Eq. (3.1).

A simulation of the creep test conducted at 10°C with S_{11}=0.078 MPa is compared to corresponding experimental data in Fig. 3.11, which shows good correlation between simulation data and experimental results. Since the creep test involves force controlled deformation, the model shown in Fig. 3.3b including a generalized Kelvin-Voigt model and the corresponding numerical integration described in Eq. (3.71) - (3.87) are used with the parameters converted by Eq. (3.94) - (3.97) for the creep simulation. Fig. 3.11 also shows the relative contributions of the linear and nonlinear components of the model. At a nominal stress of 0.078 MPa, it is clear that the linear system carries most of the creep strain. This is in accord with Cheung and Cebon's (1997b) observation that transition between non-Newtonian (nonlinear viscous) flow and Newtonian (linear viscous) flow occurs around 0.1 MPa. In other words, the model successfully captures the fact that response is dominated by linear viscoelastic behavior in this test. Other creep tests involving different stresses and temperatures are simulated and compared to test data in

Fig. 3.12. Again, the simulation results demonstrate that the proposed nonlinear viscoelastic model combined with time-temperature superposition principle is reasonably accurate, especially given that the behavior depends on temperature in an exponential manner.

(2) Simulation of Constant Strain Rate Test in Shear

Due to the lack of available shear data for B1 in Cheung and Cebon's (1997b), direct validation for shear is not possible. However, confidence in the proposed model is sought indirectly by: 1) examining the relationship between Cheung and Cebon's (1997b) model and test results for B2, and 2) checking if the relationship between the results of the proposed model and Cheung and Cebon's (1997b) model for B1 has a similar trend to that observed for B2.

Fig. 3.13 is a comparison between the shear and tension test data for B2 and corresponding models proposed in Cheung and Cebon (1997b). Cheung and Cebon (1997b) defined the nominal stress at maximum observed load as the steady state creep stress when a specimen is subjected to a constant nominal strain rate (Fig. 3.9). Similarly, when a constant force is applied (creep test, as shown in Fig. 3.12), the constant nominal strain rate observed after some duration of initial creep response was defined as the steady state strain rate. The assumption behind this definition is that the deformation after the initial response is purely viscous, and hence the relationship between the steady state stress and strain rate as shown in Fig. 3.13 represents the viscous characteristics of the material excluding elasticity. Based on their experimental data, Cheung and Cebon (1997b) concluded that the steady state is reached at $e_{11} \approx 0.2$ in the uniaxial tests and $\gamma_{12} \approx 1.0$ in the shear tests; hence the experimental data (solid circles for tension and hollow squares for shear) plotted in Fig. 3.13 are nominal stresses obtained at these strains.

According to the shear model proposed by Cheung and Cebon (1997b), the shear strain rate ($\dot{\gamma}_{12}$) should be $\sqrt{3}^{m+1}$ times higher than the axial strain rate ($\dot{e}_{11}$) at the same stress level, where *m* is the index of the stress term in Eq. (3.47). Cheung and Cebon (1997b) pointed out that while their uniaxial model matched their test data accurately,

their shear test data was not well represented by their proposed shear model. As shown in Fig. 3.13, the shear test data is located in between the uniaxial and shear models. It is proposed later on that Cheung and Cebon's (1997b) definition of the steady state deformation is the reason for the observed discrepancy.

Simulations of simple shear deformation using the proposed model are compared to Cheung and Cebon's (1997b) model for B1 at 10°C in Fig. 3.14. The solid and dotted lines represent Cheung and Cebon's (1997b) models for tension and shear, respectively. Since the recommended $m = 2.3$ for B1, the vertical distance between the dotted and the solid lines is $\sqrt{3}^{m+1} \approx 6$ in Fig. 3.14. The steady state stresses and strain rates are computed from the simulation results in the same way employed by Cheung and Cebon (1997b) as described above. The solid circles represent the data computed for the tension tests using the proposed model, while the solid squares are the simple shear simulation data. Clearly, the tensile predictions match well with Cheung and Cebon's (1997b) model, which had also matched their test data for B2. On the other hand, the shear predictions do not match their shear model well and actually lie in between the shear and uniaxial calculations made using the Cheung and Cebon (1997b) models. This pattern is similar to the disagreement between their shear model and test data displayed in Fig. 3.13 for B2. The facts that: 1) the proposed model produces shear data that follows this pattern of discrepancy; and 2) matches the proximity between the shear and tension data observed for B2, are deemed indirect evidence of its accuracy when applied to B1.

(3) Effects of Large Deformation

As mentioned above, Cheung and Cebon's (1997b) model described in terms of nominal stress and nominal strain does not consider the effects of large deformation although the strains in their steady state deformation experiments far exceeds the small strain limit. The effects of large deformation are different in uniaxial tension and shear deformations. A typical uniaxial stress-strain curve subjected to constant strain rate is compared to a shear stress-strain curve in Fig. 3.15. The curves in Fig. 3.15 were computed using the proposed model. The applied nominal strain rates are $\dot{e}_{12} = 0.5 = \dot{\gamma}_{12}/2$ (/s) for shear and $\dot{e}_{11} = 0.5$ (/s) for uniaxial tension. The uniaxial

tension test is simulated up to the nominal strain (e_{11}) of 2.6 which is the ductile fracture strain reported by Harvey and Cebon (2003), and the simple shear test is simulated up to $\gamma_{12} = 3.22$ at which the maximum principal nominal strain is 2.6.

One of the large deformation effects is the difference between true (Cauchy) and nominal stresses. As shown in Eq. (3.17), $S_{11} = \sigma_{11}/\Lambda$ in uniaxial deformation, hence the difference between the uniaxial true stress (σ_{11}) and the uniaxial nominal stress (S_{11}) increases with the increase of the stretch. Physically, the difference between σ_{11} and S_{11} is caused by the reduction in cross-sectional area. The two dotted lines in Fig. 3.15 represent the Cauchy stress versus the nominal strain ($\sigma_{11} - e_{11}$) curve and the nominal stress versus the nominal strain ($S_{11} - e_{11}$) curve obtained from the uniaxial simulation. As a result of the reduction in cross-sectional area, S_{11} is significantly smaller than σ_{11} in large strain range including $e_{11} = 0.2$, and the gap between them grows with the increase of strain. On the other hand, in pure shear deformation including simple shear, the shear components of the Cauchy and the nominal stress tensors are the same ($S_{12} = \sigma_{12}$) as shown in Eq. (3.34). In a physical sense, this is reasonable because the shear area does not vary during pure shear deformation.

Although reduction in cross-sectional area is considered, the $\sigma_{11} - e_{11}$ curve in Fig. 3.15 is still different from the shear stress-strain curve. This difference is caused by the evolution of the current configuration employed in axial deformation calculations. In finite strain kinematics, rate of deformation is described by the velocity gradient, and the axial components of the velocity gradient vary with the evolution of deformation even when the nominal strain rate is constant. For the uniaxial deformation described in Eq. (3.12), the nominal strain rate of the axial direction is $\dot{e}_{11} = \dot{\Lambda}$ (from Eq. (3.11)), and the velocity gradient of the same direction is $L_{11} = D_{11} = \dot{\Lambda}/\Lambda$ (Eq. (3.13)). The difference between L_{11} and $\dot{e}_{11}$ subjected to the uniaxial constant strain rate is illustrated in Fig. 3.16. The decrease of L_{11} under the constant $\dot{e}_{11}$ in Fig. 3.16 explains the softening behavior of $\sigma_{11} - e_{11}$ curve in Fig. 3.15. On the contrary, the velocity gradient in simple

shear does not vary with the evolution of deformation as shown in Eq. (3.28) ($\dot{\gamma}_{12} = \dot{K} = L_{12}$).

The above discussion demonstrates that the shear components of the Cauchy stress (σ_{12} and σ_{21}) and the symmetric velocity gradient (D_{12} and D_{21}) are the same as the nominal shear stress (S_{12} and S_{21}) and the nominal shear strain rate ($\dot{e}_{12}$ and $\dot{e}_{21}$) in simple shear deformation because the components of the current configuration involving the shear component (the axis perpendicular to the direction of the deformation and the reduction of the sectional area) do not vary with shear deformation. Therefore, both of the large deformation effects that appear under axial deformation vanish in the shear stress in simple shear deformation. Since the proposed model has multiple relaxation times with a sufficiently high maximum, a peak stress and steady state deformation do not occur in the shear curve.

These observations suggest a different point of view than that theorized in Cheung and Cebon (1997b). They considered the behavior around the peak stress in the uniaxial test as a purely viscous steady state flow. However, if the existence of the multiple relaxation time is true as agreed upon by various investigators (Lethersich 1942; Kim and Little 1990; Park and Kim 2001; Gibson et al. 2003), then the peak stress in uniaxial deformation can be considered to be a transition point where the effects of large deformation exceed the effect of increase in stress, as explained above. The concept of steady state deformation, therefore, is not as clear cut as outlined in Cheung and Cebon (1997b). As illustrated in Fig. 3.15, the fact that the Cauchy stress (σ_{11}) does not reach the peak at the strain of the peak nominal stress ($e_{11} \approx 0.2$), demonstrates the inappropriateness of defining steady state in terms of nominal stress. Evidence in support of this assertion can be found in the experimental data of Cheung and Cebon (1997b), where a slight decrease in stress is observed after a peak is achieved in Fig. 3.9. From a theoretical perspective, ideal steady state behavior can only be attained at a time of infinity when a generalized Maxwell model is employed because its largest characteristic time is, indeed, infinity.

The nominal strain rate and velocity gradient of the nonlinear damper ($\dot{e}_{11\_NL}$ and

L_{11_NL}) are also presented in Fig. 3.16. The ratio of $\dot{e}_{11\_NL}$ (or L_{11_NL}) to $\dot{e}_{11}$ (or L_{11}) represents the contribution of the nonlinear system to the total deformation, and as was expected in the discussion pertaining to Fig. 3.2, the contribution of the nonlinear system is small in the small strain range. The reduction of L_{11_NL} after $e_{11} \approx 0.45$ is the result of stress softening of $\sigma_{11} - e_{11}$ curve in Fig. 3.15 because the total stress (σ_{11}) generated from the linear system is the driving force of the nonlinear damper. Therefore, the increase and decrease of the nonlinear contribution ($\mathbf{L}_{NL}$) can be estimated from the variation of the Cauchy stress.

(4) Isochrones

An isochrone is a plot of stress versus strain for fixed time obtained from various creep or stress relaxation loading conditions. It is a useful visualization method for distinguishing between linear and nonlinear viscoelastic behavior. If a material is linear viscoelastic, its isochrones should be straight. Fig. 3.17a and 3.17b illustrate isochrones constructed from creep and relaxation simulations using the proposed model. The fixed times for the creep isochrone are 1, 2, and 4 seconds, and the fixed times for the stress relaxation isochrones are 0.01, 0.1, 1, and 10 seconds. The dotted lines in Fig. 3.17 are obtained from the linear system of the model and the solid lines represent total responses of the model. Therefore, the horizontal distance between the dotted and solid lines indicates the strain accumulated in the nonlinear system at the corresponding fixed time.

One of the implications of these isochrones is that the linearity limit of asphalt cannot be represented by a single parameter such as stress or strain. For example, in the creep isochrones at 1, 2, and 4 seconds, the stress linearity limit 0.1 MPa suggested by Cheung and Cebon (1997b) seems reasonable. However, the stress relaxation isochrones covering wider time range show that the linearity limit in terms of stress varies with the fixed time, and significant nonlinearity is observed at the isochrone at 10 second even below 0.1 MPa.

3.2.4 Conclusions

A three dimensional nonlinear viscoelastic constitutive model described in finite

strain was developed for asphalt. The proposed model is distinguished from other models by the viewpoint that both linear and nonlinear viscoelasticity have the same significance in asphalt behavior. The model was represented by two mechanical analogs that consist of a power law damper and a generalized Maxwell (or Kelvin-Voigt) model connected in series. The time-temperature superposition principle was used to consider temperature dependency of asphalt behavior. It was shown that the combination of linear and nonlinear viscoelasticity permitted modeling two different characteristics in the behavior of asphaltic materials –linear viscoelasticity with multiple characteristic times dominating the lower stress/strain region and power law nonlinearity prominent in higher stress/stress regions – over a wide range of strain rates and temperatures.

Numerical integration procedures to calculate responses to both displacement and force controlled deformations were suggested. Recommendations for selecting an appropriate time increment for the numerical integration algorithm were provided to ensure stability and accuracy of the simulation. A method for calibrating the parameters of the model was also proposed. The parameters in the linear system were calibrated using the power law presmoothing technique and interconversion method between relaxation and creep functions while the nonlinear parameters were calibrated by iteration. Using this calibration process, it was shown that all of the required viscoelastic parameters could be determined from a single set of constant strain rate tests.

Using parameters calibrated from uniaxial constant strain rate tests, the validity of the developed model was examined by simulating creep and constant shear strain rate tests. The simulation results demonstrated excellent applicability of the proposed model over wide range of temperature, stress, and strain levels with a single set of material parameters.

It was argued that the peak stress commonly observed in constant strain rate tension tests is a transition point where the effects of large deformation exceeds the effect of increase in stress, implying that the concept of steady state deformation in large strain range is not as clear cut as commonly accepted in the field. It was also clarified that it is inappropriate to define steady state in terms of nominal stress. Lastly, it was suggested through an analysis of isochrones that the linearity limit of asphalt cannot be represented by a single parameter such as stress or strain.

3.3. UNIAXIAL NONLINEAR VISCOELASTIC CONSTITUTIVE MODEL IN INFINITESIMAL STRAIN FOR ASPHALT CONCRETE

Asphalt concrete is a mixture of asphalt binder and aggregate. The asphalt binder constitutes 4-6% by weight in pavement applications and it is the primary source of the viscoelastic behavior exhibited by asphalt concrete. Hence, the coexistence of linear and nonlinear viscosity of asphalt binder is also observed in asphalt concrete (Airey et al. 2003; Krishnan and Rajagopal 2003).

As reviewed in the literature survey in Chapter 2, in spite of the nonlinear viscosity exhibited by asphalt concrete, many researchers have approximated its behavior based on the theory of linear viscoelasticity. Concepts of damage and/or plasticity were introduced to account for the nonlinear portion of behavior. While there is no doubt that damage evolution must be considered in describing the behavior of asphalt concrete, it may be possible to assign some portion of the nonlinearity in the mechanical response of asphalt concrete to the nonlinear nature of asphalt viscosity.

The model presented in this section is uniaxial infinitesimal strain version of the model presented in the previous section, and tailored for asphalt concrete (Fig. 3.1). Since the deformable range of asphalt concrete is far smaller than pure asphalt and can be considered to be in the small strain range, effect of large deformation is not taken into account in the infinitesimal model. Contrary to pure asphalt, the effect of damage evolution is significant in the deformation of asphalt concrete. Therefore, a damage parameter is employed within the concept of damage mechanics to account for damage evolution. The ability of the proposed model to represent the behavior of asphalt concrete is shown by using experimental data published by Schwartz et al. (2002) for compression and Chehab et al. (2002) for tension.

3.3.1 Model Description

(1) Deformable Range of Asphalt Concrete:

The deformation range of asphalt concrete is smaller than pure asphalt. The stress-strain curves at various temperatures and strain rates provided by Chehab et al. (2002)

and Schwartz et al. (2002) show that the strains at the peak stresses range from 0.005 to 0.01, and the fracture strains do not exceed 0.06. There is common consensus that infinitesimal strain theory applies for strains below 0.01. Hence, from a rigorous perspective, it should not be used for asphalt concrete after the peak stress exceeds this criterion. Hyperelasticity and finite strain theory provide a framework of treating such large deformation problems. However, considering that many engineering applications of asphaltic materials are described in terms of traditional stress and strain concepts based on infinitesimal strain theory, the representation of the constitutive model using linear elasticity and infinitesimal deformation is more practical, even if not particularly rigorous, and is followed in this work.

An alternative way of considering large deformations within the framework of infinitesimal strain theory is to use true (1st Piola-Kirchhoff) stress and true (Henky) strain for axial stress and strain components. This alternative way is useful because it permits utilization of Hooke's law, and provides an intuitive and familiar way of characterizing deformation. In this vein, the relationship between true strain (ε) and nominal strain (e) is;

$$\varepsilon_{ii} = \ln(e_{ii} + 1) \qquad i = 1, 2, 3 \text{ (no sum on } i\text{)} \qquad (3.101)$$

The relationship between true stress (σ) and nominal stress (S) is:

$$\sigma_{ii} = (e_{ii} + 1)S_{ii} = \exp(\varepsilon_{ii})S_{ii} \qquad i = 1, 2, 3 \text{ (no sum on } i\text{)} \qquad (3.102)$$

The differences between true and nominal strain at the strain of 0.01 and 0.05 are 0.5% and 2.4%, and the difference between true and nominal stress at the same strains are 1.0% and 4.8%, respectively.

(2) Derivation of the Constitutive Equation

The mechanical analog shown in Fig. 3.18a is proposed for asphaltic materials. The model consists of a nonlinear system (a nonlinear damper) and linear system (generalized Maxwell model). The behavior of the nonlinear system is assumed to have power law viscosity based on Cheung and Cebon's data (1997a; 1997b). The driving force of the nonlinear damper is the sum of stresses generated by the springs in the linear system, which is a parallel connection of Maxwell models with linearly viscous dampers.

As shown in Fig. 3.18b, total strain (ε) is divided into the strain associated with the

nonlinear system (ε_{NL}) and strain of the linear system (ε_L). The strain of linear system (ε_L) is comprised of an elastic strain (ε_{LEi}) and linear viscous strain (ε_{LVi}) for each Maxwell element. The values of each ε_{LEi} and ε_{LVi} can be different, but the sum of those in each Maxwell element should be the same ($\varepsilon_{LEi} + \varepsilon_{LVi} = \varepsilon_L$). Eq. (3.103) shows the compatibility condition for this model.

$$\varepsilon = \varepsilon_{NL} + \varepsilon_L = \varepsilon_{NL} + \varepsilon_{LEi} + \varepsilon_{LVi} \qquad \text{for any } i,\ i = 1, 2, \cdots, n \tag{3.103}$$

where, n is the number of Maxwell models in the linear system. Equilibrium can be expressed as;

$$\sigma = \sigma_{NL} = \sigma_L = \sum_{i=1}^{n} \sigma_i \tag{3.104}$$

where, σ, σ_{NL}, σ_L, and σ_i are total stress, stress of nonlinear system, total stress of linear system, and stress of i^{th} Maxwell model, respectively.

For the linear system, Hooke's law and Newtonian flow rule are employed for elemental constitutive relationships of the elastic springs and the linear dampers, as shown in Eq. (3.105) and (3.106), respectively.

$$\varepsilon_{LEi} = \frac{\sigma_i}{E_i} \tag{3.105}$$

$$\dot{\varepsilon}_{LVi} = \frac{\sigma_i}{\mu_i} \tag{3.106}$$

where, $i = 1, 2, \cdots, n$, and E_i and μ_i are elastic modulus and axial viscosity of i^{th} Maxwell model. $\dot{\varepsilon}_{LVi}$ is the strain rate of linear damper of i^{th} Maxwell model.

Elemental constitutive equation for the nonlinear damper can be expressed using a power form as shown in Eq. (3.107). The theoretical background of the nonlinear viscous flow rule can be found in Weber et al. (1990) and Morrison (2001).

$$\dot{\varepsilon}_{NL} = A\sigma_{NL}^{m} \tag{3.107}$$

where, A and m are constants.

The following constitutive equation (Eq. 3.108) for a generalized Maxwell model (the linear system) is well known (Wineman and Rajagopal 2000):

$$\left[\sum_{i=0}^{n} q_i \left(\frac{d}{dt}\right)^i\right]\varepsilon_L = \left[\sum_{i=0}^{n} p_i \left(\frac{d}{dt}\right)^i\right]\sigma_L \tag{3.108}$$

where, $p_0, p_1, p_2, \cdots, p_n$ and $q_0, q_1, q_2, \cdots, q_n$ are constants.

The constitutive equation for the whole model can be derived from Eq. (3.107) and (3.108). First, σ_L of Eq. (3.108) and σ_{NL} of Eq. (3.107) can be replaced by σ by applying the equilibrium condition. Then, operating on Eq. (3.108) by d/dt and Eq. (3.107) by $\sum_{i=0}^{n} q_i (d/dt)^i$ and adding those results leads to Eq. (3.109):

$$\left[\sum_{i=0}^{n} q_i \left(\frac{d}{dt}\right)^i\right]\left(\frac{d}{dt}\right)\varepsilon = \left[\sum_{i=0}^{n} p_i \left(\frac{d}{dt}\right)^i\right]\left(\frac{d}{dt}\right)\sigma + \left[\sum_{i=0}^{n} q_i \left(\frac{d}{dt}\right)^i\right] A\sigma^m \tag{3.109}$$

Eq. (3.109) is the constitutive equation for the suggested nonlinear viscoelastic model. As previously mentioned, an exact solution of this equation is difficult to achieve because of the nonlinear term in Eq. (3.109). Instead of solving Eq. (3.109), a numerical integration method that employs the elemental constitutive equations (3.105), (3.106), and (3.107) of the components of the mechanical analog is used to simulate the behavior of asphalt concrete.

(3) Numerical Integration Process

The numerical integration method employed in this study is based on the method in Weber et al. (1990). They suggested an objective time-integration algorithm expressed in finite strain kinematics and this algorithm was applied to describe the behavior of viscous polymers by Bergstrom and Boyce (2000), Lion (2000), and Miehe and Keck (2000). The method in Weber et al. (1990) is tailored herein to fit the proposed mechanical analog and the infinitesimal strain kinematic framework employed in this work.

The basic idea of the proposed numerical integration is to partition time into small time steps and to calculate the displacement and its rate for each damper separately using the elemental constitutive equations. The strain rate of each damper at each time step is used to calculate the strains of the dampers at the next time step, i.e. the scheme is essentially explicit. The time interval (Δt) between each step determines the accuracy and the stability of the numerical integration. For example, if a strain increment of any

linear damper ($\Delta\varepsilon_{LVi}$) calculated from the strain rate ($\dot{\varepsilon}_{LVi}$) of the previous step is larger than the strain increment of the linear system ($\Delta\varepsilon_L$), the result will diverge. Extensive simulation studies showed that stability problems can be eliminated if the time interval is smaller than the smallest characteristic time ($\tau_{Ri} = \mu_i / E_i$) of the linear dampers.

The numerical integration process depends upon whether loading is in displacement (strain) control or force (stress) control. In this section, the numerical integration process for strain control is described because of the focus on constant strain rate tests. An arbitrary strain history, $\varepsilon(t)$, is applied and the corresponding stress history, $\sigma(t)$, is computed. If it is assumed that the material has not experienced any loading previously, then the initial conditions will be as follows:

$$(\varepsilon)_0 = (\varepsilon_{NL})_0 = (\varepsilon_L)_0 = (\varepsilon_{LVi})_0 = (\varepsilon_{LEi})_0 = 0 \tag{3.110}$$

where, the subscript outside of parentheses indicates the number of the step.

When a certain strain, ε_0 is applied, the elastic springs carry the strain instantaneously ($\varepsilon_{LEi} = \varepsilon_0$), and generate corresponding stresses (σ_i) at each Maxwell model. The strain rates of the dampers ($\dot{\varepsilon}_{NL}$ and $\dot{\varepsilon}_{LVi}$) can be obtained from the stresses (σ and σ_i) to which each damper is subjected to and will be used to calculate the strains of the dampers (ε_{NL} and ε_{LVi}) at the next step. This process is repeated for each time interval ($\Delta t = t_k - t_{k-1}$) up to a designated time or strain. Therefore, when a total strain at an arbitrary step *k* is given as $(\varepsilon)_k = \varepsilon(t)$, the calculation process at the step *k* can be expressed as follows.

Update the strain components at *k*-th step;

$$(\varepsilon_{NL})_k = (\varepsilon_{NL})_{k-1} + (\dot{\varepsilon}_{NL})_{k-1}\Delta t \tag{3.111}$$

$$(\varepsilon_{LVi})_k = (\varepsilon_{LVi})_{k-1} + (\dot{\varepsilon}_{LVi})_{k-1}\Delta t \tag{3.112}$$

$$(\varepsilon_L)_k = (\varepsilon)_k - (\varepsilon_{NL})_k \tag{3.113}$$

$$(\varepsilon_{LEi})_k = (\varepsilon_L)_k - (\varepsilon_{LVi})_k \tag{3.114}$$

Update the stress components at *k*-th step;

$$(\sigma_i)_k = E_i(\varepsilon_{LEi})_k \tag{3.115}$$

$$(\sigma)_k = \sum_{i=1}^{n} (\sigma_i)_k \tag{3.116}$$

Update the strain rates at *k*-th step;

$$(\dot{\varepsilon}_{NL})_k = A(\sigma)_k^{\ m} \tag{3.117}$$

$$(\dot{\varepsilon}_{LVi})_k = \frac{(\sigma_i)_k}{\mu_i} \tag{3.118}$$

where, i = 1, 2, …, n.

(4) Temperature Dependency

Another factor that affects the behavior of asphaltic material is temperature. A concept known as time-temperature superposition or time-temperature correspondence principle (Leaderman 1943; Ferry 1950) provides a convenient way of dealing with temperature effects. The applicability of the concept to asphalt concrete was verified in the linear viscoelastic state by Goodrich (1991) and Kim and Lee (1995). Subsequently, Chehab et al. (2002) and Schwartz et al. (2002) showed that the time-temperature superposition principle can be extended to the large strain range with evolving damage in tension and compression.

According to this principle, the actual time at a specific temperature (t) can be translated into reduced time (t_R), which is an equivalent time at the reference temperature, through Eq. (3.119).

$$t_R = \frac{t}{a_T} \tag{3.119}$$

where, a_T is temperature shift factor which is a function of temperature. a_T can be calculated from Arrhenius or Williams-Landal-Ferry (WLF) equations if their parameters are known. However, direct calibration of a_T using experimental data is usually used for asphalt concrete. More details on the temperature shift factor calibration method can be found in Chehab et al. (2002) and Schwartz et al. (2002).

(5) Damage Mechanics

Many studies (Kim and Little 1990; Gibson et al. 2003; Krishnan et al. 2006; Chehab et al. 2002) agree that the deformation mechanism of asphalt concrete involves evolution

of microcracking at significantly earlier strain ranges than those leading to fracture. In this model, a damage parameter based on damage mechanics is introduced to describe the softening behavior after the peak stress is achieved in asphalt concrete. The assumptions in the proposed model are; (a) damage accumulation in asphalt concrete commences at peak stress, and (b) the damage parameter is time independent and is expressed as a function of strain.

According to Lemaitre (1984), the relationship between the actual stress (σ), the effective stress ($\tilde{\sigma}$), and the damage parameter ($D = D(\varepsilon)$) can be defined as Eq. (3.120).

$$\sigma = (1 - D)\tilde{\sigma} \tag{3.120}$$

Eq. (3.121) can be derived from Eq. (3.120) and is used to calibrate the damage parameter for the proposed model.

$$D = 1 - \frac{\sigma}{\tilde{\sigma}} = 1 - \frac{\sigma_{\text{damaged}}}{\sigma_{\text{intact}}} \tag{3.121}$$

where, σ_{damaged} is the stress measured from the damaged specimen and σ_{intact} is the stress calculated from the model assuming no damage.

3.3.2 Calibration of Model Parameters

As shown in Eq. (3.103) and Fig. 3.18b, total deformation in the proposed model is composed of linear and nonlinear components. This means that conventional calibration methods for linear models or nonlinear models are not appropriate. Therefore, it is necessary to develop a proper calibration method tailored to the proposed model. The developed calibration method is composed of four steps, each of which is described in detail later on:

(1) Linear system calibration of the modified power law (MPL) relaxation function

(2) Conversion of the relaxation function from MPL to a Prony series

(3) Nonlinear system calibration through an iterative technique

(4) Damage parameter and temperature shift factor calibration

The asphalt concrete samples that Schwartz et al. (2002) tested in uniaxial compression at 25ºC are used for calibration. The data contains four stress-strain curves obtained from uniaxial constant strain rate tests. The calibration process, as discussed

next, identifies the damage parameter and temperature shift factors as well. After the proposed model is calibrated, it is applied to show that is capable of simulating the behavior of various sets of constant strain rate tests conducted at different temperatures.

(1) Linear System Calibration

As was explained earlier, the role of the linear portion of the model is to simulate the behavior of the linear viscosity dominant region. Hence, the concept of linear viscoelasticity is employed in the linear system calibration. Linear viscoelastic materials can be characterized by the relaxation modulus or creep compliance. Properties of the relaxation modulus of asphalt concrete within the linear range were identified experimentally by Kim and Little (1989; 1990), Kim et al. (1995), and Park and Kim (2001). These studies concluded that the duration of relaxation extends over many decades of logarithmic time.

The relaxation function of a single Maxwell model with a constant viscosity can be represented by a single exponential function. The duration of transition of the exponential function in log-log space is rather narrow and does not fully cover the relaxation modulus of asphalt concrete. To capture the broadband nature of asphalt concrete relaxation function over time, a Prony series or power-law based function is used.

The relaxation function ($G(t)$) of the generalized Maxwell model is represented by a Prony series shown in Eq. (3.122).

$$G(t) = E_\infty + \sum_{i=1}^{n} E_i \exp\left(-\frac{E_i}{\mu_i} t\right) = E_\infty + \sum_{i=1}^{n} E_i \exp\left(-\frac{t}{\tau_{Ri}}\right) \tag{3.122}$$

where, τ_{Ri} is characteristic time of i^{th} Maxwell element, and $\tau_{Ri} = \mu_i / E_i$.

By adding a number of exponential functions, a Prony series is capable of simulating the broadband nature of the relaxation function. Since, each Maxwell element has two material parameters (E_i and μ_i), the total number of material parameters to be calibrated for the linear system is 2*n*. Various methods for Prony series calibration using experimentally obtained relaxation or creep data have been suggested by various researchers (Park and Kim 2001; Gibson et al. 2003). The calibration process in this study entails selecting an alternative function among the power-law based relaxation

functions in order to reduce the number of material parameters. Once, the material parameters of the power law relaxation function are determined, the power law function can be easily translated into a Prony series. This translation technique is called power-law presmoothing, and its details are provided by Park and Kim (2001).

One of the popular choices for the relaxation modulus of asphalt concrete is the modified power law (MPL) function suggested by Williams (1964). Eq. (3.123) shows the MPL function including four material parameters (E_{ins}, E_{∞}, τ_0, and r).

$$G(t) = E_{\infty} + \frac{E_{ins} - E_{\infty}}{\left(1 + t/\tau_0\right)^r} \tag{3.123}$$

where, E_{ins} and E_{∞} are instantaneous and long-term moduli of elasticity, and represent short- and long-time asymptotes of the relaxation function. τ_0 determines a starting time of transition in the relaxation function from E_{ins}, and r is the negative value of the slope of the relaxation function in log-log space.

Solid lines in Fig. 3.19 represent experimental data (Schwartz et al. 2002) obtained from constant strain rate tests with strain rates of 0.0005, 0.0015, 0.0045, and 0.0135 (strain/sec). The instantaneous elastic modulus, E_{ins}, can be estimated using the initial stiffness of the fastest strain rate test. E_{∞} is the residual stiffness after complete relaxation, and needs to be assumed. Previously published relaxation data approximated by the modified power law functions (Kim et al. 1995; Park and Kim 2001) shows that $G(10^6 \text{ sec}) \approx E_{\infty}$ is equal or lesser than 0.3% of E_{ins}. In this model, E_{∞} is assumed to be 0.1% of E_{ins}. To determine τ_0 and r, the constant strain rate tests should be simulated in the linear dominant range. In linear viscoelasticity, the nominal stress history, $S(t)$ can be expressed in terms of relaxation modulus and strain rate as shown in Eq. (3.124).

$$S(t) = e(0)G(t) + \int_0^t G(t-s)\dot{e}(s)ds \tag{3.124}$$

From the test condition of Fig. 3.19, the initial strain, $e(0) = 0$, and the nominal strain rate, $\dot{e}$, is a constant. Then, by substituting Eq. (3.123), Eq. (3.124) becomes;

$$S(t) = \dot{e}\left[E_\infty \tau_0 t + (E_{ins} - E_\infty)\frac{\tau_0}{1-r}\left\{\left(1+\frac{t}{\tau_0}\right)^{1-r} - 1\right\}\right] \tag{3.125}$$

The curve $S(t)$ associated with each strain rate can be easily plotted and compared with experimental data. Since, E_{ins} and E_∞ are already known, there are only two unknowns (τ_0 and r) for the relaxation function. The values of τ_0 and r for fitting the initial behavior of test data is then determined by trial and error through comparison of the curves of Eq. (3.125) to the test data. The dotted lines in Fig. 3.19 are curves obtained from Eq. (3.125). The calibrated MPL parameters of Fig. 3.19 are listed in Table 3.2.

The conversion of the relaxation function from MPL to Prony series can be accomplished by the least square method, and is explained in Park and Kim (2001). The values of the Prony series parameters converted from the MPL model are listed in Table 3.2. Fig. 3.20 compares the relaxation functions of MPL form, Prony series form, and exponential functions of each Maxwell elements comprising the Prony series. The same logarithmic interval of 1 (=log 10) between the characteristic times (τ_{Ri}) is selected for the Prony series, and consequently, the number of the series (n) is determined from the width of MPL function in the logarithmic time scale. Then, the stiffness of each spring (E_i) is determined to match the MPL function.

(2) Nonlinear System Calibration

The power law viscous damper of the nonlinear system illustrated in Fig. 3.18a has two material parameters that need to be calibrated, *A* and *m*. Cheung and Cebon (1997b) suggested a power form viscous constitutive equation similar to Eq. (3.107), and evaluated its parameters based on the steady state stress and strain rate. However, Cheung and Cebon's (1997b) constants are not applicable to the proposed model because of the following reasons. Cheung and Cebon (1997b) considered that once the stress reaches the steady state, additional strain is fully carried by nonlinear viscous flow. However, in the model proposed in this section, the viscous strain is decomposed into linear and nonlinear portions as shown in Fig. 3.18b. Therefore, the nonlinear damper of the proposed model carries only a part of the viscous flow. In addition, the concept of the steady state is not

clear. Cheung and Cebon (1997b) evaluated the steady state in terms of nominal stress (*S*) and nominal strain (*e*) while the proposed model uses true stress (σ) and true strain (ε). The differences between true and nominal stress/strain could be significant if the deformations are large enough.

To find the two parameters, *A* and *m* of the nonlinear system, an iterative method is introduced in this study. As the first step, a control point for the iteration is selected within the nonlinear dominant region. $e = 0.01$ where the strain at peak stress is selected to calibrate to Schwartz et al.'s (2002) data. In general, any number can be selected as a starting point of the iteration for *A* and *m*. In this example, *A* and *m* for the first iteration are chosen from the relationship between the rate of the total true strain rate ($\dot{\varepsilon} = \dot{e}/(e+1)$) and true stress ($\sigma$) at the control point.

From each simulation of the constant strain rate test, the true strain rate of the nonlinear damper, $\dot{\varepsilon}_{NL}$, at the control point is obtained and plotted on the $\dot{\varepsilon}_{NL}$ versus σ plot in log-log scale as shown in Fig. 3.21. Then, a power law function for each iteration is obtained through regression. Since, the regressed power law function has an identical form to Eq. (3.107), *A* and *m* are the coefficient and the index of the function, respectively. Then, the values of *A* and *m* are used for the next iteration. Throughout the iteration, the stresses at the control point for $\dot{\varepsilon}_{NL} - \sigma$ plot (the horizontal axis) are determined from experimental curves, and kept constant, because those are the targets of the iterative process. Fig. 3.21 demonstrates the convergence of *A* and *m* through the iteration process and Fig. 3.22 compares the simulation results after the 5th iteration to the test data. The simulated $\sigma - \varepsilon$ curves with the 5th iteration parameters (A=1.925×10^{-5} /s MPa$^{-3.294}$, m=3.294) show good agreement with the experimental data up to the peak stress.

An important advantage of the proposed calibration method is that all of the material parameters in the proposed model can be calibrated using only a set of constant strain rate tests with several different strain rates. For example, the material parameters (except for the temperature shift factor) of two applications presented in this section are calibrated using four stress-strain curves obtained from constant strain rate tests. The proposed calibration procedure greatly reduces the effort for material characterization compared to

the large number of tests required by traditional calibration methods.

(3) Calibration of Damage Parameter and Temperature Shift Factor

Evolution of damage is another important factor affecting the behavior of asphalt concrete. The solid line in Fig. 3.23 is one of the stress – strain curves in Fig. 3.22. The stress reaches the peak at a strain of about 0.01 after which softening occurs. As previously mentioned, a damage parameter, $D(\varepsilon)$, is introduced to simulate this type of behavior.

The dotted line in Fig. 3.23 is the simulation result of the proposed model without consideration of damage. Using Eq. (3.121), the damage parameter is obtained by comparing the difference between experimental data (σ_{damaged}) at 25ºC and the simulation without damage consideration (σ_{intact}). Fig. 3.24 displays the damage parameter versus strain and their regression curves using second and third order polynomials. The second order polynomial function describes the overall trend better. However, the third order polynomial function is selected in this study because it provides a smooth transition of the stress – strain curve from the strain range without damage to the damaged strain range. The calibrated third order damage parameter function is presented in Table 3.2.

An additional factor influencing the mechanical response of asphalt concrete is temperature dependency. As was mentioned previously, the temperature shift factor (a_T) based on the time-temperature superposition principle is used to take this effect into account. Since the material parameters of the proposed model are calibrated at the reference temperature (T_R =25ºC), the time scale of the simulations using those parameters is the reduced time (t_R). Therefore, the response in the actual time scale can be obtained by transforming the reduced time (t_R) to actual time (t) through Eq. (3.119). Fig. 3.25 illustrates the calibration of a_T using the relationship between the peak stresses and the applied strain rate obtained from Schwartz et al. (2002). The solid line in the figure is the regression for the data at the reference temperature, and the data at the other temperatures are shifted to be matched to the line. $a_T(T)$ presented in Table 3.2 is estimated from these shift factors at the four temperatures.

3.3.3 Simulation Results

(1) Experimental Data for the Simulation

Schwartz et al. (2002) presented four sets of uniaxial constant compressive strain rate test results at four different temperatures (5ºC, 25ºC, 40ºC, and 60ºC, respectively). The applied strain rates at each temperature were 0.0005, 0.0015, 0.0045, and 0.0135 strain/sec. The material tested by Schwartz et al. (2002) was a 12.5 mm dense graded Superpave mixture with PG 64-22 asphalt binder. This asphalt concrete is commonly used by the Maryland State Highway Administration for pavement. Cylindrical specimens with 100 mm diameter and 150 mm height were used for their tests. The specimens were prepared at Arizona State University as a part of NCHRP9-19 project.

In this study, the viscoelastic material parameters and the damage parameter of the proposed constitutive model were calibrated using the data in Schwartz et al. (2002) at 25ºC, as previously described and documented in Table 3.2. Then, for the purposes of validation, the tests conducted at different temperatures are simulated using the same set of calibration parameters with the temperature shift factor.

Additional evidence that the model is reasonable is sought by using the uniaxial tensile test data in Chehab et al. (2002), who used asphalt concrete similar to that in Schwartz et al. (2002). Chehab et al.'s (2002) tension tests were also a part of NCHRP9-19 project, and their specimens were fabricated at Arizona State University with the same specification (12.5 mm dense graded Superpave mixture with PG 64-22 asphalt binder) recommended by the Maryland State Highway Administration. Although there is no statement that the materials of Schwartz et al. (2002) and Chehab et al. (2002) are identical, it can be presumed that those materials were created according to the same specifications and, consequently, should have similar material properties. The size of Chehab et al.'s (2002) specimens were 75 mm diameter and 150 mm height.

Although the materials in both studies are considered to be identical, some of the material parameters of asphalt concrete vary because the direction of loading is different (compression in Schwartz et al. (2002) and tension in Chehad et al. (2002)). In this study, it is assumed that the responses of the linear system are the same in tension and in compression to ensure smoothness in the continuity between compressive and tensile

responses. However, the nonlinear behavior differs. This is deemed reasonable considering that the micromechanical interactions between aggregates and asphalt binder in tension and in compression must necessarily be different. Therefore, the parameters for nonlinear damper and damage for tension are calibrated using the same procedure described for compression. The control point of iteration for the parameters of the nonlinear damper and the strain at which the damage initiates in tension is 0.005 (the strain at peak stress). The calibration results for the nonlinear part of the model for Chehab et al.'s (2002) tension tests are summarized in Table 3.3.

(2) Simulation Results for Compression Tests

Fig. 3.26 compares simulations of the constant strain rate test using the proposed model to the experimental data at 25ºC of Schwartz et al. (2002). Clearly, the calibration is reasonable and the model is able to successfully describe the behavior of asphalt concrete at various strain rates in both linear and nonlinear dominant regions.

Fig. 3.27-3.29 display the simulations for constant strain rate tests at 5°C, 40°C, and 60°C using the same viscoelastic and damage parameters, but with a temperature shift factor. Although there are some discrepancies in the comparison at 40ºC and 60ºC, the proposed model still simulates the overall responses in a reasonable manner, especially given the possibility of scatter in the test data. The experimental data for each series provided by Schwartz et al. (2002) is actually averaged data for two specimens with the exception of the data for 0.0015 /s at 5ºC in Fig. 3.27. The gap between two stress-strain curves obtained from two specimens subjected to the same test conditions ($\dot{e}$ =0.0015 /s at 5ºC) is an example of the possible scatter that could occur in the behavior of asphalt concrete. The assumptions employed for obtaining the damage parameter could be another possible source for these discrepancies. In the proposed model, the damage model is assumed to be time-independent. This assumption is based on the observation that the damage parameters evaluated from test data for four different strain rates were nearly identical (Fig. 3.24). Another assumption applied to the damage model is that the damage function is activated at the strain of the peak stress. Both assumptions are deemed reasonable within the limited strain rate range, but need to be confirmed by

further investigations covering a wider strain rate range, and to be supported by theoretical background.

The comparisons in Fig. 3.27-3.29 are essentially a validation study, because the computed responses were obtained using the same material parameters used to generate the curves in Fig. 3.26, which pertained to response under different conditions than those for Fig. 3.27-3.29.

(3) Simulation for Tension Tests

The simulation results for the constant tensile strain rate tests at 25°C conducted by Chehab et al. (2002) are compared to the experimental data in Fig. 3.30. Chehab et al. (2002) conducted each test twice, and presented both stress-strain curves separately. The mean value of Chehab et al.'s (2002) data are presented as solid lines in Fig. 3.30. The dotted lines in Fig. 3.30 are the simulation results using the proposed model. Clearly, the model is able to trace the experimental behavior well.

(4) Contribution of the Linear and Nonlinear Systems

The contributions of the linear and nonlinear components of the model to total deformation during the constant strain rate simulations are illustrated in Fig. 3.31 and 3.32. The contribution of each system is calculated by dividing the strain of each system by the total strain and expressed as a percent. Distinction between strains due to the linear and nonlinear systems is useful because the strain associated with the linear system is recoverable when the force is removed whereas the nonlinear strain is not.

As shown in Eq. (3.103), the strain of the linear system can be divided again into the strain of the spring (ε_{LEi}) and the strain of the damper (ε_{LVi}). Although, this sub-division of the strain occurs separately in each Maxwell element of the linear system, the equivalent total spring strain (ε_{LE}) can still be calculated by dividing the total stress by the total elastic modulus ($\sum E_i$). Since, ε_{LE} is linearly proportional to total stress, ε_{LE} represents the magnitude of the driving force for the deformation in the nonlinear damper.

The overall trends shown in Fig. 3.31 and 3.32 confirm the trends alluded to in Fig. 3.2, i.e. linear viscoelasticity is dominant in the initial behavior, and nonlinear strain gradually increases with increase in total strain.

Two extreme cases for compressive deformation are shown in Fig. 3.31. These correspond to $\dot{e}$ =0.0005 /s at 60ºC (thinner lines in Fig. 3.31) and $\dot{e}$ =0.0135 /s at 5ºC (thicker lines in Fig. 3.31). Since the proposed model employs the time-temperature superposition method to consider the effect of temperature, the strain rates at different temperatures can be converted into equivalent strain rates ($\dot{e}_{eq}$) at the reference temperature (25ºC) with respect to the reduced time defined in Eq. (3.119). Therefore, the corresponding equivalent strain rates for two cases displayed in Fig. 3.31 are $\dot{e}_{eq}$ =0.00000391 /s and $\dot{e}_{eq}$ =0.138 /s, respectively.

Although the applied strain rates differ by 5 orders of magnitude, the difference between the contributions of linear and nonlinear strains is almost identical in both cases as shown in Fig. 3.31. An observation from Fig. 3.31 and 3.32 is that the increase of nonlinear contribution in tensile deformation shown in Fig. 3.32 is significantly more rapid than that in compression (Fig. 3.31). Since the models for tension and compression share the same linear system, it is clear that the nonlinear effects captured by the models are more dominant in tension than in compression.

A stress relaxation isochrone is a plot of stress versus strain for fixed time obtained from various relaxation loading conditions. It is a useful visualization method for distinguishing between linear and nonlinear viscoelastic behavior. If a material is linear viscoelastic, its isochrones should be straight. Fig. 3.33 illustrates isochrones constructed from relaxation simulations using the proposed model. The dotted lines in Fig. 3.33 are obtained from the linear system of the model (Eq. (3.123)) and the solid lines represent total responses of the model. Therefore, the horizontal distance between the dotted and solid lines indicates the strain accumulated in the nonlinear system at the corresponding fixed time. Fig. 3.33 demonstrates that the proposed model successfully simulates the coexistance of linear and nonlinear viscoelasticity explained in Fig. 3.2.

3.3.4 Conclusions

A nonlinear, uniaxial, viscoelastic constitutive model was developed for asphalt concrete. The mechanical analog of the model consists of a power law damper and a generalized Maxwell model connected in series. It was shown that this combination permitted modeling the different characteristics of asphaltic materials over a wide range of strain rates and temperatures. A numerical integration method was suggested to resolve the mathematical difficulty caused by the nonlinear terms in the constitutive equation. Recommendations for selecting an appropriate time increment for the numerical integration algorithm were provided to ensure stability and accuracy of the simulation. A method for calibrating the parameters of the model was also proposed. The parameters in the linear system were calibrated using the power law presmoothing technique while the nonlinear parameters were calibrated by iteration. Using this calibration process, it was shown that all of the required material parameters could be determined from a single set of constant strain rate tests.

Temperature dependency was taken into account using the time-temperature shift factor and a damage parameter was used to capture the strain softening observed in asphalt concrete. Once the model was formulated, the ability of the developed model to realistically represent the behavior of asphalt concrete was examined. It was shown that the model could simulate constant compressive strain rate tests conducted by Schwartz et al. (2002) and constant tensile strain rate tests conducted by Chehab et al. (2002). An important advantage of the proposed model is that it can simulate the entire range of asphalt concrete response of interest using a single set of the material parameters.

Table 3.1 Material parameters of B1 asphalt (Cheung and Cebon 1997b) calibrated for the proposed model

MPL parameters for linear system						
$E_\infty = 0$ MPa		$E_{ins} = 70$ MPa		$\tau_0 = 0.005$ s		$r = 0.48$
Prony parameters for linear system						
series ID	τ_R (s) or τ_C (s)	generalized Maxwell model		generalized Kelvin-Voigt model		
		E_M (MPa)	μ_M (MPa·s)	J_K (Mpa^{-1})	E_K (MPa)	μ_K (MPa·s)
0	-	0	-	1.43E-2	7.00E+1	-
1	1.E+6	1.50E-2	1.50E+4	1.25E+2	8.01E-3	8.01E+3
2	1.E+5	2.50E-2	2.50E+3	1.18E+1	8.45E-2	8.45E+3
3	1.E+4	8.20E-2	8.20E+2	7.05E+0	1.42E-1	1.42E+3
4	1.E+3	2.40E-1	2.40E+2	2.14E+0	4.67E-1	4.67E+2
5	1.E+2	7.60E-1	7.60E+1	6.94E-1	1.44E+0	1.44E+2
6	1.E+1	2.20E+0	2.20E+1	2.38E-1	4.20E+0	4.20E+1
7	1.E+0	7.00E+0	7.00E+0	7.45E-2	1.34E+1	1.34E+1
8	1.E-1	2.00E+1	2.00E+0	2.35E-2	4.25E+1	4.25E+0
9	1.E-2	3.50E+1	3.50E-1	6.70E-3	1.49E+2	1.49E+0
10	1.E-3	4.68E+0	4.68E-3	6.64E-4	1.51E+3	1.51E+0
Parameters for nonlinear system						
$m = 2.787$			$A = 2.709 \times 10^{-2}$ MPa^{-m}/s			
Constants for temperature shift factor						
*$Q_p = 228000$ J mol^{-1}		*$R = 8.314$ J mol^{-1} K^{-1}		$T_R = 10°C$		

* cited from Cheung and Cebon (1997b)

Table 3.2 Summary of the material parameter calibration results for the asphalt concrete subjected to compression tested by Schwartz et al. (2002)

MPL parameters for linear system			
$E_\infty = 10\ MPa$		$E_{ins} = 10{,}000\ MPa$	
$\tau_0 = 0.0004\ s$		$r = 0.315$	
Prony parameters for linear system			
series ID	$E\ (MPa)$	$\tau_R\ (s)$	$\mu\ (MPa{\cdot}s)$
1	7	1.E+06	7000000
2	18	1.E+05	1800000
3	38	1.E+04	380000
4	78	1.E+03	78000
5	155	1.E+02	15500
6	320	1.E+01	3200
7	720	1.E+00	720
8	1500	1.E-01	150
9	2700	1.E-02	27
10	4454	1.E-03	4
11	10	-	-
Parameters for nonlinear system			
$m = 3.294$		$A = 1.925\times10^{-5}\ MPa^{-m}/s$	
Temperature shift factor			
$Log\ a_T = 0.0007T^2 - 0.1195T + 2.5431$			
Damage parameter			
$D = 1.660\times10^4(\varepsilon+0.01)^3 + 6.007\times10^2(\varepsilon+0.01)^2 - 9.126(\varepsilon+0.01)$			

Table 3.3 Summary of the material parameter calibration results for the asphalt concrete subjected to tension tested by Chehab et al. (2002)

Parameters for nonlinear system	
$m = 2.714$	$A = 6.975\times10^{-4}\ MPa^{-m}/s$
Damage parameter	
$D = 3.55\times10^9(\varepsilon-0.005)^6 - 4.37\times10^8(\varepsilon-0.005)^5 + 2.14\times10^7(\varepsilon-0.005)^4 - 5.23\times10^5(\varepsilon-0.005)^3 + 5.65\times10^3(\varepsilon-0.005)^2 + 1.77\times10(\varepsilon-0.005)$	

* the linear parameters for tension are the same as in Table 3.2

	Displacement controlled deformation	Force controlled deformation
Asphalt	Generalized Maxwell model for linear system described in finite strain	Generalized Kelvin-Voigt model for linear system described in finite strain
Asphalt concrete	Generalized Maxwell model for linear system described in infinitesimal strain	Generalized Kelvin-Voigt model for linear system described in infinitesimal strain

Fig. 3.1 Four appearances of the proposed nonlinear viscoelastic constitutive model for asphaltic materials

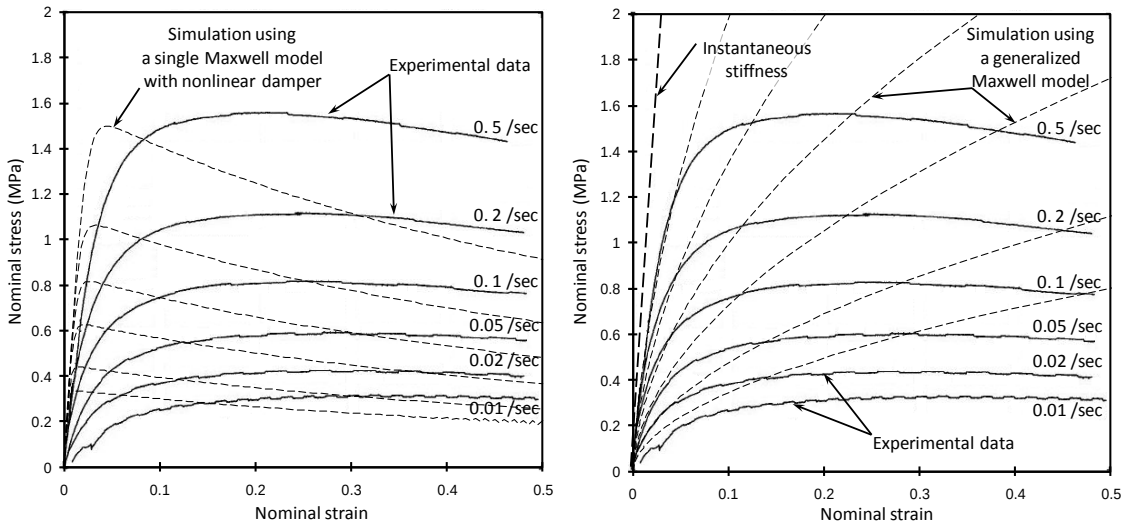

(a) compared to nonlinear model (b) compared to linear model

Fig. 3.2 Typical stress-strain curves from uniaxial constant strain rate tests (at 10°C, taken from Cheung and Cebon 1997b), compared to purely linear and nonlinear viscoelastic models.

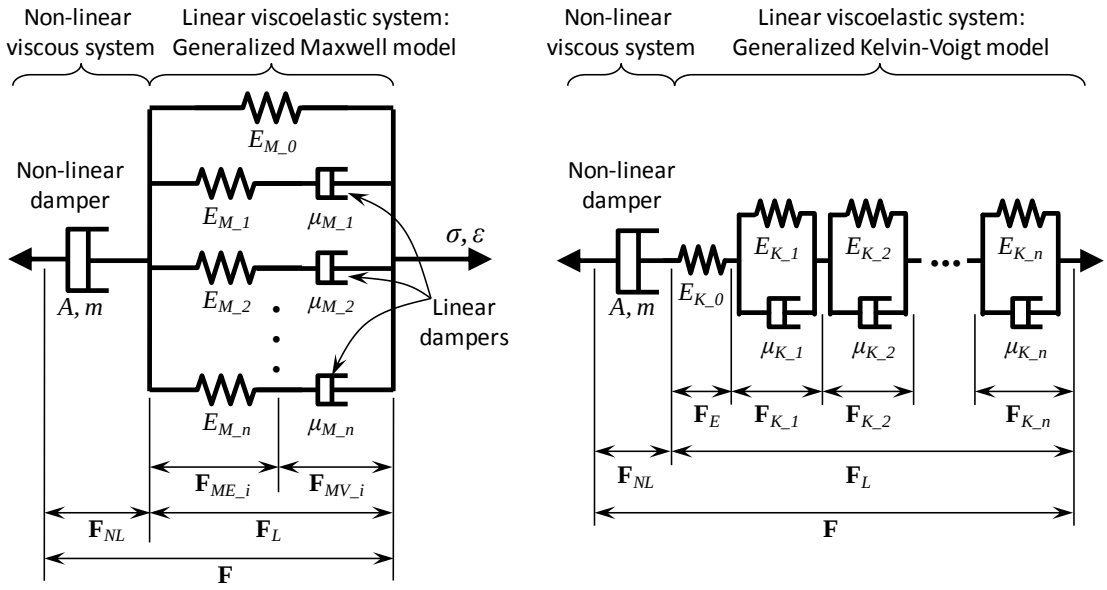

(a) displacement controlled deformation (b) force controlled deformation

Fig. 3.3 Mechanical analogs of the proposed nonlinear viscoelastic model

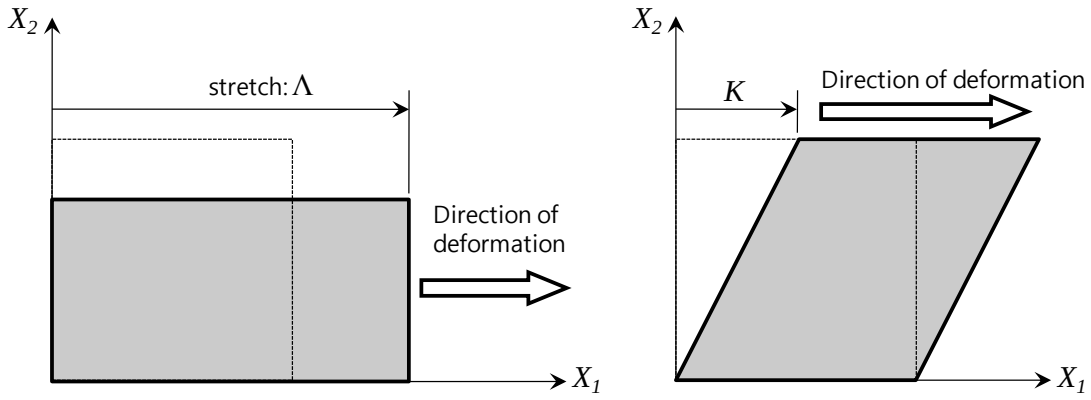

(a) uniaxial deformation (b) simple shear deformation

Fig. 3.4 Kinematics

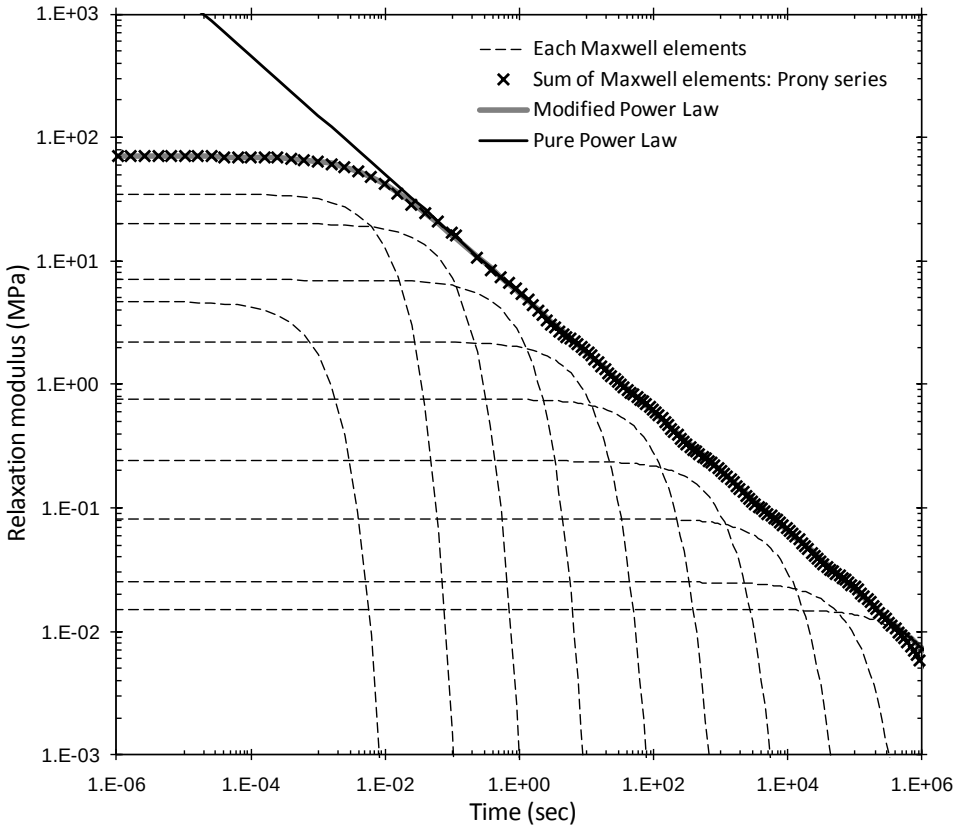

Fig. 3.5 Conversion of the relaxation function from MPL to Prony series

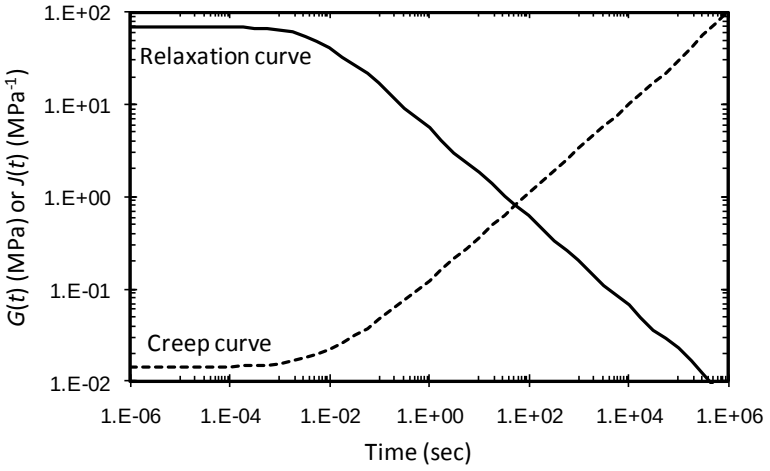

Fig. 3.6 Conversion of the relaxation function into the creep function of the linear system

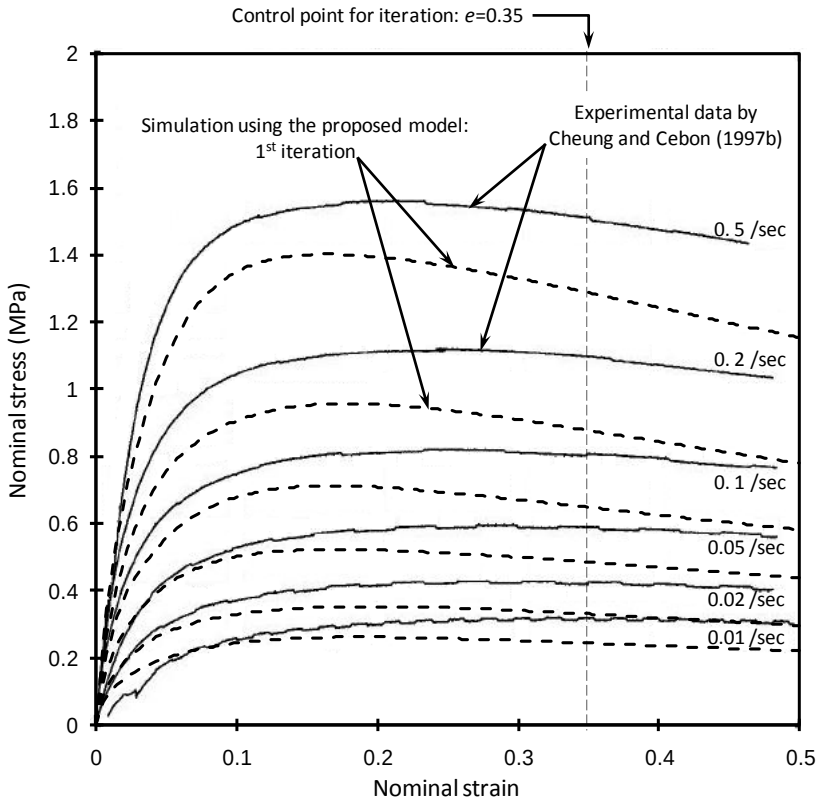

Fig. 3.7 Simulation using the nonlinear parameters of 1st iteration: comparison to constant strain rate tests at 10°C, conducted by Cheung and Cebon (1997b)

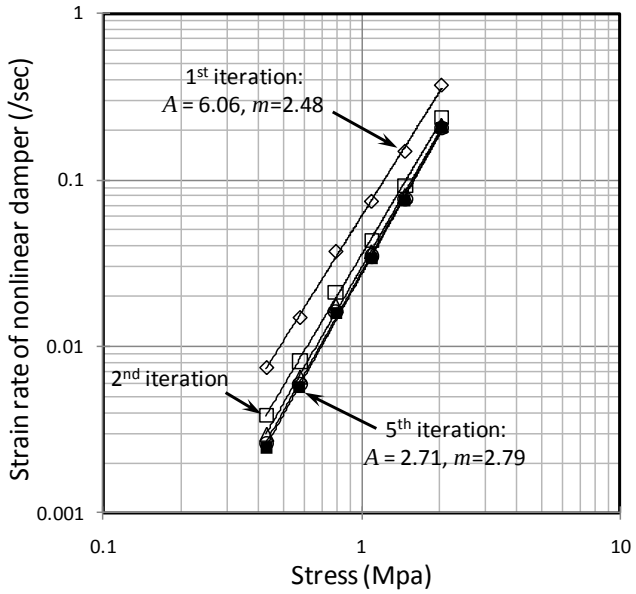

Fig. 3.8 Iteration for nonlinear system calibration: using constant strain rate tests at 10°C, conducted by Cheung and Cebon (1997b)

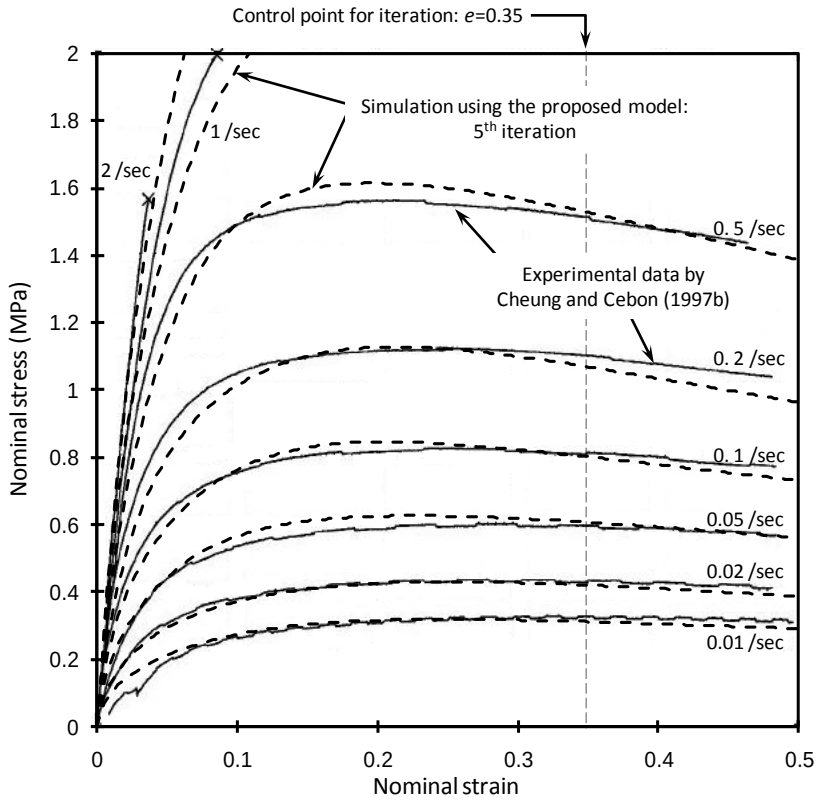

Fig. 3.9 Simulation after 5th iteration: comparison to constant strain rate tests at 10°C, conducted by Cheung and Cebon (1997b)

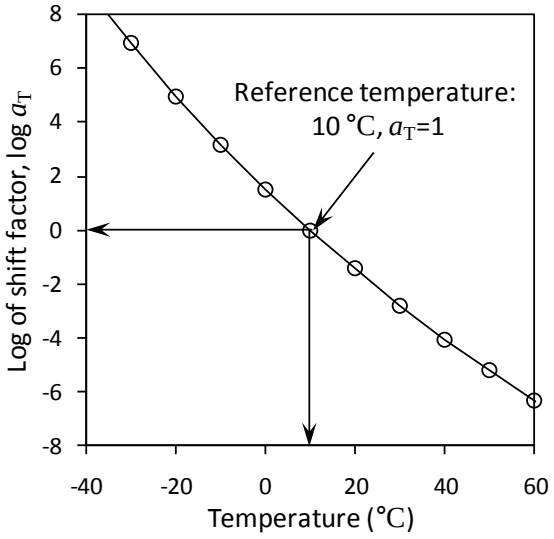

Fig. 3.10 Temperature shift factor for the asphalt tested by Cheung and Cebon (1997b)

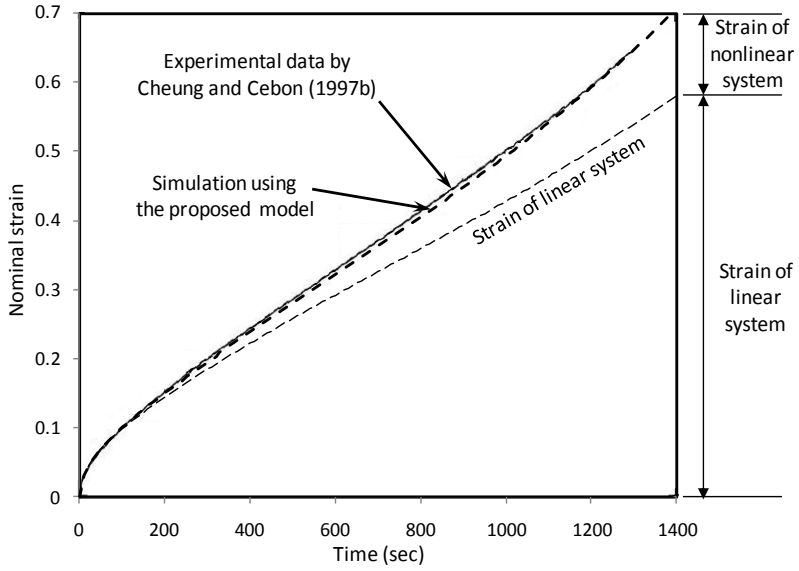

Fig. 3.11 Verification of the model by comparison to creep test, S_{11}=0.078MPa at 10°C, conducted by Cheung and Cebon (1997b)

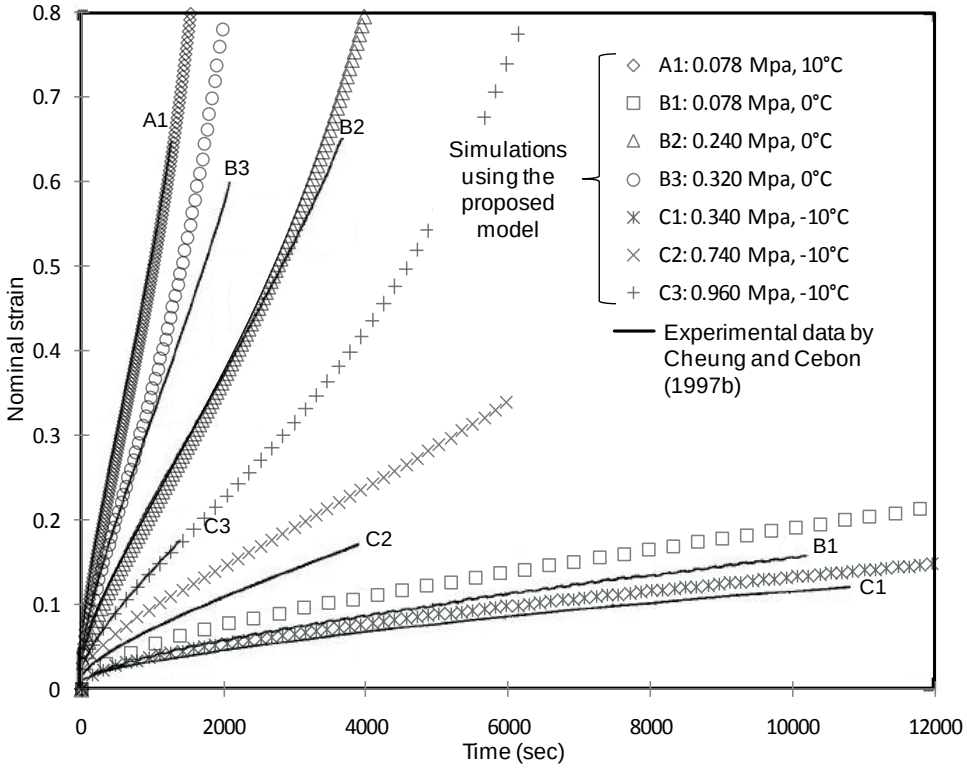

Fig. 3.12 Verification of the model by comparison to creep tests conducted by Cheung and Cebon (1997b)

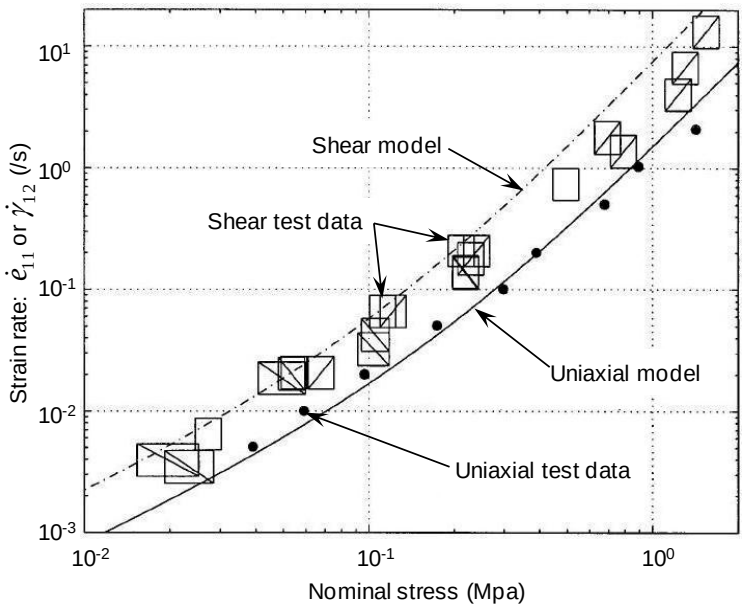

Fig. 3.13 Shear test data compared to uniaxial and shear models. The models and test data provided by Cheung and Cebon (1997b) are for asphalt B2. The test temperature is not specified for this data.

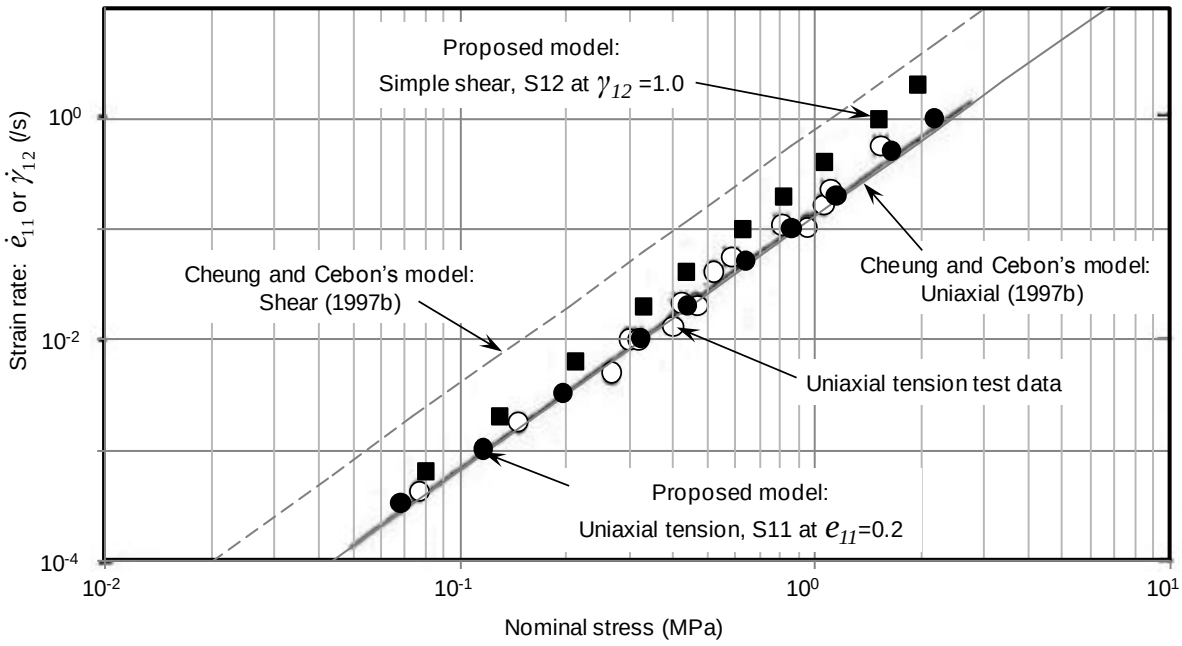

Fig. 3.14 Comparison of the shear and uniaxial simulation results to Cheung and Cebon's (1997b) models for B1 at 10°C

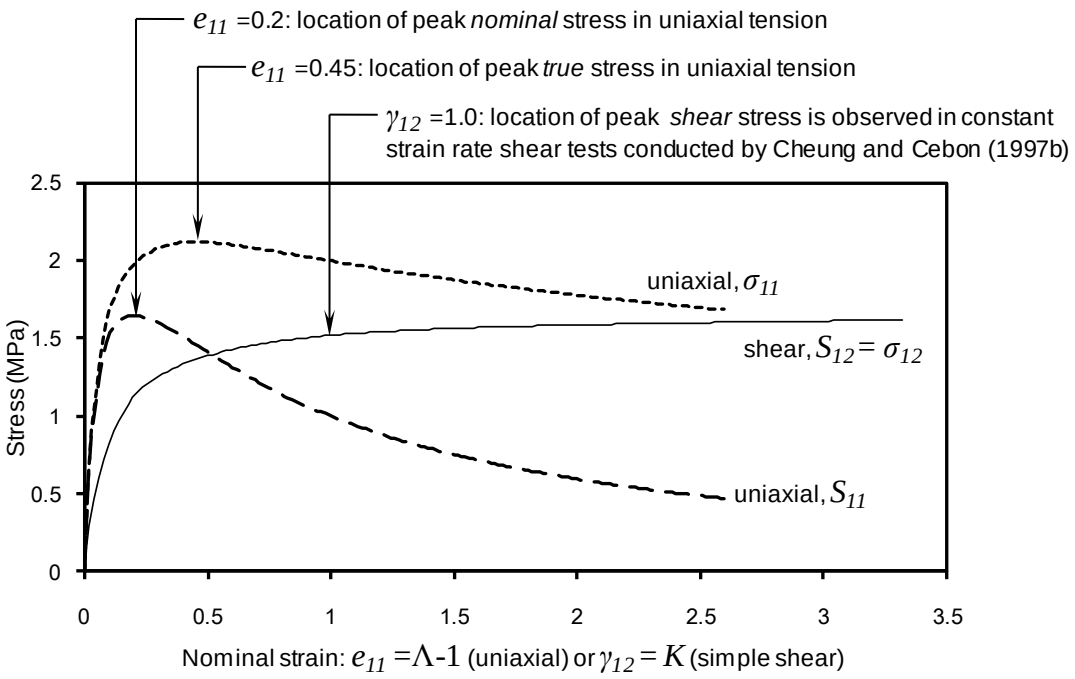

Fig. 3.15 Effects of large deformation on uniaxial tension and simple shear under constant nominal strain rates: $\dot{e}_{11} = 0.5$ and $\dot{\gamma}_{12} = 1.0$ at 10°C.

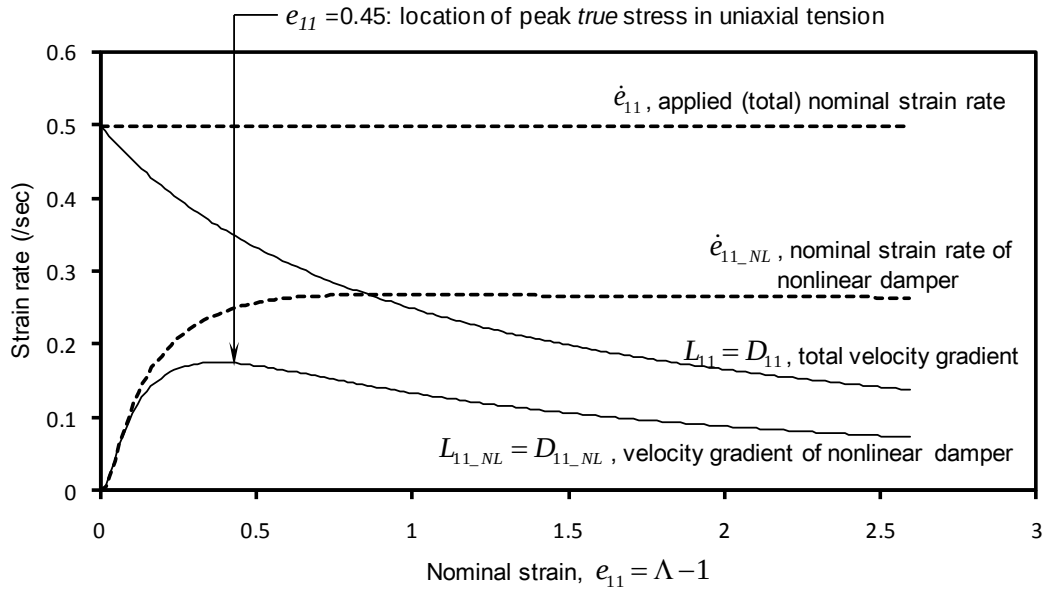

Fig. 3.16 Contribution of nonlinear system and the difference between the nominal strain rate and the velocity gradient under uniaxial tension: $\dot{e}_{11} = 0.5$ at 10°C.

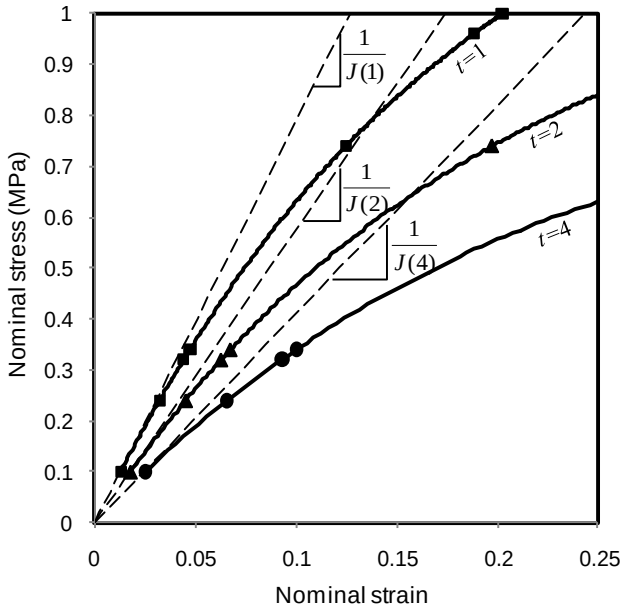

(a) creep isochrone

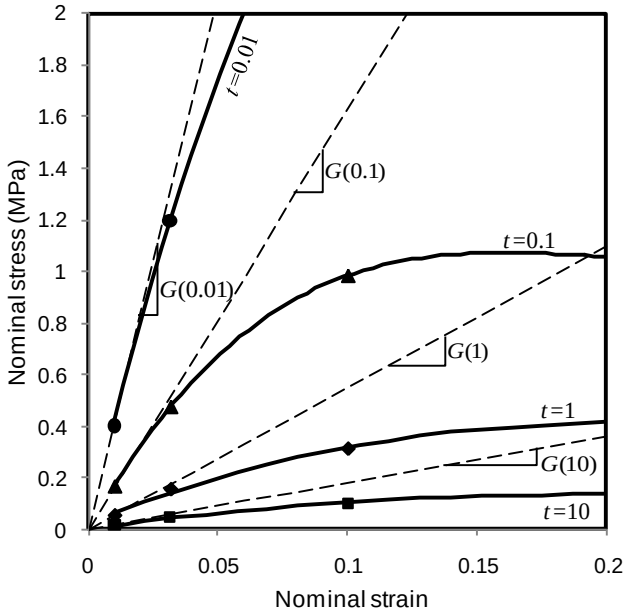

(b) stress relaxation isochrone

Fig. 3.17 Isochrones obtained from uniaxial tension simulations at 10°C.

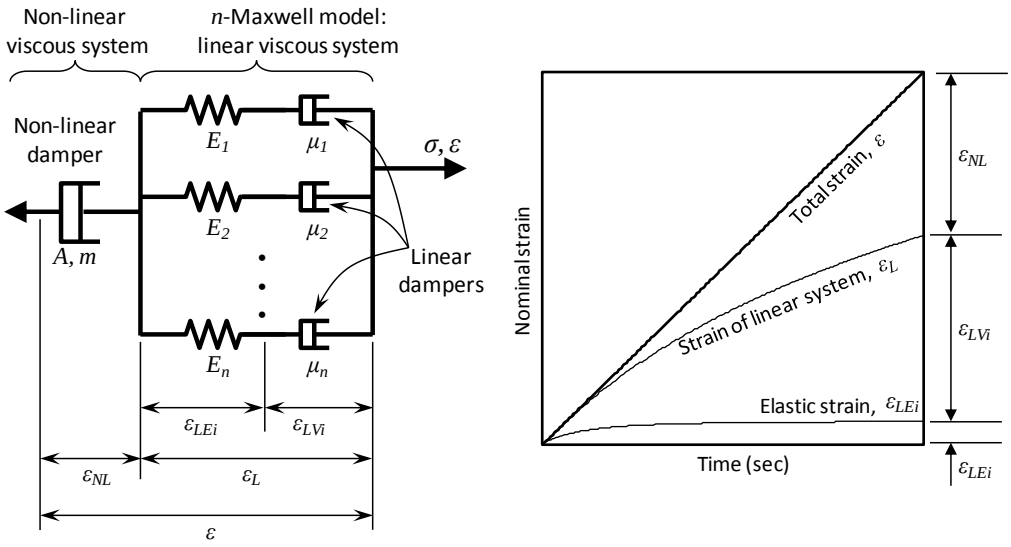

(a) mechanical analog of the proposed model

(b) decomposition of strain assuming a constant strain rate test

Fig. 3.18 Schematics of the nonlinear viscoelastic model in infinitesimal strain theory

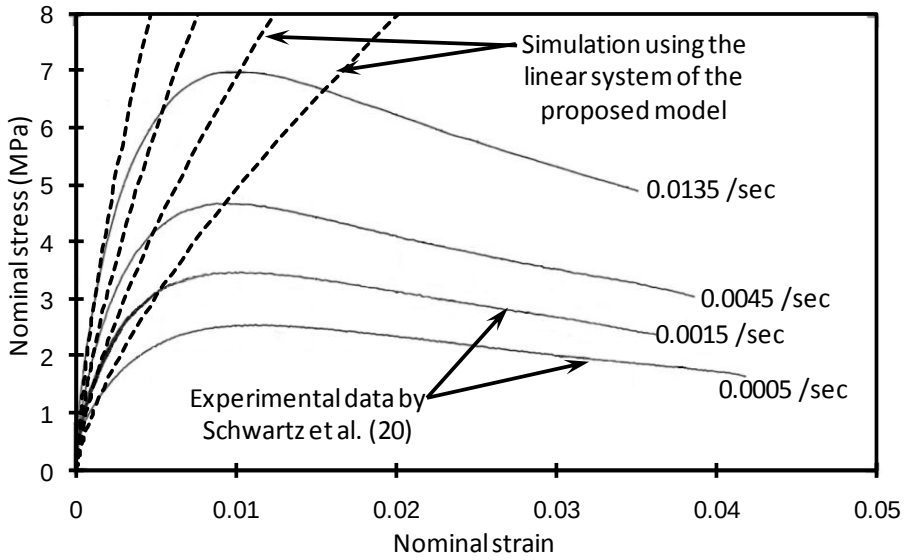

Fig. 3.19 MPL function calibration of the linear system: comparison to constant strain rate tests at 25°C, compression, conducted by Schwartz et al. (2002)

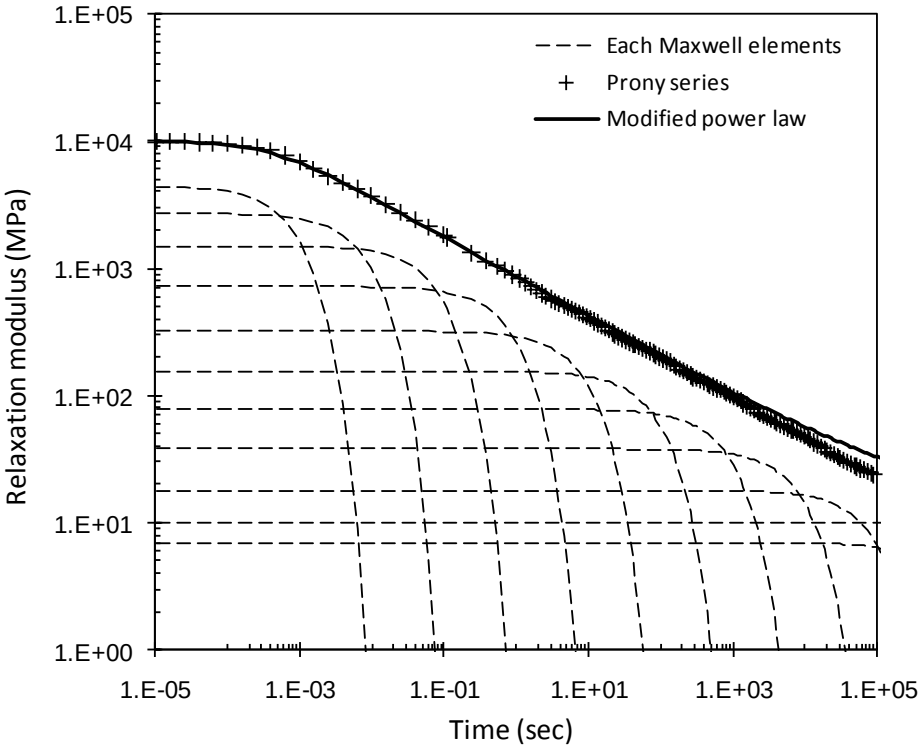

Fig. 3.20 Conversion of the relaxation function from MPL to Prony series: for the asphalt concrete in compression tested by Schwartz et al. (2002)

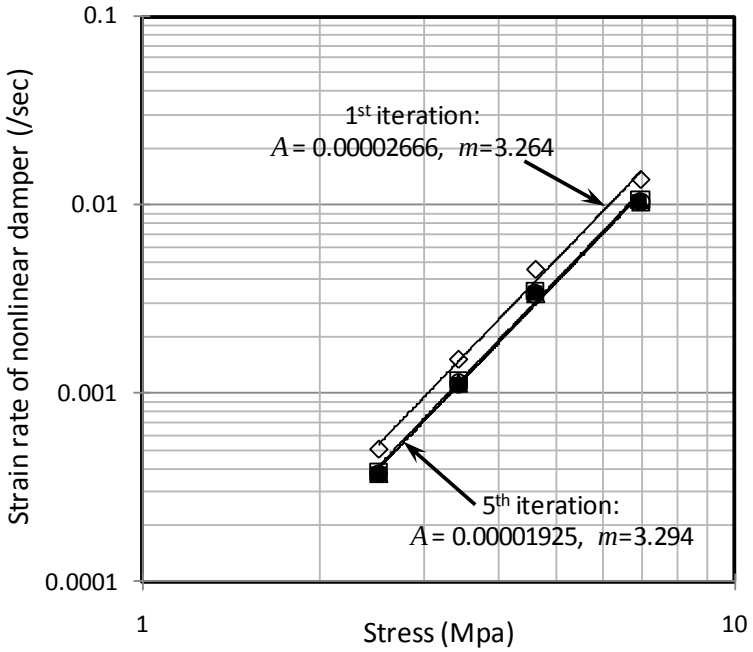

Fig. 3.21 Iteration for nonlinear system calibration: using constant strain rate tests at 25°C, compression, conducted by Schwartz et al. (2002)

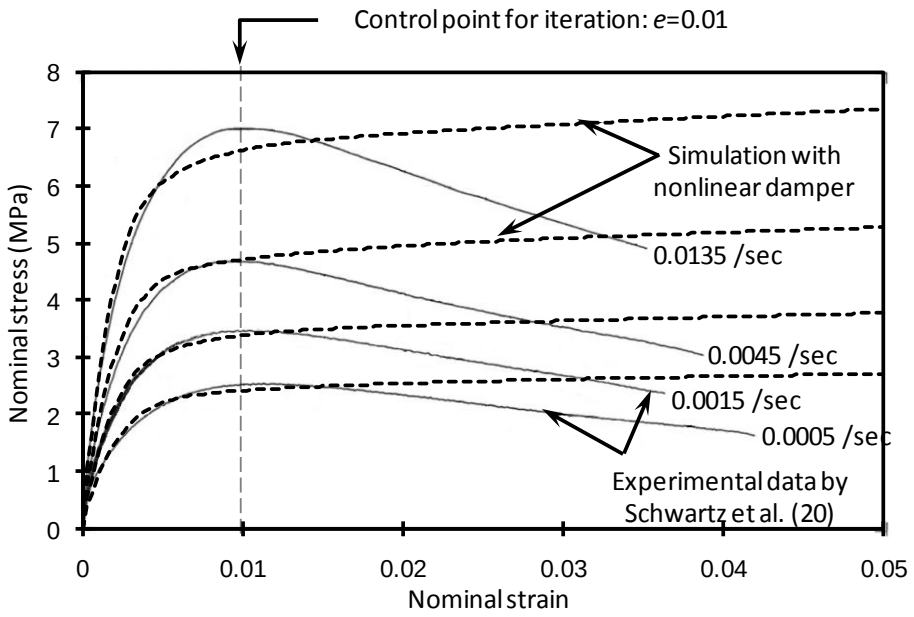

Fig. 3.22 Nonlinear system calibration, after 5th iteration: comparison to constant strain rate tests at 25°C, compression, conducted by Schwartz et al. (2002)

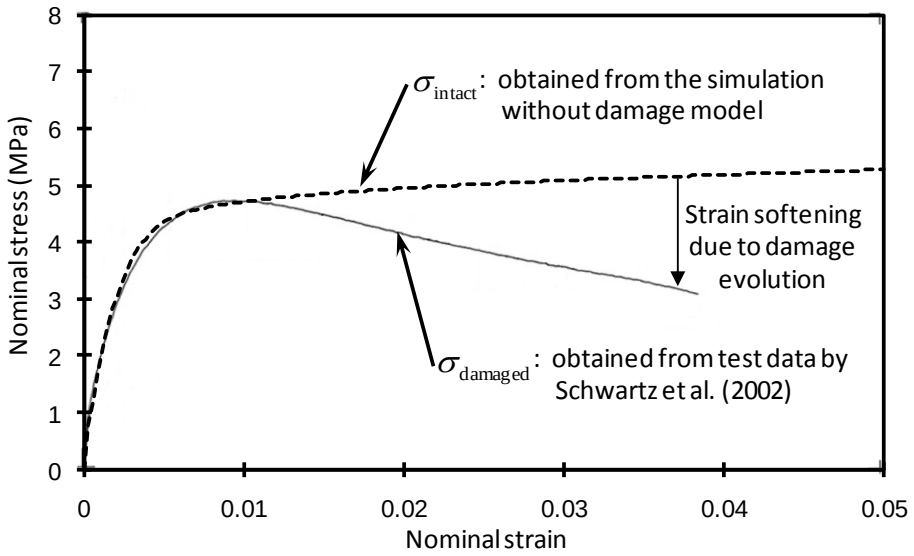

Fig. 3.23 Softening behavior of asphalt concrete: constant strain rate test, compression, $\dot{e}$ =0.0045 at 25°C, conducted by Schwartz et al. (2002)

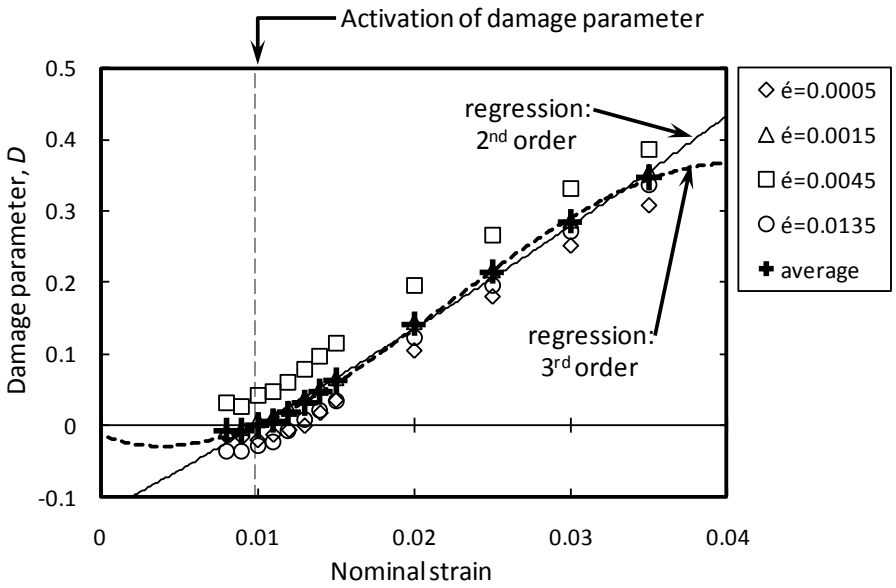

Fig. 3.24 Calibration of damage parameters for asphalt concrete: using constant strain rate test at 25°C, compression, conducted by Schwartz et al. (2002)

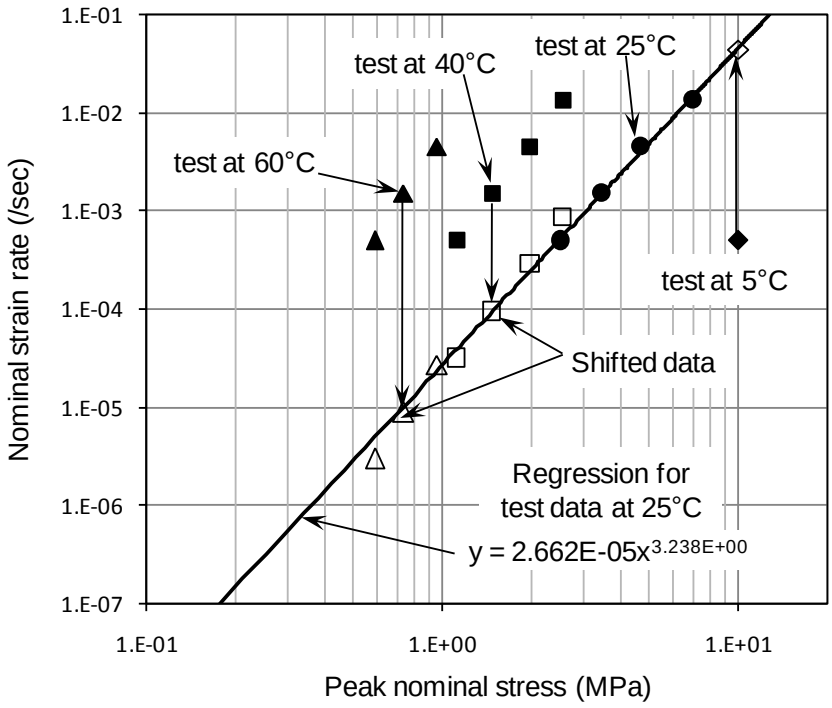

Fig. 3.25 Calibration of the temperature shift factor: using constant strain rate tests conducted by Schwartz et al. (2002)

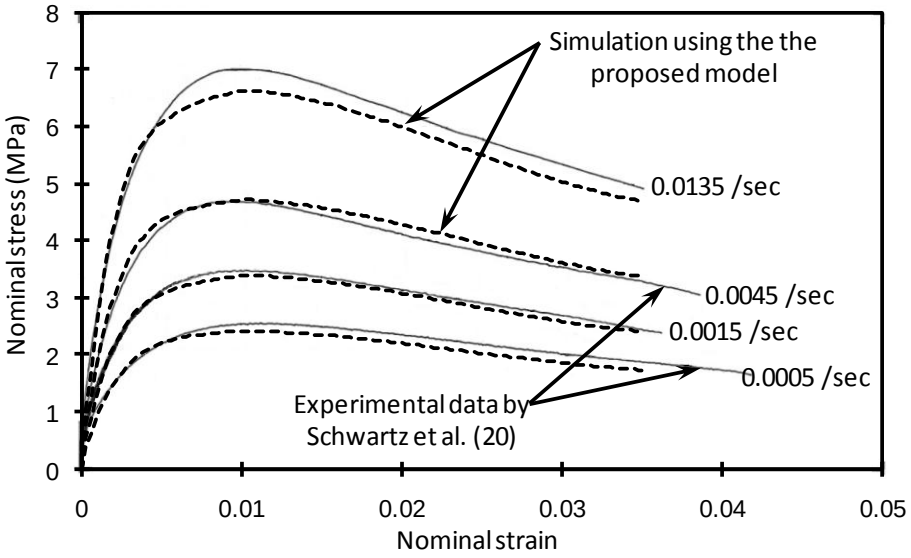

Fig. 3.26 Simulation after damage parameter calibration: comparison to constant strain rate tests at 25°C, compression, conducted by Schwartz et al. (2002)

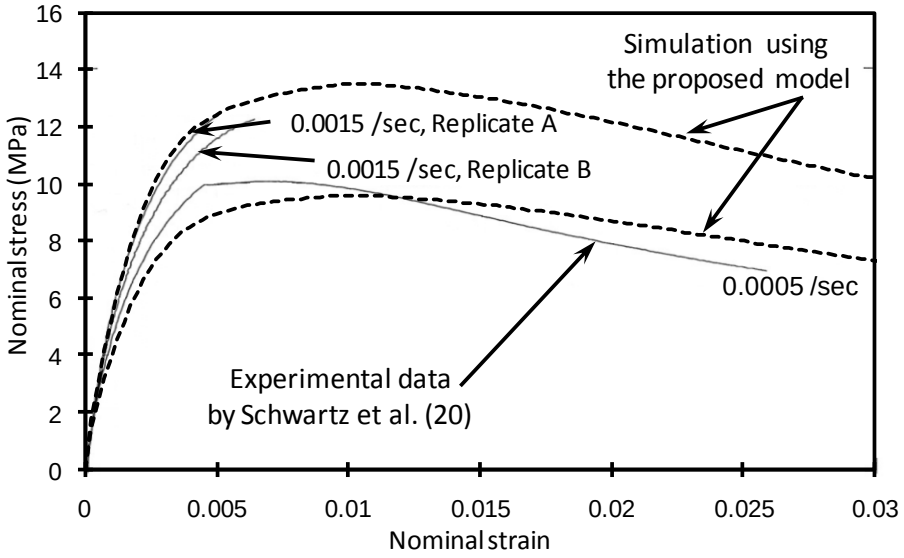

Fig. 3.27 Simulation of constant strain rate tests at 5°C, compression, conducted by Schwartz et al. (2002)

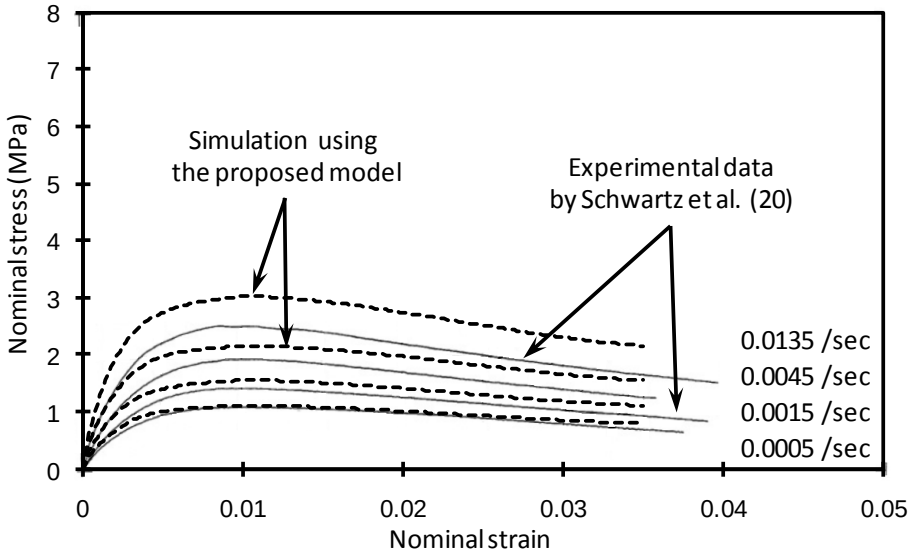

Fig. 3.28 Simulation of constant strain rate tests at 40°C, compression, conducted by Schwartz et al. (2002)

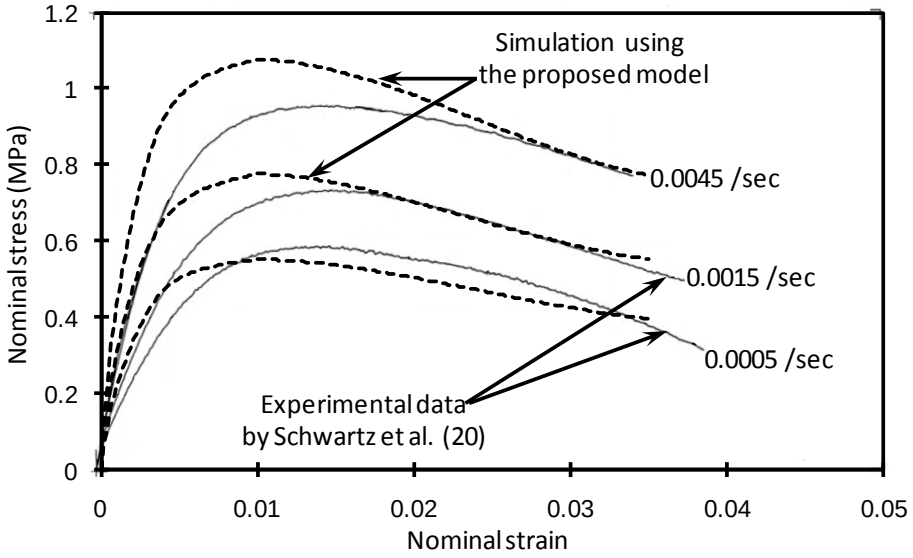

Fig. 3.29 Simulation of constant strain rate tests at 60°C, compression, conducted by Schwartz et al. (2002)

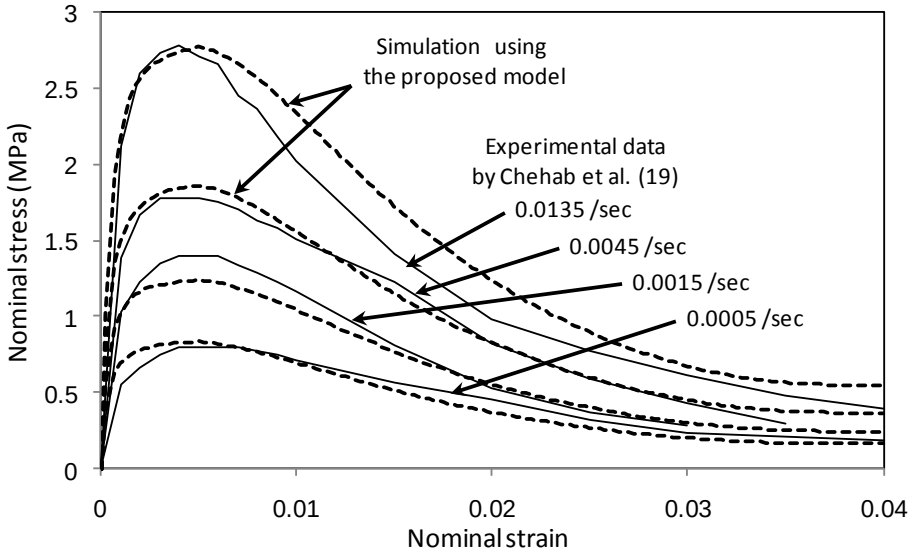

Fig. 3.30 Simulation of constant strain rate tests at 25°C, tension, conducted by Chehab et al. (2002)

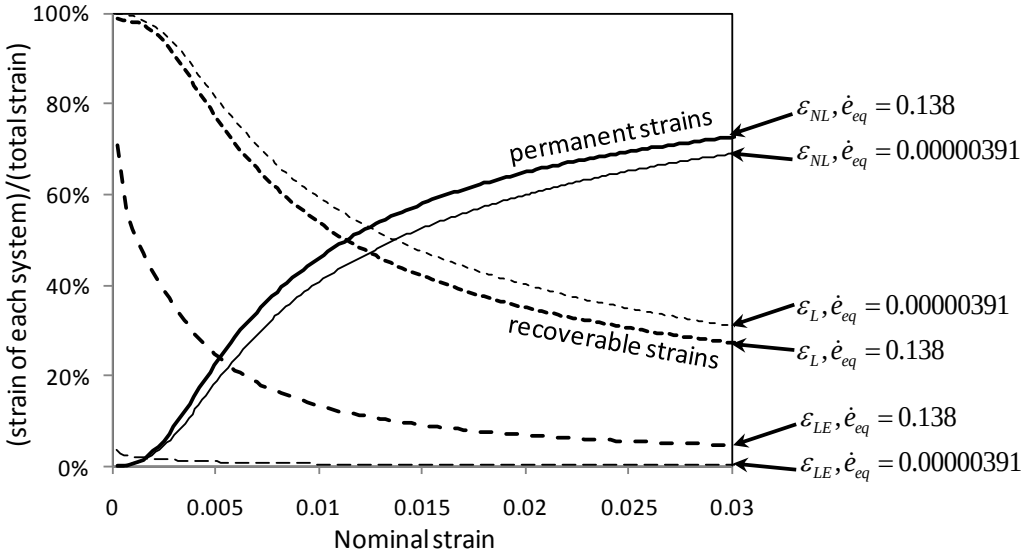

Fig. 3.31 Contribution of nonlinear and linear systems during constant strain rate deformation in compression: $\dot{e}_{eq}$ =0.00000391 is the equivalent strain rate at 25ºC to $\dot{e}$ =0.0005 /s at 60ºC and $\dot{e}_{eq}$ =0.138 is $\dot{e}$ =0.0135 /s at 5ºC

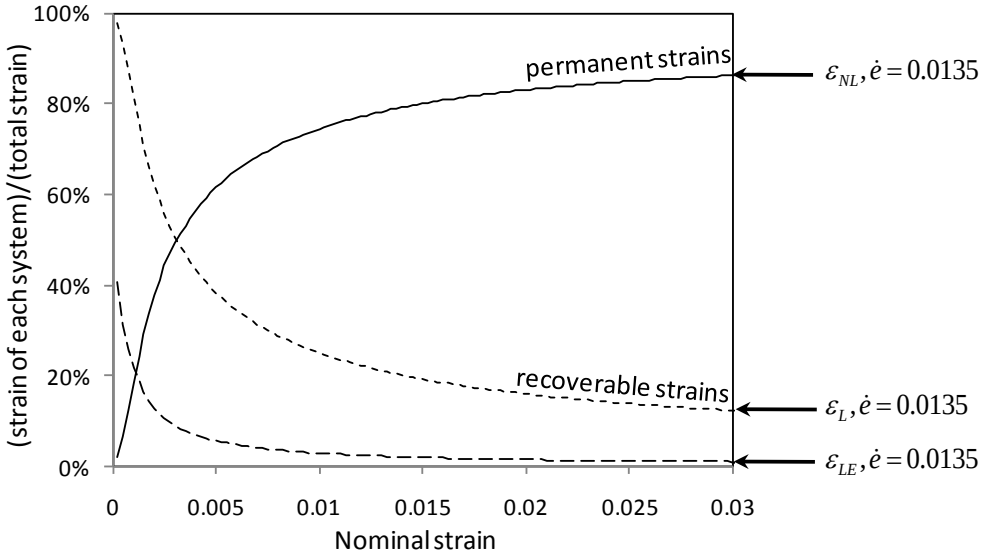

Fig. 3.32 Contribution of nonlinear and linear systems during constant strain rate deformation in tension: $\dot{e}$ =0.0135 /s at 25ºC

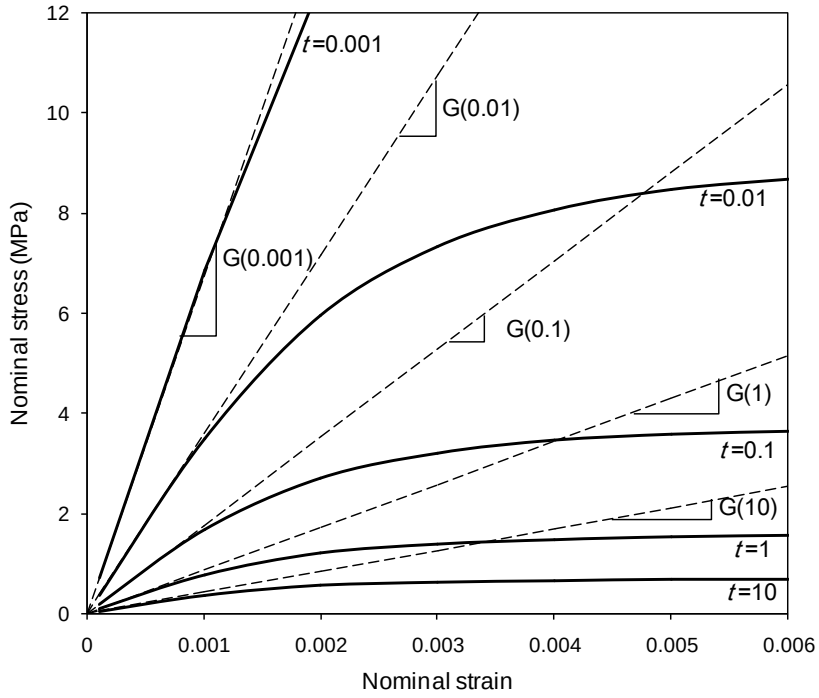

Fig. 3.33 Stress relaxation isochrone obtained from the proposed model

REFERENCES

Airey, G. D., Rahimzadeh, B., and Collop, A. C. (2003). “Viscoelastic linearity limits for bituminous materials.” *Materials and Structures*, 36, 643-647.

Bergstrom, J. S. and Boyce, M. C. (1998). “Constitutive modeling of the large strain time-dependent behavior of elastomers.” *J. Mech. Phys. Solids*, 46(5), 931-954.

Bergstrom, J. S. and Boyce, M. C. (2000). “Large strain time-dependent behavior of filled elastomers.” *Mechanics of Materials*, 32, 627-644.

Boyce, M. C., Weber, G. G., and Parks, D. M. (1989). “On the kinematics of finite strain plasticity.” *J. Mech. Phys. Solids*, 37(5), 647-665.

Chehab, G. R., Kim, Y. R., Schapery, R. A., Witczak, M. W., and Bonaquist, R. (2002). “Time-temperature superposition principle for asphalt concrete with growing damage in tension state.” *Proc. of Assoc. of Asphalt Paving Technologists*, 71, 559-593.

Cheung, C. Y., and Cebon, D. (1997a). “Deformation mechanisms of pure bitumen.” *J. Mater. Civ. Eng*., 9(3), 117-129.

Cheung, C. Y., and Cebon, D. (1997b). “Experimental study of pure bitumens in tension, compression, and shear.” *J. Rheol*., 41(1), 45-73.

Desai, C. S. (2001). *Mechanics of Materials and Interfaces: The Disturbed State Concept*, CRC Press, Boca Raton, Fl.

Dickinson, E. J., Witt, H. P., (1974). "The dynamic shear modulus of paving asphalts as a function of frequency." *Transactions of the Society of Rheology*, 18 (4), 591–606.

Dobson, G. R. (1969). "The dynamic mechanical properties of bitumen." *Proc. of Assoc. of Asphalt Paving Technologists*, 38, 123–139.

Ferry, J. D. (1950). “Mechanical properties of substance of high molecular weight; VI. Dispersion in concentrated polymer solutions and its dependence on temperature and concentration.” *Journal of the American Chemical Society*, 72(8), 3746-3752.

Findley, W. N., Lai, J. S., and Onaran K. (1976). *Creep and relaxation of nonlinear viscoelastic materials*, North-Holland Publishing Company, Amsterdam.

Gibson, N. H., Schwartz, C. W., Schapery, R. A., and Witczak, M. W. (2003). “Viscoelastic, viscoplastic, and damage modeling of asphalt concrete in unconfined compression.” *Transportation Research Record*, 1860, 3-15.

Goodrich, J. L. (1991). “Asphalt binder rheology, asphalt concrete rheology and asphalt concrete mix properties.” *Asphalt Paving Technology: Association of Asphalt Paving Technologists-Proceedings of the Technical Sessions*, 60, 80-120.

Harvey, J. A. F., and Cebon, D. (2003). "Failure mechanisms in viscoelastic films." *Journal of Materials Science*, 38, 1021-1032.

Jongepier, R., and Kuilman, B. (1969). "Characteristics of the rheology of bitumens." *Proc. of Assoc. of Asphalt Paving Technologists*, 38, 98–122.

Kim, Y. R., and Lee, Y. C. (1995). "Interrelationships among stiffnesses of asphalt aggregate mixtures." *Asphalt Paving Technology: Association of Asphalt Paving Technologists-Proceedings of the Technical Sessions*, 64, 575-609.

Kim, Y. R., Lee, Y. C., and Lee, H. J. (1995). "Correspondence principle for characterization of asphalt concrete." *Journal of Materials in Civil Engineering*, 7(1), 59-68.

Kim, Y. R. and Little, D. N. (1989). "Evaluation of healing in asphalt concrete by means of the theory of nonlinear viscoelasticity." *Transportation Research Record*, 1228, 198-210.

Kim, Y. R., and Little, D. N. (1990). "One-dimensional constitutive modeling of asphalt concrete." *Journal of Engineering Mechanics*, 116(4), 751-772.

Krishnan, J. M., and Rajagopal, K. R. (2003). "Review of the uses and modeling of bitumen from ancient to modern times." *Appl. Mech. Rev.*, 56(2), 149-214.

Krishnan, J. M., and Rajagopal, K. R. (2005). "On the mechanical behavior of asphalt." *Mechanics of Materials*, 37, 1085-1100.

Krishnan, J. M., Rajagopal, K. R., Masad, E., and Little, D. N. (2006). "Thermomechanical framework for the constitutive modeling of asphalt concrete." *International Journal of Geomechanics*, 6(1), 36-45.

Leadermann, H. (1943). *Elastic and Creep Properties of Filamentous Materials and Other High Polymers*, Textile Foundation, Washington, D. C.

Lemaitre, J. (1984). "How to use damage mechanics." *Nuclear Engineering and Design*, 80, 223-245.

Lethersich, W. (1942). "The mechanical behavior of bitumen." *Journal of the Society of Chemical Industry*, 61, 101–108.

Lion, A. (2000). "Constitutive modeling in finite thermoviscoplasticity: a physical approach based on nonlinear rheological models." *International Journal of Plasticity*, 16, 469-494.

Masad, E., Somadevan, N., Bahia, H. U., and Kose, S. (2001). "Modeling and experimental measurements of strain distribution in asphalt mixes." *Journal of Transportation Engineering*, 127(6), 477-485.

Masad, E., and Somadevan, N. (2002). "Microstructural finite-element analysis of

influence of localized strain distribution on asphalt mix properties." *Journal of Engineering Mechanics*, 128(10), 1105-1114.

Mathes, K. N. (1991). "A brief history of development in electrical insulation." *Proc. of IEEE 20th Electrical Electronics Insulation Conf.*, Boston, 147-150.Neifar, M., and Di Benedetto, H. (2001). "Thermo-viscoplastic law for bituminous mixes." *International Journal Road Materials and Pavement Design*, 2(1), 71-95.

Miehe, C., and Keck, J. (2000). "Superimposed finite elastic-viscoelastic-plastoelastic stress response with damage in filled rubbery polymers. Experiments, modeling and algorithmic implementation." *Journal of the Mechanics and Physics of Solids*, 48, 323-365.

Morrison, F. A. (2001). *Understanding Rheology*, Oxford University Press, New York, NY.

Neifar, M. and Di Benedetto, H. (2001). "Thermo-viscoplastic law for bituminous mixes." *International Journal Road Materials and Pavement Design*, 2(1), 71-95.

Park, S. W., and Kim, Y. R. (2001). "Fitting Prony-series viscoelastic models with power-law presmoothing." *Journal of Materials in Civil Engineering*, 13(1), 26-32.

Park, S. W., and Schapery, R. A. (1999). "Methods of interconversion between linear viscoelastic material functions. Part I – a numerical method based on Prony series." *International Journal of Solids and Structures*, 36, 1653-1675.

Read, J., and Whiteoak, D. (2003). *The Shell Bitumen Handbook-5th ed*., Thomas Telford Publishing, London, U.K.

Reese, S., and Govindjee, S. (1998). "A theory of finite viscoelasticity and numerical aspects." *Int. J. Solids Structures*, 35(26-27), 3455-3482.

Schwartz, C. W., Gibson, N. H., and Schapery, R. A. (2002). "Time-temperature superposition for asphalt concrete at large compressive strains." *Transportation Research Record*, 1789, 101-112.

Stastna, J., Zanzotto, L., and Berti, J. (1997). "How good are some rheological models of dynamic material functions of asphalt." *Proc. of Assoc. of Asphalt Paving Technologists*, 66, 458–485.

Van der Poel, C. (1954). "A general system describing the visco-elastic properties of bitumens and its relation to routine test data", *J. Appl. Chem*., 4, 221–236.

Weber, G. G., Lush, A. M., Zavaliangos, A., and Anand, L. (1990). "An objective time-integration procedure for isotropic rate-independent and rate-dependent elastic-plastic constitutive equations." *International Journal of Plasticity*, 6, 701-744.

Williams, M. L. (1964). "Structural analysis of viscoelastic materials." *AIAA Journal*, 2(5), 785-808.

Wineman, A. S., and Rajagopal, K. R. (2000). *Mechanical Response of Polymers: An Introduction*, Cambridge University Press, Cambridge, UK.

CHAPTER 4
PULL-OUT BEHAVIOR OF STRAIGHT STEEL FIBER FROM ASPHALT

The interaction between a straight steel fiber and the surrounding asphalt matrix is investigated through single fiber pull-out tests and numerical simulations. Based on experimental observations from 241 pull-out tests that covered various temperatures, displacement rates, and fiber dimensions, pull-out failure modes are classified into three types: matrix, interface, and mixed failure modes. It is hypothesized from the experimental data that there is a critical shear stress beyond which interfacial debonding will occur. Detailed finite element analyses employing a nonlinear viscoelastic constitutive model for asphalt are carried out to explain the observed test results. The numerical simulations show that the stress distribution along the fiber surface varies substantially with temperature and fiber dimensions. At colder temperatures, the concentration of interfacial shear stress causes a decrease in the peak pull-out force. The simulations also showed that this stress concentration reduces as the contribution of viscous behavior becomes more significant and as the fiber length becomes shorter. The simulation model clarifies apparently conflicting experimental trends and confirms the hypothesis of a critical shear stress for interfacial debonding that is independent of temperature, loading rate, and fiber dimensions.

4.1 INTRODUCTION

As discussed in the literature review (Chapter 2), fiber reinforced asphalt concrete (FRAC) has various potentials for improving mechanical performances and imparting electrical conductivity that is necessary for enabling multifunctional applications. Experimental investigation about the reinforcing effect of steel fibers (presented in Chapter 5) shows that the use of fibers as reinforcement is very promising, but that proper optimization of the composite is necessary to maximize the benefits of adding fibers.

Such optimization can only be reached if a thorough understanding of fiber interaction with the matrix is achieved, which is the purpose of this chapter.

The objective of this study is to employ experimental and computational methods to develop a fundamental understanding of the interaction between a single fiber and binder. Specifically, the goal of the study is to investigate: 1) the characteristics of interfacial bond between a steel fiber and asphalt binder, and 2) the effects on the interfacial behavior of various factors including temperature, loading rate, and fiber dimensions. Focusing on straight steel fibers, a set of single fiber pull-out tests from asphalt binder were conducted under various test conditions to obtain the pullout stress versus displacement relationship. In addition, nonlinear viscoelastic finite element analyses were carried out to investigate the interfacial stress distribution that occurs under various test conditions.

The use of discontinuous fiber reinforcement has been actively studied and applied to cement composites; see, for example, Naaman (2000) and Kim et al. (2009). In general, the postcracking behavior of fiber-reinforced composites is known to be governed by the characteristics of interfacial bond between the fiber and matrix (Naaman et al. 1991a and Kim et al. 2008). Fig. 4.1 is a photo showing the fractured surface of FRAC after an indirect tension test. The clean surface of the fibers implies that the fibers were pulled-out during the failure process, and that correspondingly, interfacial debonding is one of the key factors controlling behavior.

A bond-slip model based on the relationship between shear stress at the fiber-matrix interface and slip, defined as the relative displacement between the fiber surface and surrounding matrix, has been commonly used for describing the interfacial bond characteristics of the fiber matrix system in cementitious composites (Naaman et al. 1991a). However, the concept of a bond-slip model as used for cementitious composites cannot be generally extrapolated to FRAC because the matrix may remain attached to the fiber or part of it, as discussed later on. Therefore, the use of pullout force or stress versus displacement is a more apt way for describing the interfacial characteristics of the fiber-asphalt interaction.

To date, the only fiber pull-out tests from asphalt binder were conducted by Lee et al. (2005) to determine the critical embedded length of Nylon fibers. However, Lee et al.

(2005) did not use the tests to investigate fiber-matrix interfacial response. To the best of the authors' knowledge, the study described herein is the first to investigate the interfacial characteristics between a steel fiber and a viscoelastic asphalt matrix. The pull-out load versus displacement responses and the stress distribution at the interface provide fundamental and unique insight into the fiber reinforcing mechanisms that occur within a temperature dependent viscoelastic matrix.

4.2 SINGLE FIBER PULL-OUT TEST

4.2.1 Test Setup and Scope

The parameters for the pull-out experiments are summarized in Table 4.1, which shows that the key variables are: temperature (T), pull-out displacement rate ($\dot{\Delta}$), fiber diameter (D) and embedded depth of fiber (L_{em}). Each test is repeated at least three times for each test condition. Therefore, a total of 241 pull-out tests were conducted for this study. The stiffness, shape, and surface roughness of the fiber can play an important role, but are not included in this study because the main focus is on the behavior of the interface between a smooth steel fiber and the matrix. Since the matrix is pure asphalt, the effect of aggregate is also not considered in this study. The presence of aggregates considerably complicates the tests and analysis of the resulting data and is therefore left for future study once the fundamental interaction mechanisms between fiber and pure asphalt matrix are clarified.

(1) Materials and Specimen Preparation

PG 64-22 asphalt binder, compliant with ASTM D 6373, was used as a matrix for the pull-out tests. To prepare a pull-out specimen, the asphalt binder was heated for two hours in a lab oven at 150°C. It was then poured into a tin can with a diameter of 100 mm and a height of 40 mm. To ensure uniform temperature, the tin can with asphalt is placed back in the oven for an hour. The steel fibers were obtained by cutting them from steel wires with circular cross section and smooth surface. The fiber surface was cleaned using ethanol. The cleaned fiber was gripped by a wooden clip with the desired embedded length exposed and dipped into the hot asphalt at the center of the tin can. The wooden

clip was held in place to prevent the fiber from sinking into the hot asphalt. The specimen was left to cool down to room temperature then conditioned to the desired temperatures for a minimum of eight hours in a refrigerator. Throughout specimen preparation, the asphalt temperature was monitored using a thermocouple embedded in the specimen as shown in Fig. 4.2a.

(2) Test Setup and Procedure

Fig. 4.2 illustrates the schematic test setup and a photo of the pull-out test. The top end of the fiber is held by a specially designed fiber grip while the tin can filled with asphalt is restrained by a cylindrical grip designed to engage the tin can. The free length of the fiber between the grip and the matrix is kept to a minimum to ensure that fiber elongation in this area did not influence the results.

A closed loop servo-hydraulic material test system (MTS 810) with a maximum force capacity of 100 kN was used to apply constant rate displacement. Since the capacity of the built-in load cell is too large for the pull-out test, a supplementary load cell having a maximum capacity of 450 N was installed to measure the pull-out force. In the first few tests, pull-out displacement was measured at the bottom of the fiber grip using an external displacement transducer with 10 mm capacity, and compared with the displacement measured from the linear variable differential transducer (LVDT) built-into the test system. The difference between the displacements from the external transducer and the built-in LVDT turned out to be negligible and so the built-in LVDT was employed in the remaining tests to minimize specimen installation time.

The specimens were taken out of the conditioning refrigerator and tested immediately. An environmental chamber was not used in this study. The temperature of the specimen was monitored and recorded during the test. A displacement controlled load was applied with the designated constant displacement rate and the test was continued until the fiber was totally pulled out. The measured pull-out force and displacement were recorded by a data acquisition system. Precise control of the embedded depth during the specimen preparation is difficult because of thermal shrinkage of asphalt during cooling. Therefore, the location of the matrix surface was marked by painting the exposed part of the fiber just before the test, and the actual embedded depth could thus be easily identified and

measured after the test.

(3) Coordinate System and Parameters for the Analysis

Since the pull-out force depends on fiber dimensions, including diameter and length, it needs to be normalized. Fig. 4.3 shows the axisymmetric coordinate system employed and the stress components for the single fiber pull-out experiment. In the axisymmetric pull-out configuration, σ_{rz} is the major stress component around the fiber, which can be assumed not to vary with θ. If we denote the shear stress at the fiber-matrix interface (where $r = D/2$) as τ, τ will be a function of time, t, and depth, z, as shown in Eq. (4.1).

$$\tau(z,t) = \sigma_{rz}(D/2\,,\theta,z,t\,) \tag{4.1}$$

From equilibrium in the axisymmetric loading condition, the relationship between the pull-out force, P, and the interfacial shear stress, τ, can be expressed by Eq. (4.2).

$$P = \int_0^{L_{em}} \int_0^{2\pi} \tau\, r\, d\theta\, dz = \int_0^{L_{em}} \pi D \tau dz \tag{4.2}$$

where, L_{em} is the embedded depth of the fiber.

In general, the magnitude of τ is known to vary with z, but direct experimental determination of $\tau(z)$ has not yet been possible (Naaman et al. 1991b). However, the relationship between pull-out force, P, and end displacement, Δ, can be conveniently obtained from the pull-out test. When the distribution of τ along with z is not known, the nominal average shear stress at the interface is useful for the purpose of normalization. The average shear stress at the interface, τ_N, is defined as Eq. (4.3).

$$\tau_N = \frac{P}{\pi D L_{em}} = \frac{P}{\psi} \tag{4.3}$$

where, ψ is the surface area of the embedded part of the fiber. Although τ can differ from τ_N when τ varies with z, τ_N is considered to be a normalized indicator of the pull-out force for a given set of fiber dimensions. In analyzing the displacement controlled pull-out test data, the parameters of interest are the maximum pull-out force, $P_{\max}$, which is the peak force in the $P-\Delta$ graph, corresponding average shear stress at the interface, $\tau_{N-\max}$, and pull-out displacement $\Delta_{\max}$. The distribution of τ along z within the viscoelastic asphalt matrix and its effects are investigated later in this study through finite element analysis.

4.2.2 Test Results and Discussion

(1) Observed Failure Modes

The most conspicuous phenomenon observed in the pull-out tests is the variation of pull-out failure modes with temperature and displacement rate. Based on differences in the pull-out force-displacement relationships and the amount of matrix still adhering to pulled-out fibers, pull-out modes are classified into three distinct categories: matrix failure (MatF), interface failure (IntF), and mixed failure (MixF). Fig. 4.4a-c display the representative pull-out force – displacement curves of these three failure modes, respectively.

In the MatF mode, the asphalt matrix around the fiber is pulled out along with the fiber and continues to gradually stretch until the pull-out displacement exceeds the embedded length of the fiber. As shown in Fig. 4.4a, the load-displacement response softens gradually after the peak load is reached. At the other extreme, the IntF mode entails a sudden debonding between the fiber and matrix as shown in Fig. 4.4b. In this case, the fiber pulls out (mostly cleanly) from the matrix. The load-displacement curve is characterized by an abrupt drop after the peak. While the drop is severe, a small residual pull-out capacity, attributed to frictional resistance between the debonded fiber and matrix, is maintained and degrades slowly to zero as the fiber continues to be pulled out. The MixF mode lies in between the two other modes (Fig. 4.4c). In this mode, part of the fiber pulls out cleanly, while remainder is still covered with matrix as in the MatF mode.

The MixF mode is observed only at 0°C with displacement rates ranging from 0.423 to 8.47 mm/sec. The MatF mode happens predominantly at slower pull out speeds while the IntF mode occurs more frequently at faster pull-out speeds at 0°C. When the temperature of the matrix is +20°C, all fibers are pulled-out with the MatF mode while the IntF is the only mode observed at -20°C. Since asphalt pavement is characterized by two major types of distress: rutting at high service temperature and cracking at low service temperature, the former will benefit from a better understanding of the MatF mode while the latter will benefit from understanding the IntF mode.

(2) Failure Mechanisms

Fig. 4.5 illustrates schematically the mechanisms of the MatF and IntF modes. Typical shear stress-strain curves of asphalt binder subjected to constant strain rates are displayed at the bottom of Fig. 4.5. Due to the viscoelastic nature of asphalt, the shear stress response is higher at relatively low temperature and high loading rate. Axisymmetric equilibrium of the pull-out configuration suggests that σ_{rz} along the *r*-axis should be proportional to 1/*r* as displayed in the middle of Fig. 4.5. Hence, the maximum shear stress always occurs at the interface. Since the shear stress varies with the *r*-axis, the shear strain rate also varies with *r*-axis. Correspondingly, the shear stress versus strain responses will be different at different r as displayed in the bottom graphs in Fig. 4.5. The distribution will also vary along the embedment length (*z*-axis). To explain the interface failure mode, a critical interfacial bond stress, τ_{cr}, at which the bond between the fiber and matrix fails, can be assumed as marked in the middle of Fig. 4.5.

Fig. 4.5a demonstrates the IntF mode. At relatively low temperature or high pull-out rate, the overall stress level is high. Eventually, the shear stress at the interface reaches τ_{cr}, and it is hypothesized that the interface will start to debond. The peak pull-out force, $P_{\max}$ is considered as the force when $\tau(z) = \tau_{cr}$ at a certain point along the fiber surface.

The MatF mode is shown in Fig. 4.5b. It is helpful to separate the viscoelastic matrix into two regions: a region of large deformation and another of small deformation. As shown in the shear stress-strain curves in Fig. 4.5b, the stress levels in this mode are too low to reach τ_{cr}. With the progress of fiber pull-out, the shear strain rate in the large deformation region will grow faster closer to the fiber while the shear strain rate in the small deformation region will rise modestly. At some point, when $P = P_{\max}$, the shear stress in the large deformation region reaches the peak stress in the stress – strain curve and softening behavior initiates. In this case, the total displacement becomes accommodated by the large deformation region, which is termed hereafter effective pull-out volume.

(3) Characteristics of the MatF Pull-Out Mode

The behavior of this failure mode is dominated by the viscoelastic nature of the asphalt binder. Therefore, it is expected that $P_{\max}$ increases with increase in pull-out speed ($\dot{\Delta}$) and decrease in specimen temperature (T). The $P-\Delta$ responses obtained from the experiments confirm this expectation. Fig. 4.6 shows the variation of the normalized pull-out force (shear stress) versus displacement ($\tau_N-\Delta$) curves with the applied displacement rate obtained at 20°C. Clearly, $\tau_{N-\max}$, calculated from $P_{\max}$, increases with pull-out speed ($\dot{\Delta}$).

Fig. 4.7 shows the variation of $P_{\max}$ and $\tau_{N-\max}$ with fiber diameter, D, observed in MatF mode. It shows that while $P_{\max}$ increases with the increase of D, $\tau_{N-\max}$ actually decreases. The reduction of $\tau_{N-\max}$ with increase in D suggests that the effective pull-out volume increases with increase in D, but its increment is not proportional to the increment in D.

Fig. 4.8 shows the variation of $P_{\max}$ and $\tau_{N-\max}$ with the embedded depth, L_{em}, for fibers with 0.3 mm diameter. As with D, $P_{\max}$ increases, but $\tau_{N-\max}$ decreases with increase in L_{em}. The decrease of $\tau_{N-\max}$ with increase of D and L_{em} for this failure mode suggests that thinner and shorter fibers carry more stress at high service temperature, and are therefore more beneficial for improving rutting resistance.

(4) Characteristics of the IntF Pull-Out Mode

Fig. 4.9 illustrates typical $\tau_N-\Delta$ curves of the IntF mode for different embedded depths obtained at -20°C. Since the ascending slopes, $d\tau_N/d\Delta$, of the curves in Fig. 4.9 are nearly constant till the peak, it is inferred that the effects of viscoelasticity are negligible and that the matrix is essentially behaving elastically at a temperature of -20°C. Another notable property is that $d\tau_N/d\Delta$ decreases with increase in fiber length, or more generally, with increase in the surface area of the fiber, ψ. This implies that shorter fibers carry more stress at the same deformation level than longer fibers. A third observation is that the pull-out displacement at the peak, $\Delta_{\max}$, increases with increase in fiber length. This means that shorter fibers debond at smaller deformations than longer fibers. After brittle debonding, the remaining frictional resistance is about 10% of $\tau_{N-\max}$ in all 4 cases. Given the rapid drop of τ_N and the small frictional resistance

available after $\tau_{N-\max}$ is exceeded, it is reasonable to hypothesize that brittle debonding will occur when a critical interfacial bond stress, τ_{cr}, is achieved anywhere along the embedded fiber length.

Although the stress distribution along the fiber-matrix interface is not known, the variation of $\tau_{N-\max}$ observed in the IntF mode provides insight for understanding τ_{cr}. Fig. 4.10 and 4.11 show the variation of $\tau_{N-\max}$ of the IntF mode with embedded surface area, ψ, at 0°C and -20°C, respectively. The data are grouped according to the applied displacement rate, and plotted separately. The fiber diameter is distinguished by different symbols in the figures. $\tau_{N-\max}$ plotted in Fig. 4.10 and 4.11 are obtained from specimens exhibiting IntF mode. At 0°C, at which the three modes are observed, the occurrence of the IntF mode increases as the increase in the applied displacement rate (Fig. 4.10). Comparing Fig. 4.10a – 4.10c, it is difficult to find any different trend due to the applied strain rate. The data in Fig. 4.11 show different pattern to that in Fig. 4.10, but there is no variation with the applied displacement rate. To compare $\tau_{N-\max}$ of the IntF mode at different applied strain rates, those are plotted on the same graph as shown in Fig. 4.12. As shown in Fig. 4.12a, $\tau_{N-\max}$ for the IntF mode at 0°C is nearly independent of the surface area, which implies that the single fiber pull-out force, $P_{\max}$, in IntF mode is proportional to the surface area of the fiber. In addition, any clear dependency on displacement rate is not evident. This implies that the existence of a constant τ_{cr} that is independent of time. The measured average $\tau_{N-\max}$ at 0°C is 6.9 MPa. On the other hand, as observed in Fig. 4.12b, $\tau_{N-\max}$ at -20°C shows clear dependency on the fiber surface area, reducing as the surface area increases, but not on displacement rate. The average $\tau_{N-\max}$ at -20°C (6.3 MPa) is close to that for 0°C. The different effect of fiber surface area at 0°C and -20°C is deemed to come from the different interfacial shear stress distributions, which occur due to the temperature and rate dependency of the binder viscosity. Since the actual shear stress distribution along the *z*-axis cannot be determined from the experiment, this issue will be discussed in the following section with the help of viscoelastic finite element analysis.

Although the test conditions were carefully controlled, large scatter in $\tau_{N-\max}$ occurs in the test results. As shown in Fig. 4.12, the scatter is higher at -20°C than at 0°C. This is attributed to the increase in brittleness that occurs in asphalt behavior as

temperature decreases. To verify this argument, $\tau_{N-\max}$ is plotted in Fig. 4.13 with respect to displacement rate, which influences the brittleness of asphalt like temperature does. Many investigators agree that asphalt is a thermologically simple material, and that the time-temperature superposition principle (Leadermann 1943; Ferry 1950) is applicable (Brodnyan et al. 1960; Cheung and Cebon 1997; Andriescu and Hesp 2009). The horizontal axis in Fig. 4.13 is the equivalent displacement rate at the reference temperature ($\dot{\Delta}_R$) using the temperature shift factor, as defined in the following section. Clearly, the scatter increases with increase in equivalent displacement rate, i.e. with increasing brittleness.

The test conditions, failure modes, peak pull-out force, and $\tau_{N-\max}$ for all pull-out tests conducted can be found in Table A.1 – A.9 in Appendix A.1.

4.3 NUMERICAL SIMULATION OF FIBER PULL-OUT

Finite element analysis is conducted to investigate and help explain some of the trends seen in the test data. Specifically, the objective of the simulation is to investigate why $\tau_{N-\max}$ appears to be independent of embedded surface area at 0°C, but dependent upon embedded surface area at -20°C.

4.3.1 Finite Element Modeling

The commercial finite element code, ABAQUS 6.7.1 is used for the numerical simulation. Since the configuration of the pull-out test is axisymmetric, a two-dimensional axisymmetric finite element model with eight node quadrilateral axisymmetric elements is developed as shown in Fig. 4.14. The key focus of this analysis is on the interfacial shear stress distribution around the fiber along the z-axis ($\tau(z)$), which is obtained along the dotted line in Fig. 4.14.

It is important to note that the obtained $\tau(z)$ are extrapolated from the integration points of adjacent elements. Also, while stress singularities do exist at the corners that occur at the bottom of the fiber ($z = 0$) and at the surface of the matrix ($z = L_{em}$), singular elements are not used in these locations because the objective of the analysis is to compare differences in stress distribution patterns rather than estimate exact stress

values. Moreover, to ensure consistency of the resultant stresses, the size of the element around the fiber is taken as 0.2×0.2 mm in all simulations.

(1) Nonlinear Viscoelastic Constitutive Model

A viscoelastic constitutive model with power-law based nonlinear viscosity is selected for the simulation. As illustrated in the part of Fig. 4.14, the selected two-layer visco-elasto-plastic model (SIMULIA 2007) consists of two parallel networks: an elastic-plastic network and an elastic-viscous network. The behavior of the first network is idealized as elastic-plastic with kinematic hardening, whereas the viscous damper in the second network is modeled using a power law in accord with Cheung and Cebon (1997).

The material parameters of the model are calibrated using experimental data in Cheung and Cebon (1997), as summarized in Table 4.2. Among the calibrated parameters in Table 4.2, the parameter f, defines the contribution of the elastic-viscous network to the total stiffness, and its value is calibrated to be 0.995. This means the elastic-plastic network carries 0.5% of the total stress. Considering that the average $\tau_{N-\max}$ measured from the tests is 6.9 MPa, the stress of the elastic-plastic network will not exceed σ_{p0} (=1.0 MPa) at which the plastic element is activated. Therefore, although the two-layer model includes a plastic element, it will behave as if it is a viscoelastic model with two springs and a power law damper.

Fig. 4.15 compares the direct tensile responses computed from the model to the test data for 50 pen bitumen obtained at 10°C by Cheung and Cebon (1997). The maximum stress levels and the plateau in the large deformation range are well simulated by the nonlinear viscous two-layer model, but the responses at small strain level do not match as well. It is known that the asphalt behavior in the small strain level is better simulated by a linear viscoelastic model with multiple relaxation times (Lethersich 1942; Stastna et al. 1997; Park and Kim 2001), although it cannot describe behavior in the large deformation range. The model selected is nevertheless considered adequate because of its ability to simulate behavior at large strains (the plateau in Fig. 4.15), which is of specific interest here. Further discussions about asphalt constitutive models and their limitations can be found in Cheung and Cebon (1997); Airey et al. (2003); Krishnan and Rajagopal (2005); and Park et al. (2010); (2011).

(2) Temperature Shift Factor

Since the parameters of the constitutive model are calibrated for the 50 pen bitumen tested by Cheung and Cebon (1997), the behavior of the finite element models has to be adjusted to fit the PG 64-22 asphalt used in the pull-out tests. The adjustment is made by changing the temperature shift factor. As was mentioned previously, the influence of temperature on the asphalt behavior can be translated into that of time through the time-temperature superposition principle. Cheung and Cebon (1997) showed that the temperature dependency of asphalt behavior in the large deformation range can be described by a temperature shift factor (a_T). According to the time-temperature superposition principle, the relationship between equivalent time at a reference temperature (t_R) and actual time (t) can be defined by Eq. (4.4).

$$t_R = \frac{t}{a_T} \tag{4.4}$$

To determine a_T, a series of pull-out simulations with various $\dot{\Delta}_R$ ranging from 0.0004 to 40,000 mm/sec were conducted as shown in Fig. 4.16. Note that the pull-out displacement rate in the simulation is denoted $\dot{\Delta}_R$ to distinguish it from the applied displacement rate in the experiment ($\dot{\Delta}$). Then, the simulated pull-out force versus displacement curves are matched to the closest ones obtained from the experiments. From these comparisons, the $\dot{\Delta}_R$ that best match the test data at three different temperatures are selected to represent behavior at those temperatures. The corresponding values of a_T are then computed and a best fit second order polynomial function relating Log a_T and temperature is calculated as shown in Fig. 4.17. While the test temperature of Cheung and Cebon (1997) is 10°C, the reference temperature of PG 64-22 asphalt is determined to be 2.4°C from the regression function, which implies that the behavior of 50 pen bitumen at 10°C is the same as the behavior of PG 64-22 asphalt at 2.4°C.

The stress distributions along the fiber surface are obtained from the three simulations that represent the test at three temperatures, as listed in Table 4.3. The parameters listed in the table indicate that, for instance, the simulation condition for $\dot{\Delta}_R$=120,000 mm/sec is equivalent to the test data corresponding to $\dot{\Delta}$=1.27 mm/sec at -20°C. Since the main focus of this simulation study is to explain the different behaviors of $\tau_{N-\max}$ in IntF mode at 0°C and -20°C (Fig. 4.12), the simulations for the tests at 0°C and -20°C are

important. Fig. 4.18 compares the simulated $P-\Delta$ responses to the test data at the temperatures of interest. While the calibration method for the material parameters used in this study is not a rigorous one, Fig. 4.18 shows that the model reasonably simulates pull-out behavior of at least two test conditions for which further analyses are conducted.

Parametric simulations at different pull-out speeds (Fig. 4.16) show that asphalt can be considered a linear elastic material when the applied displacement rate is sufficiently high (in this study, $\dot{\Delta}_R \geq$ 4,000 mm/sec). As shown in Fig. 4.18a, it is clear that the test data also shows nearly elastic behavior at -20°C. At 0°C (Fig. 4.18b), the contribution of viscous behavior becomes significant and the experimental pull-out force - displacement curves show plateaus around the peak pull-out force.

4.3.2 Stress Distribution at the Fiber-Asphalt Interface

Fig. 4.19 illustrates the interfacial shear stress ($\tau(z)$) distributions for the three test conditions in Table 4.3 along the path indicated in Fig. 4.14. Since the stress levels vary with temperature and applied displacement rate, the shear stress is normalized by the average shear stress (τ_N) in Fig. 4.20 to focus on the distribution pattern and not absolute values. The horizontal axis is the distance from the bottom of the embedded fiber along the dotted path in Fig. 4.14. The dimensions of the fiber for the analyses in Fig. 4.19 and 4.20 are L_{em} =10 mm and D =0.3 mm.

The pattern of interfacial shear stress distribution varies significantly with temperature. In the simulation for -20°C (Fig. 4.20a), stress concentrations appear at the matrix surface (10 mm) and the fiber bottom (0 mm) where corners are located. With increase in pull-out displacement (Δ), the degree of the stress concentration slightly reduces, but the overall distribution remains nearly unchanged. As was discussed in Fig. 4.18a, asphalt behavior is essentially elastic at -20°C and hence the distribution pattern shown in Fig. 4.20a is similar to that for concrete (Naaman et al. 1991a). On the other hand, the stress distributions for 0°C (Fig. 4.20b) vary significantly with increasing pull-out displacement, Δ. When Δ is small (Δ=0.1 mm in Fig. 4.20b), the stress distribution pattern is similar to that for elastic behavior (Fig. 4.20a). However, as the fiber pulls out farther, the intensity of the stress concentration reduces, and the stress distribution pattern becomes substantially flatter. Since the peaks of the pull-out force are observed to occur

around Δ≈0.4 mm in the experiments (see Fig. 4.18b), it is presumed that the stress distribution curve at the moment of interface debonding at 0°C will lie between the curves for Δ=0.3 and 0.5 mm shown in Fig. 4.20b.

The significant reduction in, and even elimination of, stress concentration in Fig. 4.20b and 20c is attributed to asphalt viscosity. As illustrated in Fig. 4.15, the stress response of asphalt subjected to a constant strain rate becomes constant (plateaus out) when the stress reaches a specific level corresponding to the applied strain rate. This implies that once the stress at the stress concentration point reaches the plateau, the deformation at that point will be accommodated by viscous flow without additional increase in stress, shifting stress demands to adjacent regions, much like elasto-plastic behavior. The stress distributions obtained from the simulation for the test at +20°C (Fig. 4.19c and 4.20c) support this argument. For this situation, the contribution of viscous flow is larger due to higher temperature, and the stress concentrations disappear earlier than in Fig. 4.20b.

If the hypothesis that there is a critical bond stress (τ_{cr}) is true, the computed differences between behavior at 0°C and -20°C explain why $\tau_{N-\max}$ is lower at -20°C than at 0°C, i.e. 6.3 MPa versus 6.9 MPa, respectively, as shown in Fig. 4.12. When viscous flow is dominant in accommodating deformation, the stress distribution along the interface is flat and close to the average stress (τ_N). On the other hand, as the temperature gets colder or the displacement rate is higher, the contribution of viscosity becomes lower (Fig. 4.5a and Fig. 4.18a), and correspondingly, the stress concentration around the interface will be more significant as the behavior approaches elastic response (Fig. 4.20a). In this case, interfacial debonding will be controlled by the degree of stress concentration. As a result of the higher stress concentration, $\tau_{N-\max}$ must decrease as observed experimentally.

As previously mentioned, the data in Fig. 4.12 suggests that the maximum pull-out force ($P_{\max}$) for the IntF mode, and in turn, the degree of stress concentration, is dependent on fiber dimensions only at -20°C. To investigate the effect of the fiber dimension, a set of finite element analyses for various embedded depths (L_{em}) and diameters (D) of fibers was conducted. Simulations with different fiber diameters (D) showed that the distribution is dependent only on the aspect ratio of the fiber (L_{em}/D)

and that τ_N is nearly proportional to $(1/\psi)$. Therefore, simulations for various embedded lengths (L_{em}=2~25 mm) with a fixed diameter (D=0.3 mm) were conducted.

Fig. 4.21a and 4.21b show the variation of stress distribution with L_{em} obtained from the simulations for -20°C and 0°C, respectively. The stress distributions are obtained when Δ=0.2 mm in Fig. 4.21a and Δ=0.4 mm in Fig. 4.21b, which correspond to the peak points in Fig. 4.18a and 4.18b, respectively, when L_{em}=10 mm. Fig. 4.21 shows that the overall stress level and stress at the matrix surface (τ_{surface}) decline with increase in L_{em}. This implies that for the same loading rate, the interfacial stress around a shorter fiber reaches τ_{cr} faster than for a longer fiber, and consequently, the pull-out displacement at interfacial debonding ($\Delta_{\max}$) of the shorter fiber will be smaller if τ_{cr} is constant as hypothesized. The differences between the $\tau_N - \Delta$ curves shown in Fig. 4.9, i.e. increase in $\Delta_{\max}$ and decrease in slope with increase in L_{em}, can be clearly explained by Fig. 4.21. Comparing Fig. 4.21a and 4.21b, at higher temperature, the variation in overall stress level are smaller, and as was discussed for Fig. 4.20b, the stress is less concentrated at both top and bottom of the embedded portion of the fiber.

To more clearly appreciate the degree of stress concentration, the average shear stress (τ_N), the shear stress at the matrix surface (τ_{surface}), and their ratio ($\tau_{\text{surface}}/\tau_N$) obtained from the simulations are plotted in Fig. 4.22. The relatively rapid increase of $\tau_{\text{surface}}/\tau_N$ with the increase of L_{em} in Fig. 4.22a explains the decrease of $\tau_{N-\max}$ in Fig. 4.12b. The high $\tau_{\text{surface}}/\tau_N$ implies high stress concentration at the matrix surface. If $\tau_{\text{surface}}/\tau_N$ is higher, τ_{surface} will reach the critical bond stress (τ_{cr}) at a lower average stress (τ_N). Therefore, the experimentally measured $\tau_{N-\max}$ (the maximum average interfacial stress at the moment of debonding, Fig. 4.12) decreases with the increase of $\tau_{\text{surface}}/\tau_N$, and further, with the increase of L_{em}. On the other hand, in Fig. 4.22b representing the tests at 0°C, the rise of $\tau_{\text{surface}}/\tau_N$ with L_{em} is slower than that in Fig. 4.22a. This implies that when the contribution of viscosity to deformation increases, $\tau_{N-\max}$ becomes less sensitive to L_{em} as observed experimentally. Therefore, the constant $\tau_{N-\max}$ shown in Fig. 4.12a is attributed to the effect of matrix viscosity.

While shedding light on the differences between the pull-out test data at 0°C and -20°C, the simulation results also provide evidence that the hypothesis of constant τ_{cr} is reasonable. An exact estimation of τ_{cr} is difficult because: 1) of the large scatter in the

experimentally measured $\tau_{N-\max}$, and 2) the stress computed at the surface is dependent upon mesh density. Nevertheless, the test data coupled with the simulation results appear to suggest that a reasonable τ_{cr} is closer to $\tau_{N-\max}$ measured at 0°C (6.9 MPa) than that at -20°C.

4.4 SUMMARY AND CONCLUSIONS

The pull-out behavior of straight steel fibers from an asphalt binder matrix is investigated through experiments and numerical simulations. The variables considered in this study were temperature, displacement rate, and fiber dimensions. Single fiber pull-out experiments showed that the mode of pull-out failure varies with temperature and loading rate. Based on the differences in the pull-out force versus displacement curves and the remaining asphalt on the pulled out fiber, the pull-out modes are categorized into matrix failure (MatF), mixed failure (MixF), and interface failure (IntF) modes. The MatF mode dominates behavior when viscosity is low (the binder is watery), i.e. high temperature and/or slow loading rate, and is not accompanied by any interfacial debonding. Hence, its pull-out behavior depends completely on the viscoelastic properties of the matrix. In contrast, the IntF involves clean debonding of the fiber-matrix interface and is associated with very high viscosity (the binder is thick), which occurs at low temperatures and/or fast loading rates.

Simulation studies using a constitutive model with nonlinear viscoelastic material behavior showed that when the contribution of viscous flow to total deformation is small due to cold temperature, the interfacial shear stress is concentrated at the top and bottom of the fiber's embedded length. The degree of stress concentration rises with the fiber length, but decreases when the contributions of localized viscous deformations start to increase. Based on the observed failure mechanisms and simulation information, it is hypothesized that there exists a critical interfacial bond stress (τ_{cr}) at which interfacial debonding occurs. Evidence is provided which suggests that τ_{cr} is a key factor controlling fiber pull-out from asphalt and that it is independent of temperature and loading rate. Combining the test data with the simulation results, a reasonable value for τ_{cr} for the asphalt used in this work is 6.9 MPa.

Table 4.1 Parameters for the pull-out tests

Test parameters		unit	Test conditions
Parameters affecting material properties of asphalt binder	Temperatures, T	°C	-20, 0, 20
	Displacement rate, $\dot{\Delta}$	mm/sec	0.0423, 0.423, 1.27, 8.47, 84.7
Parameters pertaining to fiber dimension	Diameter, D	mm	0.2, 0.3, 0.5, 0.7
	Embedded length, L_{em}	mm	4~25

Table 4.2 Parameters for the finite element analysis

Elastic parameters	E_{ins} = 70 MPa	ν = 0.4999		
Plastic parameters	σ_{p0} = 1 MPa	σ_{p1} = 1.2 MPa	ε_{p0} = 0	ε_{p1} = 1
Viscous parameters	A = 0.1635	n = 2.36	m = 0	f = 0.995

* The parameter naming scheme is same as in SIMULIA (2007)

Table 4.3 Equivalent parameters for the pull-out tests and simulation studies.

Test Conditions		Simulation	Temperature shift factor, a_T
Temperature, T (°C)	Displacement rates, $\dot{\Delta}$ (mm/sec)	Displacement rate, $\dot{\Delta}_R$ (mm/sec)	
20	1.27	0.0004	0.000315
0	1.27	4	3.15
-20	1.27	120,000	94,500

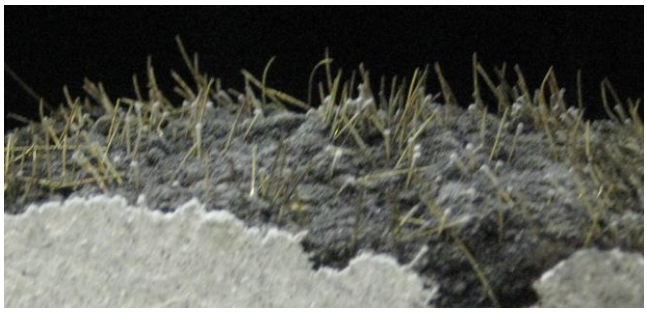

Fig. 4.1 Fractured section of FRAC after the indirect tension test.

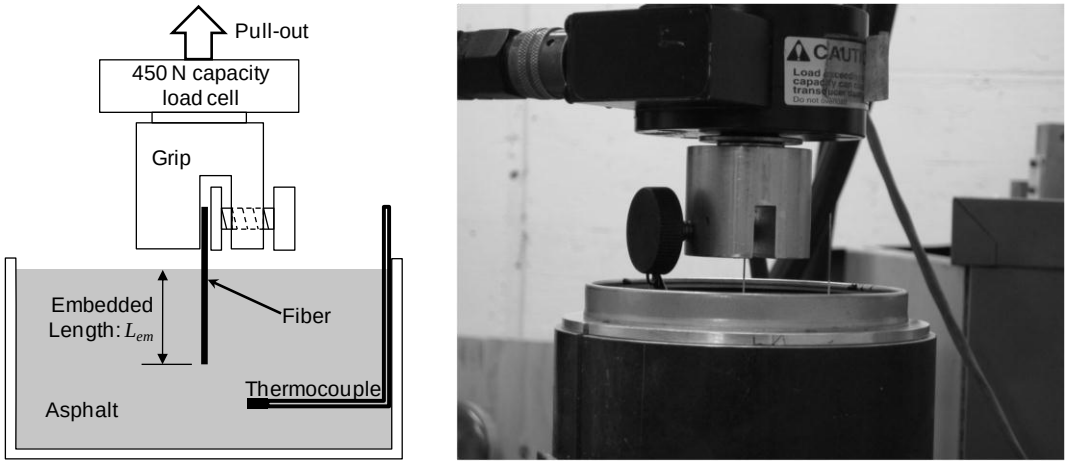

(a) schematic drawing (b) photo of the pull-out test

Fig. 4.2 Pull-out test set-up

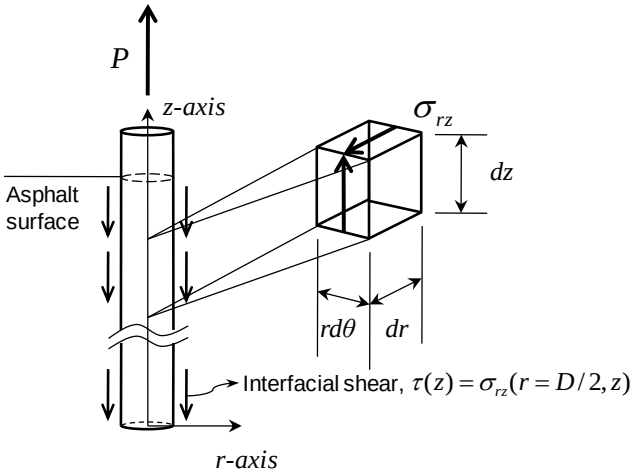

Fig. 4.3 Axisymmetric coordinate system and a stress component in the pull-out test

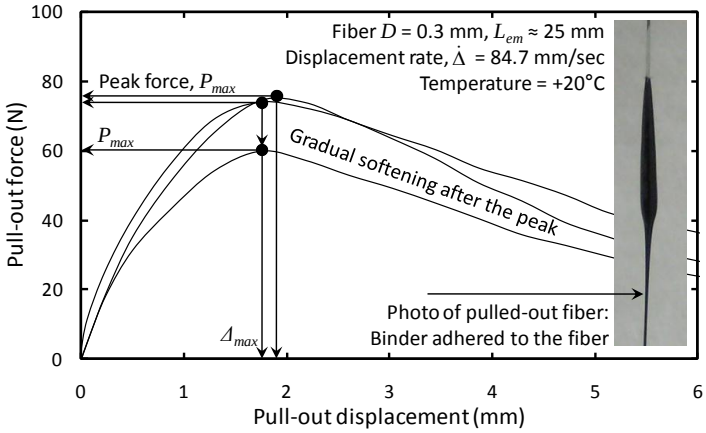

(a) MatF (matrix failure) mode

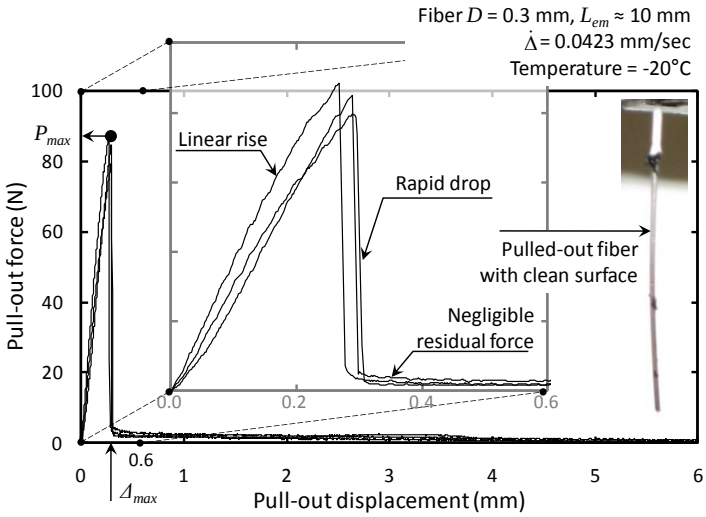

(b) IntF (interface failure) mode

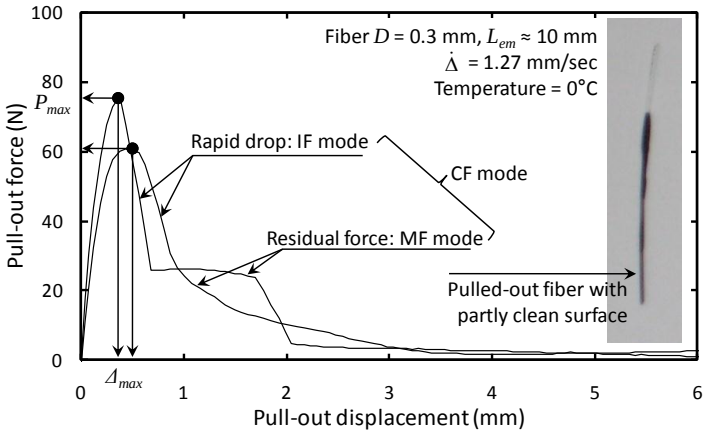

(c) MixF (mixed failure) mode

Fig. 4.4 Comparison of pull-out force – displacement curves of different failure modes.

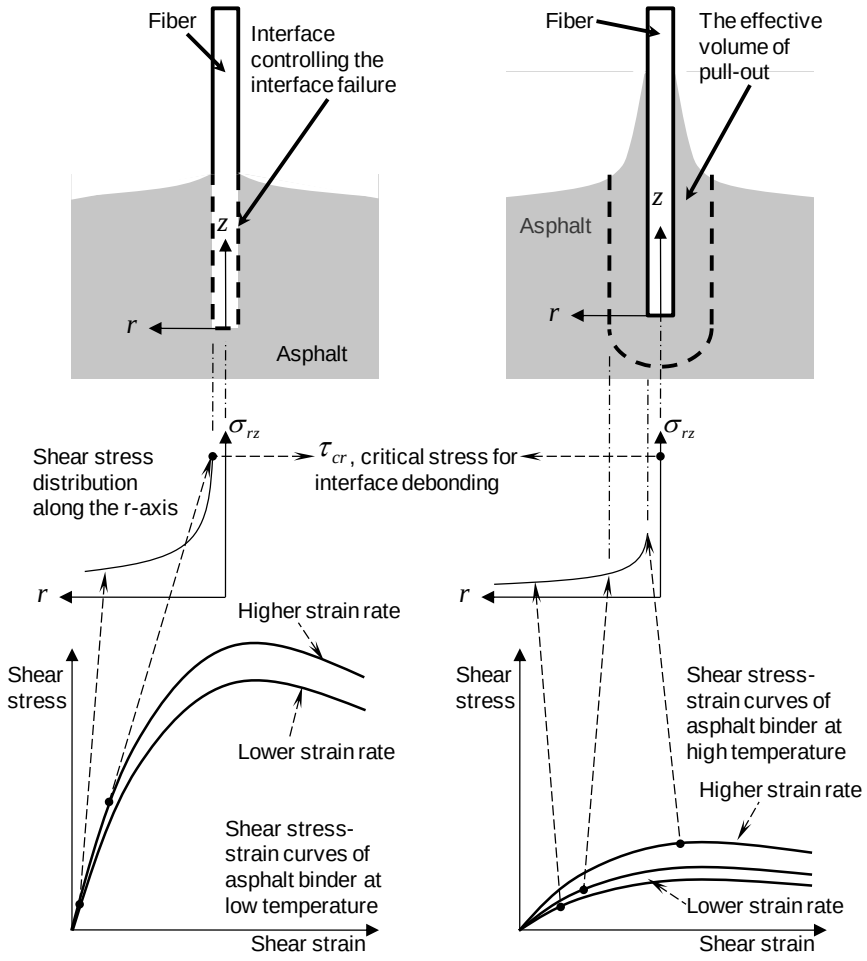

(a) interface failure mode (b) matrix failure mode

Fig. 4.5 The mechanism of single fiber pull-out behavior for the MatF and IntF modes.

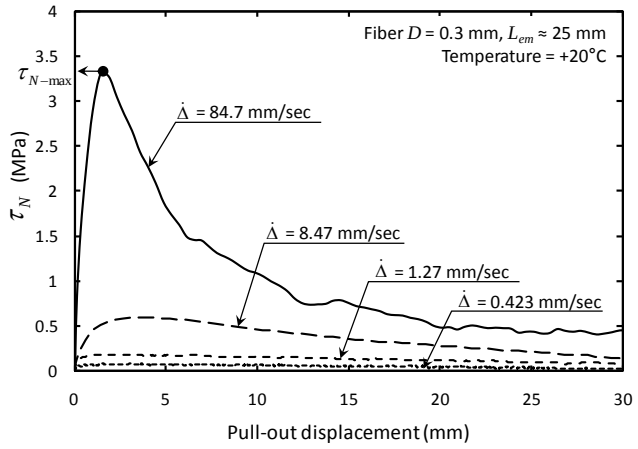

Fig. 4.6 Typical average shear stress – displacement ($\tau_N - \Delta$) curves of the MatF mode for various pull-out displacement rates

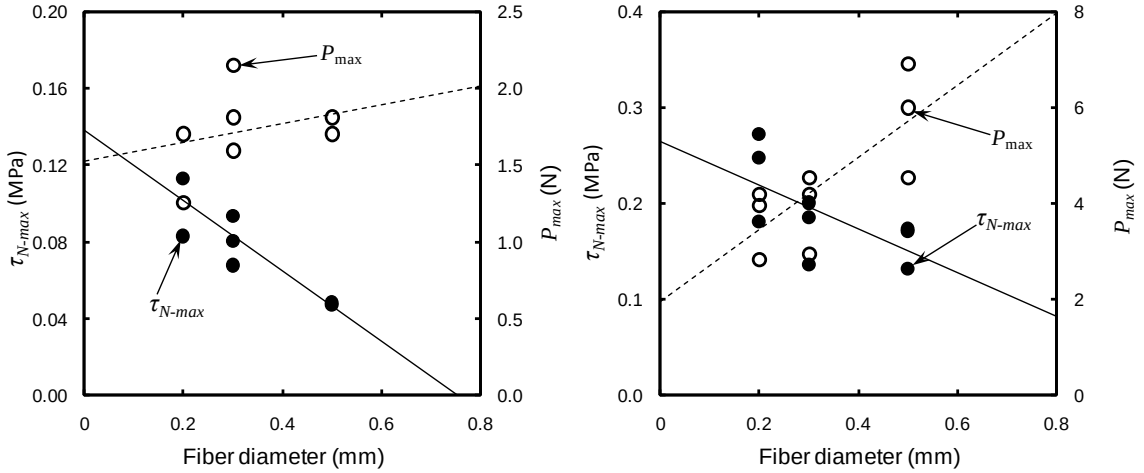

(a) rate = 0.423 mm/sec (b) rate = 1.27 mm/sec

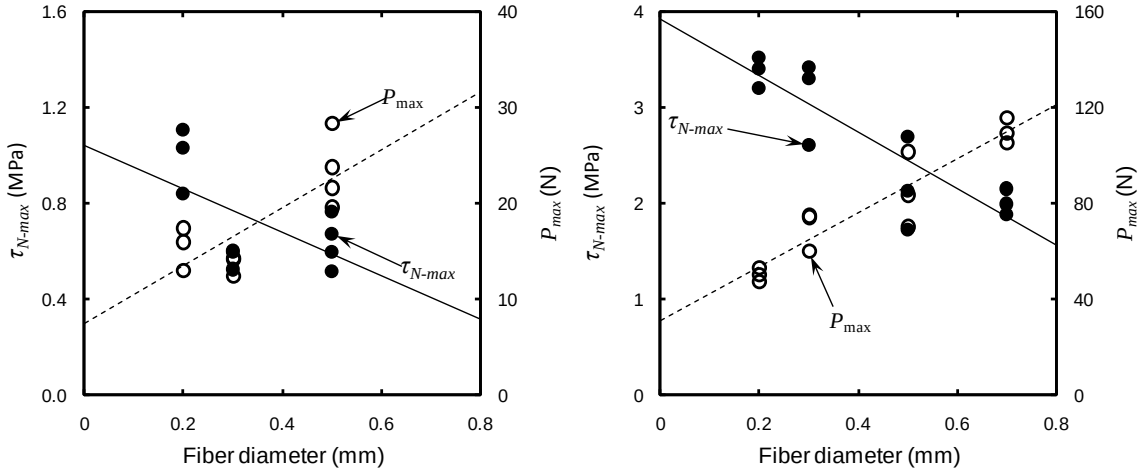

(c) rate = 8.47 mm/sec (d) rate = 84.7 mm/sec

Fig. 4.7 Effect of fiber diameter in MatF mode: embedded depths = 25±1 mm, test temperature = +20°C

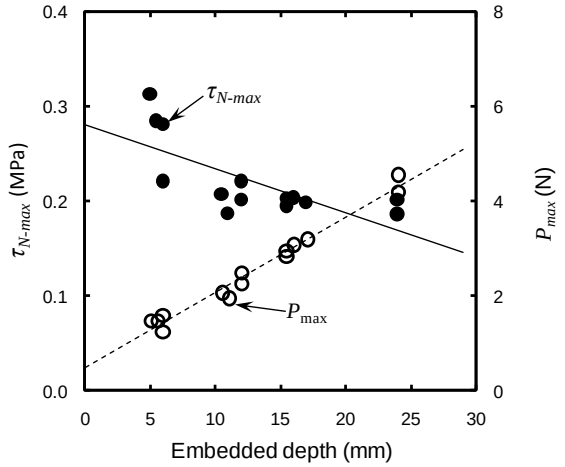

Fig. 4.8 Effect of embedded depth of fiber in MatF mode: fiber diameter = 0.3 mm, rate = 1.27 mm/sec at +20°C

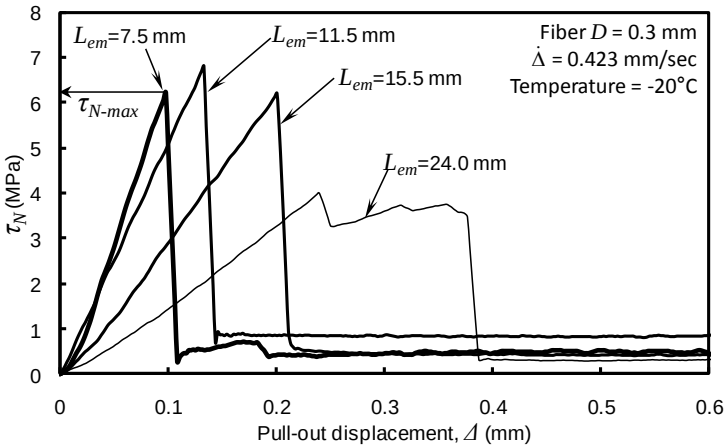

Fig. 4.9 Typical average shear stress – displacement ($\tau_N - \Delta$) curves of the IntF mode for various embedded depths

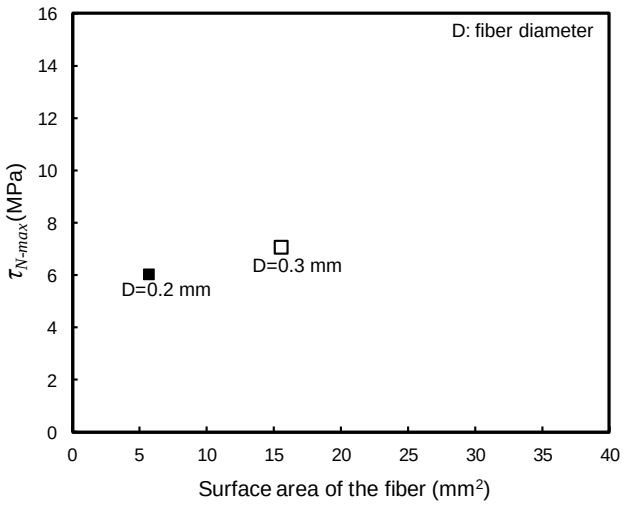

(a) rate = 0.423 mm/sec

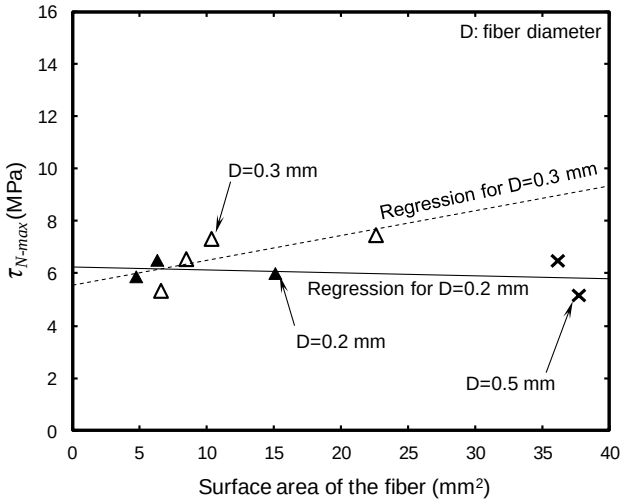

(b) rate = 1.27 mm/sec

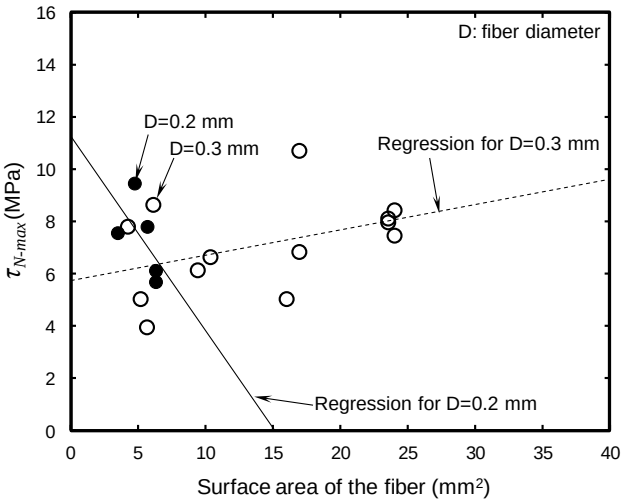

(c) rate = 8.47 mm/sec

Fig. 4.10 $\tau_{N-\max}$ versus ψ obtained at 0°C

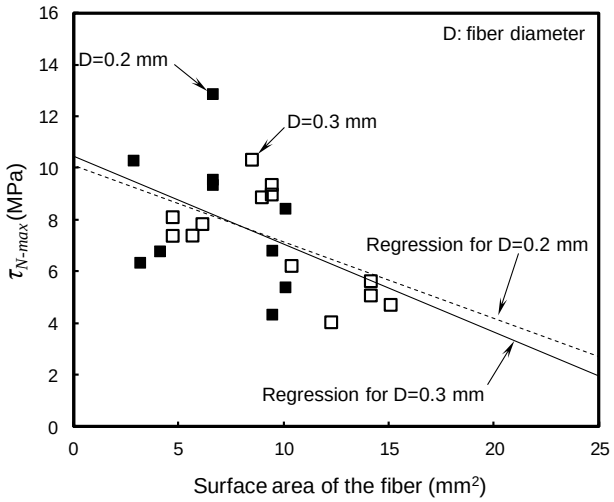

(a) rate = 0.0423 mm/sec

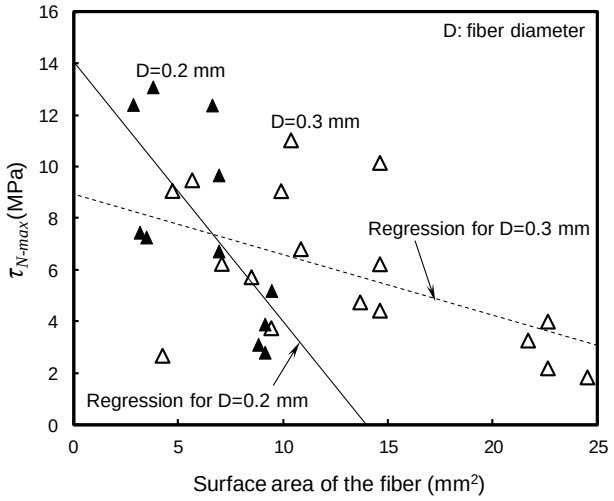

(b) rate = 0.423 mm/sec

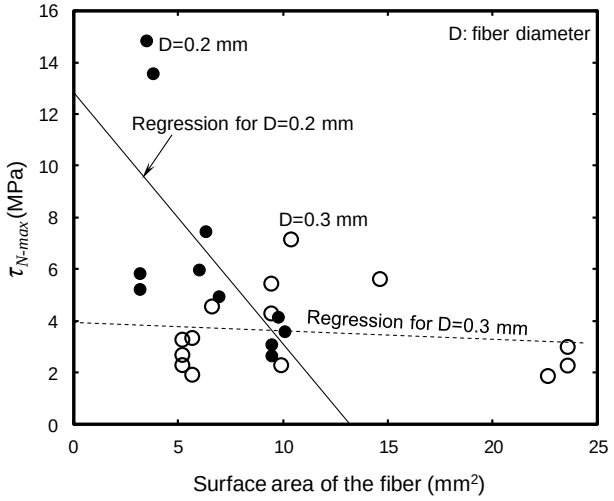

(b) rate = 1.27 mm/sec

Fig. 4.11 $\tau_{N-\max}$ versus ψ obtained at -20°C

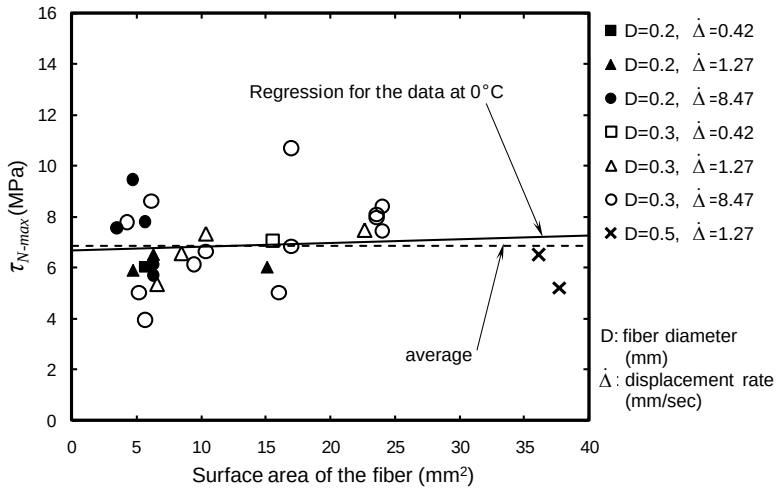

(a) at 0°C

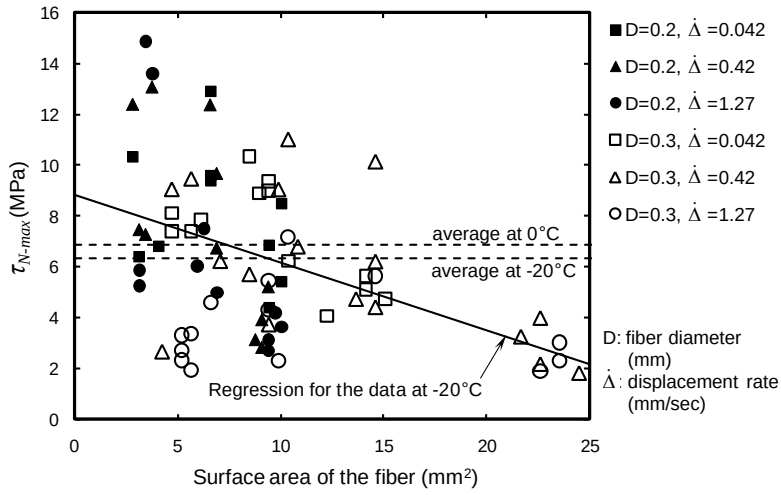

(b) at -20°C

Fig. 4.12 Variation of $\tau_{N-\max}$ with temperature, displacement rate, and fiber dimensions in interface failure mode

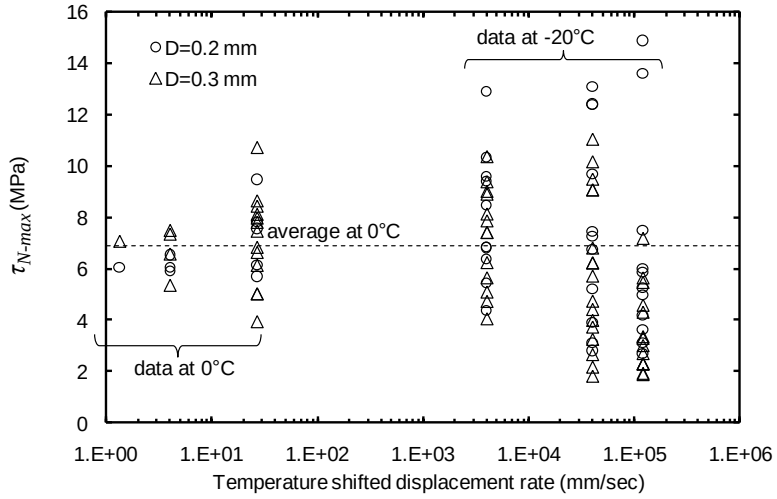

Fig. 4.13 Scatter in $\tau_{N-\max}$ in interface failure mode

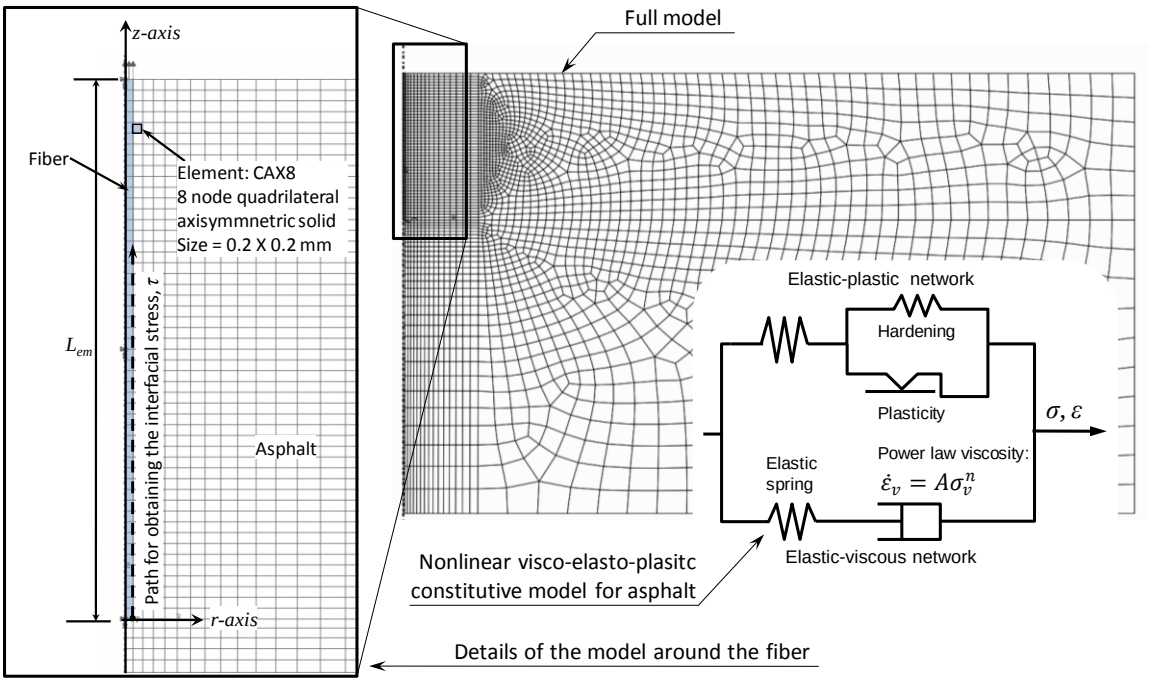

Fig. 4.14 Finite element model with nonlinear visco-elasto-plastic constitutive model

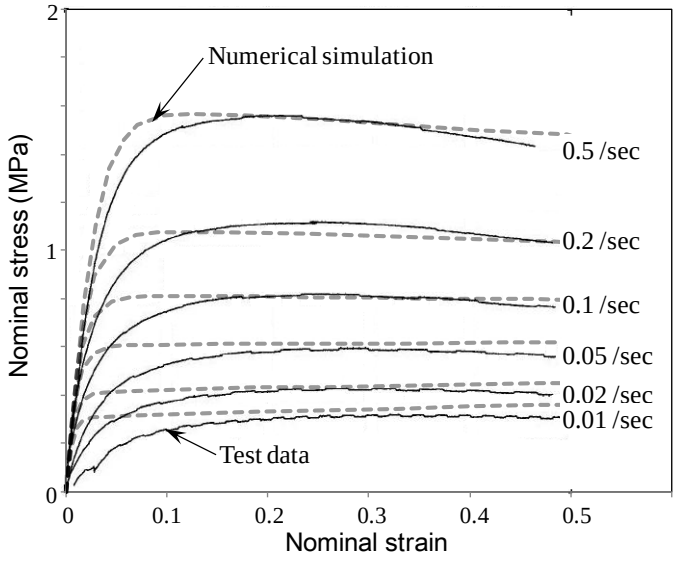

Fig. 4.15 Numerical simulation of the uniaxial tension test compared to the test data obtained by Cheung and Cebon (1997)

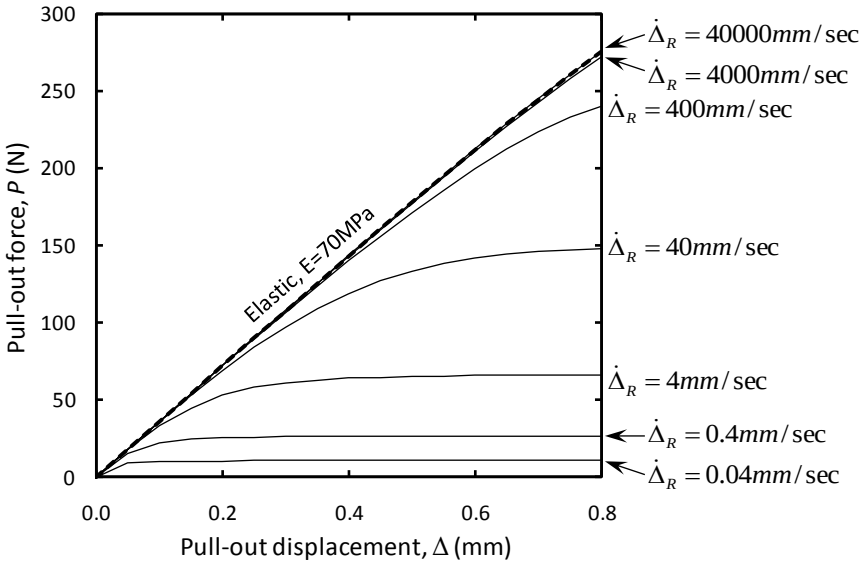

Fig. 4.16 Simulation of the pull-out test at various displacement rates

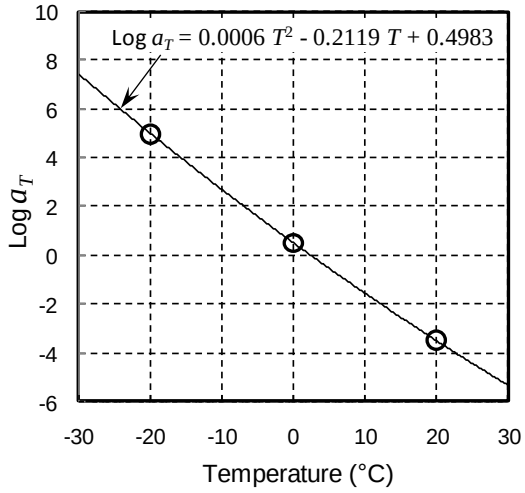

Fig. 4.17 Calibration of temperature shift factor

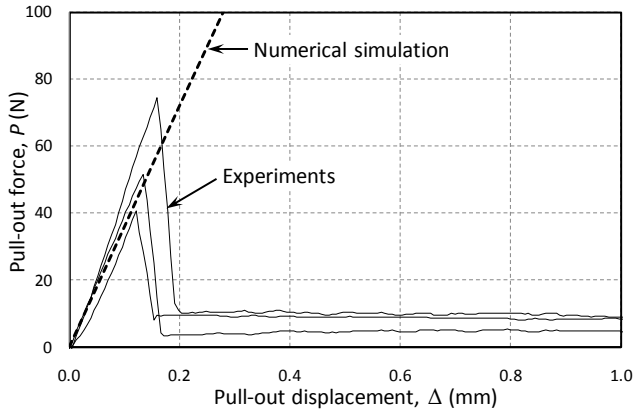

(a) finite element simulation with $\dot{\Delta}_R$=120,000 mm/sec compared to the test data at -20°C, $\dot{\Delta}$=1.27 mm/sec, and L_{em}≈10 mm

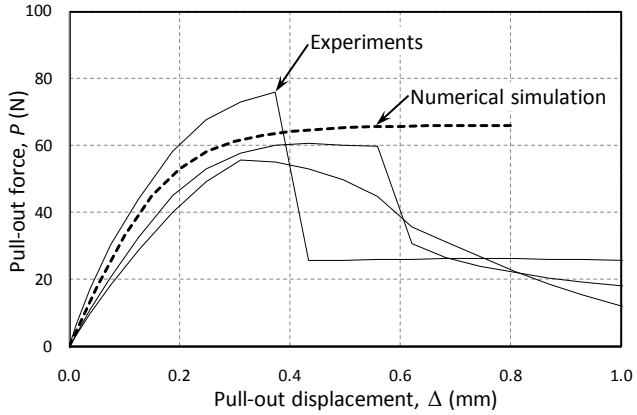

(b) finite element simulation with $\dot{\Delta}_R$=4 mm/sec compared to the test data at 0°C, $\dot{\Delta}$=1.27 mm/sec, and L_{em}≈10 mm

Fig. 4.18 Comparison of the simulated pull-out force – displacement curves to the test data

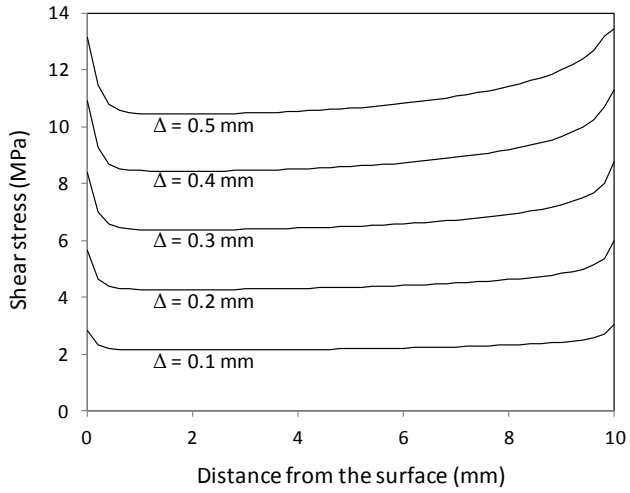

(a) at -20°C

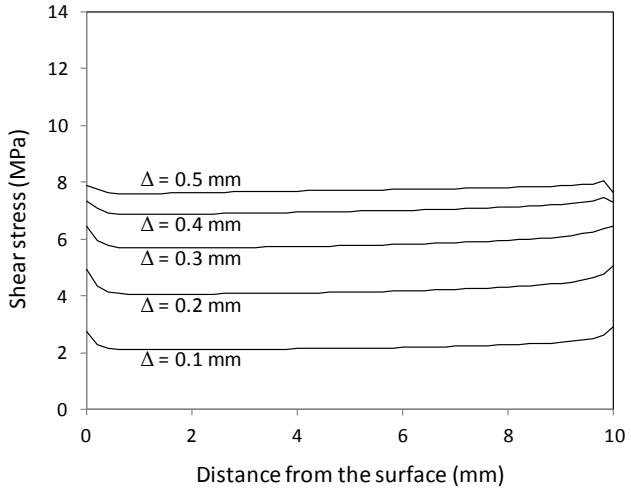

(b) at 0°C

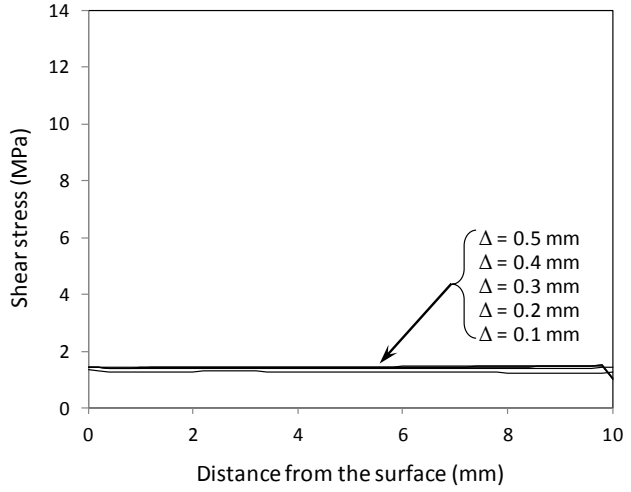

(c) at +20°C

Fig. 4.19 Shear stress ($\tau(z)$) during the pull-out over the interface obtained from the finite element analysis: L_{em} = 10 mm, D = 0.3 mm, and $\dot{\Delta}$=1.27 mm/sec

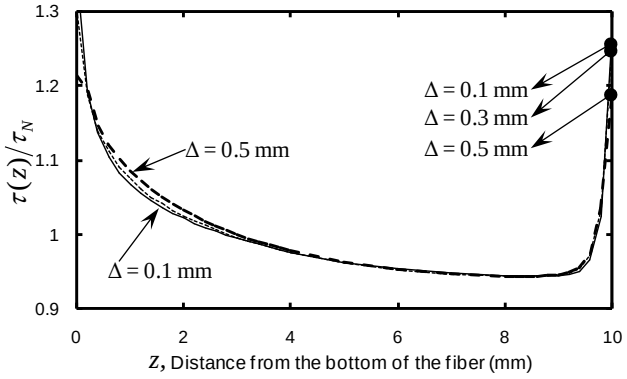

(a) at -20°C

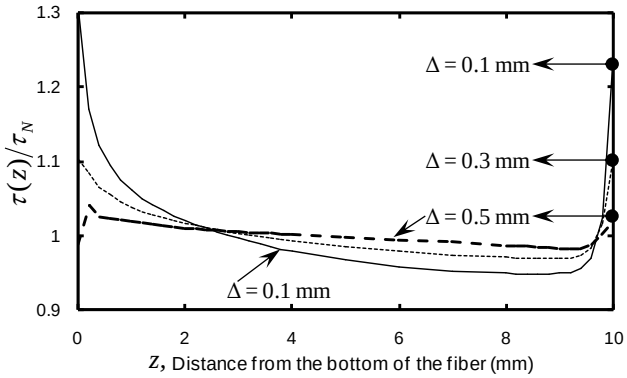

(b) at 0°C

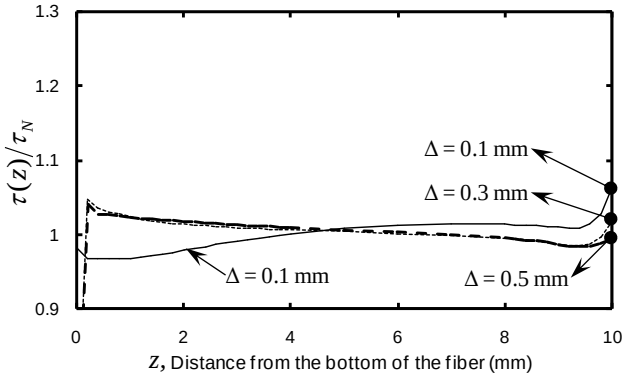

(c) at +20°C

Fig. 4.20 Shear stress distribution (τ/τ_N) during the pull-out over the interface obtained from the finite element analysis: L_{em} = 10 mm, D = 0.3 mm, and $\dot{\Delta}$=1.27 mm/sec

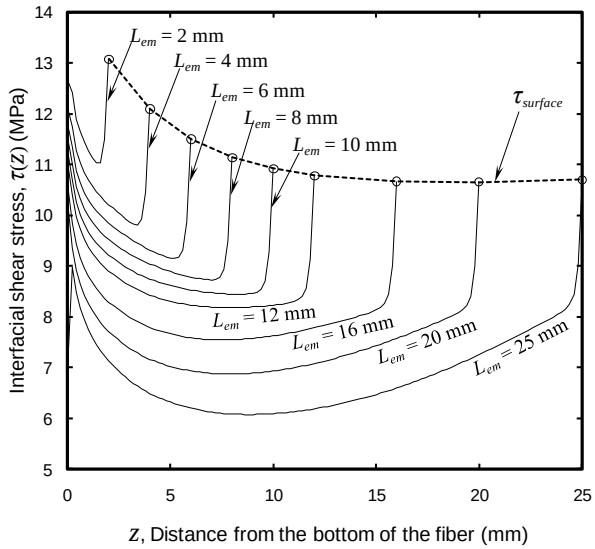

(a) at -20°C and Δ=0.2 mm

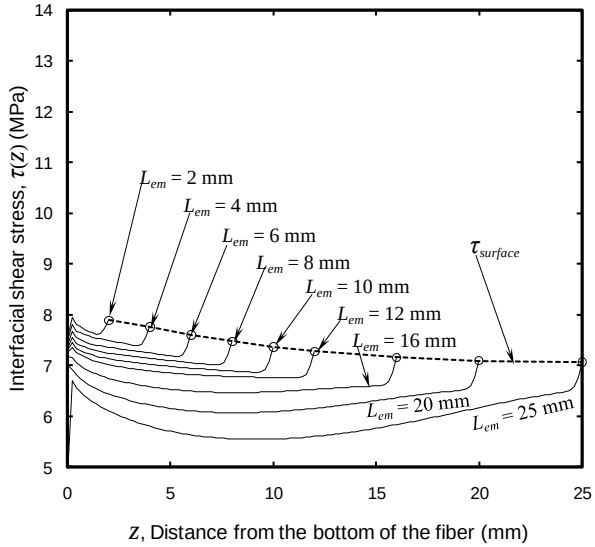

(b) at 0°C and Δ=0.4 mm

Fig. 4.21 Variation of the interfacial shear stress distribution with embedded depth obtained from the nonlinear viscoelastic model: D = 0.3 mm and $\dot{\Delta}$=1.27 mm/sec

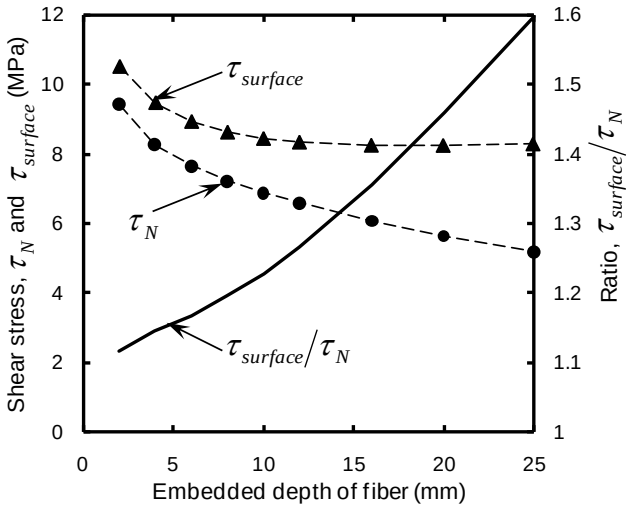

(a) at -20°C and Δ=0.2 mm

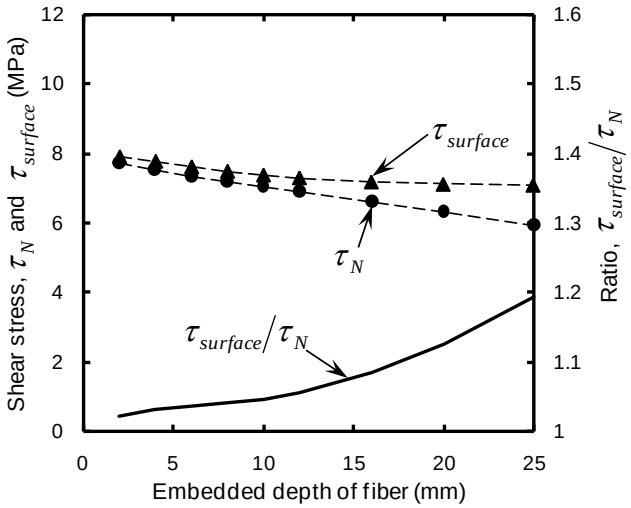

(b) at 0°C and Δ=0.4 mm

Fig. 4.22 Variation of the interfacial stress intensity, $\tau_{\text{surface}}/\tau_N$ with embedded depth and temperature: D = 0.3 mm and $\dot{\Delta}$=1.27 mm/sec

REFERENCES

Airey, G. D., Rahimzadeh, B., and Collop, A. C. (2003). "Viscoelastic linearity limits for bituminous materials." *Materials and Structures*, 36, 643-647.

Andriescu, A., and Hesp, S. A. (2009). "Time-temperature superposition in rheology and ductile fracture of asphalt binders." *International Journal of Pavement Engineering*, 10(4), 229-240.

ASTM. (2007). "Standard specification for performance graded asphalt binder." *ASTM D6373-07*, West Conshohocken, PA.

Brodnyan, J.G., Gaskins, F.H., Philippoff, W., and Thelen, E. (1960). "The Rheology of asphalt, III Dynamic Mechanical properties of asphalt." *Trans. Soc. Rheol.*, 4, 279–296.

Cheung, C. Y., and Cebon, D. (1997). "Experimental study of pure bitumens in tension, compression, and shear." *J. Rheol.*, 41(1), 45-73.

Ferry, J. D. (1950). "Mechanical properties of substance of high molecular weight; VI. Dispersion in concentrated polymer solutions and its dependence on temperature and concentration." *Journal of the American Chemical Society*, 72(8), 3746-3752.

Kim, D-J, El-Tawil, S. and Naaman, A. E. (2008), "Loading Rate Effect on Pullout Behavior of Deformed Fibers," *ACI Materials Journal*, 105(6), 576-584

Kim, D-J, El-Tawil, S. and Naaman, A. E. (2009), "Rate-Dependent Tensile Behavior of High Performance Fiber Reinforced Cementitious Composites," *Materials and Structures*, 42(3), 399-414.

Krishnan, J. M., and Rajagopal, K. R. (2005). "On the mechanical behavior of asphalt." *Mechanics of Materials*, 37, 1085-1100.

Leadermann, H. (1943). *Elastic and Creep Properties of Filamentous Materials and Other High Polymers*, Textile Foundation, Washington, D. C.

Lee, S. J., Rust, J. P., Hamouda, H., Kim, Y. R., and Borden, R. H. (2005). "Fatigue Cracking Resistance of Fiber-Reinforced Asphalt Concrete." *Textile Research Journal*, 75(2), 123-128.

Lethersich, W. (1942). "The mechanical behavior of bitumen." *Journal of the Society of Chemical Industry*, 61, 101–108.

Naaman, A. E., Namur, G. G., Alwan, J. M., and Najm, H. S. (1991a). "Fiber pullout and bond slip. I: Analytical study." *Journal of Structural Engineering*, 117(9), 2769-2790.

Naaman, A. E., Namur, G. G., Alwan, J. M., and Najm, H. S. (1991b). "Fiber pullout and bond slip. II: Experimental validation." *Journal of Structural Engineering*, 117(9),

2791-2800.

Naaman, A. E. (2000). "Fiber reinforcement for concrete: Looking back, looking ahead." *Proceedings of Fifth RILEM Symposium on Fiber Reinforced Concrete (FRC), BEFIB' 2000*, Rilem Publications S. A. R. L., Cachan, France, 65-86.

Park, P., El-Tawil, S., Park, S. Y., and Naaman, A. E. (2010). "Behavior of asphalt plug joint subjected to thermal and traffic loads." *Journal of Bridge Engineering*, ASCE, 15(3), 250-259.

Park, P., Wineman, A., and El-Tawil, S. (2011). "Uniaxial nonlinear viscoelastic constitutive model for asphalt concrete." *Journal of the Association of Asphalt Paving Technologists*, AAPT, 80.

Park, S. W., and Kim, Y. R. (2001). "Fitting Prony-series viscoelastic models with power-law presmoothing." *Journal of Materials in Civil Engineering*, 13(1), 26-32.

SIMULIA (2007). *ABAQUS - Analysis User's Manual: Version 6.7*, Providence, RI.

Stastna, J., Zanzotto, L., and Berti, J. (1997). "How good are some rheological models of dynamic material functions of asphalt." *Proc. of Assoc. of Asphalt Paving Technologists*, 66, 458–485.

CHAPTER 5
INDIRECT TENSILE STRENGTH AND TOUGHNESS OF STEEL FIBER REINFORCED ASPHALT CONCRETE AT LOW TEMPERATURE

The reinforcing effects of steel fiber additives for asphalt concrete are investigated through indirect tension tests at low temperature. Focusing on cracking resistance, indirect tensile strength, fracture energy, and post-cracking energy are obtained from tests conducted at -20°C. To provide fundamental information and to find an optimum method of fiber reinforcement, the effects of thickness, length, deformed shape, and content of steel fibers are investigated. The test results demonstrate that the low temperature cracking resistance of asphalt concrete can be significantly improved by adding the proper type and amount of steel fibers, but that the mechanical improvements are sensitive to fiber length. The indirect tensile strength and toughness of fiber reinforced asphalt concrete improve with an increase in fiber length. Overall, the indirect tensile strength and toughness of fiber reinforced asphalt concrete at low temperature are approximately proportional to the area of fiber-matrix debonding at failure. Mechanical deformations of the fibers, e.g. presence of a hook or twisting, can induce further improvements. Compared to unreinforced specimens, fiber reinforced specimens saw at most 62.5% increase in indirect tensile strength, and 370% and 895% improvements in fracture energy and toughness, respectively. These improvements are the highest documented mechanical improvements attributed to fiber reinforcement in asphalt concrete to date.

5.1 INTRODUCTION

Rutting and cracking are two major types of distress in flexible pavement. This study focuses on the improvement of cracking resistance of fiber reinforced asphalt concrete (FRAC). Among the various types of fibers, steel fibers are selected in this study because

they are cheap and widely available, and have been actively studied and successfully used for reinforcing concrete (Naaman 2000). Steel fibers also have the potential for impacting electrical conductivity, which could eventually enable various multifunctional applications such as snow and ice removal (Minsk 1968), self-monitoring of pavement integrity (Wu et al. 2005; Liu and Wu 2009), and self-healing (Garcia et al. 2009).

The objectives of this study are therefore to (1) confirm if a substantial improvement in cracking resistance can be achieved by adding steel fibers, (2) investigate the reinforcing effects of various factors such as dimensions, shape, and content of fibers, and (3) provide fundamental information for the behavior and optimization of FRAC. Indirect tension tests for specimens reinforced with various fiber types and contents are conducted, and ITS, fracture energy (FE), post-cracking energy (PE), and toughness are obtained. Since cracking is a problem at low temperature, all of the tests are conducted at -20°C, which is assumed to be a reasonable representation of a low field temperature. To the author's knowledge, this is the first study about the effect of fiber dimension and shape with the objective of achieving optimum fiber reinforcement for asphalt concrete (AC).

5.2 EXPERIMENTAL PROGRAM

5.2.1 Materials

The aggregate gradation of D7 (ASTM D3515 2001), dense graded sand asphalt mixture, was selected for making specimens. Fig. 5.1 compares the sieve analysis result for the aggregate to the specification limits. The aggregates were mixed with PG 64-22 (ASTM D6373 2007) asphalt binder produced by Marathon Petroleum Corporation. The optimum asphalt content for AC specimens (5.0% by weight) was determined by the Marshall mix design method (Asphalt Institute 1993). The binder to aggregate ratio for FRAC specimens was the same as for AC specimens to ensure consistent testing conditions. Although there evidence in Chen et al. (2009) that not adjusting the binder content to account for the added fibers could impair mechanical performance somewhat, it was felt that keeping the mix consistent would emphasize the reinforcing effect of the fibers and allow the research effort to focus directly on the reinforcing mechanisms

attributed to the fibers.

Table 5.1 lists the types of fibers employed in this study. The fibers numbered from 1 to 11 are steel fibers and their naming scheme is displayed in Fig. 5.2. For example, SC3-30 indicates a steel fiber with smooth surface, circular section, 0.3 mm in diameter, and 30 mm in length. Various deformed shapes of steel fibers are illustrated in Fig. 5.3. The twisted fiber is patented by one of the authors, and produced in the laboratory at the University of Michigan. The use of the twisted is actively studied for high-performance fiber-reinforced cementitious composite (HPFRCC, Naaman 2000; Kim et al. 2008). The smooth fiber with rectangular cross section is an interim product in making twisted fiber, and has the same sectional shape. The hooked fiber is commercially produced for reinforcing concrete (Kim et al. 2008). The remaining fiber types are carbon and PVA (see Table 5.1). Carbon fiber is known to be a chemically compatible additive to asphalt (Abtahi et al. 2010), and was tested as a conductive additive for AC (Wu et al. 2010). Polyvinyl alcohol fiber is one of the commonly used fibers for HPFRCC (Sahmaran and Li 2010; Kim et al. 2008). Various dimensions for a single fiber for each fiber type are presented in Table 5.1.

In Table 5.1, the equivalent diameter is the diameter of the fiber assuming a circular cross section that has the same area as the cross section of the original shape, and hence, is representative of the thickness of the fiber. The aspect ratio is the ratio of the fiber length to the fiber diameter, and is an important factor in mixing quality. Based on previous experience with fiber reinforced concrete behavior (Kim et al. 2008), it is surmised that a potentially influential factor is the area of fiber-matrix interface that could potentially be debonded during fracture. This variable is termed A_{int}, and is computed using Eq. (5.1).

$$A_{int} = \left[\frac{(\text{fractured surface area of a specimen}) \times V_f}{(\text{cross sectional area of a single fiber})}\right] \times (\text{perimeter of a single fiber}) \times (\text{fiber length}/4) \quad (5.1)$$

where, V_f is the volume content of fibers. Eq. (5.1) assumes that the fibers are evenly distributed and oriented throughout the specimen.

5.2.2 Specimen Preparations

Indirect tension test specimens containing 0.5%, 1.0%, and 1.5% of fibers by volume

were prepared for each fiber type listed in Table 5.1. Specimens without fibers were also prepared in the same way to serve as control specimens. Since each test was repeated three times to ensure repeatability, 9 specimens were therefore fabricated for each fiber type. Cylindrical shape specimens with 100 mm diameter and 65 mm height were fabricated following the Marshall method of mix design (Asphalt Institute 1993). The prepared binder, aggregates, and fibers were heated separately at 150°C for two hours. They were simultaneously put into the heated bucket of a rotating mixer, and mixed until the fibers and aggregates were evenly spread and completely coated by the binder. The mixture was compacted in compaction molds by applying 50 blows to each side with 4.5 kg compaction hammer at 135°C. The specimens removed from the molds were then conditioned at -20°C at least 8 hours before the tests. The diameter and height of the specimens were then measured at the conditioning temperature.

Clumping or balling of fibers during mixing is one of the important factors affecting FRAC (Abtahi et al. 2010). It was observed that the aspect ratio and amount of fibers are the most critical factors influencing the mixing quality of FRAC. Since the thicknesses of the steel fibers used in this study are relatively large, i.e. they have a smaller aspect ratio than the fibers used by previous investigators, higher volume fractions could be added to the mixture without significant clumping occurring. Light clumping of fibers was observed in the mixtures with 1.5% of fibers with high aspect ratio (≥100), which resulted in longer mixing durations. It was also observed that the deformed fibers were slightly more difficult to mix than smooth fibers with the same size (e.g. TR3-18 versus SC3-18). However, serious difficulty in mixing was not observed within the ranges of fiber size and content considered herein.

5.2.3 Test Procedures and Analysis Methods

Indirect tension tests were conducted by following the procedures of ASTM D6931 (2007), except for the test temperature (-20°C), which was different than specified (+25°C). The specimens were taken out of the conditioning freezer and tested immediately. An environmental chamber was not used in this study. A closed loop servo-hydraulic material test system (MTS 810) with a maximum force capacity of 100 kN was used to apply constant rate displacement (50 mm/min). The reaction force and the vertical

displacement were recorded by a data acquisition system.

From the measured data, indirect tensile stress, S (MPa), and strain, ε, were computed using Eq. (5.2) and (5.3).

$$S = 2P/\pi tD \quad (5.2)$$

$$\varepsilon = \Delta/t \quad (5.3)$$

where, P, t, D, and Δ are measured force (N), specimen height (mm), specimen diameter (mm), and the vertical displacement (mm), respectively. Solid lines in Fig. 5.4 show typical indirect tensile stress versus strain curves obtained from three identical test conditions (specimens with 1.5% of HC4-30). The parameters computed from the test results, i.e., ITS, FE, and PE, are graphically described in the Fig. 5.4. As suggested by Roque et al. (1997), FE is defined as the area under the stress – strain curve up to a strain at maximum stress (ε_p), and is a good indicator of the cracking potential for pavements (Roque et al. 2002). The area under the curve from ε_p to $2\varepsilon_p$ is called PE, which is representative of ductility. Toughness of the mixture is defined as the sum of FE and PE, and toughness index is toughness divided by FE (Anurag et al. 2009). All of the test results presented in this paper are averaged values of 3 identical tests, and an example of the average curve is illustrated in Fig. 5.4.

5.3 RESULTS AND DISCUSSION

5.3.1 Indirect Tensile Stress versus Strain Curves and Observations during the Tests

Two typical patterns of indirect tensile stress – strain curves observed from the FRAC specimens are compared to the response of AC specimens in Fig. 5.5. Fig. 5.6 displays some photos taken during and after the tests. The specimen faces in Fig. 5.6 are whitewashed with hydrated lime powder to more clearly promote observation of the cracks and their propagation.

The dotted line in Fig. 5.5 is an averaged indirect tensile stress – strain curve obtained from the AC specimens. According to the numerical simulation for pull-out tests presented in Chapter 4, the contribution of viscosity to asphalt behavior becomes smaller as temperature drops, and eventually, vanishes at -20°C. Due to the effect of low temperature, the stress – strain curve of the non-reinforced AC specimen is similar to that

of purely elastic-brittle materials such as plain concrete, where the stress rises up to the peak, and instantaneously drops after first cracking. Fig. 5.6a is a photo taken at the moment of crack development at a non-reinforced specimen. The crack abruptly appeared at the peak stress as shown in Fig. 5.6a, and the specimen split into two in a brittle manner. In this case, PE is negligible and the toughness index is close to 1, i.e. toughness ≈ FE.

The solid lines in Fig. 5.5a illustrate one of the typically observed reinforcing effects of fiber additives: increase in PE but not in ITS. This pattern is observed when the fiber length is short (less than or equal to 12.5 mm) or the amount of fibers is small (some cases of V_f = 0.5%). In these cases, crack initiation followed by relatively rapid propagation was similar to that for non-reinforced specimens, as shown in Fig. 5.6a. However, the specimens did not fall apart as in AC specimens. This implies that the fibers were pulled-out as the displacement increased and, therefore, it can be presumed that load after peak stress is carried by the fibers.

On the other hand, the solid lines in Fig. 5.5b show increases in ITS with increase in V_f, and correspondingly, show more substantial improvements in FE, PE, and toughness. Another notable characteristic of fiber reinforcement is that the initial stiffness does not vary when fibers are added. As a result, increase in ITS is accompanied by an increase in ε_p, as shown in Fig. 5.5b. For the most highly reinforced specimens (V_f = 1.5%), a shift in fracture mode was observed. Fig. 5.6b and 5.6c are photos of a specimen reinforced with 1.5% of HC4-30 which recorded the highest ITS (62.5% higher than the control specimens). At the peak stress, a crack initiated but its instantaneous propagation is restrained by the fiber reinforcement (Fig. 5.6b). As a result, the fracture mode was closer to a localized punching failure around the loading strip rather than full brittle splitting. Fig. 5.6c is taken after the test, and shows that the specimen did not split all the way through, while the top of the specimen is completely crushed. Fig. 5.6d is a photo of a fractured surface of FRAC after the test, and shows that the fibers exposed on the fractured surface have a clean surface. In addition, a substantial amount of crushed asphalt concrete could be poured out of the crack after the test. These observations imply that fracture of highly reinforced asphalt concrete is a combination of fiber pull-out accompanied by localized crushing of asphalt concrete. The highest toughness is

observed at the specimen with 1.5% of TR3-30, and its FE and toughness are 4.7 times and 10.0 times higher than those of non-reinforced specimens, respectively.

5.3.2 Effect of Fiber Size: Smooth Steel Fibers

In Table 5.1, the fibers numbered from 1 to 5 are smooth fibers with circular section. To investigate the effect of fiber length and thickness, ITS and toughness are compared in Fig. 5.7. SC2-25, SC3-30, and SC4-25 have fibers with similar lengths but different thickness (D = 0.2, 0.3, and 0.4 mm, respectively). Comparison of these three cases shows that the effects of fiber thickness on ITS (solid lines in Fig. 5.7a) and toughness (three bar charts at the bottom of Fig. 5.7b) are not substantial. Based on this observation, it is reasonable to attribute the low performances of SC1-06 to its short length (6 mm) rather than its diameter (0.15 mm). The improvement in ITS and toughness with increase of fiber length is obvious in comparison of SC3-18 and SC3-30 because the only difference between them is fiber length. When fibers are short, it is theorized that fibers will pull out easily from the matrix, thereby not contributing much to resist brittle cracking (similar to Fig. 5.6a). As fiber length increases, it becomes more effective in bridging a large zone, resulting in multiple cracking and making the fibers more efficient in resisting load.

5.3.3 Deformed Steel Fibers

The effect of using the deformed fibers illustrated in Fig. 5.3 is investigated. The fiber types addressed in Fig. 5.8 are all made out of the same wire. SR3-30 is flattened from SC3-30 to form a rectangular section. By changing the sectional shape, the perimeter of the single fiber and correspondingly the area of fiber-matrix interface increase 15% while all of the other conditions are similar to SC3-30. TR3-30 is a twisted fiber with the same sectional shape as SR3-30. Fig. 5.8a shows that ITS of SR3-30 is slightly but consistently higher than SC3-30, and is similar to the ITS of TR3-30. These results imply that increase in the fiber-matrix contact area improves ITS, while twisting of fibers does not. On the other hand, FE, PE, and toughness of those three fibers show different trends. In Fig. 5.8b, the toughness of TR3-30 is clearly higher than SR3-30 while there is no significant difference between SC3-30 and SR3-30. The high toughness

of TR3-30 is due to the increase in PE rather than FE. Therefore, it can be said that increase in the fiber-matrix contact area improves the performance of FRAC before crack development, and that twisting of fibers is beneficial to the performance after cracking. The comparison for relatively shorter fibers (SC3-18 and TR3-18) shows similar benefits of twisting in Fig. 5.8.

The test results for the hooked (HC4-30) and crimped (CR5-25) fibers are displayed in Fig. 5.9. Since there is not a smooth fiber exactly corresponding to the hooked fiber in size among the tested fibers, SC4-25 (same thickness but different length) and SC3-30 (same length but different thickness) are compared to HC4-30. As was observed for Fig. 5.7, fiber thickness does not make significant differences in ITS and toughness, and the length difference between 25 and 30 mm is too close to make clear distinction. Hence, the performances of SC4-25 and SC3-30 are similar. Compared to SC4-25 and SC3-30, the specimens reinforced with 1.0% and 1.5% of the hooked fibers have higher ITS and toughness than the other specimens.

SR5-25 is a flattened smooth fiber having the same sectional properties to CR5-25. As shown in Fig. 5.9, the reinforcing efficiency of SR5-25 and CR5-25 is not as good as other fibers, especially in toughness. Different from the observation in Fig. 5.7 on the effect of thickness, the weakened reinforcing effect of SR5-25 and CR5-25 is ascribed to their thickness. The equivalent diameter of those fibers (0.5 mm) is thicker than that for the other fibers. Although the wide flattening of SR5-25 maintains the area of fiber-matrix interface similar to SC4-25 a presented in Table 5.1, the number of fibers in the fracture section is smaller than the thinner fibers of the same volume.

5.3.4 Comparison to Other Fibers

The reinforcing effects of steel fibers are compared to the fibers made of other materials (carbon and polyvinyl alcohol) in Fig. 5.10. As shown in Table 5.1, a single carbon fiber is very thin, and a bundle of fibers are adhered to each other when it is shipped. The adhered fibers can be separated by being rubbed. However, because the separated fibers are easily tangled and cause mixing problems, the carbon fibers are mixed to asphalt concrete without being separated into each piece. As presented in Fig. 5.5a and 5.10, the benefit of adding carbon fibers is limited to a relatively small

improvement in post-cracking ductility. The thickness and length of PVA (polyvinyl alcohol) fiber is within the range of the tested steel fibers. As shown in Fig. 5.10, slight improvements in ITS and toughness are observed, but the beneficial effects are lower than the longer steel fibers.

5.3.5 Effect of Fiber-Matrix Interfacial Area

Fig. 5.11 – 5.14 compare ITS and toughness plotted with respect to the area of fiber-matrix interface debonded during the indirect tensile fracture (A_{int}) in groups that is grouped in Fig. 5.7 – 5.10, and the plots of all test cases are shown in Fig. 5.15 and 5.16. A_{int} of the tested fibers are listed in Table 5.1 for each volume fraction of fibers. Each dot in the figures represents the averaged value of three identical tests. Different fiber types are distinguished by using different symbols, and different volume fraction of fibers are distinguished by having different A_{int}. As shown in Fig. 5.15, ITS of fibers is approximately proportional to A_{int}, but there are some variations. For example, as shown in Fig. 5.7, fibers with different thicknesses do not cause significant changes in ITS and toughness when the same volume of fibers are used. On the other hand, as shown in Fig. 5.11a, thicker fibers have higher ITS than thinner fibers when compared for the same fiber-matrix interfacial area. Comparison of SC4-25 to SC2-25 (connected by solid lines in Fig. 5.11) clearly shows this trend. Therefore, considering that thicker fibers of the same length are easier to mix than thinner fibers because of the lower aspect ratio, thicker fibers appear to be more beneficial for improve ITS.

Excluding the effect of deformation, toughness of FRAC has a clearer dependency on A_{int} than ITS, as shown in Fig. 5.11b. Correspondingly, the effect of deformation is clearly seen in Fig. 5.16. As an example, consider SC3-30 with V_f = 1.5% (see dotted arrows in Fig. 5.16). By flattening the fiber, SR3-30 specimen has larger A_{int} (increase in x-axis), and corresponding improvement in toughness follows the trend of other smooth fibers. In other words, this implies that the improvement in toughness by flattening can also be attained by using thinner fibers. By twisting SR3-30, TR3-30 promotes an additional increase in toughness without increase in A_{int} (Fig. 5.12b). As marked with the dotted arrows in Fig. 5.15 and 5.16, the deformations of fibers such as hooked end and twisting can improve ITS and toughness of FRAC. However, a

comparison between the cost and energy required for the deformation and the benefits due to the additional reinforcements is needed prior to practical application.

Table 5.2 lists ITS, FE, PE, and toughness of all test cases. Each number in Table 5.2 is averaged value of three identical tests. The indirect tensile stress versus strain curves for all test cases can be found in Appendix A.2.

5.4 SUMMARY AND CONCLUSIONS

Focusing on low temperature cracking, performance improvements in asphalt concrete attributed to fiber reinforcement are investigated using the indirect tension test. Cylindrical specimens reinforced by various fiber types are tested to investigate the effects of type, thickness, length, deformed shape, and content of fibers. The indirect tensile strength, fracture energy, post-cracking energy, and toughness of the specimens are obtained and compared to each other.

The indirect tension test results demonstrate that low temperature cracking resistance of asphalt concrete can be significantly improved by using discrete steel fiber reinforcement of proper size, shape, and content. By retarding brittle damage localization, the fracture of indirect tension specimens is shifted to local punching fracture, and is accompanied by significant amounts of crushing of asphalt concrete around the fracture surface. Comparison of test results for smooth fibers shows that the length of fibers is critical for performance improvements. The ITS and toughness of FRAC are improved with increase in fiber length. On the other hand, the effect of thickness is not significant within the diameter range from 0.2 to 0.4 mm, but the decrease in toughness is observed at the specimens with higher thickness. Test results for deformed fibers show that the hooked end of fibers is beneficial for improving ITS, and that twisting contributes to increase post-cracking energy. Overall ITS and toughness of FRAC at low temperature are approximately proportional to the area of fiber-matrix debonding at failure, and additional improvement can be obtained by deforming fibers. The highest ITS and toughness are observed at the specimens reinforced with the hooked fibers having 30 mm length and 0.4 mm diameter and the specimens with the twisted fibers having 30 mm length and 0.3 mm diameter, respectively. Table 5.3 compares the maximum

improvements achieved in this study to that of previous publications, and shows that 62.5% increase in indirect tensile strength, and 370% and 895% improvements in fracture energy and toughness, respectively, are the highest improvements attributed to fiber reinforcement in asphalt concrete to date. Balling or clumping of fibers were observed to occur during mixing. However, the problems were mild and were more likely to occur as the aspect ratio became higher and as the amount of fiber increased.

The results presented in this paper demonstrate that adding steel fibers is an efficient way of improving low temperature cracking resistance of AC. The findings presented in this paper are based on phenomenological observations, and therefore, further investigations are needed to understand the reinforcing mechanism. For example, understanding single fiber pull-out behavior from the viscoelastic matrix such as asphalt concrete will provide a fundamental insight for the behavior of FRAC. The single fiber pull-out behavior from pure asphalt was investigated in Chapter 4, but the fiber pull-out from AC containing aggregates should be explored for more efficient field application of FRAC.

Table 5.1 Fibers added to the specimens

ID no.	Designation	Fiber type	Cross-sectional shape	Single fiber					A_{int}* (cm^2)		
				Equivalent diameter, D (mm)	Length, L (mm)	Aspect ratio, L/D	Cross-sectional area (mm^2)	Perimeter (mm)	V_f**= 0.5%	V_f**= 1.0%	V_f**= 1.5%
1	SC1-06	smooth steel	circular	0.15	6	40	0.018	0.47	13.1	26.2	39.3
2	SC2-25			0.2	25	125	0.031	0.63	40.9	81.8	122.7
3	SC3-18			0.3	18	60	0.071	0.94	19.6	39.3	58.9
4	SC3-30			0.3	30	100	0.071	0.94	32.7	65.4	98.1
5	SC4-25			0.4	25	63	0.126	1.26	20.4	40.9	61.3
6	SR3-30	smooth steel	rectangular (.32×.22 mm)	0.3	30	100	0.071	1.08	37.5	75.0	112.4
7	TR3-18	twisted steel		0.3	18	60	0.071	1.08	22.5	45.0	67.5
8	TR3-30			0.3	30	100	0.071	1.08	37.5	75.0	112.4
9	SR5-25	smooth steel	rectangular (.76×.25 mm)	0.5	25	50	0.194	2.03	21.2	42.3	63.5
10	CR5-25	crimped steel		0.5	25	50	0.194	2.03	21.2	42.3	63.5
11	HC4-30	hooked steel	circular	0.4	30	75	0.128	1.26	24.5	49.1	73.6
12	CB-13	carbon		0.01	13	1,270	7.8E-5	0.03	415.4	830.8	1,246.2
13	PVA-13	polyvinyl alcohol		0.2	13	64	0.031	0.63	20.8	41.5	62.3

* A_{int}: Area of fiber-matrix debonding at failure
** V_f: Fiber contents by volume

Table 5.2 Indirect tension test data: averaged from three specimens per series

ID no.	Designation	Volume contents of fibers, V_f	Indirect tensile strength, ITS (MPa)	Fracture Energy, FE (kPa)	Post-cracking Energy, PE (kPa)	Toughness (kPa)
	Non-reinforced	0.0%	2.367	6.74	2.02	8.76
1	SC1-06	0.5%	2.325	6.79	4.50	11.28
		1.0%	2.425	7.39	11.00	18.39
		1.5%	2.415	7.90	12.35	20.25
2	SC2-25	0.5%	2.829	17.19	22.68	39.86
		1.0%	3.111	23.41	31.36	54.77
		1.5%	3.327	26.14	44.93	71.07
3	SC3-18	0.5%	2.503	7.76	13.46	21.21
		1.0%	2.873	12.33	22.24	34.57
		1.5%	3.357	17.98	28.79	46.77
4	SC3-30	0.5%	2.706	14.82	19.47	34.29
		1.0%	3.251	20.48	30.30	50.78
		1.5%	3.484	24.15	36.99	61.14
5	SC4-25	0.5%	2.935	10.21	18.82	29.02
		1.0%	3.207	18.66	28.11	46.76
		1.5%	3.629	20.90	34.36	55.26
6	SR3-30	0.5%	2.962	13.37	18.48	31.84
		1.0%	3.352	23.67	36.52	60.18
		1.5%	3.788	25.98	41.10	67.09
7	TR3-18	0.5%	2.311	10.88	12.69	23.57
		1.0%	3.078	18.65	28.93	47.59
		1.5%	3.425	21.72	35.06	56.79
8	TR3-30	0.5%	2.928	18.06	28.99	47.05
		1.0%	3.464	23.24	38.26	61.50
		1.5%	3.688	31.67	55.54	87.21
9	SR5-25	0.5%	2.461	10.32	7.20	17.51
		1.0%	2.772	13.16	11.81	24.97
		1.5%	3.459	17.42	20.40	37.82
10	CR5-25	0.5%	2.463	9.23	6.84	16.06
		1.0%	3.121	13.59	10.50	24.09
		1.5%	3.240	15.92	17.81	33.74
11	HC4-30	0.5%	2.653	9.15	17.86	27.01
		1.0%	3.444	24.97	39.07	64.04
		1.5%	3.847	26.04	46.43	72.47
12	CB-13	0.5%	2.306	8.98	5.87	14.85
		1.0%	2.332	10.93	10.90	21.83
		1.5%	2.422	14.33	16.63	30.95
13	PVA-13	0.5%	2.207	5.20	4.57	9.78
		1.0%	2.704	11.18	12.52	23.70
		1.5%	2.659	11.61	14.42	26.03

Table 5.3 Comparison of the documented strength improvements attributed to fiber additives: only the highest improvements are selected from each publication

Citation	Maximum improvement*				Fibers (L=length, W_f = fiber content by weight, V_f = fiber content by volume)	approximated V_f	note
	ITS**	FE***	Toughness	MS****			
Freeman et al. 1989	15%				polyester fibers, L=6 mm, W_f=0.35%	0.60%	wet ITS and wet toughness, adjusted optimum binder content
			117%		Polyester fibers, L=13 mm, W_f=0.50%	0.85%	
Kim et al. 1999	5%			10%	Polyester fibers, L=6 mm	-	dry ITS
Bueno et al. 2003				-57%	polypropylene fibers, L=20 mm, W_f=0.5%	1.3%	maximum strength reduction
Lee et al. 2005	-18%	85%			recycled carpet (nylon) fibers, L=12 mm, V_f=1.0%	1.0%	test at +20°C
Tapkin 2008				58%	polypropylene fibers, L=10 mm, W_f=1.0%	2.5%	
Li et al. 2008	28%				carbon fibers, L=5 mm, W_f=0.3%, mixed with 18% graphite filler	0.38%	ITS with loading rate of 1 mm/min
Anurag et al. 2009	31%		80%		waste polyester fibers, L=13mm, W_f=0.5%	0.85%	wet ITS and wet toughness
Chen et al. 2009				8%	polyacrylonitrile, W_f=0.3%	0.60%	adjusted optimum binder content
Xu et al. 2010	8%		71%		polyacrylonitrile, L=5 mm, W_f=0.3%	0.60%	adjusted optimum binder content
Kaloush et al. 2010	49%	75%			blend of polypropylene and aramid fibers, L=19mm, W_f=0.045%	0.10%	test at -10°C
This study	63%				hooked steel fibers, L=30mm, W_f=5.0%	1.5%	test at -20°C
		370%	896%		twisted steel fibers, L=30mm, W_f=5.0%	1.5%	test at -20°C

* $\text{Improvement} = \frac{(\text{strength of FRAC})}{(\text{non-reinforced strength})} \times 100 - 100 \ (\%)$

** ITS = indirect tensile strength

*** FE = fracture energy

**** MS = Marshall stability

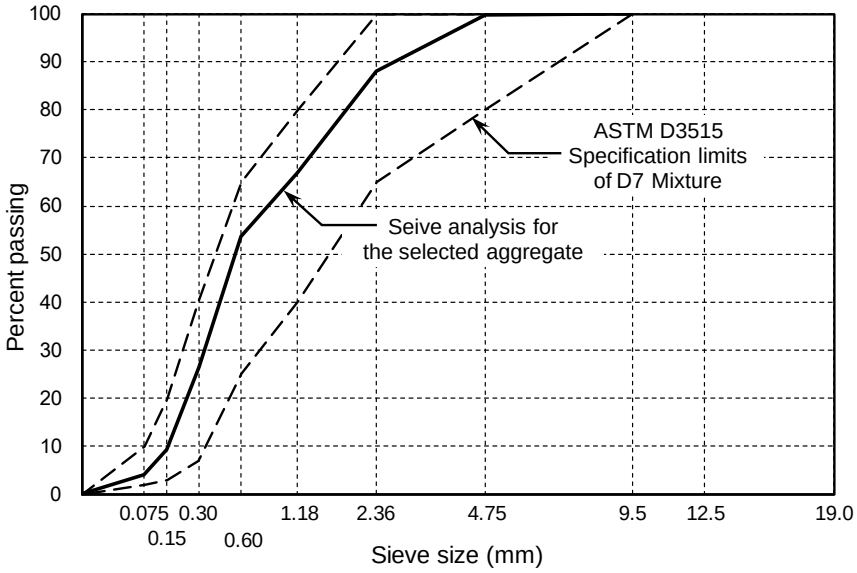

Fig. 5.1 Aggregate gradation of the specimens

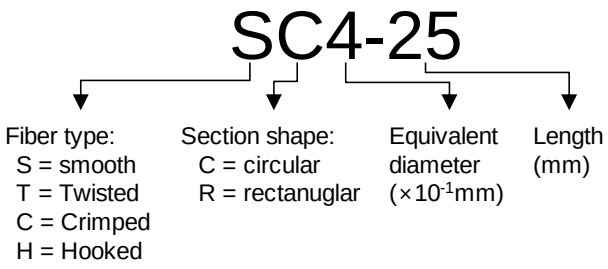

Fig. 5.2 Naming scheme for steel fibers

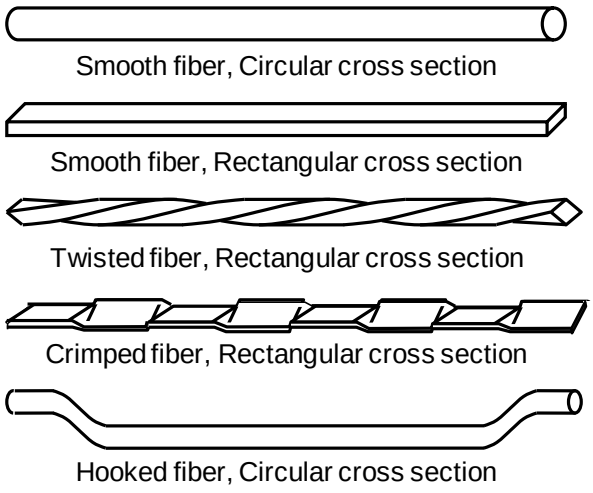

Fig. 5.3 Types of steel fibers

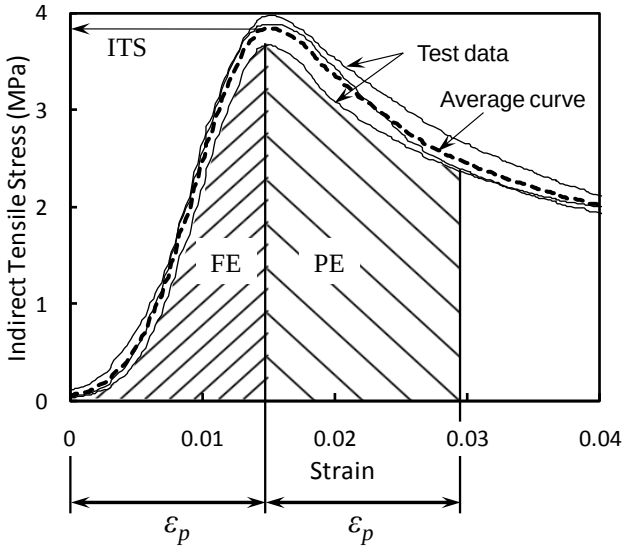

Fig. 5.4 Indirect tensile strength, fracture energy, and post-cracking energy: the curves obtained from the specimens reinforced with 1.5% of HC4-30 fibers

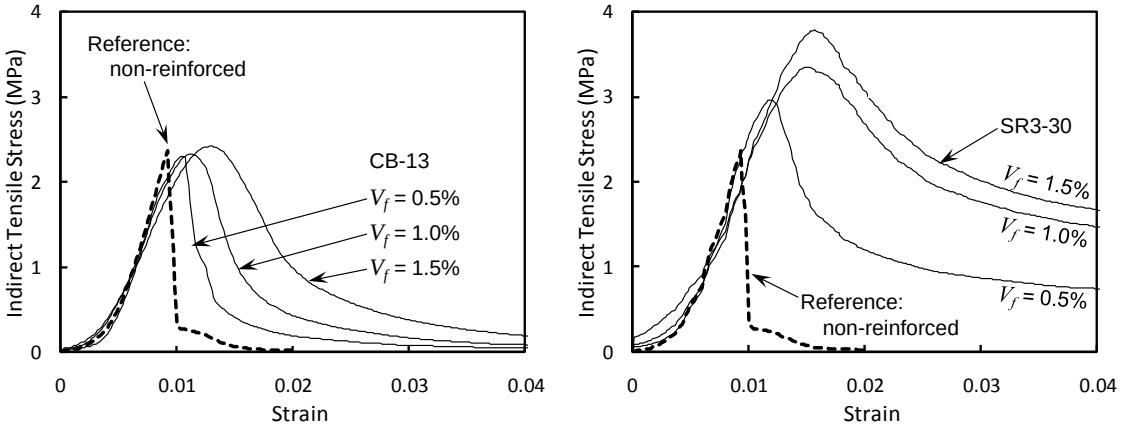

(a) reinforced with CB-13 (b) reinforced with SR3-30

Fig. 5.5 Two typical patterns of indirect tensile stress-strain curves (averaged) of FRAC

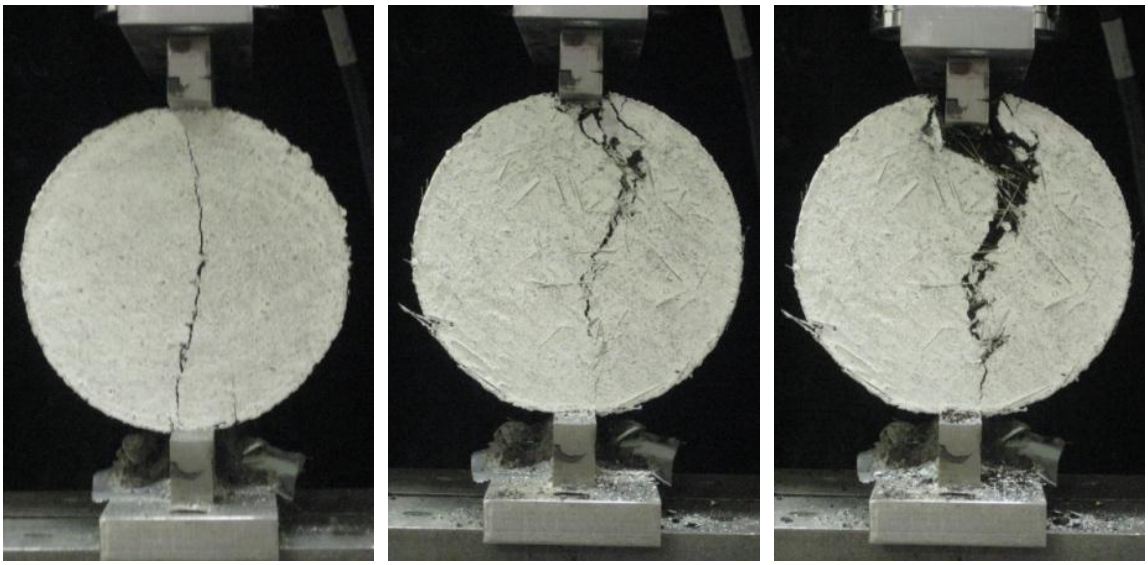

(a) (b) (c)

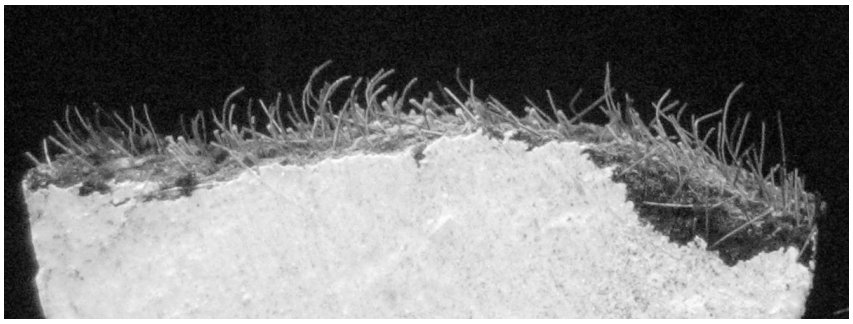

(d)

Fig. 5.6 Fracture mode of non-reinforced specimen and highly-reinforced specimen: (a) non-reinforced specimen right after the peak stress, a crack initiated and propagated through the specimen instantaneously; (b) HC4-30 V_f = 1.5%, right after the peak stress, a crack developed but does not propagate to the other end yet; (c) HC4-30 V_f = 1.5%, after the test, the top of the specimen crushed but the specimen does not completely split down into two pieces; (d) SC3-30 V_f = 1.5%, fractured surface showing the fibers pulled-out cleanly.

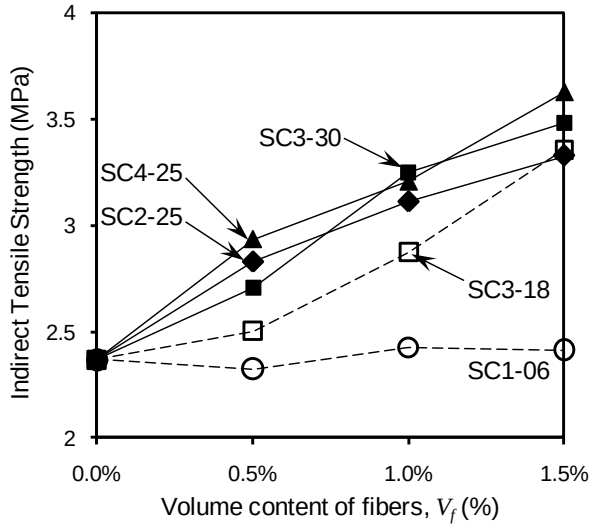

(a) ITS

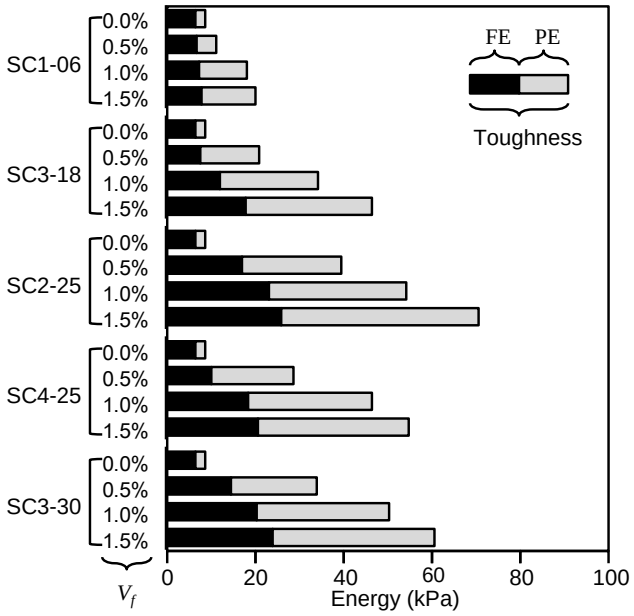

(b) FE, PE, and toughness

Fig. 5.7 Variation of ITS and toughness with fiber dimensions: smooth fibers with circular section

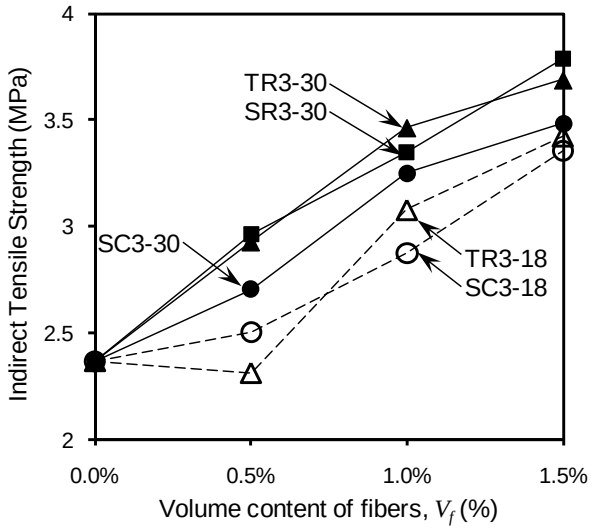

(a) ITS

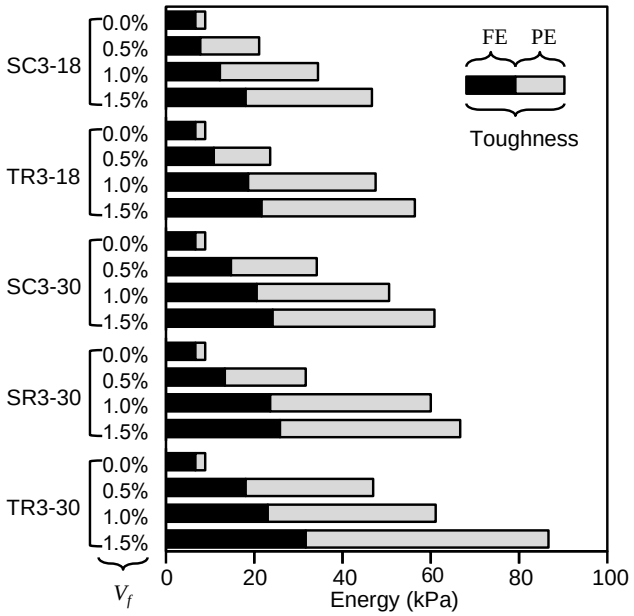

(b) FE, PE, and toughness

Fig. 5.8 Variation of ITS and toughness with fiber deformation: flattened and twisted fibers

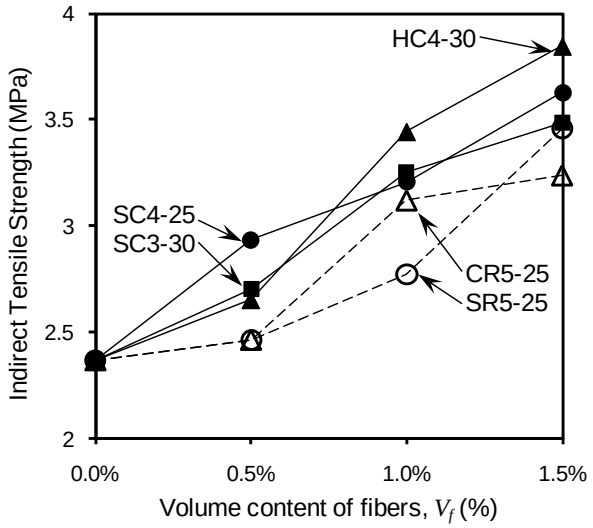

(a) ITS

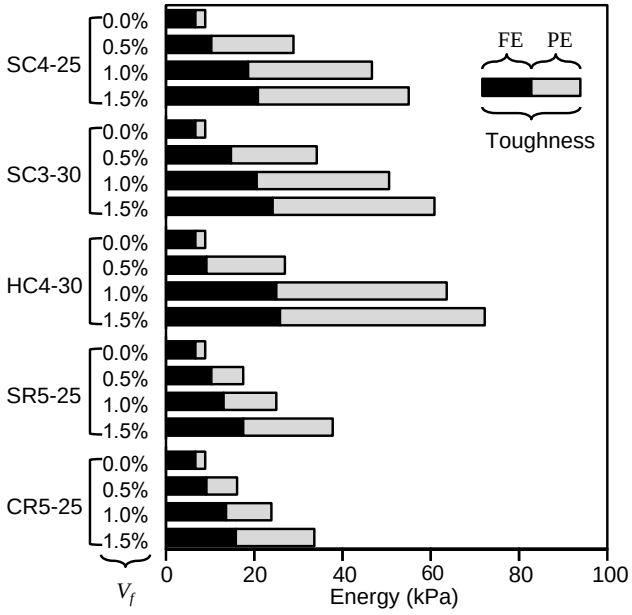

(b) FE, PE, and toughness

Fig. 5.9 Variation of ITS and toughness with fiber deformation: crimped and hooked fibers

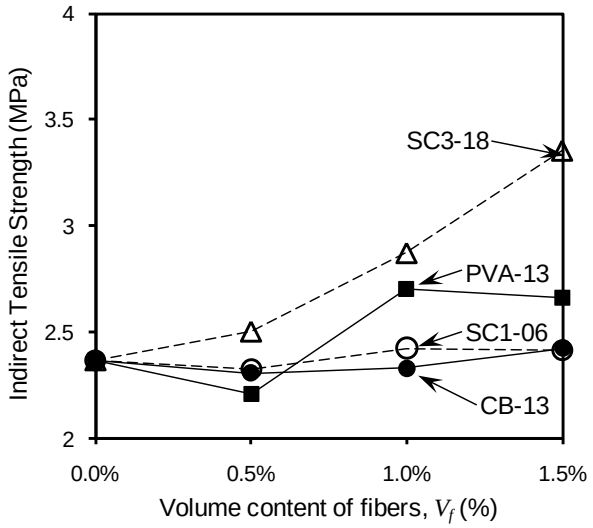

(a) ITS

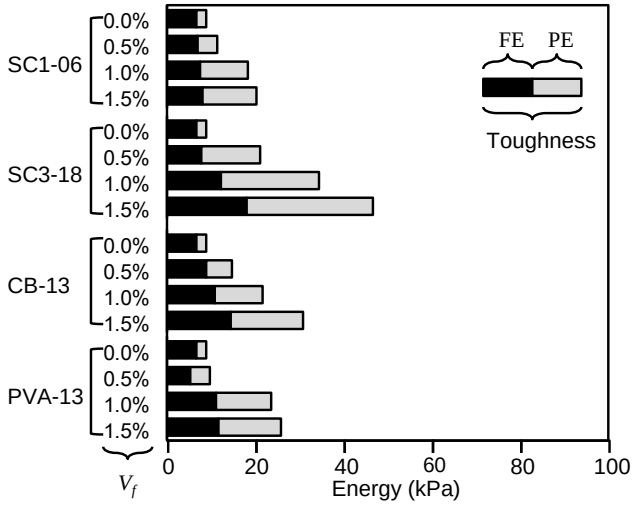

(b) FE, PE, and toughness

Fig. 5.10 Comparison of steel fibers to the fibers with other materials: carbon and polyvinyl alcohol fibers

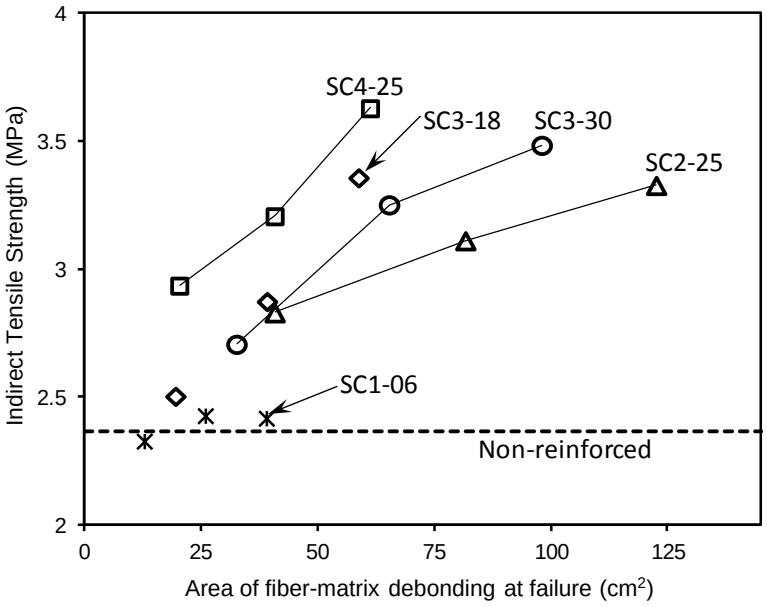

(a) ITS versus A_{int}

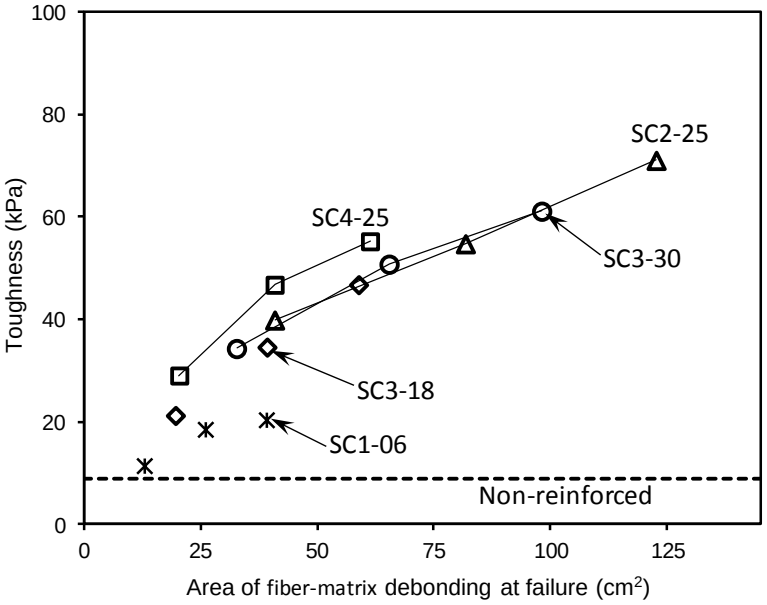

(b) Toughness versus A_{int}

Fig. 5.11 Effect of area of fiber-matrix debonding at failure: smooth steel fibers with circular section

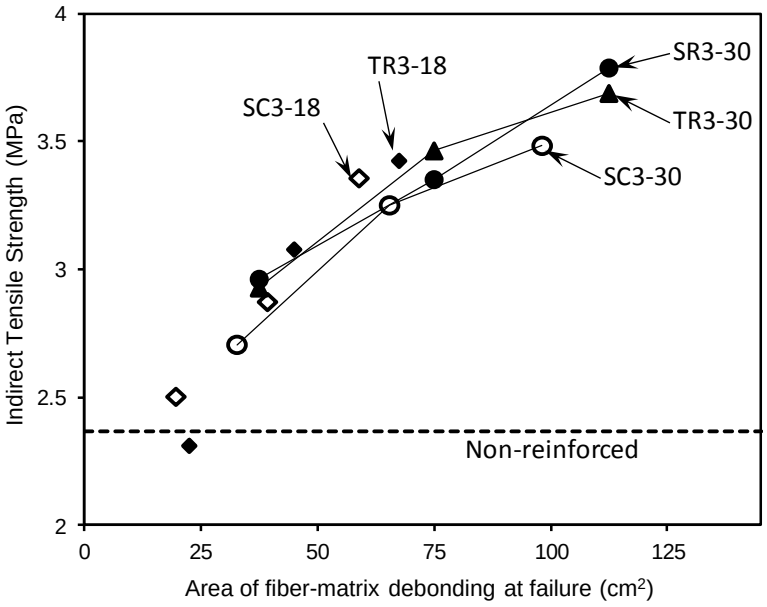

(a) ITS versus A_{int}

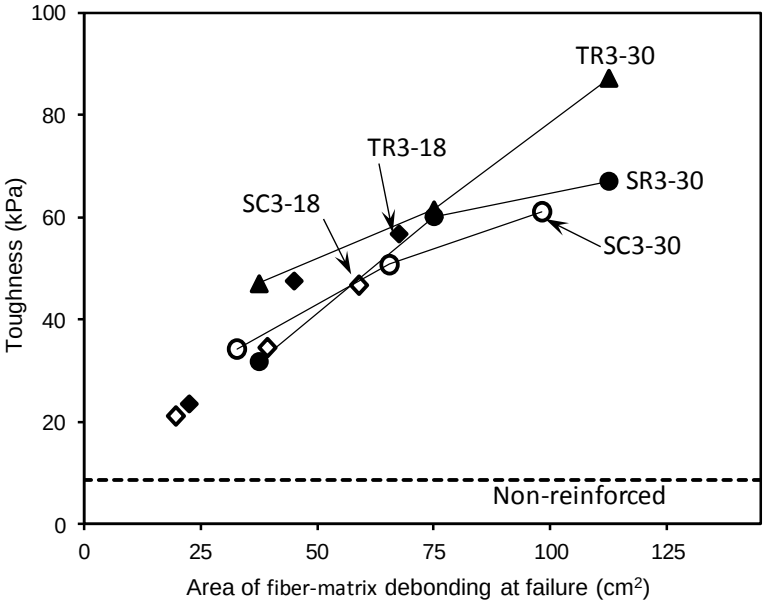

(b) Toughness versus A_{int}

Fig. 5.12 Effect of area of fiber-matrix debonding at failure: flattened and twisted steel fibers

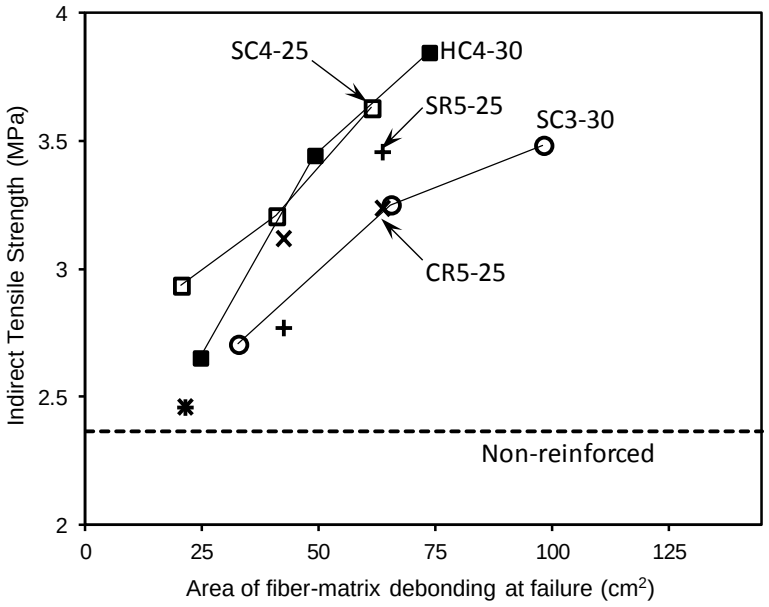

(a) ITS versus A_{int}

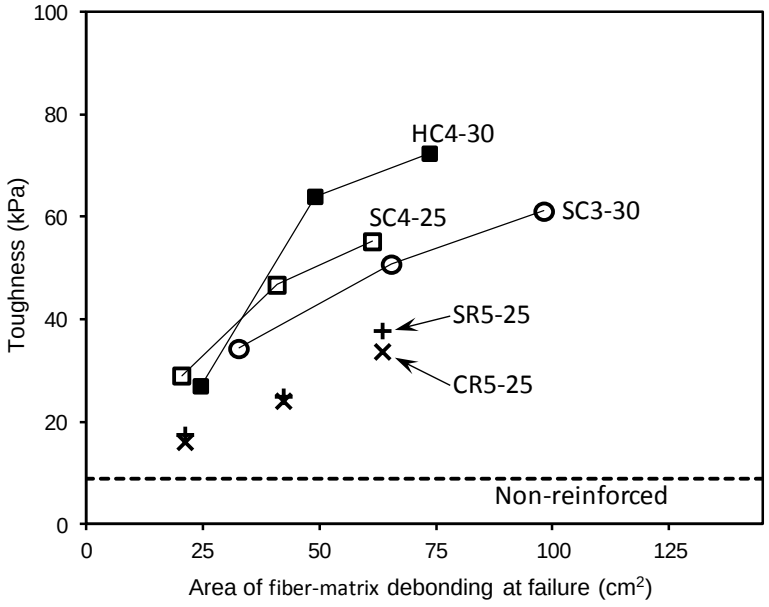

(b) Toughness versus A_{int}

Fig. 5.13 Effect of area of fiber-matrix debonding at failure: crimped and hooked steel fibers

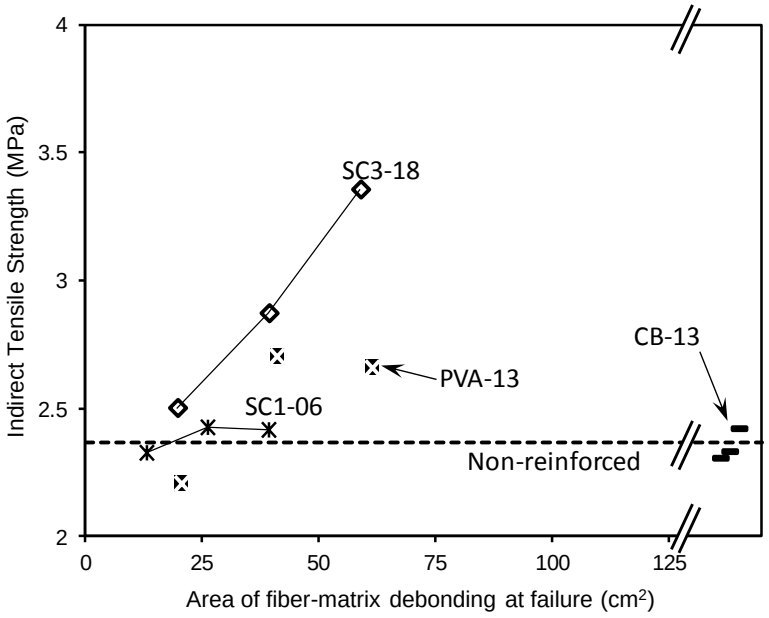

(a) ITS versus A_{int}

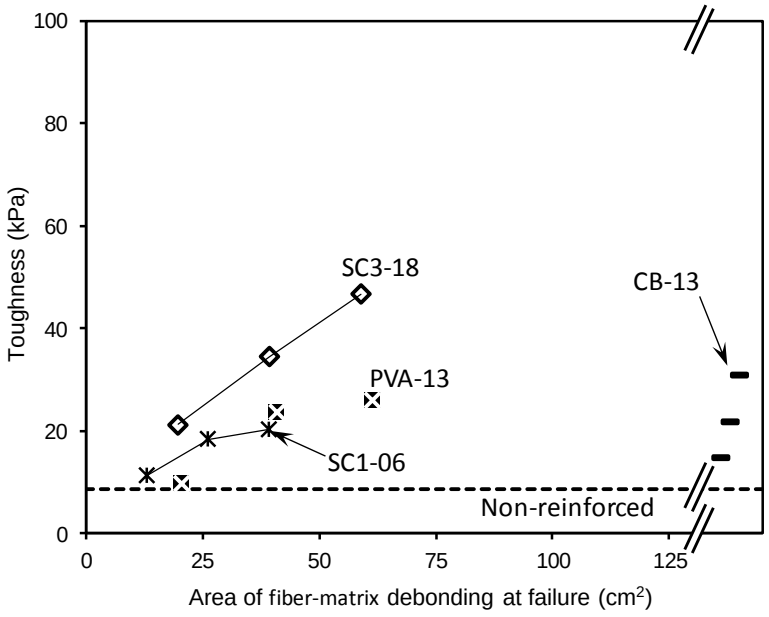

(b) Toughness versus A_{int}

Fig. 5.14 Effect of area of fiber-matrix debonding at failure: carbon, polyvinyl alcohol, and steel fibers

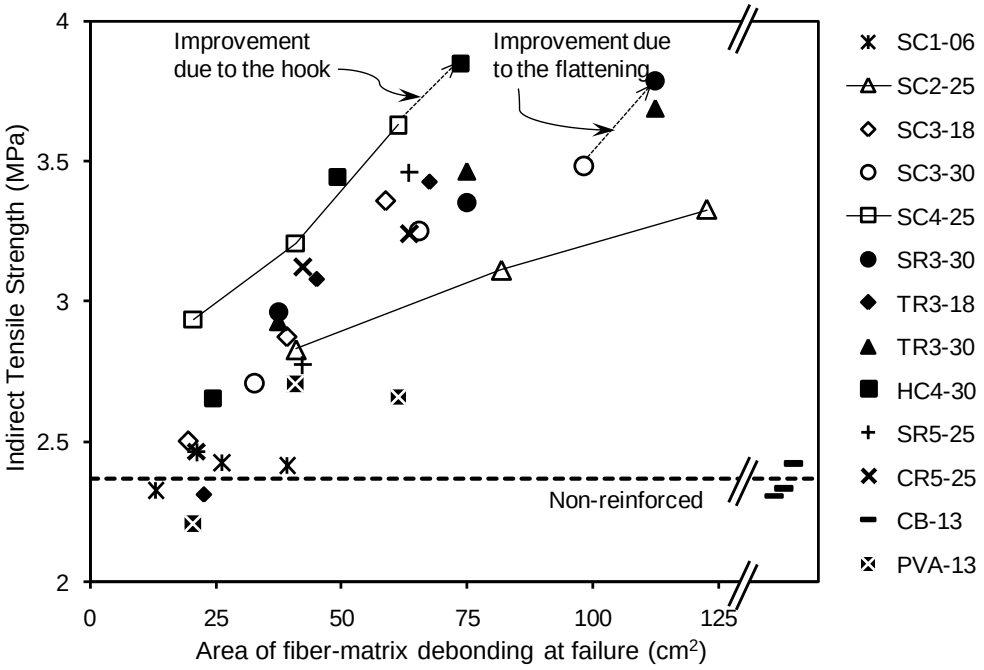

Fig. 5.15 Indirect tensile strength versus area of fiber-matrix debonding at failure

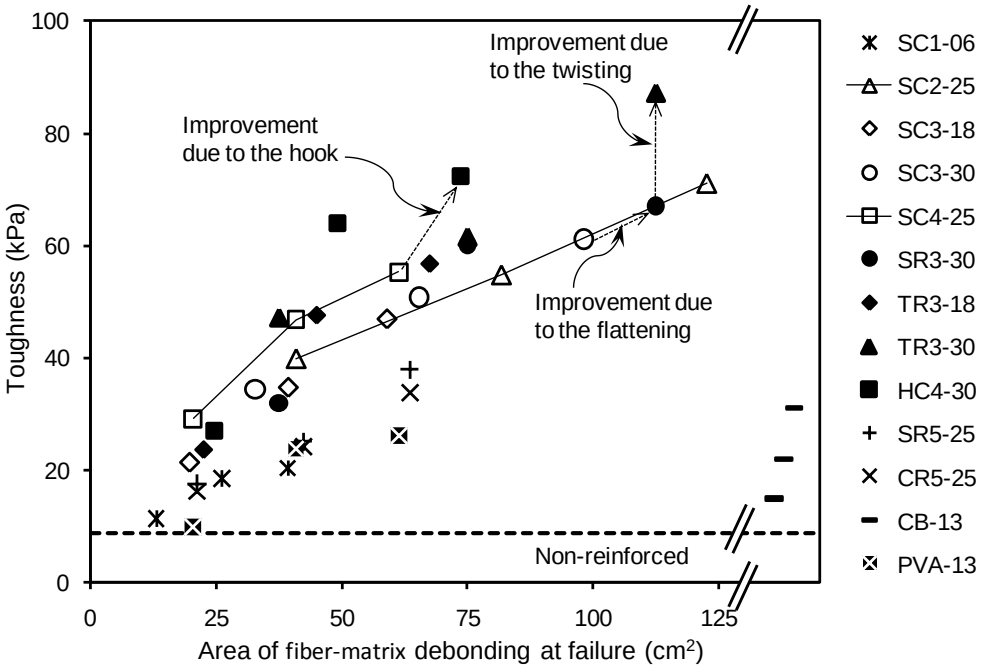

Fig. 5.16 Toughness versus area of fiber-matrix debonding at failure

REFERENCES

Abtahi, S. M., Sheikhzadeh, M., and Hejazi, S. M. (2010). "Fiber-reinforced asphalt-concrete - A review." *Construction and Building Materials*, 24(6), 871-877.

Anurag, K., Feipeng X., and Amirkhanian, S. N. (2009). "Laboratory investigation of indirect tensile strength using roofing polyester waste fibers in hot mix asphalt." *Construction and Building Materials*, 23(5), 2035-2040.

Asphalt Institute. (1993). *Mix Design Methods for Asphalt Concrete (MS-2)*. Asphalt Institute, Lexington, KY.

ASTM. (2001). "Standard Specification for Hot-Mixed, Hot-Laid Bituminous Paving Mixtures." *ASTM D3515-01*, West Conshohocken, PA.

ASTM. (2007). "Standard Specification for Performance Graded Asphalt Binder." *ASTM D6373-07*, West Conshohocken, PA.

ASTM. (2007). "Standard Test Method for Indirect Tensile (IDT) Strength of Bituminous Mixtures." *ASTM D6931-07*, West Conshohocken, PA.

Chen, H., Xu, Q., Chen, S., and Zhang, Z. (2009). "Evaluation and design of fiber-reinforced asphalt mixtures." *Materials and Design*, 30(7), 2595-2603.

García, Á., Schlangen, E., Van de Ven, M., and Liu, Q. (2009). "Electrical conductivity of asphalt mortar containing conductive fibers and fillers." *Construction and Building Materials*, 23(10), 3175-3181.

Kim, D-J, Naaman, A. E. and El-Tawil, S. (2008), "Comparative Flexural Behavior of Four Fiber Reinforced Cementitious Composites." *Cement and Concrete Composites*, 30(10), 917-928.

Liu, X., and Wu, S. (2009). "Research on the conductive asphalt concrete's piezoresistivity effect and its mechanism." *Construction and Building Materials*, 23(8), 2752-2756.

Minsk, L. D. (1968). "Electrically conductive asphalt for control of snow and ice accumulation." *Highway Research Record*, 227, 57-63.

Naaman, A. E. (2000). "Fiber reinforcement for concrete: Looking back, looking ahead." *Proceedings of Fifth RILEM Symposium on Fiber Reinforced Concrete (FRC), BEFIB' 2000*, Rilem Publications S. A. R. L., Cachan, France, 65-86.

Roque, R., Buttlar, W. G., Ruth, B. E., Tia, M., Dickison, S. W., and Reid, B. (1997). *Evaluation of SHRP indirect tension tester to mitigate cracking in asphalt pavements and overlays - Final Report to the Florida Department of Transportation*, University of Florida, Gainesville, FL.

Roque, R., Birgisson, B., Zhang, Z., Sangpetngam, B., and Grant, T. (2002). *Implementation of SHRP indirect tension tester to mitigate cracking in asphalt pavements and overlays - Final Report to the Florida Department of Transportation*, University of Florida, Gainesville, FL.

Sahmaran, M., and V.C. Li, (2010). "Engineered Cementitious Composites: Can it be Accepted as a Crack-free Concrete?", *TRB Transportation Research Record*, 2164, 1-8.

Wu, S., Mo, L., Shui, Z., and Chen, Z. (2005). "Investigation of the conductivity of asphalt concrete containing conductive fillers." *Carbon*, 43, 1358-1363.

Wu, S., Zhang, Y., and Chen, M. (2010). "Research on mechanical characteristics of conductive asphalt concrete by indirect tensile test." *Proceedings of the SPIE - The International Society for Optical Engineering*, 7522, 752265, doi: 10.1117/12.851473.

CHAPTER 6
IMPARTING ELECTRICAL CONDUCTIVITY INTO ASPHALTIC COMPOSITE

Precise control of the electrical resistivity of asphaltic composites is required in order to enable multifunctional applications. To this end, the effects of adding steel fibers and various conductive fillers on the resistivity of asphaltic composite were examined experimentally through 130 measurements for 40 asphalt mastics and mixtures. The electrical conductivity of asphalt mastics varies significantly with the type of conductive fillers, and among the tested fillers, natural flake graphite powder turned out to be most efficient for imparting conductivity into asphalt. Measurements showed that volume resistivity of asphalt mastic containing the natural flake graphite powder decreases as the content of the graphite increases, and sufficiently low resistivity can be obtained only adding the graphite powder without conductive fibers. These results imply that the electrical resistivity of asphaltic composite can be manipulated over a wide range to fit the requirements of various multifunctional applications.

6.1 INTRODUCTION

Multifunctional materials are structural materials that have non-structural functions in addition to the traditional structural functions. According to Gibson (2010), technical papers on multifunctional materials have been published since 2000, and have steadily increased till now. Multifunctional concrete (cement-based composites) is one of the actively studied multifunctional materials. Possible non-structural applications of multifunctional concrete include vibration damping, strain sensing, electromagnetic /magnetic shielding, electrical conductivity (for grounding, lightning protection, electrical contacts, and cathodic protection), and thermal insulation (Chung 2003). As reviewed in Chapter 2, the idea of utilizing electrical conductivity in asphalt concrete was suggested as early as 1968 (Minsk 1968) although interest in it has recently increased as evinced by

the publication of a number of research studies. Among the suggested non-structural functions of asphalt concrete are snow and ice removal (Minsk 1968), self-sensing (Liu and Wu 2009; Huang et al. 2006), self-healing and deicing (Garcia et al. 2009), and energy harvesting (Mallick et al. 2008; Lee and Correia 2010).

In theory, electrical conductivity of asphalt concrete entails exploitation of useful non-structural properties such as piezo-resistivity and electrical heating. Piezo-resistivity is the property wherein varying electrical resistivity can be achieved as a result of the application of pressure. Such a property enables self-sensing. Self-healing and deicing are applications that stem from the ability to electrically heat asphalt. For energy harvesting from asphalt pavement, Mallick et al. (2008) and Lee and Correia (2010) suggested installation of a heat exchange system beneath the pavement surface. Although the practicality of the proposed heat exchange system appears doubtful, the studies in Mallick et al. (2008) and Lee and Correia (2010) suggest that there is much available energy on the pavement surface that can be harvested. Other promising methods for energy harvesting entail the use of materials with piezo-electrical, pyro-electrical, and thermo-electrical properties. Fig. 6.1 summarizes the possible non-structural applications of conductive asphalt and their benefits.

A prerequisite for enabling multifunctional applications is the ability to precisely control the electrical conductivity of asphalt concrete. As listed in Table 6.1, asphalt and asphalt concrete have very high electrical resistivity, and are actually considered to be insulting materials. However, previous investigators agree that the poor electrical conductivity of asphaltic materials can be improved by adding conductive fillers and/or fibers (Liu and Wu 2009; Huang et al. 2006; Garcia et al. 2009). Fig. 6.2 illustrates a typical pattern of electrical resistivity variation with the addition of conductive additive content as provided by Garcia et al. (2009). In their trials, which entailed adding various contents of graphite and steel wool, the transition between insulated phase and conductive phase is very rapid. Such a sudden increase in electrical conductivity is called the percolation threshold (Wu et al. 2005), and is commonly observed in other studies on conductive asphalt (Huang et al. 2006). Another common observation from the previous investigators is necessity of employing conductive fibers as well as conductive fillers. For example, according to Garcia et al. (2009), when the steel wool was not added, the

volume resistivity of asphalt mortar steadily decreases with increase in graphite content. However, the reduction in volume resistivity due to the graphite alone was not sufficient to make the asphalt mortar conductive.

By narrowing the adjustable volume resistivity range of conductive asphalt, the percolation threshold introduces limitations for developing various multifunctional applications. For example, assuming the situation of heating asphalt pavement for self-healing or deicing, the resistivity of the asphalt pavement should be controlled to be properly to ensure the safety on the roadway in service as well as the good energy efficiency. Therefore, as illustrated in Fig. 6.2, the rapid drop of the volume resistivity versus conductive content curve needs to be transformed into a curve with gradual slope to enable precise manipulation of electrical resistivity over a wide range. This is the objective of the study presented in this chapter.

Fig. 6.3 illustrates the strategy employed for controlling the electrical resistivity of asphalt concrete. The top left part of Fig. 6.3 shows the composition of a traditional asphalt concrete mixture made of asphalt binder and aggregate. This is a non-conductive configuration. The top right figure shows a situation when a certain amount of conductive fibers, which is sufficient for reinforcement but not sufficient for imparting conductivity, is added into the mixture. Adding more conductive fibers, the mixture passes the percolation threshold, and becomes conductive as illustrated in the bottom left part of Fig. 6.3. In this situation, conductivity stems from continuous contact of conductive fibers, thereby making manipulation of the resistivity difficult. The premise of this study is that the electrical resistivity of asphalt mastic containing asphalt binder and conductive filler can be manipulated when the proper type and quantity of conductive filler is added. As illustrated in the bottom right part of Fig. 6.3, the resistivity of the asphalt mixture can also be precisely controlled by filling the gap between aggregates and conductive fibers with conductive mastic. Therefore, this study investigates the effect of fibers and fillers separately.

6.2 EXPERIMENTAL SET-UP

6.2.1 Materials

Conductivity measurements were made for two asphaltic composites: steel fiber reinforced asphalt concrete (SFRAC) and asphalt mastic (a mixture of asphalt binder and filler containing conductive filler). The former was achieved by measuring the electrical resistivity of the SFRAC specimens described in Chapter 5, while the latter employed a new type of asphalt mastic specimen as described next. PG 64-22 (ASTM D6373 2007) asphalt binder was used for both SFRAC and asphalt mastic specimens.

Table 6.2 lists the types and properties of the conductive fillers used in this study. Four types of graphite having different particle shape and size and one type of carbon black were selected from thousands of commercially available graphite types. The maximum particle size was selected to be less than 75 μm to satisfy the particle size requirement for filler (pass #200 sieve). Although the shape of idealized graphite crystal is thin hexagonal plate (Fig. 6.4), the actual particle shape of graphite varies with the source and manufacturing process. Fig. 6.5 compares pictures of natural flake graphite and synthetic graphite taken from scanning electron microscope (SEM). As listed in Table 6.2, G146, G508, and GA99 have similar particle size but different particle shapes. The name for G508, amorphous graphite, combines two words carrying conflicting meaning because the graphite should have a crystalline structure. Therefore, the meaning of amorphous in this case is that the shape of the particles is irregular. On the other hand, CB 5303, carbon black, is an amorphous material literally, and hence, the average particle size of CB5303 is far smaller than graphite. G4827 is manufactured to have high surface area, and its particle size is small as is with CB5303.

6.2.2 Specimen and Equipment

Two types of SFRAC specimens (TR3-18 and TR3-30) were used to investigate the effect of fibers on the conductivity of asphalt concrete. Specimens containing 0.5%, 1.0%, and 1.5% of steel fibers were prepared following the procedures described in Section 5.2.2.

Asphalt mastics were prepared for examining the effect of conductive filler. In the

mixture design for the indirect tension test specimens described in Chapter 5, the weight fraction of asphalt binder and traditional filler is 5.0% each. Therefore, the asphalt mastic is produced to have 50% asphalt binder and 50% filler by weight. Portland cement is used as traditional filler, and a part or whole of the cement filler is replaced by the conductive filler. Fig. 6.6 shows the naming scheme for the asphalt mastics, where the latter part of the name represents the content of conductive filler. For example, 'G146-m30' implies the mastic is composed of 50% asphalt binder, 20% non-conductive (cement) filler, and 30% G146 graphite. Since the weight fraction of the filler is 50% of the asphalt mastic, the maximum content of conductive filler is 50%.

The prepared binder and fillers were heated at 150°C for two hours, and then mixed manually. The mixed mastic was then spread over oven dried wood blocks as shown in Fig. 6.7a. The size of the wood blocks is 38×19×300 mm (width×height×length). The completed specimens were conditioned at 150°C for an hour before and after the mastic was spread on. The average thickness of the spread mastic was then computed by weighing the wood panels before and after applying the asphalt mastics, estimating the volume of the applied mastic by dividing the weight by the density, then dividing the volume by the area of the block.

The asphalt mastic specimens were conditioned at room temperature for at least eight hours before conductivity measurements were taken. The thin and bright bands over the mastic specimens displayed in Fig. 6.7a are copper tape, which were installed to serve as electrodes. To ensure full contact, silver paste was applied between the mastic and the copper tape. The distance between electrodes is 50 mm. When traditional two terminal sensing is used, several different measurements are possible by selecting different electrodes. As shown in Fig. 6.7b, four terminal sensing was also employed. Fig. 6.8a shows the SFRAC specimen. Silver paste is applied to the top and bottom of the specimen, and copper tape is attached over the silver paste. Hence, only two terminal sensing was used for SFRAC.

Impedance/Gain-Phase Analyzer 1260 (Solartron Inc.) was used to measure the conductivity of the SFRAC and asphalt mastic specimens. The device can measure electrical resistivity up to 100 MΩ. Fig. 6.7b and 6.7c show the measurement setup.

6.2.3 Electrical Resistivity

Electrical resistance was measured at room temperature. Volume resistivity (ρ, Ω·cm) can be calculated from the measured resistances (R, Ω) as shown in Eq. (6.1).

$$\rho = R\frac{A}{l} \tag{6.1}$$

where, A and l are the cross sectional area (cm^2) and the length (cm) of the specimen, which is assumed to be of uniform cross-section. The electric field is assumed to be constant, and the end-effects are considered to be negligible because the electrodes are installed over the thin mastics.

6.3 RESULTS AND DISCUSSION

6.3.1 Effect of Steel Fibers

Fig. 6.8b shows the conductivity measurements for SFRAC specimens. The electrical resistance was measured using AC current for the frequency range from 0.1 to 10^6 Hz. The flat line at the bottom of Fig. 6.8b is the resistance of TR3-30 specimen reinforced with 1.5% steel fibers. As shown in the figure, when the conductivity of the material is in the measurable range, the measured resistivity will be constant over the frequency range. The other three lines in Fig. 6.8 show a typical signal pattern for non-conductive materials. For those, resistance fluctuates up to 100 Hz and exceeds 100 MΩ, which is the measurable limit of the equipment. Such a signal pattern indicates that the measured value is meaningless, and the material is considered to be non-conductive in this study.

Fig. 6.8b implies that only the specimen containing 1.5% steel fiber passes over the percolation threshold that was reported by the previous investigators. In other words, the steel fibers in the specimen are in contact with each other, making the material conductive. Other SFRAC specimens, i.e. TR3-18 with various fiber contents, turned out to be non-conductive even with 1.5% fiber content. This results support the hypothesis in Fig. 6.3 that high fiber content can make asphalt concrete conductive, but that conductivity cannot be solely manipulated by the use of fibers.

6.3.2 Effect of Conductive Fillers

Fig. 6.9 compares the frequency sweep results for asphalt mastics containing G146,

G508, and GA99 at 50%. The figure demonstrates two important observations for conductive asphalt that have not been reported previously: (1) electrical conductivity of asphalt mastic containing graphite powder significantly varies with the type of graphite, and (2) sufficiently low electrical resistivity can be obtained only by adding proper graphite filler without conductive fibers. The first observation means that the adjustable resistivity range depends on the type of conductive filler. The second observation implies that the adjustable resistivity range of using conductive filler is much wider than previously reported. Considering that previous investigators reported that the conductive fillers can cause gradual change in resistivity of asphaltic materials, the precise control of electrical resistivity is just a matter of selecting the proper graphite type. As shown in Fig. 6.9, G146 induces the highest improvements in conductivity among the tested fillers, and the volume resistivity calculated from the measured resistance (R = 297Ω) is 3.96 Ω·cm.

To enable precise conductivity manipulation, electrical resistivity needs to decrease gradually with the increase of the content of conductive filler. Fig. 6.10 compares the resistances of the asphalt mastics containing different amount of G146 graphite. Starting at 20% filler content of G146 graphite, the asphalt mastic becomes conductive, and the resistance decreases as the graphite content increases. Such stepwise improvement in conductivity implies the possibility of precisely controlling asphalt conductivity.

To construct a master curve relating electrical resistivity and content of G146, a number of measurements were made focusing on G146 content ranging from 20% to 40%. Resistance measurements were made from three different specimens having the same G146 content to ensure repeatability. As shown in Fig. 6.11, the scatter range is wide when the content of G146 is 20% and decreases with increase of G146 content.

The variations of conductivity with the amount of fillers were investigated for other fillers in Table 6.2. Fig. 6.12 and 6.13 show the variation of volume resistivity of the mastics containing G508 and GA99, respectively. Those mastics are non-conductive up to filler contents of 40%, and become conductive at 50%, the maximum content of conductive fillers. Considering the price of graphite listed in Table 6.2, G508 still has a competitive edge in cost compared to GA99 and G146, but is less efficient in terms of imparting conductivity.

Fig. 6.14 displays the variation of volume resistivity with the content of G4827. The

mastics with G4827 were produced with up to 30% content only (and not up to 50%) because of difficulty in mixing. In particular, the mastic with 30% G4827 was very stiff, and it is presumed that the high surface area of G4827 is to be blamed for the difficulty since all the surface area needs to be coated by asphalt binder as the mixing progresses. The most difficulty encountered in mixing was observed in CB5303. Even with 10% filler content, the mastic was thick and did not allow additional filler. In contrast, the mastic with GA99 was most watery, followed by G508 and G146. Therefore, it was concluded that G4827 and CB5303 are not suitable for imparting conductivity.

The conductivity effect of the fillers is summarized and compared in Fig. 6.16. Each dot in the figure represents the averaged volume resistivity measured from the same conditions. Fig. 6.16 confirms that G146 is most efficient for imparting conductivity into asphalt, and provides the greatest possibility for manipulating resistivity over a wide range.

6.4 CONCLUSIONS

The electrical conductivity of asphalt concrete containing steel fibers and asphalt mastic with conductive filler was measured to investigate the possibility of manipulating volume resistivity of asphalt concrete. The effect of steel fiber and conductive filler are evaluated separately. Two types of SFRAC and five types of conductive fillers were tested in this study. The important findings can be summarized as follows.

- A sudden change in electrical resistivity from no conduction to conduction, i.e. the so-called percolation threshold, is observed in specimen containing steel fibers. Achieving this threshold implies that the asphalt concrete is conductive and it is therefore impossible to manipulate its resistivity.
- Sufficiently low electrical resistivity can be obtained by replacing a part of the fillers by a proper type of graphite powder in asphalt mastics. This means that the adjustable range of resistivity using conductive filler can be controlled.
- Electrical conductivity of asphalt mastics varies significantly with the type of conductive fillers. Five types of conductive fillers including four graphite types and a

type of carbon black were tested in this study. It turned out that natural flake graphite powder is the most efficient in imparting conductivity into asphalt.

- The volume resistivity of asphalt mastic with natural flake graphite powder varies widely with the amount of the graphite powder mixed in the mastic. This implies that the resistivity of asphaltic composite can be manipulated over a wide range of conditions thereby various multifunctional applications.

Table 6.1 Volume resistivity of the materials used in the study

Materials	Volume Resistivity (Ω·cm)	Reference
Asphalt	$10^{13} – 10^{15}$	Wu et al. (2003)
Asphalt Concrete	$10^{9} – 10^{11}$	Wu et al. (2003)
Steel	$7×10^{-7}$	Garcia et al. (2009)
Wood – Oven dry	$10^{17} – 10^{18}$	Forest Products Laboratory (2010)
Wood – Wet (at fiber saturation)	$10^{5} – 10^{6}$	Forest Products Laboratory (2010)

Table 6.2 Types of conductive fillers tested for conductive asphalt (data provided by Asbury Carbons Co.)

ID	Description	Price/lb @2,500 lbs	Resistivity @200 psi (Ω•cm)	Particle size (μm)	Surface area (m^2/g)	True density (g/cc)
G146	Natural flake graphite	$1.27	0.03-0.05	< 44	6.35	2.32
G508	Amorphous graphite	$0.64	0.1	< 44	-	-
GA99	Synthetic Graphite	$1.01	0.03-0.05	< 44	8.47	2.22
G4827	Graphite with ultra high surface area	$4.47	0.25	< 10	249	-
CB5303	Carbon black	$7.87	0.3	0.030	254	-

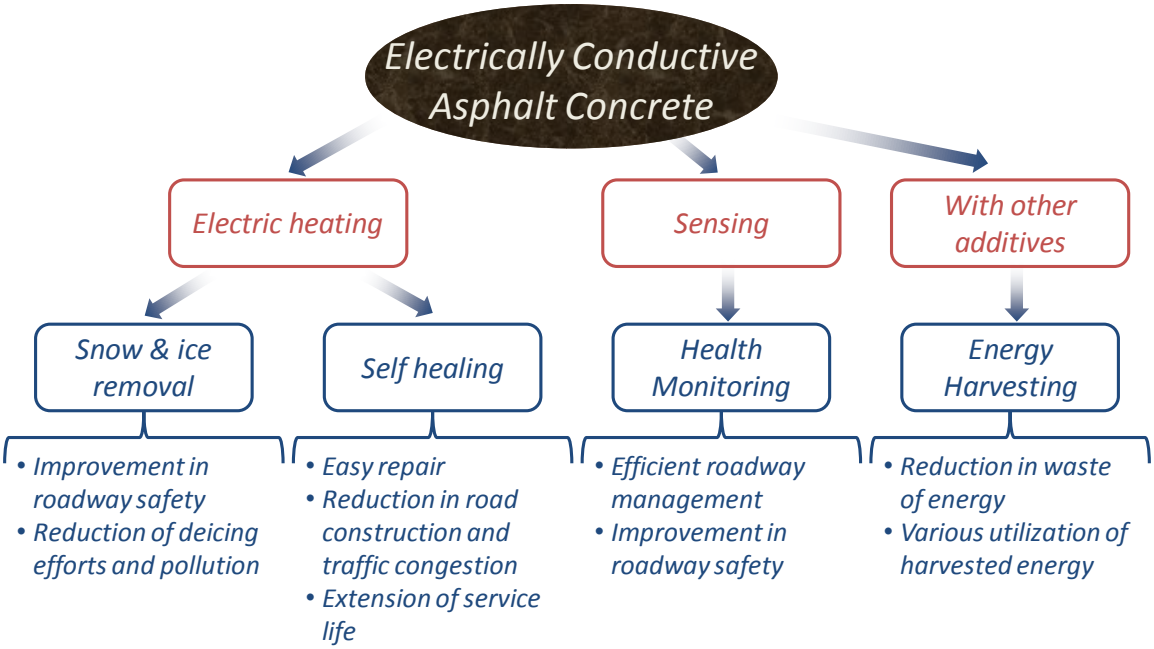

Fig. 6.1 Possible applications of conductive asphalt concrete

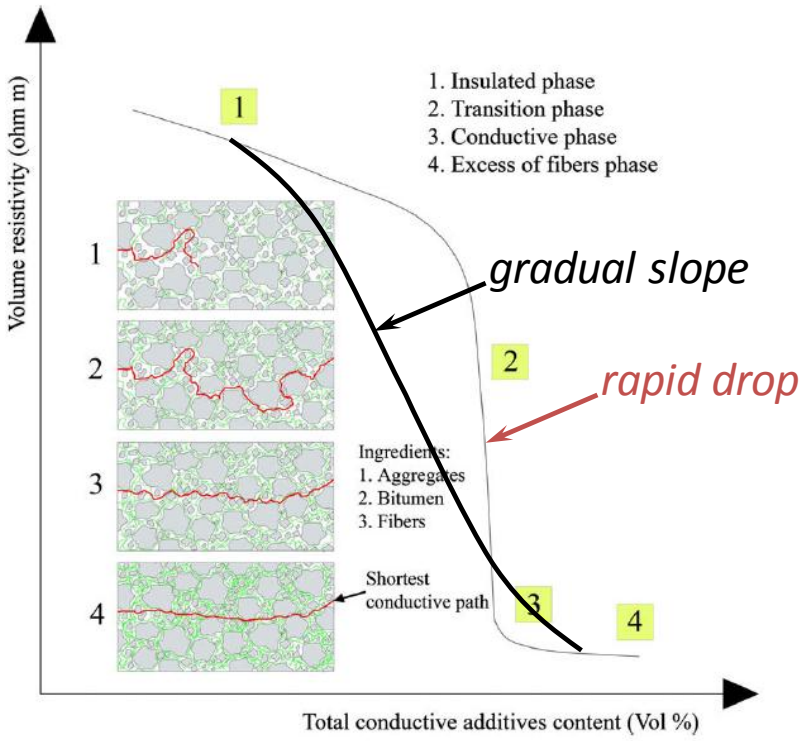

Fig. 6.2 Objective of imparting conductivity (compared to the result of Garcia et al. 2009)

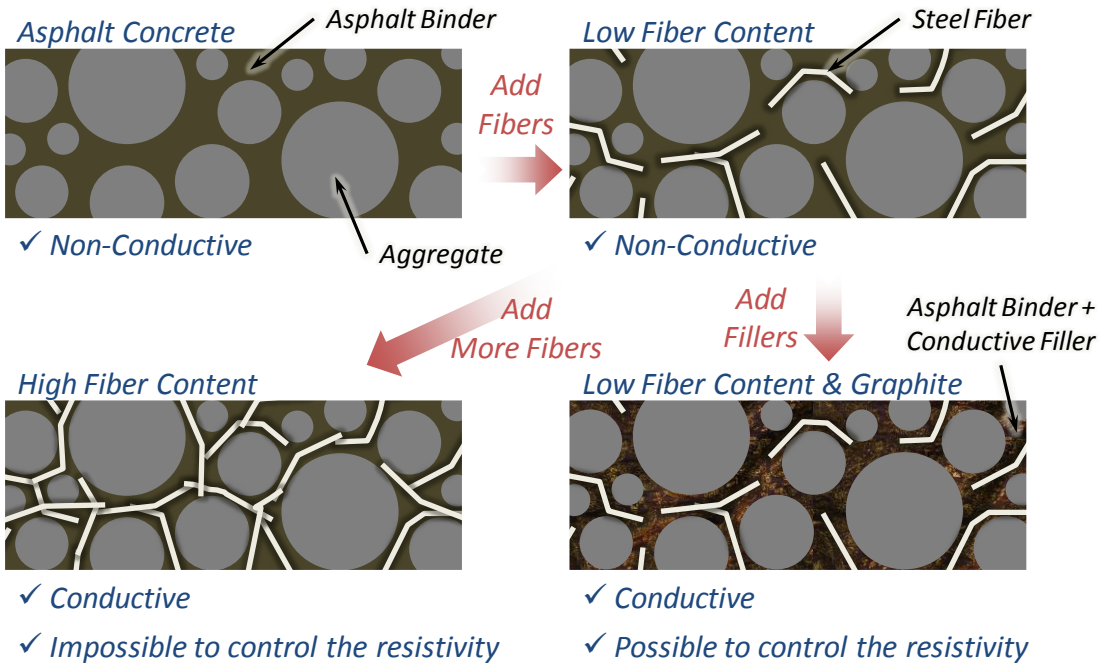

Fig. 6.3 Strategy for manipulating electrical resistivity of asphalt concrete

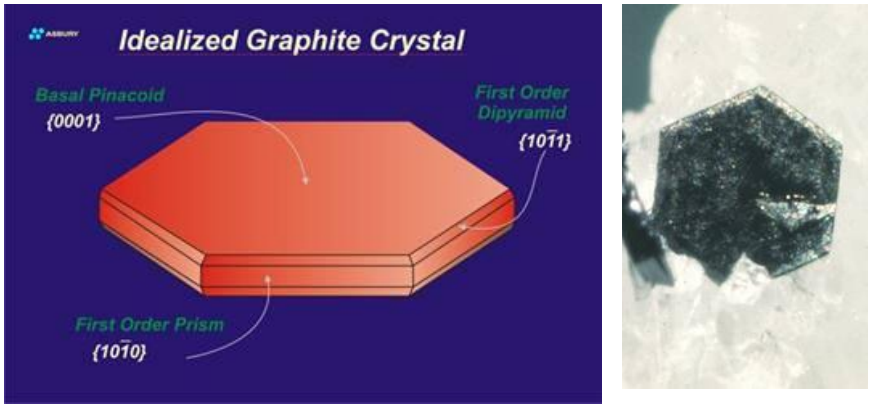

Fig. 6.4 Crystal structure of ideal graphite (Asbury Carbons 2011a)

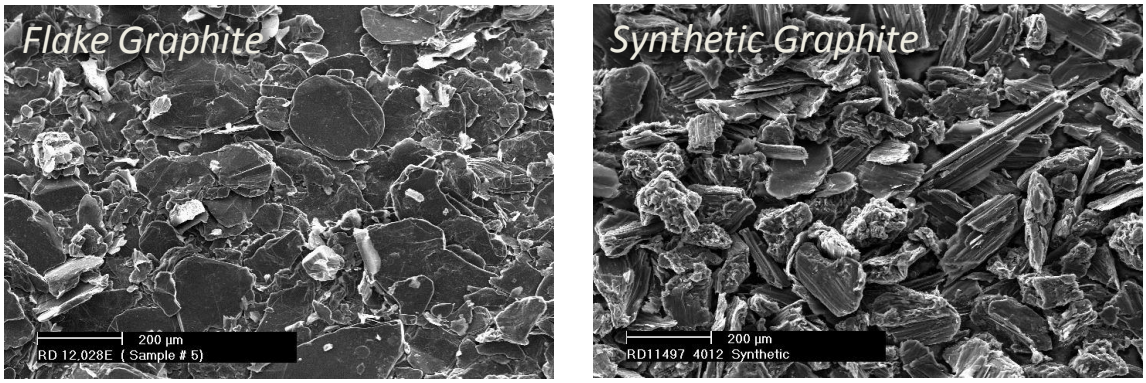

(a) natural flake graphite (Asbury Carbons 2011a)

(b) synthetic graphite (Asbury Carbons 2011b)

Fig. 6.5 SEM photo of graphites

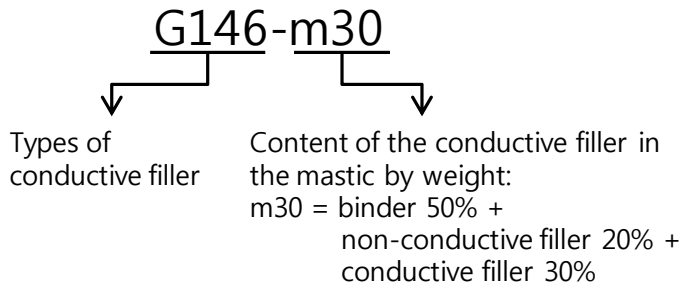

Fig. 6.6 Naming scheme for asphalt mastic specimens

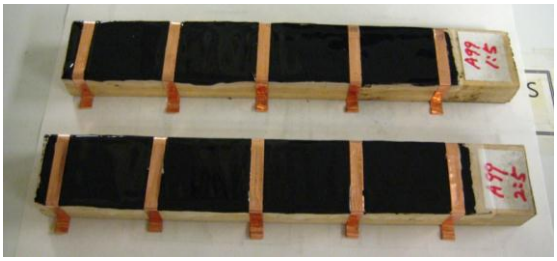

(a) specimen

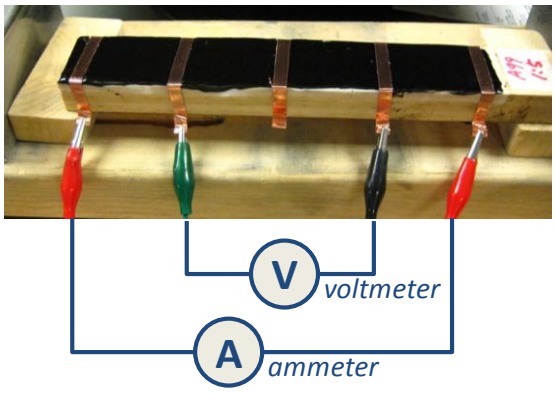

(b) four terminal sensing

(c) measurement setting: Solartron 1260A

Fig. 6.7 Specimens and measurement setup for conductivity measurement

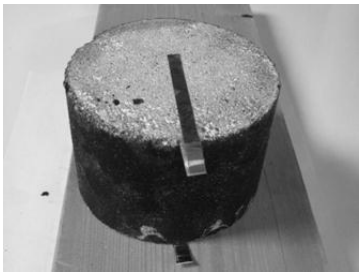

(a) fiber reinforced cylindrical specimen

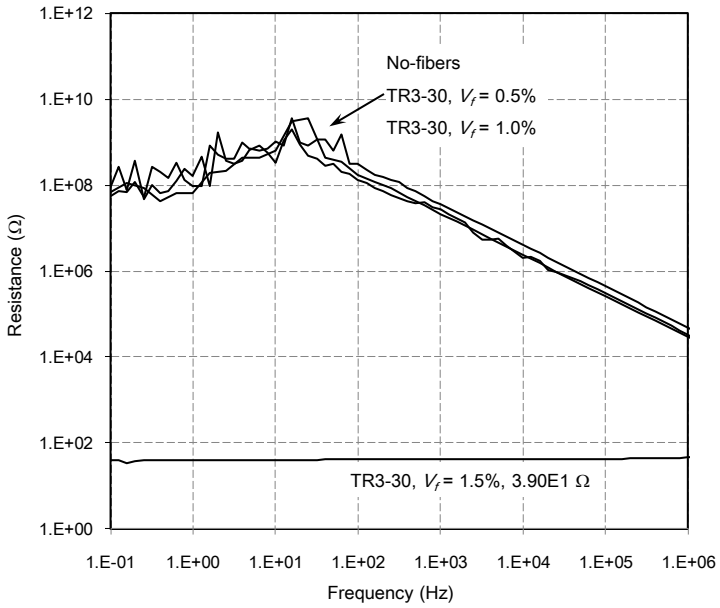

(b) conductivity measurement

Fig. 6.8 Examples of conductivity measurement of fiber reinforced asphalt concrete: TR3-30

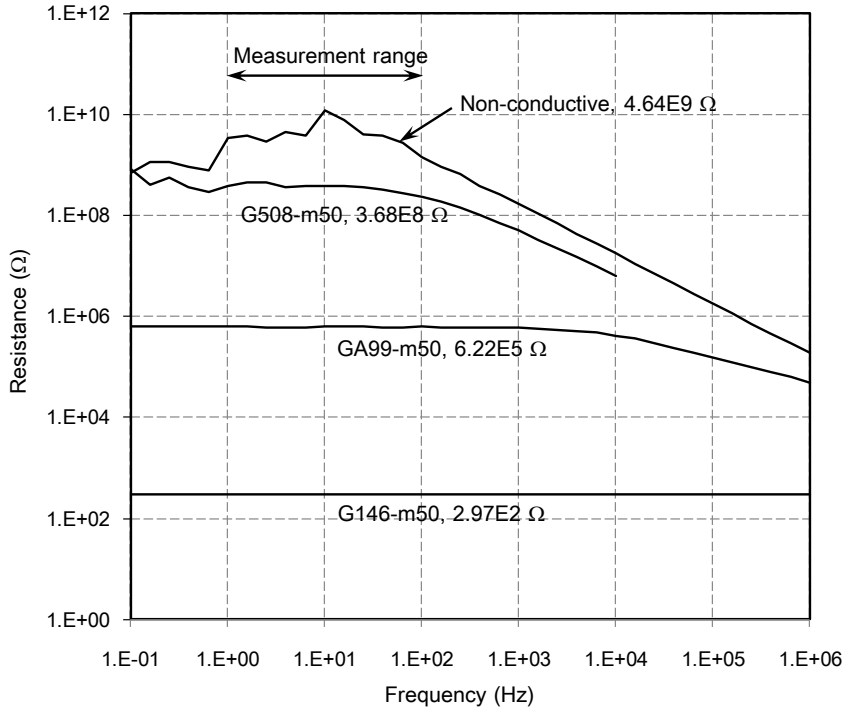

Fig. 6.9 Conductivity measurement of asphalt mastics with various conductive fillers

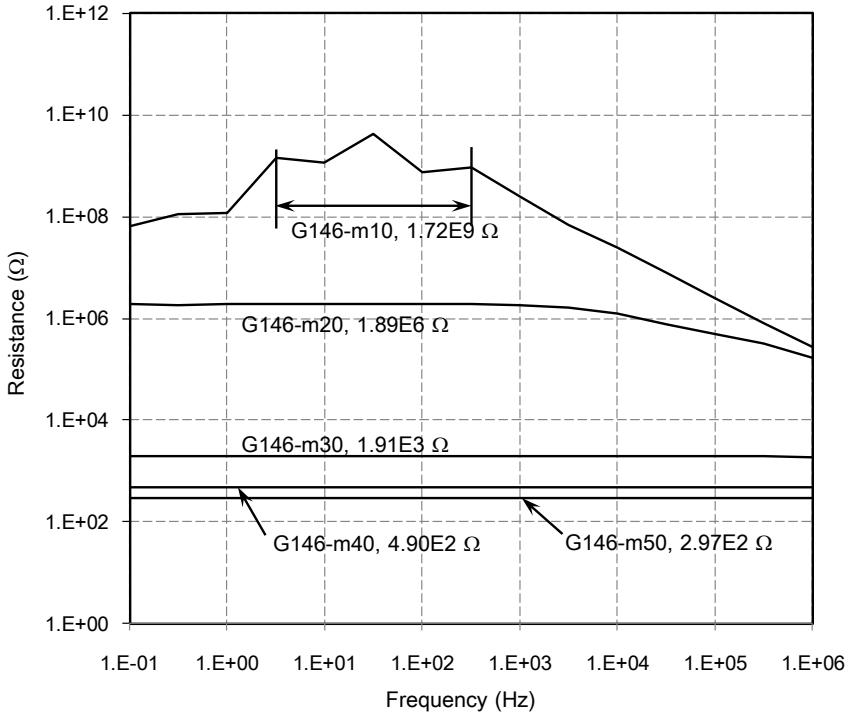

Fig. 6.10 Variation of resistivity with G146 contents

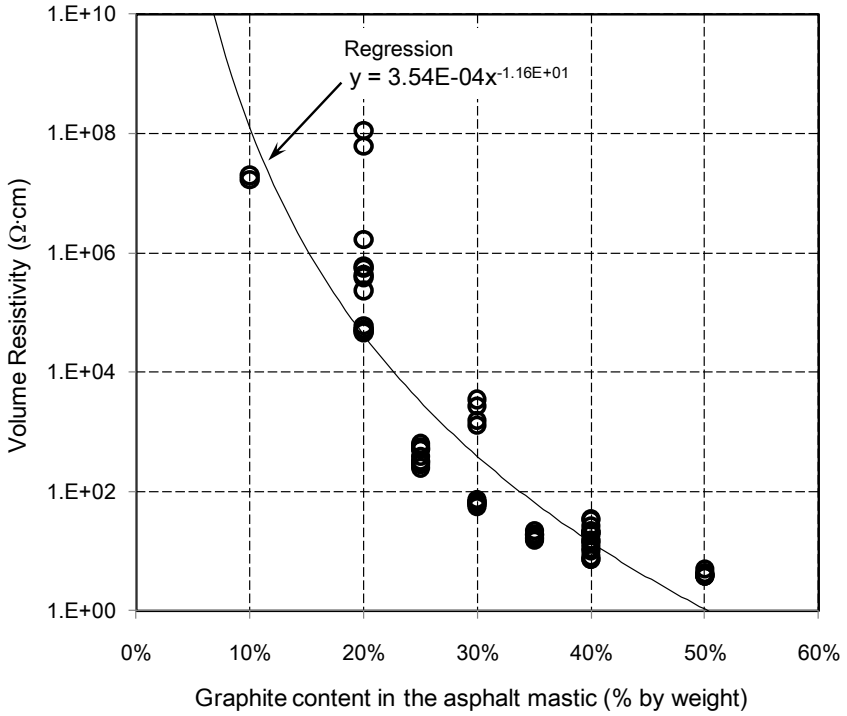

Fig. 6.11 Variation of volume resistivity with graphite contents: G146

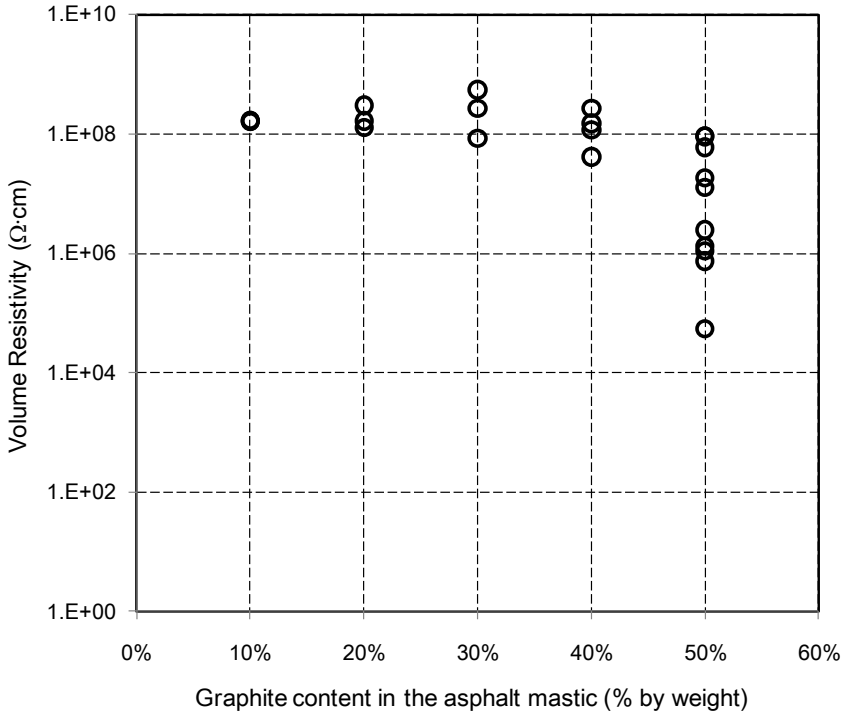

Fig. 6.12 Variation of volume resistivity with graphite contents: G508

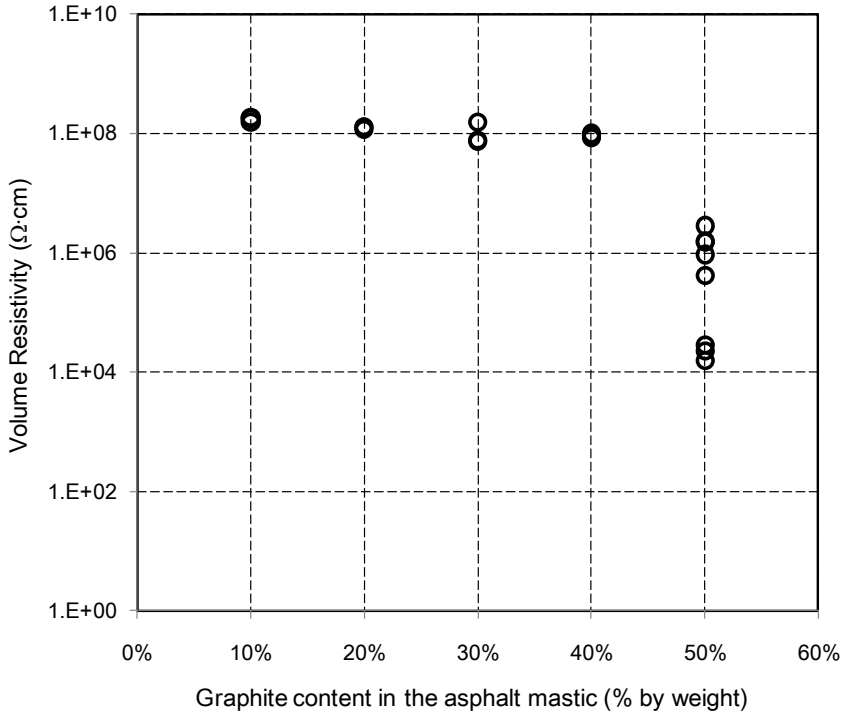

Fig. 6.13 Variation of volume resistivity with graphite contents: GA99

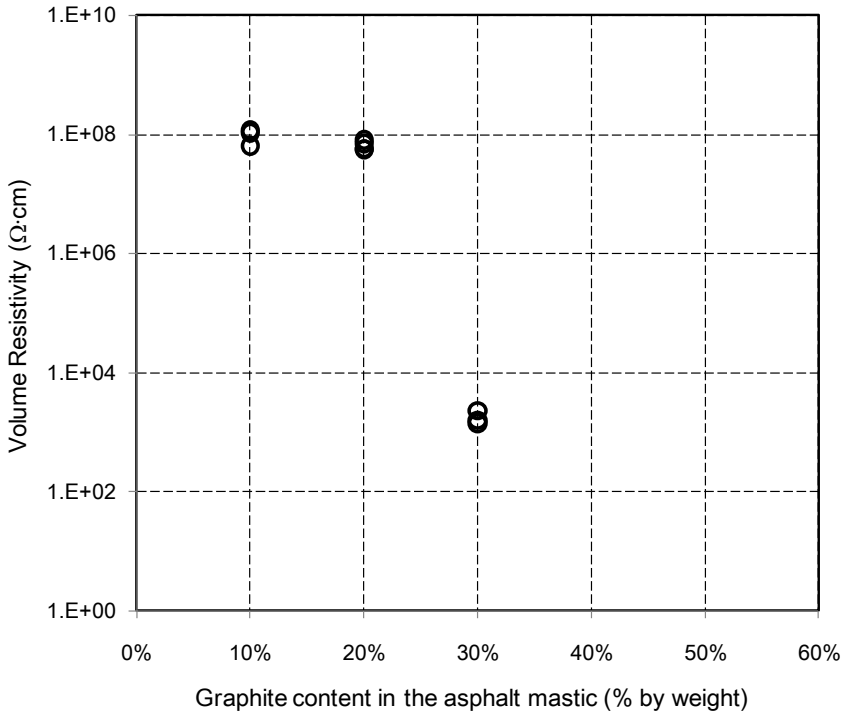

Fig. 6.14 Variation of volume resistivity with graphite contents: G4827

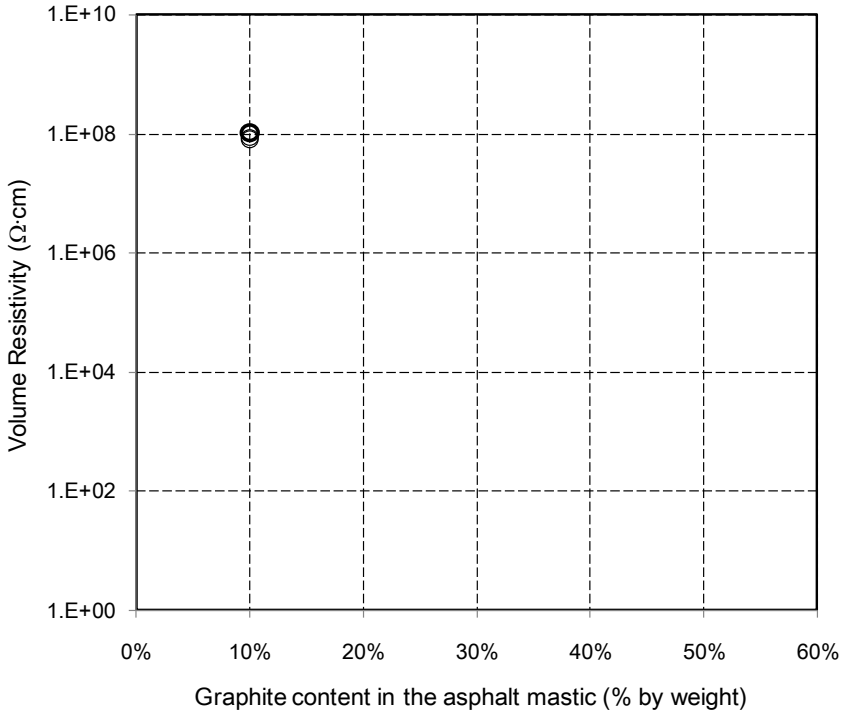

Fig. 6.15 Variation of volume resistivity with graphite contents: CB5303

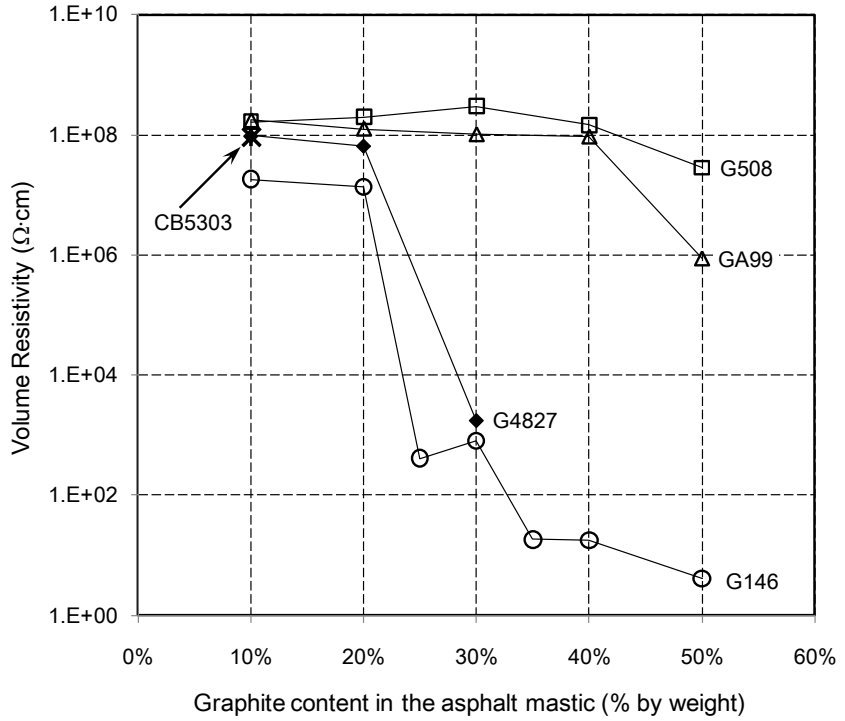

Fig. 6.16 Comparison of averaged volume resistivity

REFERENCES

Asbury Carbons (2011a). “Natural flake graphite.” *Materials*, <http://www.asbury.com/Natural-Flake-Graphite.html> (Apr. 21, 2011).

Asbury Carbons (2011b). “Synthetic Graphite Advanced Topics; Morphology.” *Materials*, <http://www.asbury.com/images/pdf/SyntheticGraphitePartII.pdf> (Apr. 21, 2011)

ASTM. (2007). "Standard Specification for Performance Graded Asphalt Binder." *ASTM D6373-07*, West Conshohocken, PA.

Chung, D. D. L. (2003). *Multifunctional Cement-Based Materials*, Marcel Dekker, Inc., New York, NY.

Forest Products Laboratory. (2010). *Wood handbook – Wood as an engineering material*. General Technical Report FPL-GTR-190., U.S. Department of Agriculture, Forest Service, Forest Products Laboratory, Madison, WI.

García, Á., Schlangen, E., Van de Ven, M., and Liu, Q. (2009). "Electrical conductivity of asphalt mortar containing conductive fibers and fillers." *Construction and Building Materials*, 23(10), 3175-3181.

Gibson, R. F. (2010). "A review of recent research on mechanics of multifunctional composite materials and structures." *Composite Structures*, 92, 2793-2810.

Huang, B., Cao, J., Chen, X., Shu, X., and He, W. (2006). "Laboratory Investigation into Electrically Conductive HMA Mixtures." *Journal of the Association of Asphalt Paving Technologists*, 75, 1235-1253.

Lee, K. W. and Correia, A. J. (2010). *A Pilot Study for Investigation of Novel Methods to Harvest Solar Energy from Asphalt Pavements*, A Final Report for Korea Institute of Construction Technology (KICT), University of Rhode Island, Kingston, RI

Liu, X., and Wu, S. (2009). "Research on the conductive asphalt concrete's piezoresistivity effect and its mechanism." *Construction and Building Materials*, 23(8), 2752-2756.

Mallick, R. B., Chen. B. L., Bhowmick, S., and Hulen, M. S. (2008). “Capturing Solar Energy from Asphalt Pavements.” *Proceedings of International ISAP Symposium on Asphalt pavements and Environment*, International Society for Asphalt Pavements (ISAP), Zurich, Switzerland, August 18-20, 2008.

Minsk, L. D. (1968). "Electrically conductive asphalt for control of snow and ice accumulation." *Highway Research Record*, 227, 57-63.

Wu, S., Mo, L., and Shui, Z. (2003). "Piezoresistivity of graphite modified asphalt-based composites." *Key Engineering Materials*, 249, 391-396.

Wu, S., Mo, L., Shui, Z., and Chen, Z. (2005). "Investigation of the conductivity of asphalt concrete containing conductive fillers." *Carbon*, 43, 1358-1363.

CHAPTER 7
IMPROVED GEOMETRIC DESIGN OF BRIDGE ASPHALT PLUG JOINT

An asphalt plug joint (APJ) is a type of bridge expansion joint providing quick, easy, and cheap installation along with good surface flatness. However, APJs are known to suffer from premature failure, and their behavior, especially under thermal movement, has not yet been fully understood. In this chapter, the behavior of a typical APJ subjected to thermal and traffic loads is examined through a series of finite element analyses employing a temperature-dependent visco-plastic material model. The material parameters are calibrated by using previously published test data, and the model is validated by comparing simulated responses to APJ test data. The developed models are then used to investigate stress and strain distributions, vulnerable locations to cracking failure, and local demands at those locations when a prototype APJ is subjected to various loading and temperature conditions. Sensitivity studies are also conducted to quantify the effect of debonding the bottom of the APJ and loading rate. The model results shed light about APJ response under traffic and thermal loading and provide new, fundamental information that can be used to improve the durability of APJs. For example, the simulation results suggest that intentionally debonding the interface between the gap plate and the APJ is a practical and low cost solution to mitigate the risk of premature APJ failure. In addition, using the developed finite element model, a parametric study is conducted to find an optimized geometry to prevent the premature failure. The key parameters investigated are gap plate width, gap plate thickness, gap plate edge geometry and geometry of the interface between pavement and APJ. The resulting information is synthesized into a proposed alternative APJ design that minimizes local demands deemed to be responsible for the observed early failures.

7.1 INTRODUCTION

Thermal expansion or contraction of structural members can cause high internal stresses that adversely affect the response and load carrying resistance of a structure. Many engineers prefer to release thermally induced stresses, typically through installation of expansion joints. In bridges, expansion joints must also be capable of supporting traffic across the joint.

An asphalt plug joint (APJ) is a type of bridge expansion joint that is becoming popular with some State Departments of Transportation in the United States (Transportation Research Board 2003). According to Bramel et al.'s survey (1999), 41 states have installed APJs. Of those, 23 states still use APJs for either new construction or retrofit, without geographic preference. APJs are made of flexible asphalt concrete usually comprising 20% asphalt and 80% aggregates by weight. The APJ material is placed into a prepared space between pavements permitting a smooth ride across the joint while accommodating thermal movements of the bridge deck at the same time. According to the Bridge Joint Association of the United Kingdom (2003), the typical size of an APJ is 500 mm wide and 100 mm deep and its allowable movement without cracking at the lowest operating design temperature is ±20 mm. ASTM D6297-01 specifies that the standard minimum blockout dimensions for an APJ are 50×500 mm, and the maximum allowable movement is 25 mm. Fig. 7.1 shows an illustration of a typical APJ.

APJs offers better bridge surface flatness than other types of joints. Additional advantages of APJs are their simplicity and low installation cost (Qian et al. 2000). They are also easily repaired with relatively low cost. On the other hand, APJs suffer from premature failure, sometimes as early as 6 months after installation even though they are generally expected to have a service life of about 6-7 years (Qian et al. 2000). Bramel et al. (1999) reported that premature failure was one of the important problems hindering widespread acceptance of APJs in the US.

APJs have been developed by trial and error and are widely used without a good understanding of their behavior (Bramel et al. 1999). In fact, to date, very few research projects have actually investigated the performance and behavior of APJs. Comprehensive studies on APJ were conducted by Bramel et al. (1999) in the United

States and Partl et al. (2002) in the EU. Both studies aimed to establish a practical guideline for installation and design of APJs.

The various failure modes in APJs can be categorized into two classes: cracking related failures and rutting. According to Bramel et al. (1999), two locations within an APJ are especially vulnerable to cracking as a result of bridge movement: 1) the interface between the pavement and joint, and 2) the edges of the embedded steel gap plate (Fig. 7.1). Based on the premise that APJ failures occur as a result of traffic-related fatigue, Reid et al. (1998) suggested two alternative geometries that are less prone to fatigue than the standard configuration. Subsequently, Qian et al. (2000) proposed an optimum shape for one of the alternative designs suggested by Reid et al. (1998). These two studies provided good insight into the reasons for early failure in APJs. However, both studies made assumptions that limit their generality: 1) only traffic loading was considered in the analysis, i.e. loading due to bridge thermal movement was not considered, and 2) the stress concentration at the end of the gap plate was not considered.

The goal of the study reported in this chapter is to (1) develop a thorough understanding of APJ behavior subjected to traffic and thermal loads and (2) develop an improved and practically feasible APJ design that mitigates stress and strain concentrations through detailed visco-plastic finite element analyses. The premise of the study is that improved APJ performance can be obtained by minimizing stress and strain demands within the APJ, a task achieved through parametric simulations. The model results provide new, fundamental information that can be used to improve durability and serviceability of APJs.

7.2 DEVELOPMENT OF FINITE ELEMENT MODEL

Two-dimensional, plane strain finite element models are used in the investigation of APJ response. The typical APJ design (500×100 mm of width×depth with 200×10 mm gap plate) suggested by the Bridge Joint Association (2003) is used as a prototype. Eight-node isoparametric elements are used to mesh the concrete deck, pavements, main APJ region, and gap plate as shown in Fig. 7.2. The developed models are run on ABAQUS V6.7.

Since the mesh contains corners, the stress level at those locations will rise as the element size is decreased. To ensure that meaningful results are achieved, the mesh is graded such that the element size in critical zones, where cracks are expected to initiate, is 1 mm and quantities of interest within each element are averaged over the element domain. The chosen 1 mm element size is deemed appropriate for representing the processes that lead to direct or fatigue crack initiation and is similar to that used in fracture studies conducted by Kim et al. (2008), albeit they used a particle element model rather than a finite element model as used herein. It should be noted that the objective of this study is not to model crack initiation and propagation in the APJ material itself, which involve complex phenomena associated with time- and temperature-dependencies as well as healing of asphalt (Di Benedetto et al. 2004; Lytton et al. 1993). Rather, the intent is to evaluate stress and strain measures that are deemed indicative of the propensity for direct or fatigue cracking in the main APJ body.

7.2.1 Loading and Boundary Conditions

The two dominant loading cases considered are thermal movement and traffic load. Traffic load is applied as a moving traction over the surface of the APJ, which has two components: normal and shear. The former is due to the weight of the vehicle while the later is caused by positive or negative acceleration of the vehicle. Simple calculations considering highway speeds of vehicles crossing over an APJ suggest that the strain rate is rapid enough to consider the material elastic and that a time-independent analysis is reasonable when considering traffic load. In this study, a standard single axle dual tire load (axle load = 80 kN) is applied as a moving traffic load. The tire load is transformed into a uniformly distributed normal traction (W) of 0.6375 MPa. Shear traction (S) which is generated by acceleration or deceleration of the vehicle is varied so that the applied tractions are 0, 0.1W, 0.25W, and 0.5W.

Joint movement due to thermal expansion or contraction of the bridge span causes much slower loading than traffic loads; strain rate is approximately six orders of magnitude lower. Thermal movement is modeled by applying a given displacement field to the APJ boundaries. The actual boundary conditions of an APJ subjected to thermal movement are, however, complex. The vertical faces are connected to the pavements,

whereas portions of the bottom surface are attached to the concrete deck or to the gap plate resting on the concrete deck. When thermal movement is applied to the APJ, the gap plate and concrete deck move away from one another, forcing the bottom of the joint to debond around the edge of the gap plate. The debonded length is an influential parameter whose effect is evaluated through sensitivity studies as described later on.

7.2.2 Performance Criteria of APJ

According to fracture tests on pure asphalt reported by Cheung and Cebon (1997a), tensile failure occurs at a specific stress range irrespective of temperature and strain rate, except for extremely slow strain rates. The tensile failure stress range identified by Cheung and Cebon (1997a) is 1-3 MPa. Based on this observation, the potential for cracking failure is assumed to be indicated by tensile principal stress level; the higher this level, the higher the propensity for direct or fatigue cracking. In other words, the maximum principal stress at critical locations is considered as a performance parameter for cracking-related failure in this work.

In the case of slow loading rates, creep failure will occur before the stress reaches a critical value because viscous flow constrains increases in stress. In this case, failure is better described by a strain-based criterion. Harvey and Cebon (2003) divided tensile failure strains into three regions: ductile, transition, and brittle failure regions. The measured tensile failure strains for the ductile failure region were larger than 1.0, and in the brittle failure region, the failure strains were about 0.1. Brittle failure of bitumen occurs when the strain rate is very high or when the temperature of the material is lower than the glass transition temperature, and in those cases, the stress criterion controls failure. Based on Harvey and Cebon's (2003) data, the potential for ductile cracking is assumed to be indicated by the presence of high tensile principal strains. As described above for stress, maximum principal tensile strain demand at critical locations is also considered to be a performance parameter.

In addition to cracking, excessive deformation due to thermal movement can cause functional failure of the APJ, e.g. a bump due to excessive deformations in the APJ impedes their ability to transfer traffic smoothly over the joint. Bumps degrade rideability, and when excessive, can prompt replacement of an APJ. According to a survey of

Departments of Transportation in the United States, an allowable bump of 19 mm is tolerable (Bramel et al. 1999). The 'bump size' is therefore used a serviceability performance parameter.

The use of the previously defined performance parameters in lieu of actual failure criteria is necessitated by the difficulty of specifying the latter. APJs are subjected to cyclic loading due to thermal bridge response on a daily basis. These conditions also vary by season and are therefore difficult to quantify. Hence this study is focused only on performance parameters that represent demand in a general sense. While not suitable for explicit failure studies, they are particularly useful for comparative and parametric studies and are used as such herein.

7.2.3 APJ Constitutive Model

As a viscous, temperature-dependent material, asphalt exhibits a stiffer and stronger response at high strain rate or cold temperatures compared to response under slow strain rates or high temperatures. Therefore the model used in this work is a time- and temperature-dependent model. Fig. 7.3 shows a schematic of the visco-plastic model used herein. The model consists of two parallel networks: an elastic-plastic network and an elastic-viscous network. The material is assumed isotropic and the total stress (σ_T) is split up into two components corresponding to the elastic-plastic network (σ_{EP}) and the elastic-viscous network (σ_{EV}). Corresponding to these stresses are strains ε_{EP} and $\varepsilon_{EV\_s} + \varepsilon_{EV\_d}$, respectively, where ε_{EV_s} is the strain in the elastic spring and ε_{EV_d} is the strain in the viscous damper. σ_y and E'_{EP} are the yield stress and hardening modulus of the elastic-plastic network, respectively. The behavior of the elastic-plastic network (σ_{EP} - ε_{EP} relationship) is idealized as elastic-plastic with kinematic hardening, while a linearly elastic constitutive relationship is used for the spring in the elastic-viscous network (σ_{EV} - ε_{EV_s} relationship). If E_{EP} and E_{EV} are the elastic modulii of each network, $E_{EP} + E_{EV}$ is the instantaneous elastic modulus (E_i) of the system. The ratio of E_{EP} to E_{EV} is determined from relaxation tests. E_i of the system varies with temperature. Test data for APJ material in Bramel et al. (1999) suggests that the

relationship between the main variables can be expressed as:

$$E_i = A\exp\left(\frac{B}{T}\right) \tag{7.1}$$

A generalized and comprehensive time-dependent non-linear viscous model for asphalt was provided by Cebon and his colleagues at Cambridge University. Based on various uniaxial tension tests for pure asphalt (Cheung and Cebon 1997a) and asphalt concrete (Deshpande and Cebon 1999; Deshpande and Cebon 2000) over a wide range of temperatures, stresses, and strain rates, Cheung and Cebon (1997b) suggested a set of relationships between steady-state stress and strain rates termed 'deformation mechanism map'. In constant strain rate tests, the stress level at the plateau is called the steady-state stress. Similar to the steady state stress, the steady-state strain rate is the constant strain rate observed in a creep test, i.e. constant stress test. One of the key features of the Cambridge research effort applicable over a wide range of parameters for asphalt concrete is the Power Law Model (PLM). As described in Deshpande and Cebon (1999), the PLM is expressed as:

$$\frac{S_{agg}\dot{\varepsilon}}{\dot{\varepsilon}_{0p}} = \left(\frac{\sigma}{\sigma_{0p}}\right)^{n_p} \exp\left(-\frac{Q_p}{RT}\right) \tag{7.2}$$

Where, $\dot{\varepsilon}$ is the steady-state strain rate, σ is the steady-state stress, n_p is a creep exponent, and T is temperature on the Kelvin scale. Other parameters, S_{agg}, $\dot{\varepsilon}_{0p}$, σ_{0p}, Q_p, and R, are constants depending on aggregate content and type of the asphalt. The values of the constants were given by Cheung and Cebon (1997a) and Deshpande and Cebon (2000), but those were for specific type of asphalt produced in the United Kingdom. In this study, Eq. (7.2) is simplified into the temperature-dependent, non-linear viscous form, represented by the dashpot in Fig. 7.3, and expressed in Eq. (7.3). As described next, the coefficients, *A*, *B*, *C*, *D* and *n* in Eq. (7.1) and (7.3) are calibrated using Bramel et al.'s (1999) material test data for APJ materials.

$$\dot{\varepsilon}_{EV\_d} = C\exp\left(-\frac{D}{T}\right)\sigma_{EV}^{n} \tag{7.3}$$

7.2.4 Calibration of Material Parameters and Failure Conditions

The parameters of the visco-plastic material model described above are calibrated to test results for APJ materials in Bramel et al. (1999) that include uniaxial tension tests at four different temperatures and relaxation tests. However, because Bramel et al. (1999) conducted all of their tension tests at a same strain rate, strain rate dependency, represented by n in Eq. (7.3), is determined using the PLM suggested by Cheung and Cebon (1997a). According to Cheung and Cebon (1997a), the PLM consists of two regions: Newtonian flow region (n=1.0) and power law creep region (n=2.4). The in-situ operating conditions of APJ subjected to thermal movement cause very small strain rate placing the response in the Newtonian flow region, which means n=1. Variables A, B, C, and D of Eq. (7.1) and (7.3) were calibrated as 1.184×10^{-3} Pa, 6,370 K, 20,811 $(\text{MPa}\cdot\text{sec})^{-1}$, and 4,540 K, respectively, by using Bramel et al.'s (1999) uniaxial tension test data. For the plastic component in Fig. 7.3, a yield stress of 1 MPa and strain hardening of 2% are assumed.

7.2.5 Model Assumptions

A number of assumptions were made in this research. While APJ material is comprised of aggregate and pure asphalt, the model employed herein assumes that the material is homogenous. In addition, the stress and strain performance criteria employed were developed from data on pure asphalt but are being applied to APJ material. This assumption is, however, deemed reasonable because the 1-mm element size employed in the simulations samples results over a small enough region to permit consideration of the asphalt matrix response. Another assumption is that the bond strength between APJ material and the surrounding boundaries is equal to or greater than the strength of pure asphalt. In other words, failure at the interface will occur in the asphalt and not at the boundary. There is evidence in Bramel et al. (1999) that this is a reasonable assumption.

7.2.6 Model Validation

The near full scale APJ test results in Bramel et al. (1999) are used to validate the proposed material model. In that study, the APJs were tested under cyclic loading at a strain rate of $\dot{\varepsilon} = 0.001250$ /sec. The width and depth of Bramel et al.'s (1999) APJ

specimen were 500 and 100 mm, respectively, and the test temperature was 20°C. The gap plate was 200 mm wide and 10 mm thick, and ±10 mm of thermal movement was applied. The bottom boundaries were assumed to be fully debonded since its actual condition was not known (this assumption is discussed in more detail later on). Fig. 7.4 shows a comparison between the horizontal reactions obtained from the test and the finite element model. While the thickness of the loops is not accurately captured, the general trends including stiffness variation with displacement and strength at peak deformations are considered reasonable. The overall comparison is deemed acceptable given the significant uncertainties regarding actual testing conditions and material response parameters.

Additional validation is sought by comparing model results to data from two full scale APJ tests conducted by Moon et al. (2008). Since the APJ material used in the test program is not the same material used in Bramel et al.'s (1999), successful comparisons between the model, which uses a model calibrated to Bramel et al.'s (1999) material test data, and test results do not imply model validation in a strict sense. However, as will be shown later on, the calibrated model captures the trends reasonably well, lending credence to its ability to model APJ response with reasonable accuracy.

Moon et al.'s (2008) specimens are designated APJ-1 and APJ-2. The dimensions of APJ-1 were 350 (width) × 90 (depth) mm and the gap plate was 180×5 mm, while APJ-2 was 400×90 mm, and its gap plate was 270×5 mm. Another difference between the two specimens is the applied average strain rate, which was 11.9×10^{-6} /sec for APJ-1 and 20.8×10^{-6} /sec for APJ-2. A horizontal movement of ±25 mm, applied over 5 cycles, was applied to both specimens to simulate thermal field demands. Fig. 7.5 shows top and side views of APJ-2, which was white-washed to facilitate observation of cracks and damage propagation. Average surface strains are measured along two lines from the displacement of small spikes installed over the surface of the specimens as shown in Fig. 7.5a. The intervals between measurement points for APJ-1 and APJ-2 are 25 mm and 40 mm, respectively. Fig. 7.6 compares the horizontal strain distributions computed from the model to those measured from the tests. The experimental results in both figures are shown as a range of measurements made over the 5 loading cycles during the test. Fig. 7.6 shows that not only do the computed strains match reasonably well with the experimental measurements, but also the distribution of strains and the locations of strain

concentrations are also well represented.

7.2.7 Presentation of Results

To present the results and facilitate comparisons between various configurations in the future, the results of the simulations are plotted along the path AFDBCE-E'C'B'D'F'A' shown in Fig. 7.7. Points D and E (along with corresponding points E' and D') represent the tips of the debonded interface. Preliminary analyses showed that the most critical points are located along this boundary. Due to symmetry, only one half of the model is used for thermal movement analysis, whereas, in case of moving traffic load, a full model was used because the loading condition is not symmetric.

The main quantities of interest (maximum principal stresses and strains) are computed 0.5 mm away from the boundary, which coincides with the center of the smallest elements at the critical points. To observe the relative degree of stress or strain concentration, normalized stresses and strains are used in some figures. Eq. (7.4) and (7.5) show how the normalization is achieved in the case of thermal loading.

$$\varepsilon_H^N = \varepsilon_p / \varepsilon_{avg-H} \tag{7.4}$$

$$\sigma_H^N = \sigma_p / \sigma_{avg-H} \tag{7.5}$$

ε_H^N and σ_H^N are the normalized strain and stress for thermal movement whereas ε_p and σ_p are the principal strain and stress. ε_{avg-H} is average strain under thermal movement obtained by dividing the applied horizontal displacement by the length of the APJ. σ_{avg-H} is the average stress under thermal movement obtained by dividing the computed reaction by the APJ cross-sectional area. In a similar manner, Eq. (7.6) shows the normalized stress for traffic load (σ_{nt}^N), where *W* is the applied normal traction.

$$\sigma_{nt}^N = \sigma_p / W \tag{7.6}$$

7.3 BEHAVIOR OF APJ SUBJECTED TO THERMAL MOVEMENT

Assuming a bridge with 30 m spans subjected to temperatures of 20±40℃, the prototype APJ will be subjected to horizontal displacements of ±18 mm. This translates

into a corresponding equivalent average strain rate of 4×10^{-6} /sec if the temperature swings from one extreme to the other over a 3 hour period, i.e. 26.7 ℃/hour, which is a plausible extreme condition. Tensile and compressive deformations are cycled 5 times and the maximum response is then used in the subsequent analyses. In the following discussions, tensile effects (associated with dropping temperatures) are taken as positive while compressive effects (associated with rising temperature) are considered negative.

Preliminary analysis indicated that: 1) debonding at the edge of the gap plate is physically unavoidable when thermal movement occurs, and 2) most of the deformation demand at the bottom boundary is concentrated within the debonded region. The analyses also showed that the debonded length is a key factor controlling the response of the joint. However, computing a debonded length for particular conditions is not possible because the length varies with traffic loading, temperature conditions and the potential for autogenous healing. Therefore, rather than specifying the debonded length, sensitivity studies are used to quantify the effect of this parameter. Two sets of studies are conducted where the debonded length is the main variable. Only horizontal debonding along the bottom boundary is considered, and the debonded surfaces are modeled as frictionless. In the first set (designated as BC-C0 through BC-C5), the ratio of debonded length along the concrete-APJ interface (DB in Fig. 7.7) to that of along the gap plate-APJ interface (CE in Fig. 7.7) is set constant at 3:2. In the second set (designated as BC-D0 through BC-D5), the gap plate-APJ interface is fully debonded, and the length of DB varies. The debonded length for each case is specified in Table 7.1.

Fig. 7.8 shows hysteresis loops for reaction versus thermal movement obtained from BC-C0, which has minimum debonded length, and BC-C5, which has a fully debonded bottom. The effect of temperature is clearly demonstrated in the loops. The reactions under compressive movement tend to zero, indicating that APJ accommodates thermal movement under increasing temperature with negligibly low stress. On the other hand, the sharp rise at low temperature implies that the maximum tensile movement induces high force (and therefore stress) levels that make the joint vulnerable to cracking.

Fig. 7.9 illustrates the variation of maximum principal stress distribution along the path defined in Fig. 7.7 for the BC-C cases. It is clear from the figure that points A, C, D, and E are locations of stress concentration. Key results are also summarized in Table 7.2.

Several other observations can be made: 1) the peak stresses drop rapidly as the debonded length increases, 2) the average stress levels between peak points drop rapidly as the debonded length increases, and 3) the debonded length has little effect on point A. Another important observation is that all of the stress demands are below the lower limit of the tensile failure stress range (1-3 MPa), implying that direct tensile failure under thermal loading is unlikely. However, these points are still vulnerable to fatigue cracking. Similar trends are obtained for strain demands as shown in Table 7.2, which also shows key results for Set BC-D. Clearly, the most critical case of the BC-D scenarios has much lower demands than the BC-C0 case. For example, BC-D0 has 51%, 61% and 10% of the principal stress demands at points C, D and E, respectively, compared to the BC-C0 case.

According to Bramel et al. (1999) and Partl et al. (2002), there are two typical crack paths causing functional failure of the APJ: the path connecting point A-F-D-B, and the path starting around point C then propagating vertically to the APJ surface. Either of these cracks will allow infiltration of water and deicing agents through the APJ, which can damage bridge components beneath the joint. As shown in Fig. 7.9, local demands at point A are generally lower than at other points, implying that the former cracking path is less likely to occur than the latter under thermal movement.

Under field conditions, autogeneous crack healing of asphalt and variability in bond strength could create conditions where the debonded length is small. As illustrated by case BC-C0 in Fig. 7.9, a small debonded length leads to large demand around the gap plate edge. On the other hand, debonding along the bottom boundary only will not lead to functional failure of the APJ because this will not allow water infiltration. Therefore, a logical and low cost solution by which the risk for developing a vertical crack at the gap plate edge can be mitigated is to intentionally introduce debonding along the APJ bottom. Debonding along the entire gap plate (region CE), while keeping the concrete-APJ interface bonded (region BD), is practically feasible, and as previously noted, leads to significant reductions in the stress and strain demands.

The applied displacement rate is another important factor influencing APJ response. To investigate this variable, a set of analyses with various average strain rates ranging from 4×10^{-6} /sec to 0.00125 /sec are conducted. The former rate corresponds to a feasible in-situ average strain rate due to temperature change while the latter is the rate of Bramel

et al.'s (1999) test. All the simulation cases in this set are run with a constant debonded length (DE) of 125 mm (DB=90 mm and CE=35mm) at a constant temperature of 20℃. Fig. 7.10a shows the principal stresses at Points A and C for the range of strain rates considered. The figure shows that the stress level increases exponentially with strain rate, exceeding 1 MPa at the highest strain rate.

As previously discussed, stresses in excess of 1 MPa could lead to direct tensile failure depending on the APJ mixture. The results in the previous paragraph therefore suggests that data from accelerated tests employing high strain rates should be evaluated with care since the high strain rates will significantly increase local demands, potentially influencing the primary reasons behind failure modes observed in the field. At the experimental strain rate of Bramel et al. (1999), the stress demands at point A and C are 2 orders of magnitude higher than that at the strain rate corresponding to field conditions at 20℃ temperature as shown in Fig. 7.10a. Under field conditions, however, the critical operating temperature is much lower than 20℃ and the stresses at A and C are therefore likely to be significantly higher than at 20℃ because of the temperature dependence of APJ materials as illustrated in Fig. 7.8. Therefore, care should be taken to ensure that the stress demands during experiments conducted at room temperature are comparable to those obtained under field conditions at low temperatures.

Fig. 7.10b provides a rough means for estimating stress under field condition from accelerated tests. The figure shows that the normalized stresses (σ_H^N) are fairly constant with strain rate, which implies that the reaction and stress at the critical points are linearly related. It is therefore feasible to approximately estimate the stress at the critical points if the reaction and σ_H^N is known for a particular APJ geometry.

As was described earlier, the allowable vertical displacement (bump) is a performance parameter too. Fig. 7.11 shows the distribution of vertical surface displacements for various debonded lengths when the maximum horizontal movement (±18 mm) is applied. The peak values are ±6 (mm) for tensile and compressive movements, and are far lower than the 19 mm proposed by Bramel et al. (1999). Clearly, the debonded length has little effect on this performance parameter.

7.4 BEHAVIOR OF APJ SUBJECTED TO TRAFFIC LOAD

Reid et al. (1998) and Qian et al. (2000) investigated the effect of traffic loading on APJ response. However, their analyses mainly focused on the stress at the interface between the APJ and pavement, i.e. region AF in Fig. 7.7. In this study, the stress distribution along with the entire interface of the APJ is explored and discussed. In these analyses, the interface is assumed to fully bonded to the surrounding structure. In addition, the fast rate of loading eliminates the influence of the time-dependent nature of the APJ materials, making a static elastic analysis reasonable. The simulations are carried out for two temperatures: 20℃ and -18℃. The movement of the traffic load is divided into 18 loading steps, and the load is assumed to move forward 50 mm each step. Fig. 7.7 shows the location of the applied tractions at steps 5, 9 and 13.

Although the distribution of stress along the APJ interface varies with the location of the load, the locations of stress concentration are similar to the case of thermal loading. While the geometry is symmetric, the loading is not because of the direction of the applied shear traction, which results in different stress demands in C and C' as well as A and A'. Fig. 7.12 shows how the maximum and minimum principal stresses vary at Points A (A') and C (C'), respectively, as the load travels across the joint when the temperature of the joint is 20°C. Fig. 7.12a shows that the principal stresses at A and A' depend strongly on the level of shear traction assumed. This is true of both principal stresses, which can approach peak values of 3 MPa in both tension and compression for S=0.5W. On the other hand, Fig. 7.12b shows that the demands at C and C' are not much dependent upon the shear traction level, perhaps because these points are located deep in the APJ, away from the surface effect of the shear traction. For example, Point C' will encounter maximum principal stresses that vary from -0.5 MPa to +0.45 MPa when S=0.5W and -0.57 MPa to +0.25 MPa when S=0, as the tire rolls across.

Distinction between points A and A' or C and C' is generally immaterial because the direction of shear traction, vehicle travel, and vehicle acceleration are all reversible. Therefore, only the absolute maximum values of the principal maximum and minimum stresses and strains are plotted in Fig. 7.13 for the two temperatures of interest. It is clear from the figure as well as from Fig. 7.12 that the tensile stress and strain demands (σ_p

and ε_p, respectively) at Point A (A') are significantly (up to 6 times) higher than those at Point C (C') as *S* increases. Another observation, which is expected given the fact that asphalt is much softer when warm, is that temperature influences strain demands (Fig. 7.13b) more than stress demands (Fig. 7.13a).

The conditions when S=0.25W or 0.5W represent extreme loading cases in which a truck is undergoing emergency braking, i.e. they represent a rather rare condition. Strong acceleration could be represented by S=0.1W. In this case, the traction will be generated by the powered axle only. The most common loading case is when S=0, i.e. where unpowered axles are crossing over the APJ.

The loading conditions discussed in the preceding paragraph must be kept in mind when evaluating the potential for failure. In other words, $S > 0$ is not likely associated with the accumulation of fatigue damage whereas the case of $S = 0$ is likely associated with fatigue damage since it represents the majority of truck axles crossing the APJ. Clearly, points A and A' are subjected to high principal stresses when $S > 0$. For example, the principal stress is 1.19 MPa in tension when S=0.1W, 1.79 MPa in tension when S=0.25W, and it approaches 3 MPa when S=0.5W. These numbers fall within the failure stress range identified by Cheung and Cebon (1997a), i.e. 1-3 MPa, and therefore sharp braking or acceleration of a heavy truck on APJ can cause direct cracking at points A or A'. When $S = 0$, points A sees principal stresses that range from 0 to 1 MPa as a tire moves across. On the other hand, points C' see stresses that alternate between -0.57 MPa to +0.25 MPa. Although it is difficult to be certain because only principal stresses are computed, i.e. stress demands may not occur in the same direction, the fact that the principal stresses fluctuate suggests that fatigue-related damage can potentially accumulate at both A (A') and C (C') as trucks roll across the APJ. Contrary to the cases of thermal movement, the higher stress levels at A (A') indicate that point A (A') is more vulnerable to fatigue cracking than point C (C') when traffic loads are applied. This is in addition to its greater vulnerability to braking and accelerating tractions, which can lead to direct cracking. Along with the thermal loading calculations previously mentioned, these results suggest that cracking along path A-F-D-B occurs as a function of the combined effect of thermal movement and traffic load. The vertical interface crack along the path A-F can be developed by traffic load, whereas horizontal debonding can

propagate due to thermal movement. Functional failure of the APJ occurs once both cracks meet.

7.5 PARAMETRIC STUDY FOR IMPROVED APJ DESIGN

Detailed finite element simulations are conducted to develop a better understanding of the parameters that influence APJ response under traffic and thermal loading conditions. Based on the information obtained from the parametric studies, an improved and practically feasible APJ design is proposed and its superiority over the traditional design is demonstrated.

The main variables in the parametric study are the width and the thickness of the gap plate, the shape of its edge, and the shape of the interface between pavement and APJ. These variables are considered through 4 sets of alternative geometries as outlined in Fig. 7.14. Each analysis configuration is designated by a unique set of characters to simplify referring to the various analysis cases. The first two letters denote the basic analysis set, which addresses one main parameter of interest. For example, Set IF, which studies the effect of the interface between the pavement and APJ, has 3 configurations each with different APJ interface geometries, i.e. traditional, trapezoidal and rounded. Set GT, which focuses on gap plate thickness, contains 4 configurations in which the gap plate thickness to APJ thickness ratios range from 0.04 to 0.1. Set GE focuses on gap plate edge detail and has configurations with 4 different gap plate edges, i.e. traditional, trapezoidal, rounded and combined. Set GL investigates gap plate width and contains 5 different configurations with gap plate width to APJ width ratios that range from 0.3 to 0.7 (see Table 7.3). The effect of thermal loading is investigated in all sets, while traffic loading is examined only through sets IF and GT. Furthermore, while thermal loading is investigated in the presence of a debonded interface as described above, full bonding of the APJ to its surrounding components is assumed for all traffic loading cases.

7.5.1 Loading and Boundary Conditions

In the previous section, the effect of shear traction on local demands of APJ by applying shear tractions of S=0, 0.1W, 0.25W (the recommended braking force in the

AASHTO LRFD (2004)), and 0.5W is investigated. The results showed that the stress and strain demands at point A significantly rise with the increase of applied shear traction. In this section, two extreme conditions are selected for further study: tire load without shear traction (S=0) representing passage of unpowered truck axles; and tire load with maximum shear traction (S=0.5W) representing an extreme deceleration of a truck on the APJ. The fast rate of loading in these cases eliminates the influence of the time-dependent nature of the APJ materials, implying that response is linear elastic, i.e. stress and strain demands under traffic loads are linearly proportional to the magnitudes of the applied load. The movement of the traffic load is divided into 18 loading steps, and the location of the traffic load is assumed to move forward 50 mm each step as shown in Fig. 7.7.

One of the important findings of the previous section is that an important factor in simulating joint movement of APJ is the debonding that occurs at the bottom boundaries. When thermal movement is applied to an APJ, the gap plate and concrete deck move in opposite directions, and consequently the bottom of the joint must debond to accommodate motion around the edge of the gap plate. Hence, most of the deformation demand at the bottom boundary is concentrated within the debonded region. The previous analyses also showed that the debonded length is a key factor controlling the response of the joint. However, computing a debonded length for particular conditions is not possible because the length varies with traffic loading, temperature conditions and the potential for autogenous healing. Therefore, rather than specifying the debonded length or computing it by tracking fracture propagation along the boundary, configurations with fixed total debonded lengths are used, although the makeup of the debonded length, i.e. where it occurs in the APJ, is varied to provide sensitivity information. Only horizontal debonding along the bottom boundary is considered, and the debonded surfaces are modeled as frictionless. Table 7.3 shows details of the assumed debonded length for each analysis where configurations with appended ‘S’ or ‘L’ indicate models with short or long debonded lengths, respectively. The rationale for selecting the values shown in Table 7.3 is provided later on.

Joint movement due to thermal expansion and contraction of the bridge span is modeled by applying a horizontal displacement to the APJ boundaries, as shown in Fig. 7.7. Under field conditions, thermal movement causes much slower loading than traffic

loads, i.e. the strain rate of the former is approximately six orders of magnitude lower than that of the latter. Assuming a bridge with 37.5 m (125 ft.) span subjected to temperatures of 20±40 °C, the joint will be subjected to horizontal displacements of ±18 mm. This translates into a corresponding equivalent average strain rate of 4×10^{-6} /sec if the temperature swings from one extreme to the other over a 3 hour period, i.e. 26.7 °C/hour, which is a plausible extreme condition. Stress and strain demands at maximum tensile movement (18 mm at -20°C) – as opposed to maximum compressive movement (-18 mm at 60°C) – are reported and used in the parametric study since such a case is associated with critical cracking conditions.

7.5.2 Results of Parametric Study

The performance of each alterative configuration is judged by comparing its response parameters, i.e. stress and strain demands at vulnerable points, to corresponding quantities in the prototype design. In all of the analysis results, variations in strain demands were observed to follow the same trends as stress demands. Therefore, in the interest of space, most of the analysis results presented herein pertain to stress demands.

According to analyses in the previous section, the locations of greatest stress concentration were points A, C, D, and E labeled in Fig. 7.7. However, this study focuses only on points A and C, but not on D and E for three reasons. First, the mode of loading at the debonding tips, point D and E, is in-plane shear (fracture mode II) which causes horizontal debonding. An extension of the bottom crack will increase the horizontal debonded length, but that does not necessarily constitute a functional failure because water cannot still infiltrate the joint. Second, local demands at point E can be eliminated by intentionally debonding the gap plate from the plugged material. A final argument that the demands at points D and E are benign is that documented cracks do not originate at arbitrary points along FB, but are known to remain confined within other regions in the APJ, specifically around points A and C. Therefore, in this section, local demands at points A and C are used for evaluating the effect of varying parameter values as discussed next.

(1) Effects of Gap Plate Width

The effect of gap plate width is evaluated through set-GL, shown in Fig. 7.14. As previously described, two situations with different debonded lengths are considered since the actual debonded length cannot be reliably obtained. For the case with long debonded length, i.e. set-GL-L described in Table 7.3, the gap plate is assumed to be debonded from the plug material along its entire length as recommended by the previous analysis. Since the location of points D and E are fixed in set GL-L, this implies that the lengths of DB and CE vary as shown in Table 7.3. On the other hand, set GL-S, which has a short debonded length, simulates a situation in which debonding occurs only locally at the tips of the gap plate to permit motion of the APJ. In this case, DB=CE=25 mm.

Fig. 7.15 illustrates the effect of gap plate width on local stress demands at maximum tensile movement, i.e. at 18 mm displacement at -20°C. It is clear from the figure that the local stress demand at point C for set GL-S is significantly higher than the corresponding demand for set GL-L. Another observation is that the stress demand at point C varies little with gap plate width, which implies that the local demands at point C are dominated by the total debonded length and not the gap plate width. Both of these conclusions are in agreement with the observation of the previous section that deformation demands are concentrated within the debonded part.

At point A, the local demand for set GL-S clearly rises with increasing gap plate width, whereas such a trend does not occur in set GL-L. As the gap plate grows in size, its tip approaches point A. Furthermore, when the debonded length is short, the overall level of stress and strain at the debonded region will be high, since deformation demands are concentrated in this small region. Therefore, as the tip of the gap plate approaches point A, these high demands start to influence the stress conditions at point A, causing the local demands to rise. On the other hand, when the debonded length is long enough to distribute the deformation demand over the joint, the demands around point C will be correspondingly low, shielding point A from excessive demands. This set of analyses therefore implies that reducing gap plate width will correspondingly reduce the demands, and hence, the risk of cracking at point A. However, practicality of the field installation process dictates a minimum width, deemed to be 150 mm, or 30% of the APJ width, in this study.

(2) Effects of Gap Plate Thickness

The effect of gap plate thickness is investigated through sets GT-S and GT-L. In both sets, thicknesses less than that used in the prototype, which is 0.1 times the APJ thickness, are investigated. As shown in Fig. 7.16a, the stress demands at point C drop with decrease in gap plate thickness for both analysis sets, while the demands at point A are not influenced by the thickness. Clearly, a thinner gap plate is beneficial for mitigating local demands around the gap plate.

However, there is another competing consideration for determining gap plate thickness. The role of the gap plate is to prevent the APJ material from getting into the expansion gap, and at the same time, support the weight of APJ and traffic load travelling over the expansion gap. In other words, the gap plate should be thick enough to carry the APJ weight and traffic load. ASTM D6297-01 specifies the minimum thickness of the gap plate to be 6 mm. Fig. 7.16b shows the effect of gap plate thickness versus the maximum principal stress demand within the gap plate. In all analyses, the expansion gap is assumed to be 50 mm. As illustrated in Fig. 7.7, point GC is located at the bottom center of the gap plate while GS is located at the top of the gap plate just above the edge of concrete deck. The simulations showed that even a 2 mm thick gap plate can support an 80 kN axle load. However, in the improved APJ design proposed later on, a 4 mm plate is selected to ensure that there is an adequate factor of safety against plate overloading and high cycle fatigue.

(3) Effects of Gap Plate Edge Shape

There is no specification that defines the shape of the gap plate edge. As illustrated in Fig. 7.14, gap plates with rectangular edges are commonly used. In this situation, point C becomes a rectangular notch and causes stress and strain concentrations, which may contribute to premature APJ failure. Park et al (2010) demonstrated that peak demands of stress and strain occur at point C for both thermal and traffic loads. Indeed, crack propagation from point C is a common failure mode observed in Bramel et al.'s (1999) near full scale test. To alleviate concentrations of local demands, three alternative shapes of the gap plate edge are suggested as shown in set GE in Fig. 7.14, and their performance is compared to the commonly used rectangular edge.

The principal stresses at points A and C are shown in Fig. 7.17 for sets GE-L and GE-S. It is clear from Fig. 7.17 that the rounded and combined shapes of the gap plate edge have the best performance, i.e. they have the lowest principal stresses. In particular, the rounded shape has a principal stress of 0.22 MPa (set GE-L at C) versus 0.26 MPa for the traditional shape (set GE-L at C). A similar trend is observed in set GE-S where the greatest principal stress demand decreases from 0.39 MPa for the traditional edge to 0.32 MPa for the rounded. From a practical perspective, rounding off the top edge of gap plate is a simpler way of reducing the local demand at point C than forming the combined edge shown in Fig. 7.14. Therefore, a rounded edge is proposed instead of the traditional rectangular edge.

(4) Effects of Shape of Interface between APJ and Pavement

The traditional interface between APJ and pavement is rectangular. As illustrated in set-IF in Fig. 7.14, two alternatives, namely trapezoidal and rounded, are explored as options through sets IF-S and IF-L. The idea of using a trapezoidal interface was originally suggested by Reid et al. (1998). Qian et al. (2000) also studied this alternative and suggested that an optimum inclination angle ranges from 45° to 60°. In this study, a 45° interface angle is selected for the trapezoidal interface, and the rounded interface is introduced as another alternative. As it was explained earlier, the simulations in Reid et al. (1998) and Qian et al. (2000) studied responses to traffic loading only, whereas in this work response to thermal loading was also considered.

Fig. 7.18a and 7.18b show the stress demands at point A and C for thermal and traffic loads, respectively. As shown in Fig. 7.18a, the stress demand for the trapezoidal shape under thermal loading is comparatively very low at point A. For example, the maximum principal stress drops from 0.22 MPa for set IF-L for the traditional rectangular shape to 0.04 MPa for the trapezoidal shape. The same trends can be seen in Fig. 7.18b, i.e. that the trapezoidal interface shape also has the lowest demands under traffic loading. For example, at point A, for the case of S=0.5W, the principal stress demand drops from 2.99 MPa for the traditional edge shape to 1.27 MPa for the trapezoidal, which confirms the results in Qian et al. (2000). As expected, Point C, which is far away from the interface, is insensitive to the interface shape for all conditions considered. These

simulation results therefore suggest that the trapezoidal interface has the best performance among the alternatives considered.

7.5.3 Proposed Alternative APJ Geometry

In the parametric studies described above, the optimum width, thickness, gap plate edge shape and interface shape were independently identified. By combining them, an improved APJ geometry is proposed as shown in Fig. 7.19. The dimensions of the revised APJ studied further in this work are: 100 mm thickness, 600 mm top width, 400 mm bottom width, gap plate width of 150 mm and gap plate thickness of 4 mm. The top edge of the gap plate is rounded and a trapezoidal APJ-pavement interface is assumed.

As previously alluded to, the risk of a vertical crack initiation from the edge of the gap plate can be mitigated by intentionally debonding the gap plate from the plug material. The benign effect of long horizontal debonding is consistently observed in the analysis results presented in this section as well, i.e. the local demands at point C of the models with longer debonded length are always lower than models with shorter debonded length. Therefore, intentional debonding of the gap plate is also recommended for the improved APJ. In the field, this intentional debonding can be attained by covering the gap plate with a thin film to eliminate adhesion between the plug material and steel plate.

Fig. 7.20 compares maximum principal strains of the traditional and the improved APJs subjected to thermal movement. The results are shown at +18 mm of thermal movement corresponding to -20°C plotted along the interface path defined in Fig. 7.7. The debonded length at the concrete-APJ interface (region DB) is specified as listed in Table 7.3. In both models, the locations of point D are the same, but the length of DB in the improved APJ is increased because the gap plate has been shortened.

The plot in Fig. 7.20 shows that the proposed modified APJ geometry results in a significant reduction in the demands along the entire path. The only exception is point D, which is the tip of the bottom crack along the debonded interface. At this point, the stress demand is the same in both modified and traditional cases. However, it is important to recall that the length of the bottom crack (DB) is arbitrarily chosen because its actual length varies with numerous parameters as previously pointed out. Furthermore, the demands at point D are deemed benign for reasons that were previously presented and

discussed.

The improvements of the local demands at the vulnerable points due to the geometric modification are summarized in Fig. 7.21. For example, the principal stresses at A and C under thermal load dropped by 83% and 50%, respectively. Similar trends can be seen in the principal strain demand. Significant improvements under traffic loading also occurred at points A and C. For example in the case where S=0, the principal stress demand at point A dropped to negligible values, while that at point C dropped by 56%. When S=0.5W, the principal stress demand at points A and C dropped 58% and 53%, respectively.

7.6 SUMMARY AND CONCLUSIONS

The behavior of APJs subjected to thermal and traffic loads was investigated by using detailed finite element analysis employing a rate- and temperature-dependent visco-plastic material model. In addition, four sets of alternative designs were parametrically investigated to develop an improved asphaltic plug joint that can mitigate the risk of premature failure. The parameters of the APJ material model pertaining to viscosity and temperature dependency were calibrated using previously published material test data. The developed models were then validated by comparing simulation results to previously published full-scale test data from two different test programs. Reasonably good comparisons were obtained between simulation results and test data providing confidence in the developed models. Following are conclusions that can be drawn from the limited study conducted:

- Accelerated tests employing high strain rates create high localized strain rates at critical points, which significantly increase the local demands, potentially influencing the primary reasons behind failure modes observed in the field. Therefore, care should be taken to ensure that the stress demands during accelerated experiments conducted at room temperature are comparable to those obtained under field conditions at low temperatures, especially when the local mode of failure being investigated is related to the stress level. The data in Fig. 7.10b, coupled with

analyses of the sort presenter, are useful tools for achieving this objective.

- The simulations results show that stress concentrations at critical points increase as the debonded length at the bottom interface becomes shorter. Intentional debonding of the interface between the APJ and gap plate is therefore suggested as a practical and low cost solution to mitigate the risk of developing a vertical crack from the gap plate edge.
- Although the distribution of stress along the APJ interface varies with the location of traffic loading, the locations of high stress and strain demands are generally similar to the case of thermal loading.
- The simulation results suggest that fatigue-related damage will accumulate at points A (A') and C (C') when truck axles roll across an APJ. For truck loading, local demand computations show that points A (A') are more vulnerable to fatigue cracking than point C (C'), while local demand at point C is generally higher than point A for thermal movement.
- The computed demands indicate that there is a significantly increased chance for direct cracking at points A and A' when trucks axles on the joint accelerate or brake sharply. This is proposed as a likely reason for some of the premature failures observed in the field.
- The parametric study for an alternative design showed that shortening the gap plate width reduces the demands, and hence, risk of premature cracking, especially at point A. However, practicality of the field installation process dictates a minimum width, deemed to be 150 mm in this study.
- Decreasing gap plate thickness reduces local demands at point C, while demands at point A were not influenced by this parameter. However, it is important to use a thick enough plate to ensure that traffic loads are safely carried by the joint. Therefore a minimum practical thickness is suggested to be 4 mm.
- An influential parameter turned out to be the geometry of the edge of the gap plate. Rounding off the gap plate edge significantly reduced local stress and strain demands and is recommended for use among the various edge geometries studied.
- The final parameter studied is the shape of the interface between APJ and pavement. The simulation results suggest that the trapezoidal interface has the best performance

among the alternatives considered.

- Synthesizing all the information presented in the parametric study, it is evident that, together, the proposed geometric modifications significantly reduce the local demands at vulnerable points under both thermal and traffic loads. It is not clear how much these reduced demands translate into increased service life since it was not possible to relate failure resistance to the performance measures employed in this study. However, the significantly reduced demands indicate that there is strong likelihood that the proposed design will perform better under service conditions than the traditional APJ.

This study used stress and strain responses as indicators for the risk of local fracture initiation and provided much needed insight into the behavior of APJ that can be used to improve durability of these types of products. However, additional work needs to be done to quantify fatigue damage initiation and propagation and to determine rutting life. The key difficulty of achieving this is that existing fatigue and rutting models have been developed for pavement materials and not for APJ material. Therefore, the proposed research must be preceded by model development based upon material testing that adequately simulates field demands in APJs, which differ greatly from those in traditional pavements. It is important to note that the effects of overall geometric dimensions (APJ thickness and width) were not investigated in this research and should be studied in future research. Furthermore, extensive testing is recommended to provide conclusive experimental evidence that the proposed modifications are indeed effective.

Table 7.1 Details of debonded length at the bottom boundary for various analysis sets

case ID	DB	CE	total debonded length
BC-C0	15	10	25
BC-C1	30	20	50
BC-C2	60	40	100
BC-C3	90	60	150
BC-C4	120	80	200
BC-C5	150	100	250
BC-D0	15	100	115
BC-D1	30	100	130
BC-D2	60	100	160
BC-D3	90	100	190
BC-D4	120	100	220
BC-D5	150	100	250

*BC-D5 is the same to BC-C5 (unit: mm)

Table 7.2 Stress and strain demands at vulnerable points

Case ID	maximum principal stress (MPa)				maximum principal strain			
	point A	point C	point D	point E	point A	point C	point D	point E
BC-C0	0.25	0.85	0.52	0.88	0.13	0.36	0.37	0.62
BC-C1	0.25	0.55	0.52	0.63	0.13	0.22	0.35	0.45
BC-C2	0.26	0.34	0.37	0.46	0.13	0.13	0.24	0.30
BC-C3	0.26	0.27	0.25	0.37	0.14	0.10	0.16	0.22
BC-C4	0.25	0.24	0.24	0.27	0.13	0.09	0.10	0.15
BC-C5	0.22	0.22	0.18	0.08	0.11	0.08	0.10	0.04
BC-D0	0.21	0.43	0.32	0.09	0.11	0.16	0.20	0.05
BC-D1	0.22	0.35	0.36	0.08	0.11	0.13	0.24	0.05
BC-D2	0.24	0.27	0.32	0.08	0.12	0.10	0.21	0.05
BC-D3	0.25	0.24	0.24	0.07	0.13	0.09	0.15	0.04
BC-D4	0.25	0.23	0.24	0.07	0.13	0.09	0.10	0.04
BC-D5	0.22	0.22	0.18	0.08	0.11	0.08	0.10	0.04

Table 7.3 Length of intentionally debonded regions for thermal loading cases

Set ID	Parameter	DB (mm)	CE (mm)	Total debonded length (mm)
GL-L	0.3	115	75	190
	0.4*	90	100	
	0.5	65	125	
	0.6	40	150	
	0.7	15	175	
All cases of GT-L, GE-L, IF-L		25	100	125
All cases of GL-S, GT-S, GE-S, IF-S		25	25	50
Traditional APJ*		25	25	50
Improved design		50	75	125

* prototype APJ

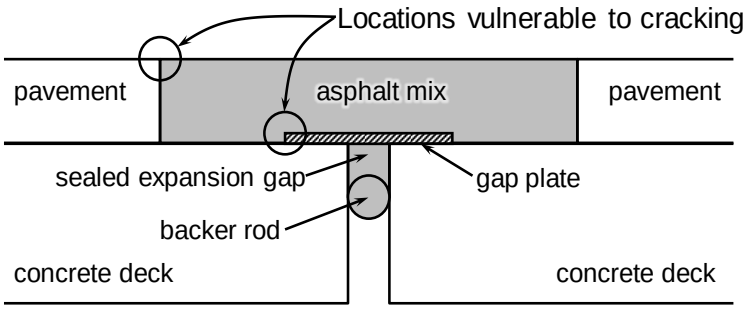

Fig. 7.1 Schematic sketch of asphalt plug joint

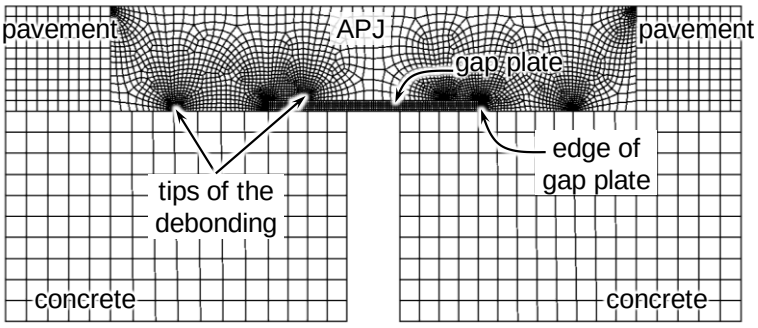

Fig. 7.2 Finite element model

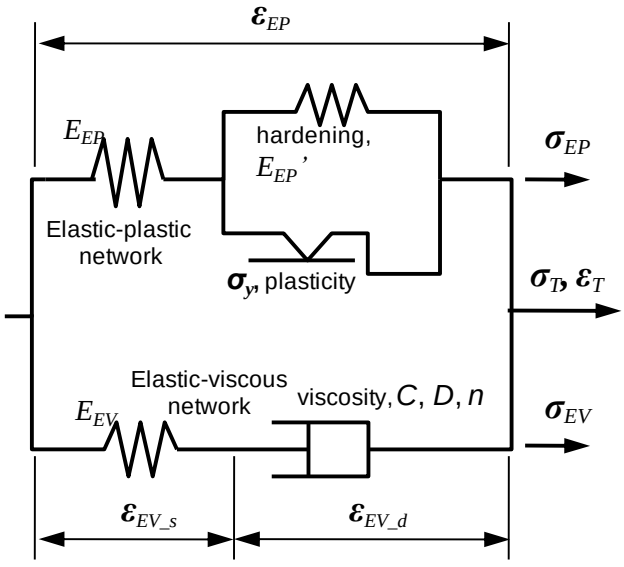

Fig. 7.3 Double network visco-plastic material model

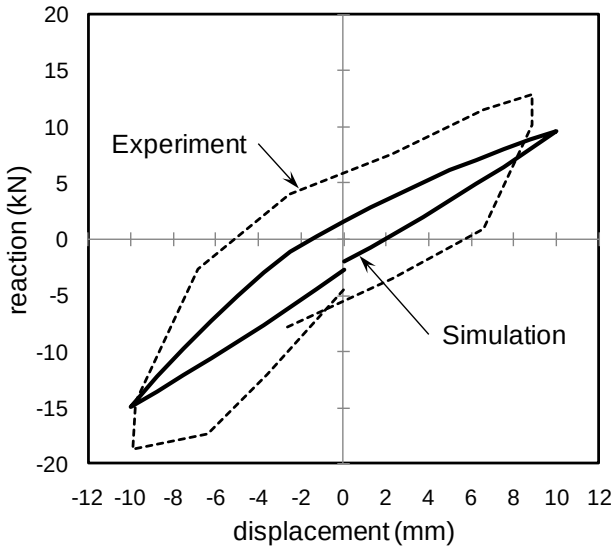

Fig. 7.4 Simulation of near-full scale test by Bramel et al. (1999)

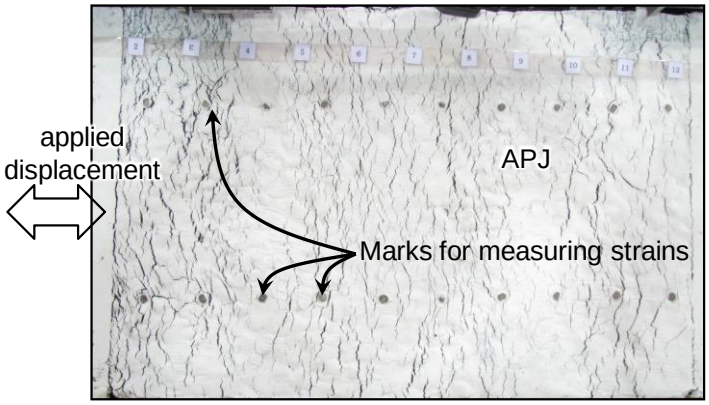

(a) Top view

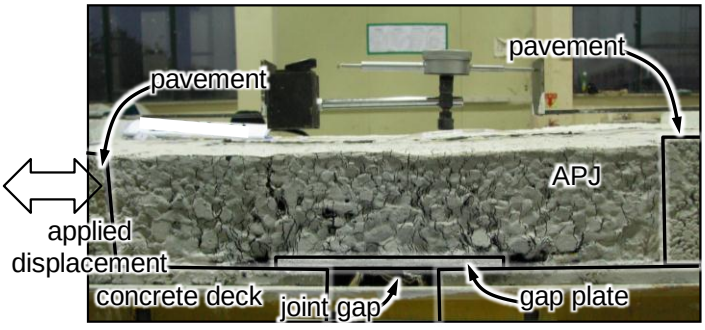

(b) Side view

Fig. 7.5 APJ specimens tested by Moon et al. (2008)

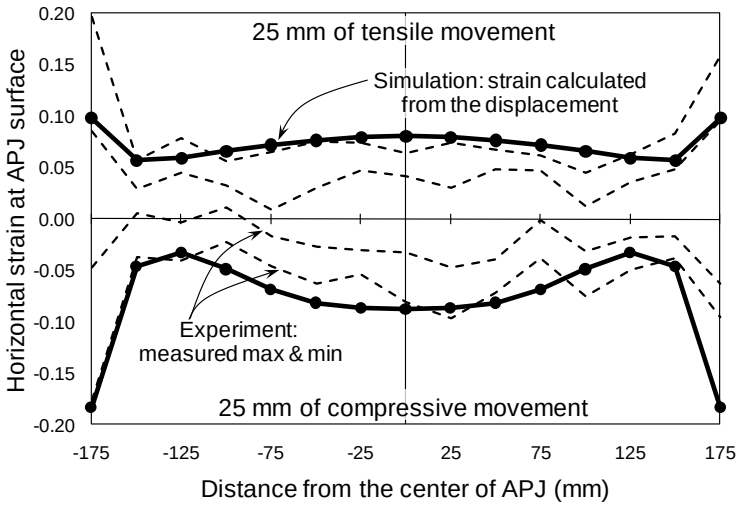

(a) Specimen APJ-1

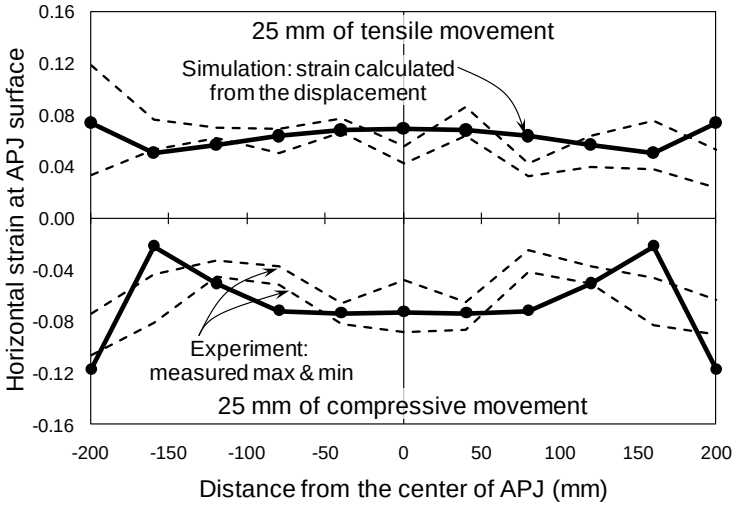

(b) Specimen APJ-2

Fig. 7.6 Comparison between simulation and test results: horizontal strain at the surface

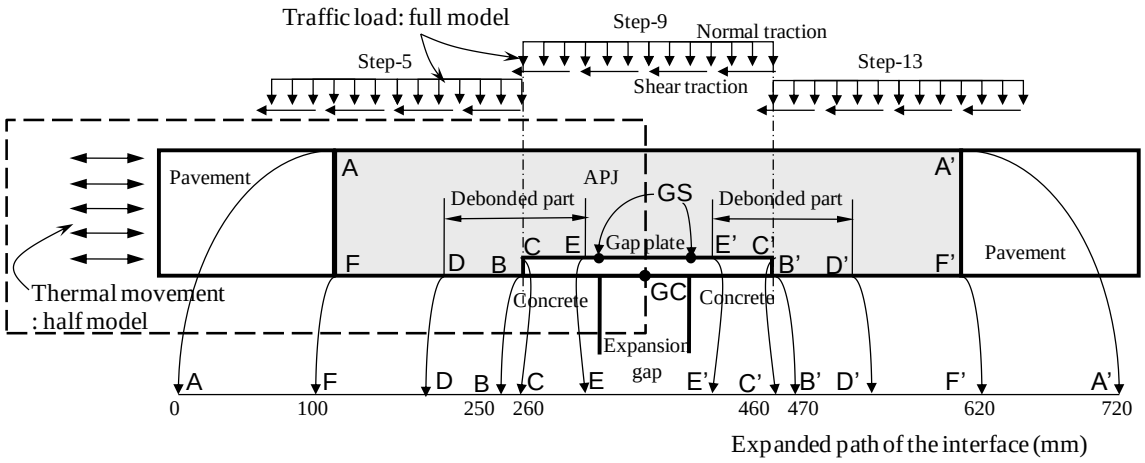

Fig. 7.7 Locations of interest, loading conditions, and path along which results are sampled

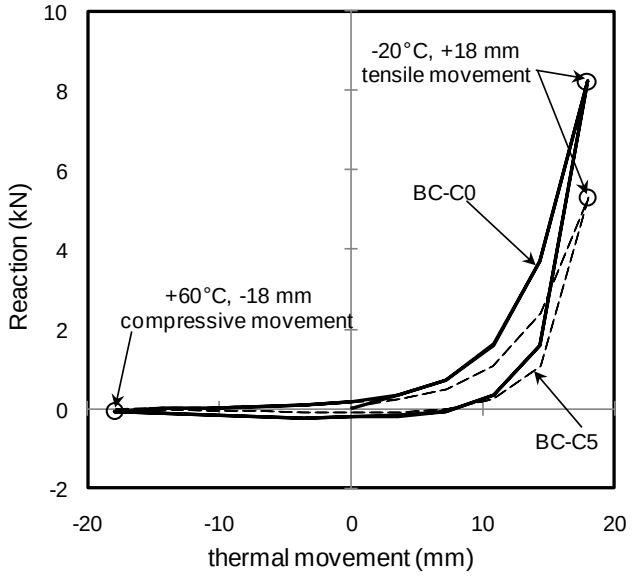

Fig. 7.8 Reactions due to thermal movement 20±40°C (±18 mm) with έ=0.000004 /sec

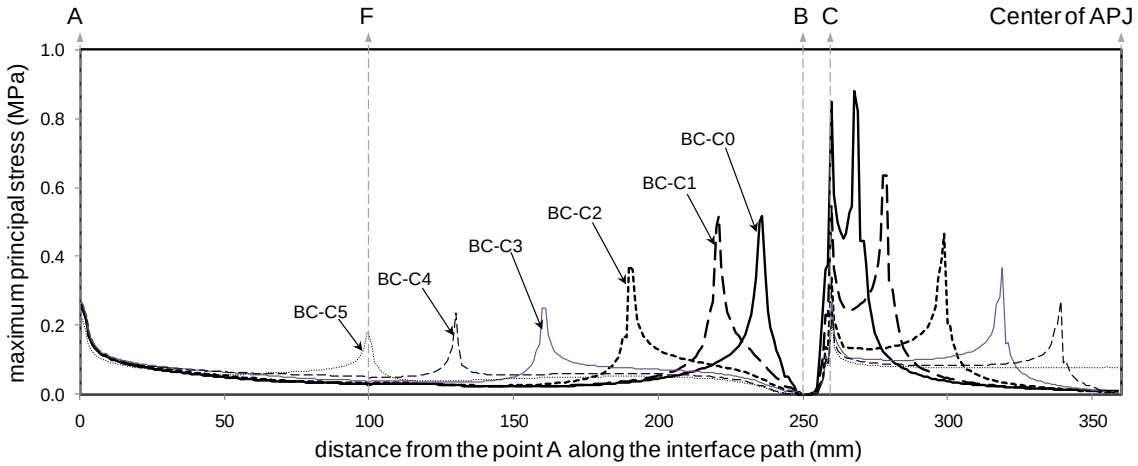

Fig. 7.9 Distribution of maximum principal stress along the interface path: 18 mm of tensile thermal movement (-20°C), cases BC-C0 through BC-C5

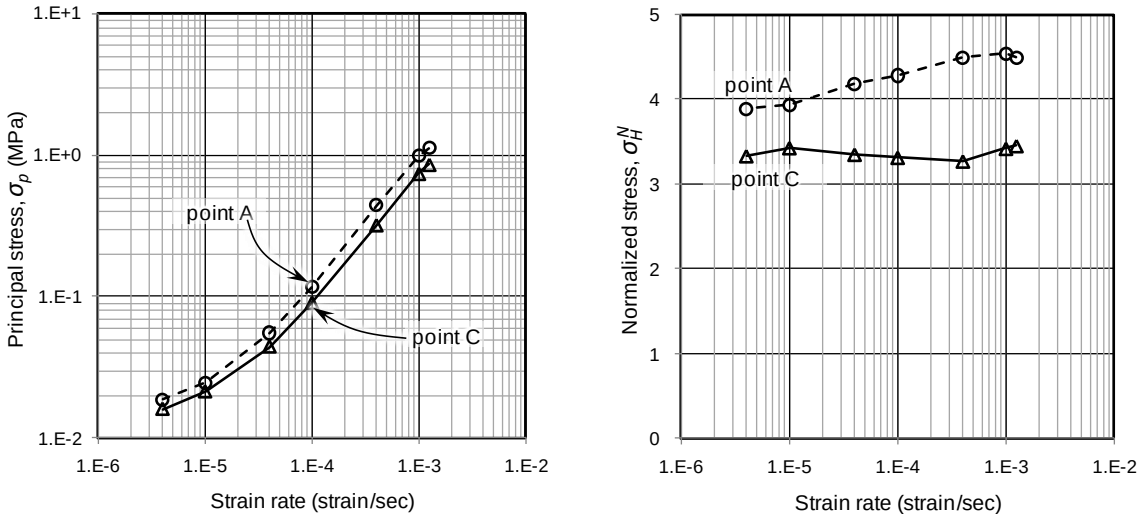

(a) Principal stress, σ_p (b) Normalized stress, σ_H^N

Fig. 7.10 Variation of principal and normalized stresses at point A and C with strain rate. APJ subjected to 20 mm of tensile movement at 20°C

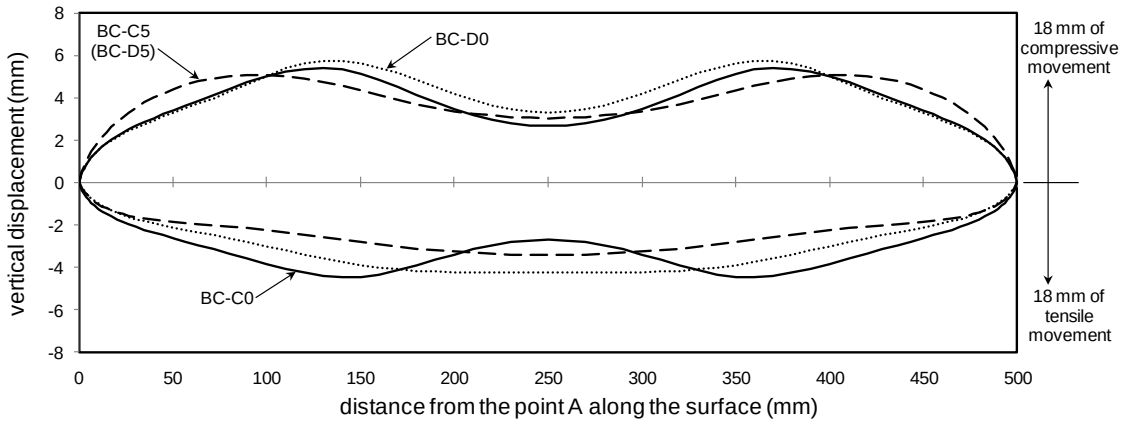

Fig. 7.11 Vertical profile of APJ when subjected to ±18 mm of thermal movement

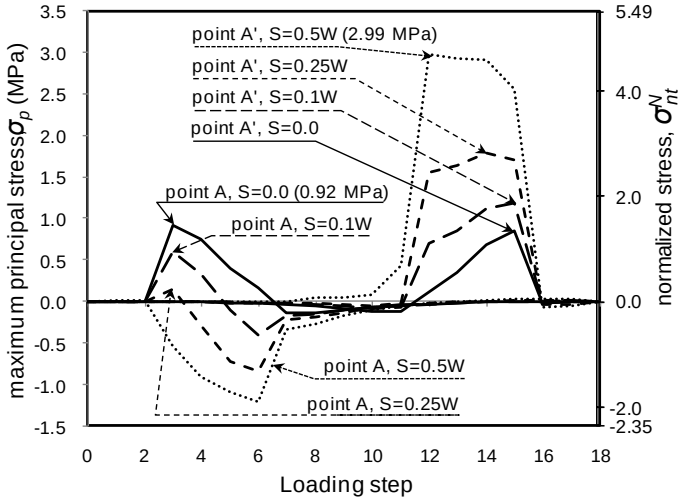

(a) Point A and A'

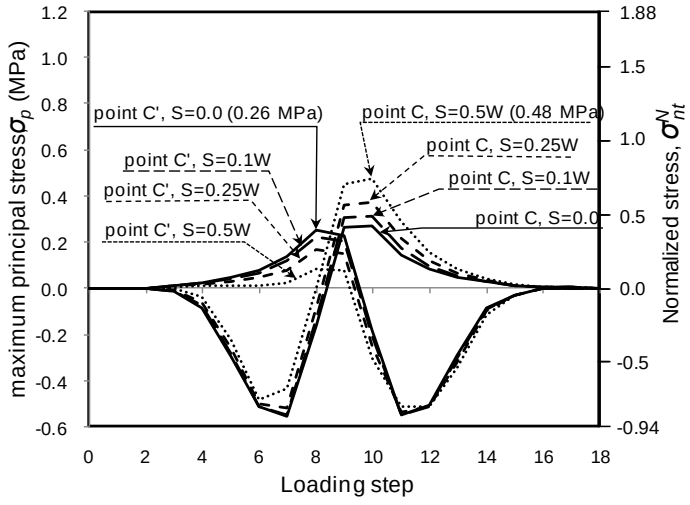

(b) Point C and C'

Fig. 7.12 Maximum principal stresses at critical points (A and C) during passage of a tire over the APJ for various shear tractions at 20°C

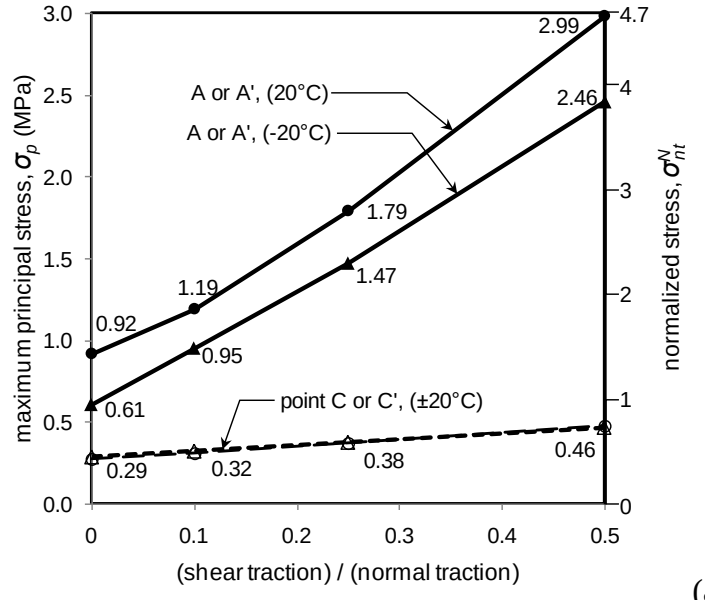

(a) Principal stress

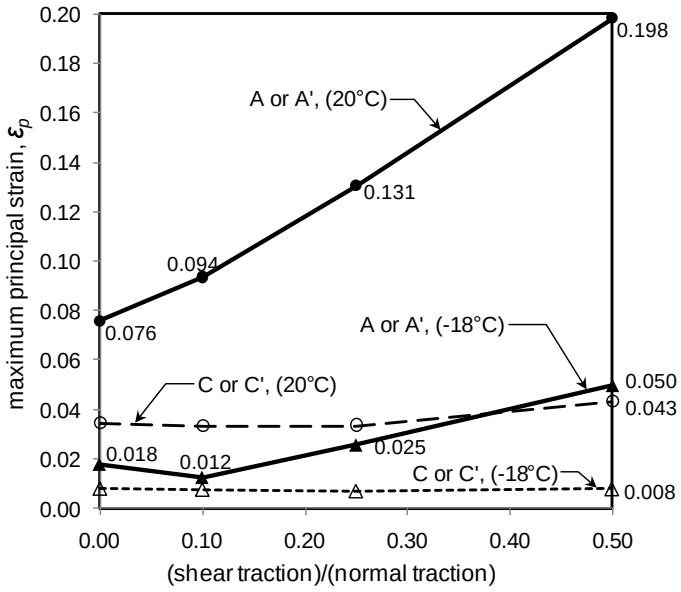

(b) Principal strain

Fig. 7.13 Variation of peak values of maximum principal stresses and strains with shear traction and temperature, at point A (or A') and point C (or C') during passage of a tire over the APJ

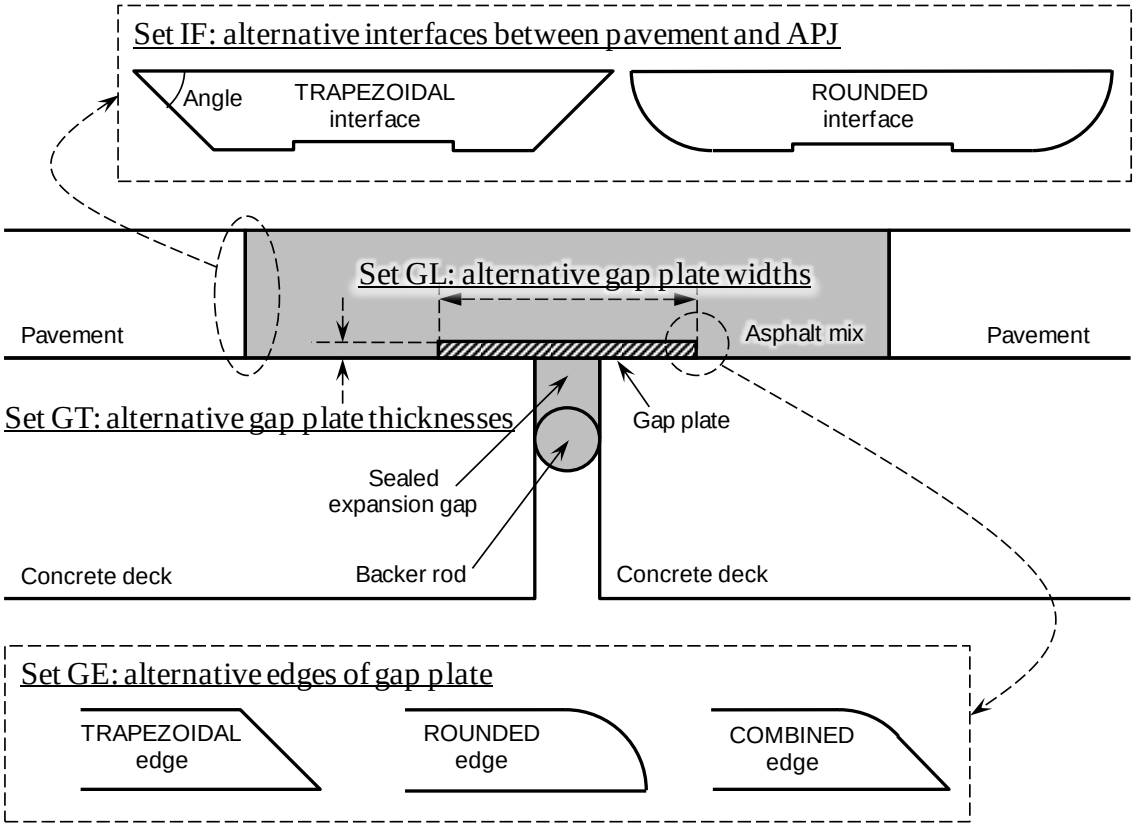

Fig. 7.14 Schematic view of traditional APJ and alternative designs being investigated through parametric study

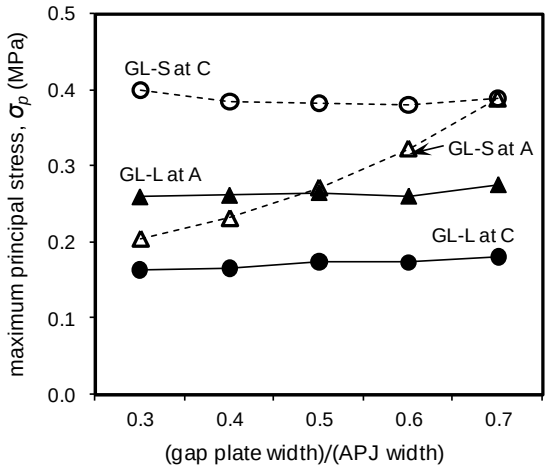

Fig. 7.15 Variations of maximum principal stress at point A and C with gap plate width (set GL): maximum tensile movement (+18 mm corresponding to -20°C) with $\dot{\varepsilon} = 4\times10^{-6}$ /sec

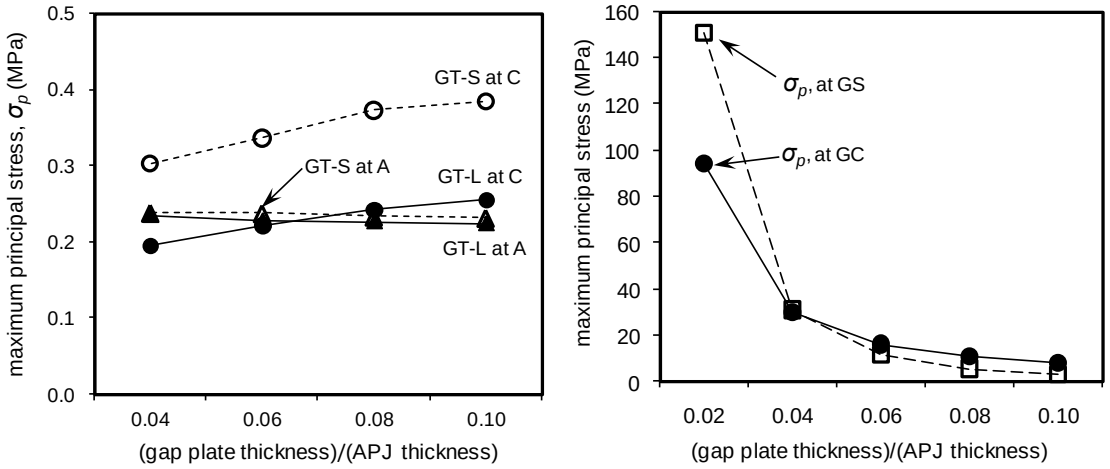

(a) stress at point A and C subjected to thermal load: maximum tensile movement (+18 mm corresponding to -20°C) with $\dot{\varepsilon} = 4\times10^{-6}$ /sec

(b) maximum principal stress at the gap plate subjected to traffic load: 80 kN of axle load (W=0.6375 MPa, S=0)

Fig. 7.16 Variations of stresses at APJ and gap plate with gap plate thickness (set-GT)

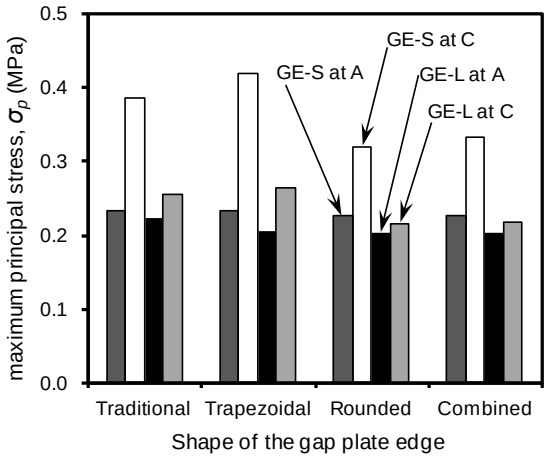

Fig. 7.17 Variations of principal stress at point A and C with gap plate edge shape (set-GE): maximum tensile movement (+18 mm corresponding to -20°C) with $\dot{\varepsilon} = 4\times10^{-6}$ /sec

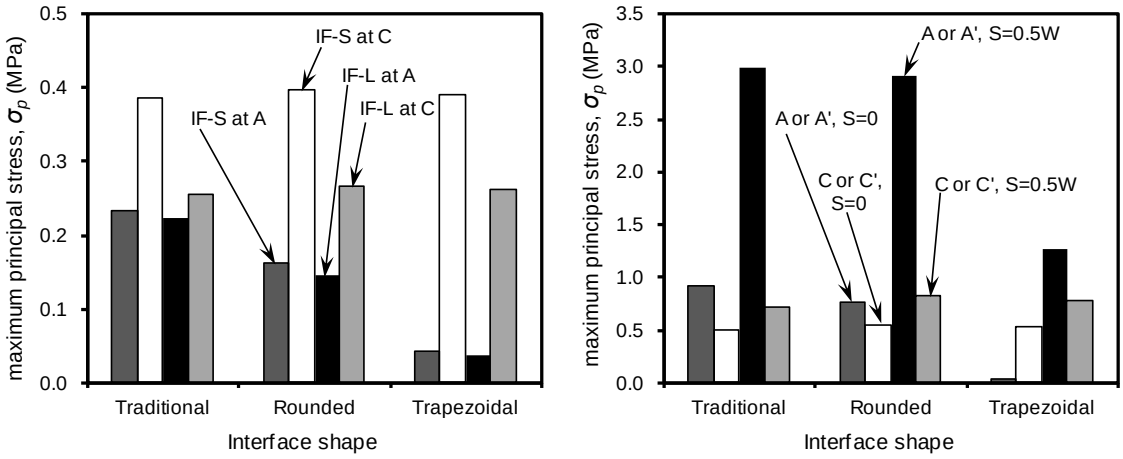

(a) thermal load: maximum tensile movement (+18 mm corresponding to -20°C) with $\dot{\varepsilon} = 4\times10^{-6}$ /sec

(b) traffic load: 80 kN of axle load (W=0.6375 MPa)

Fig. 7.18 Variations of principal stress at point A and C with interface shape (set-IF)

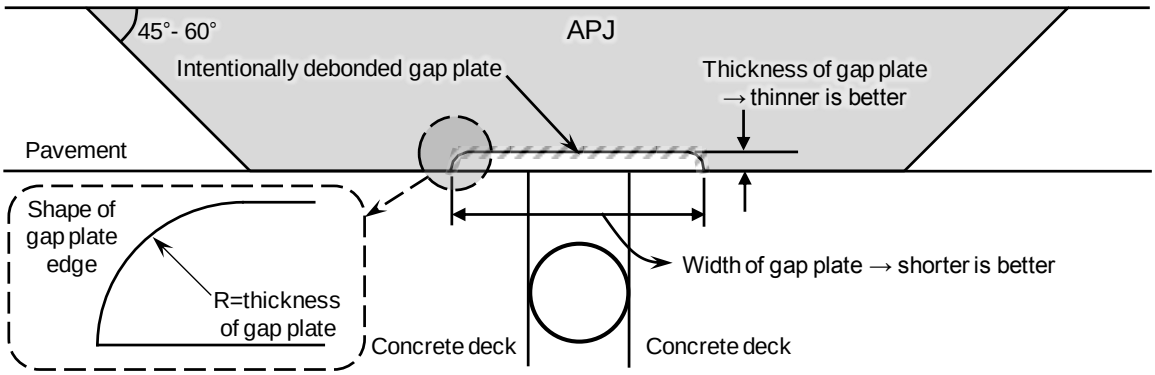

Fig. 7.19 Improved geometric design of APJ

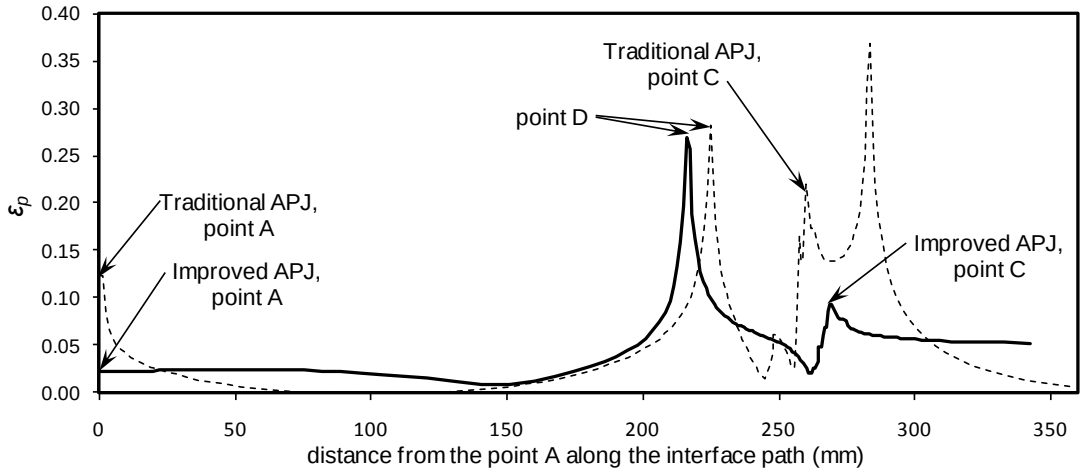

Fig. 7.20 Comparison of improved APJ to traditional APJ: maximum principal strain distributions along the interface path subjected to 18 mm of tensile movement (-20°C)

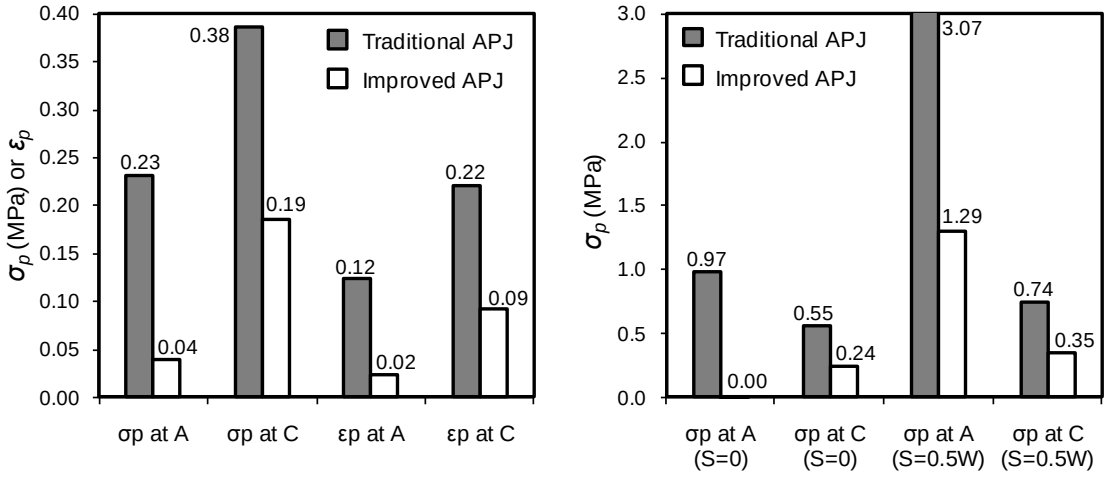

(a) thermal load (b) traffic load

Fig. 7.21 Comparison of improved APJ to traditional APJ: maximum principal stresses and strains at point A and C

REFERENCES

AASHTO (2004). *AASHTO LRFD Bridge Design Specifications, Customary U.S. Units, 3rd Ed.*

ASTM D 6297-01 (Reapproved 2007). Standard Specification for Asphaltic Plug Joints for Bridges.

Di Benedetto, H, de La Roche, C., Baaj, H., Pronk, A., and Lundstrom, R. (2004). "Fatigue of bituminous mixtures." *Materials and Structures*, 37, 202-216.

Bramel, B. K., Dolan, C. W., Puckett, J. A., and Ksaibati, K. (1999). *Asphalt Plug Joints: Characterization and Specifications*, Ph. D. Dissertation, University of Wyoming, Department of Civil and Architectural Engineering.

Bridge Joint Association (2003). *Standard for Asphaltic Plug Joints*, Concrete Bridge Development Group, UK.

Cheung, C. Y. and Cebon, D. (1997a). "Experimental Study of Pure Bitumens in Tension, Compression, and Shear." *Journal of Rheology*, 41(1), 45-73.

Cheung, C. Y. and Cebon, D. (1997b). "Deformation Mechanisms of Pure Bitumen." *Journal of Materials in Civil Engineering*, 9(3), 117-129.

Deshpande, V. S. and Cebon, D. (1999). "Steady-state constitutive relationship for idealised bituminous mixes." *Mechanics of Materials*, 31, 271-287.

Deshpande, V. S. and Cebon, D. (2000). "Uniaxial Experiments on Idealized Asphalt Mixes." *Journal of Materials in Civil Engineering*, ASCE, 12(3), 262-271.

Di Benedetto, H, de La Roche, C., Baaj, H., Pronk, A., and Lundstrom, R. (2004). "Fatigue of bituminous mixtures." *Materials and Structures*, 37, 202-216.

Harvey, J. A. F. and Cebon, D. (2003). "Failure Mechanisms in Viscoelastic Films." *Journal of Materials Science*, 38, 1021-1032.

Kim, H., Wagoner, M. P. and Buttlar, W. G. (2008), "Micromechanical Fracture Modeling of Asphalt Concrete Using a Single-Edge Notched Beam Test," *Materials and Structures*, Springer Netherlands, ISSN 1359-5997 (Print) 1871-6873 (Online).

Lytton, R. L., Uzan, J., Fernando, E. G., Roque, R., Hiltunen, D., and Stoffels, S. M. (1993). *Development and Validation of Performance Prediction Models and Specifications for Asphalt Binders and Paving Mixes*, SHRP-A-357, Strategic Highway Research Program, National Research Council, Washington, DC.

Moon, K. T., Park, P., Park, S. Y., Hong, S. H., and Kim, H. B. (2008) "Evaluation for behavior of asphalt plug joint with using a FEM analysis." *Proceedings of Korean Society of Road Engineers 2008 Fall Conference*, Seoul, Korea, pp. 15-23, Oct.

2008.

Partl, M. N., Hean, S., and Poulikakos, L. (2002). "Asphaltic Plug Joint Characterization and Performance Evaluation." *Proceedings of 9th International Conference on Asphalt Pavements*, ISAP, Copenhagen.

Qian, Z., Akisanya, A. R., and Imbabi, M. S. (2000). "Effects of Geometry on the Deformation of Asphaltic Plug Joints Subjected to Surface Tractions." *Journal of Strain Analysis*, 35(5), 403-413.

Reid, M. D., Imbabi, M. S., and Coutellier, D. (1998). "Effects of Joint Geometry on Response of Asphaltic Plug Joints." *Journal of Transportation Engineering*, 124(4), 311-318.

Transportation Research Board (2003). *Bridge Deck Joint Performance – A Synthesis of Highway Practice, NCHRP Synthesis 319*, TRB.

CHAPTER 8
SUMMARY, CONCLUSIONS AND FUTURE RESEARCH

8.1 SUMMARY AND ACCOMPLISHMENTS

With the aim of developing a multifunctional, high performance asphaltic composite, the research reported in this dissertation addressed five inter-related topics: (1) constitutive modeling of asphalt and asphalt concrete, (2) interaction between steel fiber and asphalt, (3) performance of steel fiber reinforced asphalt concrete (SFRAC), (4) imparting conductivity into asphalt, and (5) behavior and modification of asphalt plug joint (APJ). A summary of the achievements in each of these areas is as follows:

8.1.1 Constitutive Modeling for Asphalt Binder and Mixture

A rigorous constitutive model for asphaltic materials is necessary for developing realistic computational tools for better understanding the behavior of high performance asphaltic composites. To this end, a nonlinear viscoelastic constitutive model was proposed for asphaltic materials. The proposed model is distinguished from other existing models by its capability of simulating, with a single set of material parameters, two different characteristics in the behavior of asphaltic materials: linear viscoelasticity with multiple characteristic times dominating the lower stress/strain region and power law nonlinearity prominent in higher stress/stress regions. The model was represented by mechanical analogs that consisted of a power law damper and a generalized Maxwell (or Kelvin-Voigt) model connected in series. The time-temperature superposition principle was used to consider temperature dependency. Numerical integration procedures to calculate responses to both displacement and force controlled deformations were suggested. Two different versions of the model, which are distinguished by the deformable range, are presented: finite strain version for asphalt binder and infinitesimal

strain version for asphalt concrete. The model for asphalt binder was fully three dimensional and described in finite strain kinematics in order to simulate large deformation. For asphalt concrete, a uniaxial model was formulated in infinitesimal strain theory. In addition, damage mechanics was employed to account for damage evolution of asphalt concrete, which was not necessary for asphalt binder. Extensive validation studies were conducted to show that the model produces reasonable results over a wide range of conditions.

8.1.2 Interaction between Steel Fiber and Asphalt

The interaction between a straight steel fiber and the surrounding asphalt matrix was investigated through single fiber pull-out tests and numerical simulations. The pull-out load versus displacement responses and the stress distribution at the fiber-matrix interface provided fundamental and unique insights into the fiber reinforcing mechanisms that occur within a temperature dependent viscoelastic matrix. The variables considered in the study were temperature, displacement rate, and fiber dimensions; a total of 241 pull-out tests were conducted. The stress distributions along with the fiber-matrix interface at various temperatures were examined through numerical simulations using a nonlinear viscoelastic finite element model. To the best of the author's knowledge, this is the first rational effort to investigate the interfacial characteristics between a fiber and a viscoelastic asphalt matrix.

8.1.3 Performance of Steel Fiber Reinforced Asphalt Concrete

The reinforcing effects of steel fiber additives for asphalt concrete were investigated through indirect tension tests at low temperature. Focusing on cracking resistance, indirect tensile strength (ITS), fracture energy (FE), and post-cracking energy (PE) were obtained from tests. To provide fundamental information and to find an optimum method of fiber reinforcement, the effects of thickness, length, deformed shape, and content of steel fibers were investigated. To the author's knowledge, this is the first study to investigate the effect of fiber dimension and shape with the objective of achieving optimum fiber reinforcement for asphalt concrete. The results demonstrated that adding steel fibers is an efficient way of improving low temperature cracking resistance of

asphalt concrete.

8.1.4 Imparting Electrical Conductivity into Asphalt

To enable multifunctional applications using conductive asphaltic composites, precise control of electrical resistivity is required. To this end, the effects of adding steel fibers and various conductive fillers on the resistivity of asphaltic composite were examined experimentally through 130 measurements for 40 asphalt mastics and mixtures.

8.1.5 Behavior and Modification of Asphalt Plug Joint

The behavior of a typical APJ subjected to thermal and traffic loads was examined through a series of finite element analyses employing a temperature-dependent visco-elasto-plastic material model with nonlinear viscosity. The material parameters were calibrated by using previously published test data, and the model was validated by comparing simulated responses to APJ test data. The developed models were then used to investigate stress and strain distributions, vulnerable locations to cracking failure, and local demands at those locations. In addition, four sets of alternative designs were parametrically investigated to develop an improved APJ that can mitigate the risk of premature failure.

8.2 CONCLUSIONS

The most important conclusions of the research summarized above are listed next.

8.2.1 Constitutive Modeling for Asphalt Binder and Mixture

- The developed constitutive model was able to simulate both linear and nonlinear viscoelastic ranges of asphaltic materials simultaneously with a single set of material parameters.
- A method for calibrating the parameters of the model was proposed. Demonstration of the calibration procedure showed that all the required viscoelastic parameters could be determined from a single set of constant strain rate tests.

- The finite strain version of the developed model was validated by simulating creep and constant shear strain rate tests. The simulation results demonstrated excellent applicability of the proposed model to asphalt over wide ranges of temperature, stress, and strain levels.
- From the simulations for asphalt undergoing large deformation, it was argued that the peak stress commonly observed in constant strain rate tension tests is a transition point where the effects of large deformation exceed the effect of increase in stress, implying that the concept of steady state deformation in large strain range is not as clear cut as commonly accepted in the field. It was also clarified that it is inappropriate to define steady state in terms of nominal stress.
- An analysis of isochrones suggested that the linearity limit of asphalt cannot be represented by a single parameter such as stress or strain.
- Constant compressive and tensile strain rate tests for asphalt concrete were simulated using the infinitesimal strain, damage dependent version of the proposed model. The validation studies demonstrated that the model was able to successfully capture the behavior of asphalt concrete.

8.2.2 Interaction between Steel Fiber and Asphalt

- Experimental investigation showed that the mode of pull-out failure varied with temperature and loading rate. Based on the differences in the pull-out force versus displacement curves and the remaining asphalt on the pulled out fiber, the pull-out modes were categorized into 3 main types: matrix failure (MatF), mixed failure (MixF), and interface failure (IntF) modes.
- Test results showed that the MatF mode dominated behavior when viscosity was low (the binder is watery), i.e. high temperature and/or slow loading rate, and was not accompanied by any interfacial debonding. Hence, its pull-out behavior depended completely on the viscoelastic properties of the matrix. In contrast, the IntF involved clean debonding of the fiber-matrix interface and was associated with very high viscosity (the binder is thick), which occurred at low temperatures and/or fast loading rates.

- Simulation studies using a nonlinear viscoelastic constitutive model showed that when the contribution of viscous flow to total deformation was small due to cold temperature, the interfacial shear stress was concentrated at the top and bottom of the fiber's embedded length. The degree of stress concentration rose with the fiber length, but decreased when the contributions of localized viscous deformations started to increase.
- Based on the observed failure mechanisms and simulation information, it was hypothesized that there exists a critical interfacial bond stress (τ_{cr}) at which interfacial debonding occurs. Evidence was provided which suggests that τ_{cr} is a key factor controlling fiber pull-out from asphalt and that it is independent of temperature and loading rate. Combining the test data with the simulation results, a reasonable value for τ_{cr} for the asphalt used in this work was 6.9 MPa.

8.2.3 Performance of Steel Fiber Reinforced Asphalt Concrete

- The test results demonstrated that low temperature cracking resistance of asphalt concrete can be significantly improved by using discrete steel fiber reinforcement of proper size, shape, and content.
- By retarding brittle damage localization, the fracture of indirect tension specimens shifted from brittle fracture to local punching failure, and was accompanied by significant amounts of crushing of asphalt concrete around the fracture surface.
- Comparisons of test results for smooth fibers showed that fiber length was critical for performance improvements. In particular, the ITS and toughness of SFRAC improved with increase in fiber length. Test results for deformed fibers showed that the hooked end of fibers is beneficial for improving ITS, and that twisting contributes to increased post-cracking energy.
- ITS and toughness of SFRAC at low temperature were approximately proportional to the area of fiber-matrix debonding at failure, and additional improvements can be obtained by deforming fibers.
- The highest ITS and toughness were observed for the specimens reinforced with hooked fibers having 30 mm length and 0.4 mm diameter and the specimens with twisted fibers having 30 mm length and 0.3 mm diameter, respectively. The

maximum improvements achieved in this study were 62.5% increase in indirect tensile strength, and 370% and 895% improvements in fracture energy and toughness, respectively. These improvements are the highest documented mechanical improvements attributed to fiber reinforcement in asphalt concrete to date.

- Balling or clumping of fibers were observed to occur during mixing. However, the problems were mild and were more likely to occur as the aspect ratio became higher and as the amount of fiber increased.

8.2.4 Imparting Electrical Conductivity into Asphalt

- A sudden change in electrical resistivity from no conduction to conduction, i.e. the so-called percolation threshold, is observed in specimen containing steel fibers. Achieving this threshold implies that the asphalt concrete is conductive and it is therefore impossible to manipulate its resistivity.
- Sufficiently low electrical resistivity can be obtained by replacing a part of the fillers by a proper type of graphite powder in asphalt mastics. This means that the adjustable range of resistivity using conductive filler can be controlled.
- Electrical conductivity of asphalt mastics varies significantly with the type of conductive fillers. Five types of conductive fillers including four graphite types and a type of carbon black were tested in this study. It turned out that natural flake graphite powder is the most efficient in imparting conductivity into asphalt.
- The volume resistivity of asphalt mastic with natural flake graphite powder varies widely with the amount of the graphite powder mixed in the mastic. This implies that the resistivity of asphaltic composite can be manipulated over a wide range of conditions thereby potentially enabling various multifunctional applications.

8.2.5 Behavior and Modification of Asphalt Plug Joint

- Accelerated tests employing high strain rates create high localized strain rates at critical points, which significantly increase the local demands, potentially influencing the primary reasons behind failure modes observed in the field. Therefore, it was suggested that care should be taken to ensure that the stress demands during accelerated experiments conducted at room temperature are

comparable to those obtained under field conditions at low temperatures, especially when the local mode of failure being investigated is related to the stress level.

- Analytical investigations of APJ behavior showed that stress concentrations at critical points increased as the debonded length at the bottom interface became shorter. Intentional debonding of the interface between the APJ and gap plate was therefore suggested as a practical and low cost solution to mitigate the risk of developing a vertical crack from the gap plate edge.
- Although the distribution of stress along the APJ interface varied with the location of traffic loading, the locations of high stress and strain demands were generally observed to be similar to the case of thermal loading. The simulation results suggested that fatigue-related damage will accumulate at the top of interface between the APJ and pavement and the edge of the gap plate when truck axles roll across an APJ.
- For truck loading, local demand computations showed that the APJ-pavement interface is more vulnerable to fatigue cracking than the gap plate edge while local demand at the latter was generally higher than the former for thermal movement. The computed demands indicated that there was a significantly increased chance for direct cracking at the APJ-pavement interface when trucks axles on the joint accelerate or brake sharply. This was proposed as a likely reason for some of the premature failures observed in the field.
- The parametric study for an alternative design showed that the local demands can be reduced by (1) shortening the gap plate width, (2) decreasing gap plate thickness, (3) rounding off the gap plate edge, and (4) making the APJ-pavement interface inclined. Synthesizing all the information presented in the parametric study, it was evident that, together, the proposed geometric modifications significantly reduced the local demands at vulnerable points under both thermal and traffic loads. The significantly reduced demands indicate that there is strong likelihood that the proposed design will perform better under service conditions than the traditional APJ.

8.3 FUTURE RESEARCH

Future research efforts stemming from the results of this dissertation are recommended as follows.

8.3.1 Constitutive Modeling for Asphalt Binder and Mixture

In this dissertation, the material parameters of the developed constitutive model were calibrated by using the data of uniaxial constant strain rate tension tests. Since the method requires at least 4-6 sets of data obtained at different strain rates, a more simplified test method with non-homogeneous deformation configuration will significantly reduce the effort for material parameter calibration. A generalized method of material calibration that can use any kind of test data is an alternative way of reducing the calibration effort.

8.3.2 Development of Multifunctional High Performance Asphalt Concrete

The indirect tension test results demonstrate that adding steel fibers is an efficient way of improving low temperature cracking resistance of asphalt concrete (AC). The findings from the indirect tension test are based on phenomenological observations, and therefore, further investigations are needed to understand the reinforcing mechanism. For example, understanding single fiber pull-out behavior from the viscoelastic matrix such as asphalt concrete will provide a fundamental insight for the behavior of SFRAC. The single fiber pull-out behavior from pure asphalt was investigated in this dissertation, but the fiber pull-out from AC containing aggregates should be explored for more efficient field application of SFRAC. In addition to cracking resistance, improvements in rutting and fatigue resistance due to fiber additives should be examined. Eventually, efficiency of the fiber reinforcement should be verified through field applications.

Imparting conductivity into asphalt concrete opens a door to various multifunctional applications. Characteristics of conductive asphalt such as piezo-resistivity, piezo-electricity, pyro-electricity, and thermo-electricity need to be explored, and the methodology for the applications – self-sensing, self-healing, energy harvesting, and ice removal – should be developed.

8.3.3 Geometric Improvement of Asphalt Plug Joint

The study on APJ used stress and strain responses as indicators for the risk of local fracture initiation and provided much needed insight into the behavior of APJ that can be used to improve durability of these types of products. However, additional work needs to be done to quantify fatigue damage initiation and propagation and to determine rutting life. The key difficulty of achieving this is that existing fatigue and rutting models have been developed for pavement materials and not for APJ material. Therefore, the proposed research must be preceded by model development based upon material testing that adequately simulates field demands in APJs, which differ greatly from those in traditional pavements. It is important to note that the effects of overall geometric dimensions (APJ thickness and width) were not investigated in this research and should be studied in future research. Furthermore, extensive field testing is recommended to provide conclusive experimental evidence that the proposed modifications are indeed effective.

APPENDIX
EXPERIMENTAL DATA

A.1 SINGLE FIBER PULL-OUT TEST DATA

The single fiber pull-out behavior is investigated and described in Chapter 4. Below tables list all test data obtained from the pull-out tests.

Table A.1 Pull-out test data: straight steel fiber with 0.2 mm diameter at +20°C

Test ID	Test Speed	Sampling rate	Temperature	Embedded depth	Failure mode	Peak force	Force /Length	τ at peak	Frictional resistance	
	mm/sec	Hz	°C	mm		N	N/mm	MPa	N	%
PO-0716-D2-1	8.47	20	20.0	25.0	MatF	17.32	0.693	1.103		
PO-0716-D2-2	8.47	20	20.0	24.5	MatF	15.85	0.647	1.030		
PO-0716-D2-3	8.47	20	20.0	24.5	MatF	12.90	0.527	0.838		
PO-0716-D2-4	1.27	20	20.0	24.5	MatF	4.19	0.171	0.272		
PO-0716-D2-5	1.27	20	20.0	25.5	MatF	3.96	0.155	0.247		
PO-0716-D2-6	1.27	20	20.0	25.0	MatF	2.83	0.113	0.180		
PO-0716-D2-7	0.423	20	20.0	24.0	MatF	1.70	0.071	0.113		
PO-0716-D2-8	0.423	20	20.0	24.0	MatF	1.70	0.071	0.113		
PO-0716-D2-9	0.423	20	20.0	24.0	MatF	1.25	0.052	0.083		
PO-0716-D2-10	84.7	200	20.0	24.0	MatF	53.09	2.212	3.521		
PO-0716-D2-11	84.7	200	20.0	23.5	MatF	50.26	2.139	3.404		
PO-0716-D2-12	84.7	200	20.0	23.5	MatF	47.31	2.013	3.204		

Table A.2 Pull-out test data: straight steel fiber with 0.3 mm diameter at +20°C

Test ID	Test Speed	Sampling rate	Temperature	Embedded depth	Failure mode	Peak force	Force /Length	τ at peak	Frictional resistance	
	mm/sec	Hz	°C	mm		N	N/mm	MPa	N	%
PO-0716-D3-1	8.47	20	20.0	25.0	MatF	14.15	0.566	0.601		
PO-0716-D3-2	8.47	20	20.0	25.0	MatF	14.04	0.562	0.596		
PO-0716-D3-3	8.47	20	20.0	25.0	MatF	12.34	0.494	0.524		
PO-0716-D3-4	1.27	20	20.0	24.0	MatF	4.53	0.189	0.200		
PO-0716-D3-5	1.27	20	20.0	24.0	MatF	4.19	0.175	0.185		
PO-0716-D3-6	1.27	20	20.0	23.0	MatF	2.94	0.128	0.136		
PO-0716-D3-7	0.423	20	20.0	24.5	MatF	2.15	0.088	0.093		
PO-0716-D3-8	0.423	20	20.0	24.0	MatF	1.81	0.075	0.080		
PO-0716-D3-9	0.423	20	20.0	25.0	MatF	1.59	0.064	0.067		
PO-0716-D3-10	84.7	200	20.0	23.0	MatF	74.14	3.223	3.420		
PO-0716-D3-11	84.7	200	20.0	24.0	MatF	74.71	3.113	3.303		
PO-0716-D3-12	84.7	200	20.0	24.5	MatF	60.11	2.453	2.603		
PO-0716-D3-21	1.27	20	20.0	17.5	MatF	5.21	0.298	0.316		
PO-0716-D3-22	1.27	20	20.0	19.0	MatF	5.66	0.298	0.316		
PO-0716-D3-23	1.27	20	20.0	17.0	MatF	5.54	0.326	0.346		
PO-0716-D3-24	1.27	20	20.0	11.5	MatF	3.85	0.335	0.355		
PO-0716-D3-25	1.27	20	20.0	9.5	MatF	4.30	0.453	0.480		
PO-0716-D3-26	1.27	20	20.0	12.0	MatF	4.41	0.368	0.390		

Table A.3 Pull-out test data: straight steel fiber with 0.5 mm diameter at +20°C

Test ID	Test Speed	Sampling rate	Temperature	Embedded depth	Failure mode	Peak force	Force /Length	τ at peak	Frictional resistance	
	mm/sec	Hz	°C	mm		N	N/mm	MPa	N	%
PO-0716-D5-1	8.47	20	20.0	22.5	MatF	23.66	1.052	0.669		
PO-0716-D5-2	8.47	20	20.0	23.0	MatF	21.51	0.935	0.595		
PO-0716-D5-3	8.47	20	20.0	24.0	MatF	19.47	0.811	0.516		
PO-0716-D5-4	8.47	20	20.0	23.5	MatF	28.19	1.200	0.764		
PO-0716-D5-5	1.27	20	20.0	22.5	MatF	6.00	0.267	0.170		
PO-0716-D5-6	1.27	20	20.0	22.0	MatF	4.53	0.206	0.131		
PO-0716-D5-7	1.27	20	20.0	25.5	MatF	6.91	0.271	0.173		
PO-0716-D5-8	84.7	200	20.0	25.0	MatF	83.42	3.337	2.124		
PO-0716-D5-9	84.7	200	20.0	26.0	MatF	70.18	2.699	1.718		
PO-0716-D5-10	84.7	200	20.0	24.0	MatF	101.53	4.230	2.693		
PO-0716-D5-12	0.423	20	20.0	23.0	MatF	1.70	0.074	0.047		
PO-0716-D5-13	0.423	20	20.0	24.0	MatF	1.81	0.075	0.048		

Table A.4 Pull-out test data: straight steel fiber with 0.7 mm diameter at +20°C

Test ID	Test Speed	Sampling rate	Temperature	Embedded depth	Failure mode	Peak force	Force /Length	τ at peak	Frictional resistance	
	mm/sec	Hz	°C	mm		N	N/mm	MPa	N	%
PO-0716-D7-1	84.7	200	20.0	24.5	MatF	115.57	4.717	2.145		
PO-0716-D7-2	50.8	200	20.0	24.0	MatF	81.95	3.415	1.553		
PO-0716-D7-3	25.4	200	20.0	24.5	MatF	52.07	2.125	0.966		
PO-0716-D7-4	84.7	200	20.0	25.5	MatF	105.16	4.124	1.875		
PO-0716-D7-5	84.7	200	20.0	25.0	MatF	109.23	4.369	1.987		

Table A.5 Pull-out test data: straight steel fiber with 0.2 mm diameter at 0°C

Test ID	Test Speed	Sampling rate	Temperature	Embedded depth	Failure mode	Peak force	Force /Length	τ at peak	Frictional resistance	
	mm/sec	Hz	°C	mm		N	N/mm	MPa	N	%
PO-0803-D2-1	0.423	5	0.0	24.5	MatF	54.332	2.218	3.529		
PO-0803-D2-2	0.423	5	0.0	24.5	MixF	80.593	3.290	5.235		
PO-0803-D2-3	0.423	5	0.0	25.5	MixF	75.952	2.979	4.740		
PO-0803-D2-4	1.27	5	0.0	24.0	MatF	56.143	2.339	3.723		
PO-0803-D2-5	1.27	5	0.0	24.5	MixF	70.971	2.897	4.610		
PO-0803-D2-6	1.27	20	0.0	24.0	IntF	91.006	3.792	6.035		
PO-0803-D2-7	1.27	20	0.0	24.5	IntF	78.103	3.188	5.074		
PO-0803-D2-8	1.27	20	0.0	24.0	IntF	75.726	3.155	5.022		
PO-0803-D2-9	1.27	20	0.0	23.5	IntF	76.518	3.256	5.182		
PO-100211-D2-1	0.423	20	1.7	6.0	MatF	12.791	2.132	3.393		
PO-100211-D2-2	0.423	20	-0.6	8.0	MatF	17.432	2.179	3.468		
PO-100211-D2-3	0.423	20	0.0	8.0	MixF	29.090	3.636	5.787		
PO-100211-D2-4	0.423	20	0.0	7.0	MixF	22.072	3.153	5.018		
PO-100211-D2-5	1.27	20	0.0	7.5	IntF	27.845	3.713	5.909		
PO-100211-D2-6	1.27	20	0.0	7.0	MixF	25.808	3.687	5.868		
PO-100211-D2-7	1.27	20	0.0	7.0	MixF	21.733	3.105	4.941		
PO-100211-D2-10	8.47	200	0.0	7.5	IntF	44.598	5.946	9.464		
PO-100211-D2-11	8.47	200	0.0	5.5	IntF	26.147	4.754	7.566		
PO-100211-D2-12	8.47	200	0.0	10.0	IntF	35.769	3.577	5.693		
PO-100211-D2-13	8.47	200	0.0	10.0	IntF	38.485	3.849	6.125		
PO-100211-D2-14	8.47	200	0.0	9.0	IntF	44.145	4.905	7.807		
PO-100211-D2-15	1.27	200	0.0	11.0	MixF	44.145	4.013	6.387		
PO-100211-D2-16	1.27	200	0.0	10.0	IntF	41.089	4.109	6.539		
PO-100211-D2-17	1.27	200	0.0	10.0	MixF	43.353	4.335	6.900		
PO-100211-D2-18	0.423	200	0.0	9.0	IntF	34.184	3.798	6.045		
PO-100211-D2-19	0.423	20	0.6	11.0	MatF	28.977	2.634	4.193		
PO-100211-D2-20	0.423	20	0.0	10.5	MixF	35.090	3.342	5.319		
PO-100211-D2-21	0.423	20	0.0	10.5	MixF	35.542	3.385	5.387		
PO-100211-D2-22	0.042	20	0.0	9.0	MatF	10.300	1.144	1.822		
PO-100211-D2-23	0.042	20	0.6	10.0	MatF	14.036	1.404	2.234		

Table A.6 Pull-out test data: straight steel fiber with 0.3 mm diameter at 0°C

Test ID	Test Speed	Sampling rate	Temperature	Embedded depth	Failure mode	Peak force	Force /Length	τ at peak	Frictional resistance	
	mm/sec	Hz	°C	mm		N	N/mm	MPa	N	%
PO-0803-D3-1	0.423	5	0.0	24.5	MixF	100.515	4.103	4.353		
PO-0803-D3-2	0.423	5	0.0	23.5	MixF	97.656	4.156	4.409		
PO-0803-D3-4	1.27	20	0.0	24.0	MatF	91.572	3.816	4.048		
PO-0803-D3-5	1.27	20	0.0	24.0	IntF	169.222	7.051	7.481		
PO-0803-D3-6	1.27	20	0.0	25.0	MatF	105.495	4.220	4.477		
PO-0803-D3-21	0.423	20	0.0	25.5	MixF	110.023	4.315	4.578		
PO-0803-D3-22	8.47	200	0.0	25.5	IntF	179.070	7.022	7.451		
PO-0803-D3-23	8.47	200	0.0	25.0	IntF	190.955	7.638	8.104		
PO-0803-D3-24	8.47	200	0.0	25.5	IntF	202.387	7.937	8.421		
PO-0803-D3-25	8.47	200	0.0	25.0	IntF	187.559	7.502	7.960		
PO-0806-D3-1	0.423	20	0.0	9.5	MatF	20.375	2.145	2.276		
PO-0806-D3-2	0.423	20	0.0	10.0	MatF	28.524	2.852	3.027		
PO-0806-D3-3	0.423	20	0.0	9.5	MatF	40.070	4.218	4.475		
PO-0806-D3-4	8.47	200	0.0	10.0	IntF	57.728	5.773	6.125		
PO-0806-D3-5	8.47	200	0.0	10.0	MixF	61.124	6.112	6.485		
PO-0806-D3-6	8.47	200	0.0	11.0	IntF	68.708	6.246	6.627		
PO-0806-D3-7	0.423	20	0.0	18.5	MatF	51.163	2.766	2.934		
PO-0806-D3-8	0.423	20	0.0	17.5	MatF	61.463	3.512	3.727		
PO-0806-D3-9	0.423	20	0.0	16.5	IntF	109.796	6.654	7.060		
PO-0806-D3-10	8.47	200	0.0	17.0	IntF	80.480	4.734	5.023		
PO-0806-D3-11	8.47	200	0.0	18.0	IntF	181.447	10.080	10.696		
PO-0806-D3-21	1.27	20	0.0	18.0	MixF	104.816	5.823	6.179		
PO-0806-D3-22	1.27	20	0.0	19.0	MatF	89.988	4.736	5.025		
PO-0806-D3-23	1.27	20	0.0	18.0	MatF	67.236	3.735	3.963		
PO-0806-D3-24	1.27	20	0.0	10.5	MixF	60.671	5.778	6.131		
PO-0806-D3-25	1.27	20	0.0	11.0	MatF	47.880	4.353	4.618		
PO-0806-D3-26	1.27	20	0.0	11.0	IntF	76.065	6.915	7.337		
PO-0806-D3-27	8.47	200	0.0	18.0	IntF	115.796	6.433	6.826		
PO-100211-D3-1	0.423	20	1.1	6.0	MatF	16.300	2.717	2.882		
PO-100211-D3-2	0.423	20	-3.9	7.0	MixF	34.071	4.867	5.164		
PO-100211-D3-3	0.423	20	-4.4	8.0	MixF	45.164	5.645	5.990		
PO-100211-D3-4	1.27	20	3.3	8.0	MatF	25.921	3.240	3.438		
PO-100211-D3-5	1.27	20	-4.4	9.0	IntF	55.691	6.188	6.565		
PO-100211-D3-6	1.27	20	-0.6	7.0	MixF	35.316	5.045	5.353		
PO-100211-D3-7	1.27	20	0.0	9.0	MatF	42.673	4.741	5.031		
PO-100211-D3-8	0.423	20	-0.6	8.5	MatF	23.318	2.743	2.911		
PO-100211-D3-9	1.27	20	3.9	7.5	MatF	22.752	3.034	3.219		

Table A.7 Pull-out test data: straight steel fiber with 0.5 mm diameter at 0°C

Test ID	Test Speed	Sampling rate	Temperature	Embedded depth	Failure mode	Peak force	Force /Length	τ at peak	Frictional resistance	
	mm/sec	Hz	°C	mm		N	N/mm	MPa	N	%
PO-0803-D5-1	0.423	20	0.0	24.5	MatF	90.10	3.678	2.341		
PO-0803-D5-2	0.423	20	0.0	25.0	MatF	104.70	4.188	2.666		
PO-0803-D5-3	0.423	20	0.0	26.0	MatF	154.51	5.943	3.783		
PO-0803-D5-4	1.27	20	0.0	26.0	MatF	183.82	7.070	4.501		
PO-0803-D5-5	1.27	20	0.0	23.5	MatF	129.61	5.515	3.511		
PO-0803-D5-6	1.27	20	0.0	24.0	IntF	195.94	8.164	5.197		
PO-0803-D5-9	8.47	20	0.0	22.0	MixF	182.58	8.299	5.283		
PO-0803-D5-11	1.27	20	0.0	23.0	IntF	235.55	10.241	6.520		
PO-0803-D5-12	0.423	20	0.0	23.5	MixF	193.45	8.232	5.241		

Table A.8 Pull-out test data: straight steel fiber with 0.2 mm diameter at -20°C

Test ID	Test Speed	Sampling rate	Temperature	Embedded depth	Failure mode	Peak force	Force /Length	τ at peak	Frictional resistance	
	mm/sec	Hz	°C	mm		N	N/mm	MPa	N	%
PO-100218-D2-1	0.423	200	-18.9	14.5	IntF	35.542	2.451	3.901	14.602	41.08%
PO-100218-D2-2	1.27	200	-18.3	15.0	IntF	29.429	1.962	3.123	13.922	47.31%
PO-100218-D2-4	0.423	200	-20.0	15.0	IntF	49.012	3.267	5.200	15.054	30.71%
PO-100218-D2-5	0.423	200	-20.0	14.5	IntF	25.581	1.764	2.808	7.584	29.65%
PO-100218-D2-6	0.423	200	-20.0	14.0	IntF	27.393	1.957	3.114	8.603	31.41%
PO-100218-D2-7	1.27	200	-12.2	15.5	IntF	40.749	2.629	4.184	14.262	35.00%
PO-100218-D2-8	1.27	200	-20.0	16.0	IntF	36.448	2.278	3.626	12.677	34.78%
PO-100218-D2-9	1.27	200	-18.9	15.0	IntF	25.355	1.690	2.690	13.696	54.02%
PO-100218-D2-13	0.423	200	-20.0	10.5	IntF	81.724	7.783	12.387	11.772	14.40%
PO-100218-D2-14	0.423	200	-20.0	11.0	IntF	46.522	4.229	6.731	5.999	12.89%
PO-100218-D2-15	0.423	200	-20.0	11.0	IntF	66.896	6.081	9.679	9.734	14.55%
PO-100218-D2-16	1.27	200	-20.0	9.5	IntF	35.882	3.777	6.011	8.716	24.29%
PO-100218-D2-17	1.27	200	-20.0	11.0	IntF	34.410	3.128	4.979	8.942	25.99%
PO-100218-D2-18	1.27	200	-10.6	10.0	IntF	47.088	4.709	7.494	7.244	15.38%
PO-100218-D2-22	0.0423	20	-20.0	10.5	IntF	85.120	8.107	12.902	8.036	9.44%
PO-100218-D2-23	0.0423	20	-20.0	10.5	IntF	61.916	5.897	9.385	4.754	7.68%
PO-100218-D2-24	0.0423	20	-20.0	10.5	IntF	63.275	6.026	9.591	4.754	7.51%
PO-100218-D2-25	0.0423	20	-21.1	4.5	IntF	29.203	6.490	10.328	1.924	6.59%
PO-100218-D2-26	0.0423	20	-20.0	6.5	IntF	27.846	4.284	6.818	4.981	17.89%
PO-100218-D2-27	0.0423	20	-20.0	5.0	IntF	20.035	4.007	6.377	1.132	5.65%
PO-100218-D2-28	0.423	200	-19.4	5.0	IntF	23.430	4.686	7.458	2.829	12.07%
PO-100218-D2-29	0.423	200	-20.0	6.0	IntF	49.352	8.225	13.091	1.698	3.44%
PO-100218-D2-30	0.423	200	-20.0	4.5	IntF	35.089	7.798	12.410	0.679	1.94%
PO-100218-D2-31	0.423	200	-20.0	5.5	IntF	25.129	4.569	7.272	1.811	7.21%
PO-100218-D2-32	1.27	200	-20.0	5.0	IntF	18.450	3.690	5.873	2.716	14.72%
PO-100218-D2-33	1.27	200	-20.0	6.0	IntF	51.276	8.546	13.601	2.377	4.64%
PO-100218-D2-34	1.27	200	-20.0	5.5	IntF	51.389	9.343	14.871	1.245	2.42%
PO-100218-D2-35	1.27	200	-20.0	5.0	IntF	16.526	3.305	5.260	1.811	10.96%
PO-100218-D2-36	0.0423	20	-20.0	15.0	IntF	41.202	2.747	4.372	9.621	23.35%
PO-100218-D2-37	0.0423	20	-20.0	16.0	IntF	54.559	3.410	5.427	10.980	20.13%
PO-100218-D2-38	0.0423	20	-20.0	15.0	IntF	64.519	4.301	6.846	-	
PO-100218-D2-39	0.0423	20	-20.0	16.0	IntF	85.120	5.320	8.467	13.585	15.96%

Table A.9 Pull-out test data: straight steel fiber with 0.3 mm diameter at -20°C

Test ID	Test Speed	Sampling rate	Temperature	Embedded depth	Failure mode	Peak force	Force /Length	τ at peak	Frictional resistance	
	mm/sec	Hz	°C	mm		N	N/mm	MPa	N	%
PO-100218-D3-1	0.423	20	-20.0	6.0	IntF	53.540	8.923	9.468	1.585	2.96%
PO-100218-D3-4	0.423	200	-19.4	9.0	IntF	48.446	5.383	5.711	5.546	11.45%
PO-100218-D3-5	0.423	200	-19.4	10.5	IntF	89.535	8.527	9.048	10.866	12.14%
PO-100218-D3-6	0.423	200	-20.0	10.0	IntF	35.203	3.520	3.735	4.868	13.83%
PO-100218-D3-7	0.423	200	-19.4	7.5	IntF	44.031	5.871	6.229	3.056	6.94%
PO-100218-D3-8	0.423	200	-18.3	5.0	IntF	42.673	8.535	9.055	0.000	0.00%
PO-100218-D3-10	0.423	200	-20.0	4.5	IntF	11.319	2.515	2.669	1.811	16.00%
PO-100218-D3-11	0.423	200	-20.0	11.0	IntF	114.210	10.383	11.016	22.751	19.92%
PO-100218-D3-12	0.423	200	-7.2	11.5	IntF	73.688	6.408	6.799	9.508	12.90%
PO-100218-D3-13	1.27	200	-17.2	10.0	IntF	51.502	5.150	5.465	3.735	7.25%
PO-100218-D3-14	1.27	200	-20.0	10.5	IntF	22.865	2.178	2.311	5.999	26.24%
PO-100218-D3-15	1.27	200	-20.0	11.0	IntF	74.367	6.761	7.173	10.187	13.70%
PO-100218-D3-20	1.27	200	-12.2	5.5	IntF	11.998	2.181	2.315	2.377	19.81%
PO-100218-D3-21	1.27	200	-20.0	7.0	IntF	30.222	4.317	4.581	7.018	23.22%
PO-100218-D3-22	1.27	200	-20.6	5.5	IntF	14.036	2.552	2.708	3.169	22.58%
PO-100218-D3-23	1.27	200	-20.6	6.0	IntF	10.980	1.830	1.942	4.301	39.17%
PO-100218-D3-27	1.27	200	-20.0	15.5	IntF	82.403	5.316	5.641	12.338	14.97%
PO-100218-D3-28	1.27	200	-20.0	25.0	IntF	54.106	2.164	2.296	9.508	17.57%
PO-100218-D3-29	1.27	200	-20.0	25.0	IntF	71.085	2.843	3.017	20.035	28.18%
PO-100218-D3-31	1.27	200	-15.6	24.0	IntF	42.786	1.783	1.892	10.074	23.55%
PO-100218-D3-32	0.423	200	-18.9	15.5	IntF	90.780	5.857	6.214	7.584	8.35%
PO-100218-D3-33	0.423	200	-17.8	14.5	IntF	64.746	4.465	4.738	7.811	12.06%
PO-100218-D3-34	0.423	200	-20.0	15.5	IntF	148.169	9.559	10.143	21.960	14.82%
PO-100218-D3-35	0.423	200	-20.0	15.5	IntF	64.520	4.163	4.417	8.489	13.16%
PO-100218-D3-36	0.423	200	-20.0	24.0	IntF	49.352	2.056	2.182	10.980	22.25%
PO-100218-D3-37	0.423	200	-20.0	24.0	IntF	90.327	3.764	3.993	17.092	18.92%
PO-100218-D3-38	0.423	200	-20.0	26.0	IntF	44.824	1.724	1.829	10.640	23.74%
PO-100218-D3-39	0.423	200	-20.0	23.0	IntF	70.632	3.071	3.258	16.979	24.04%
PO-100218-D3-40	0.0423	20	-18.9	9.5	IntF	79.574	8.376	8.887	2.604	3.27%
PO-100218-D3-41	0.0423	20	-20.0	11.0	IntF	64.633	5.876	6.234	6.226	9.63%
PO-100218-D3-42	0.0423	20	-20.0	10.0	IntF	88.290	8.829	9.368	6.112	6.92%
PO-100218-D3-43	0.0423	20	-20.0	9.0	IntF	87.716	9.746	10.341	9.963	11.36%
PO-100218-D3-44	0.0423	20	-19.4	10.0	IntF	84.781	8.478	8.996	5.433	6.41%
PO-100218-D3-45	0.0423	20	-20.0	16.0	IntF	71.311	4.457	4.729	6.565	9.21%
PO-100218-D3-46	0.0423	20	-20.0	15.0	IntF	71.990	4.799	5.092	7.471	10.38%
PO-100218-D3-47	0.0423	20	-20.0	15.0	IntF	79.801	5.320	5.645	5.547	6.95%
PO-100218-D3-48	0.0423	20	-20.0	13.0	IntF	49.692	3.822	4.056	5.547	11.16%
PO-100218-D3-49	0.0423	20	-19.4	5.0	IntF	34.863	6.973	7.398	0.792	2.27%
PO-100218-D3-50	0.0423	20	-20.0	5.0	IntF	38.259	7.652	8.119	0.000	0.00%
PO-100218-D3-51	0.0423	20	-20.0	6.0	IntF	41.881	6.980	7.406	0.453	1.08%
PO-100218-D3-52	0.0423	20	-20.0	6.5	IntF	48.106	7.401	7.853	1.811	3.76%
PO-100218-D3-53	1.27	200	-20.0	5.5	IntF	17.092	3.108	3.297	2.603	15.23%
PO-100218-D3-54	1.27	200	-20.0	6.0	IntF	19.016	3.169	3.363	5.207	27.38%
PO-100218-D3-57	1.27	200	-20.0	10.0	IntF	40.636	4.064	4.312	9.508	23.40%

A.2 INDIRECT TENSION TEST DATA

The reinforcing effects of fiber additives for asphalt concrete are investigated through indirect tension tests described at Chapter 5. The indirect tensile stress versus strain curves obtained from the tests are listed in this section.

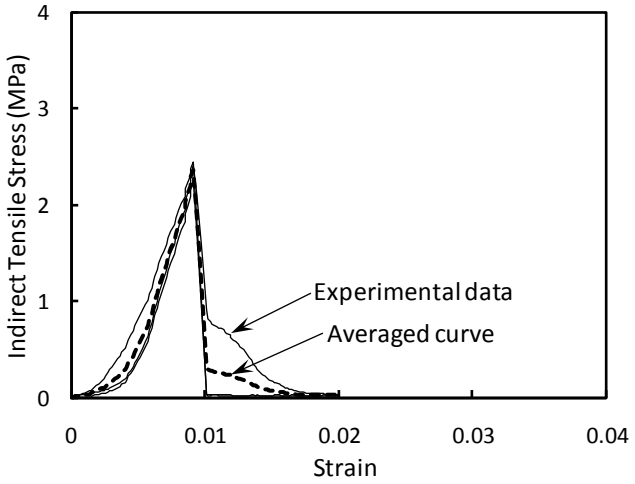

Fig. A.1 Indirect tensile stress – strain curves of non-reinforced asphalt concrete specimens

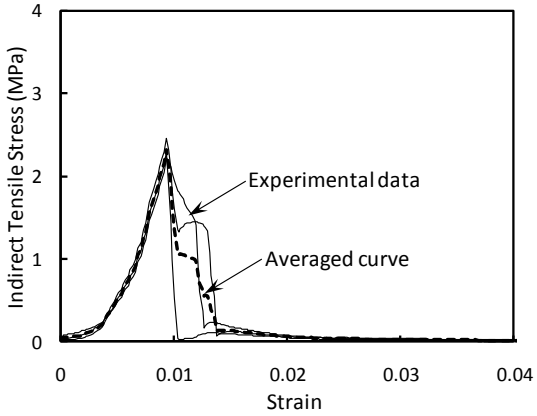

(a) SC1-06, V_f = 0.5%

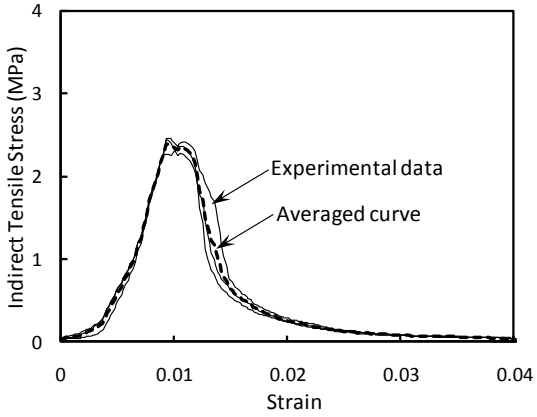

(b) SC1-06, V_f = 1.0%

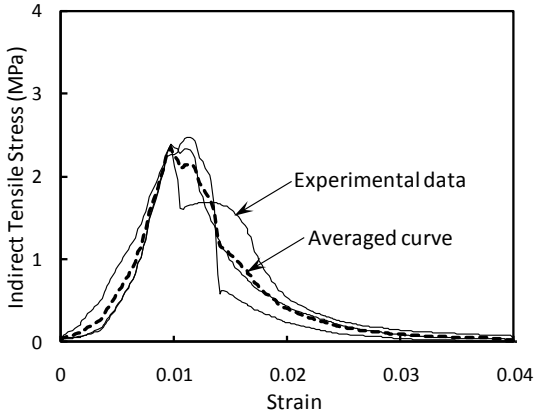

(c) SC1-06, V_f = 1.5%

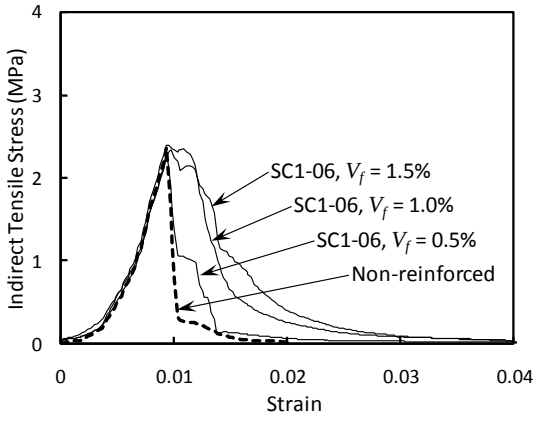

(d) the average curves compared to non-reinforced asphalt concrete

Fig. A.2 Indirect tensile stress – strain curves of SC1-06

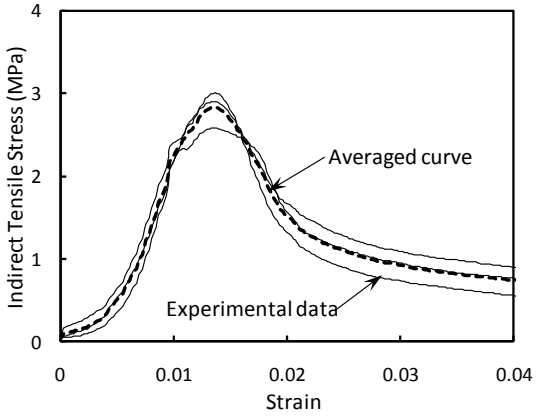

(a) SC2-25, V_f = 0.5%

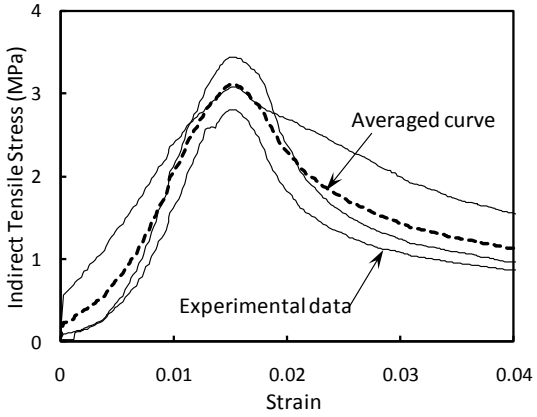

(b) SC2-25, V_f = 1.0%

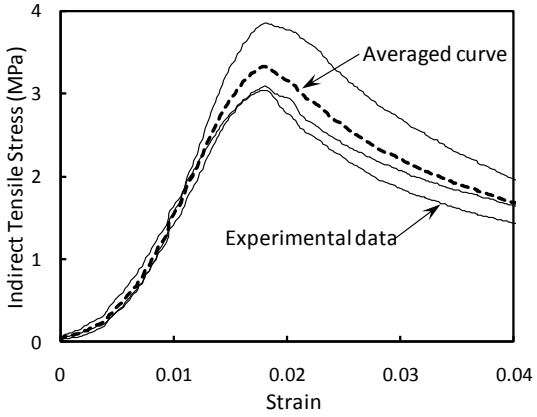

(c) SC2-25, V_f = 1.5%

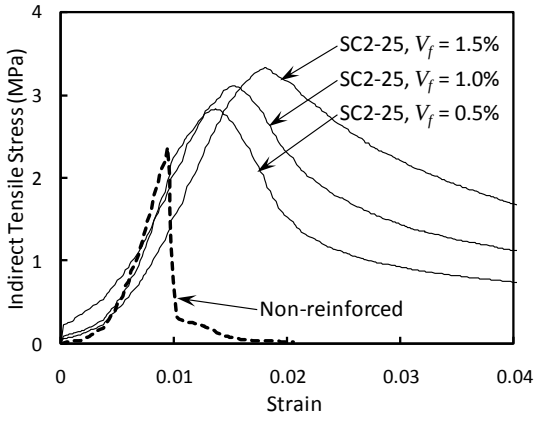

(d) the average curves compared to non-reinforced asphalt concrete

Fig. A.3 Indirect tensile stress – strain curves of SC2-25

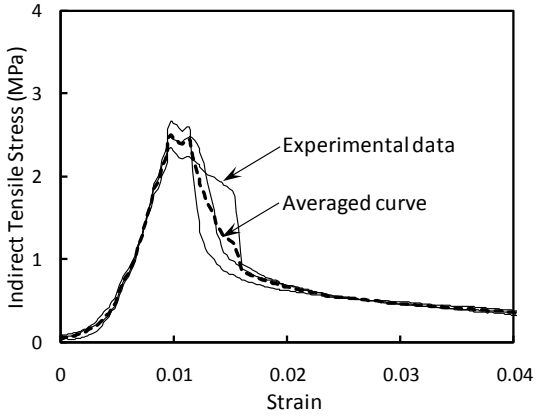

(a) SC3-18, V_f = 0.5%

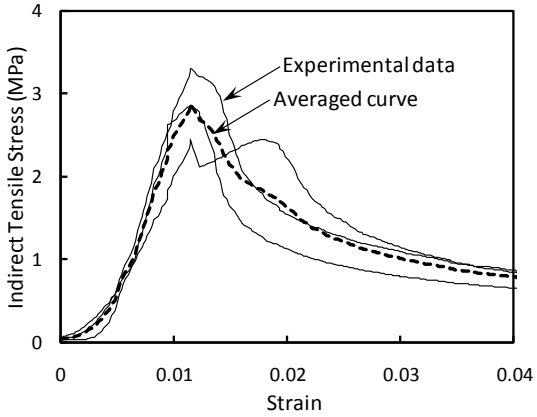

(b) SC3-18, V_f = 1.0%

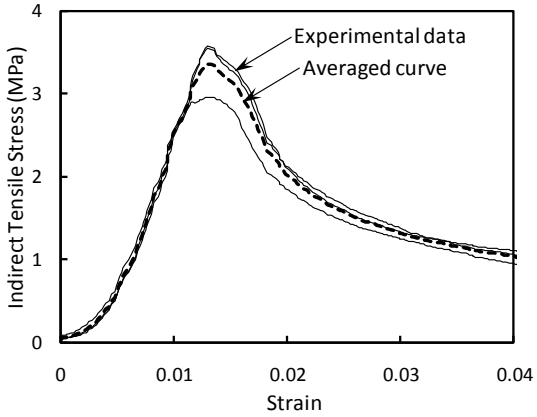

(c) SC3-18, V_f = 1.5%

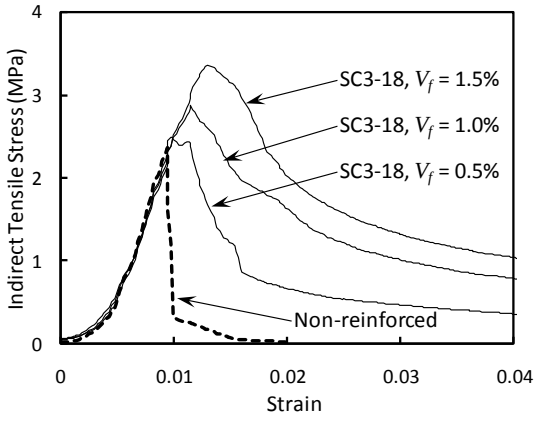

(d) the average curves compared to non-reinforced asphalt concrete

Fig. A.4 Indirect tensile stress – strain curves of SC3-18

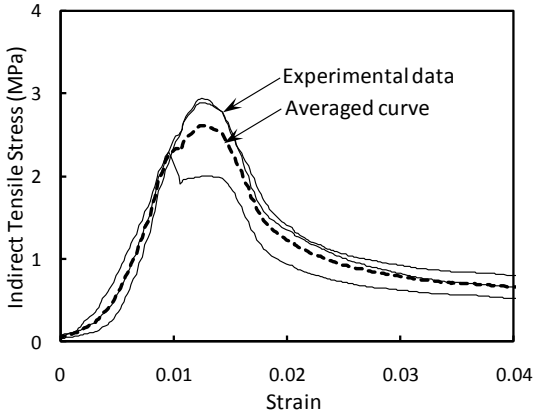

(a) SC3-30, V_f = 0.5%

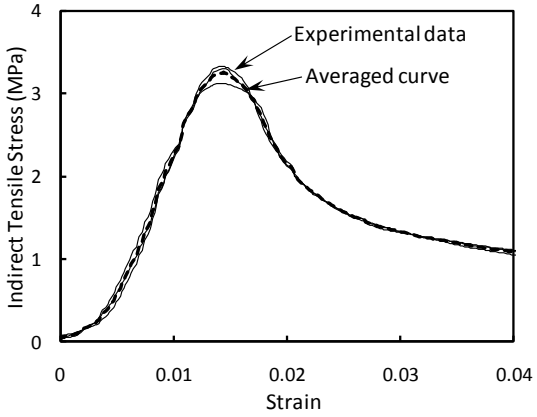

(b) SC3-30, V_f = 1.0%

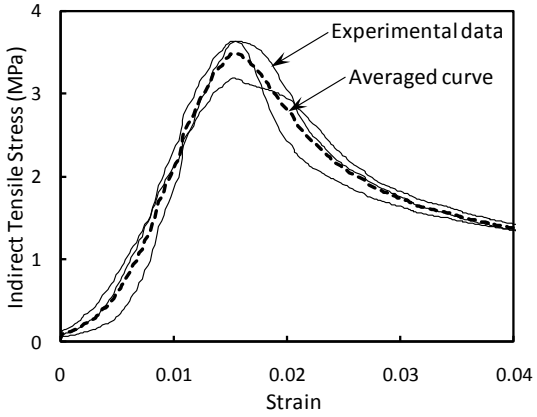

(c) SC3-30, V_f = 1.5%

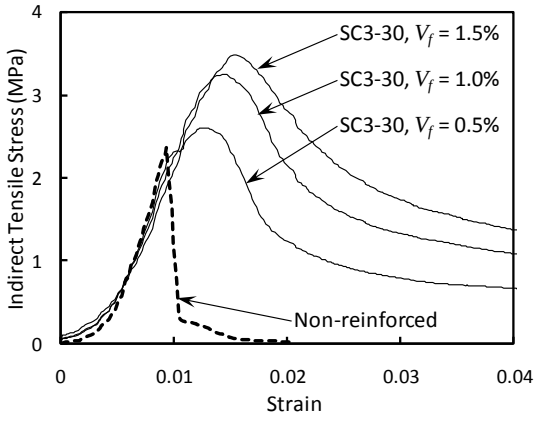

(d) the average curves compared to non-reinforced asphalt concrete

Fig. A.5 Indirect tensile stress – strain curves of SC3-30

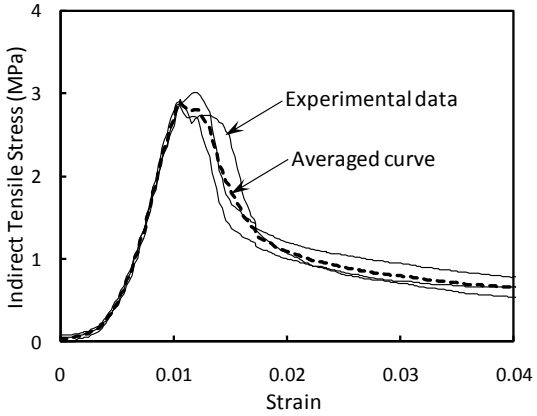

(a) SC4-25, V_f = 0.5%

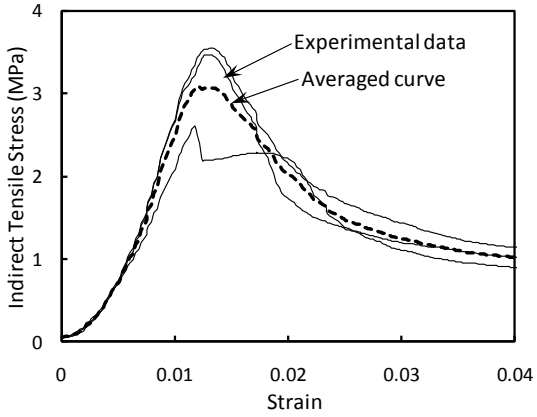

(b) SC4-25, V_f = 1.0%

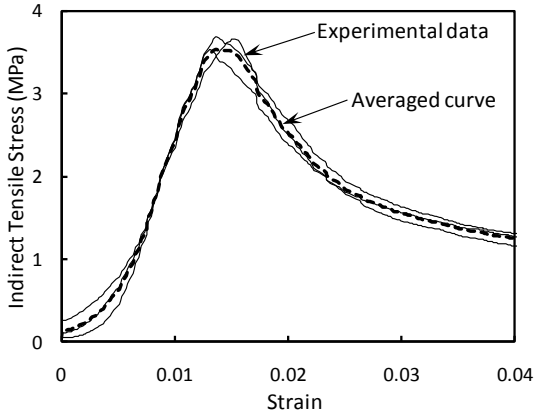

(c) SC4-25, V_f = 1.5%

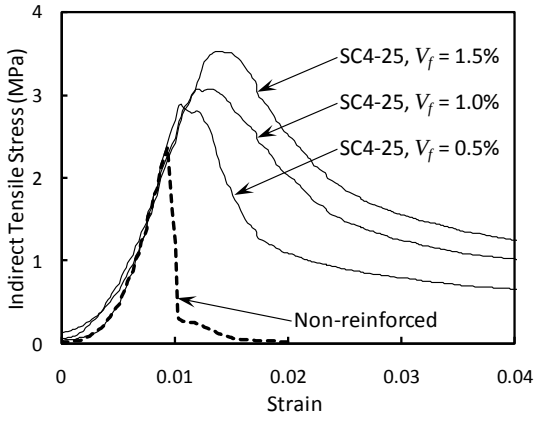

(d) the average curves compared to non-reinforced asphalt concrete

Fig. A.6 Indirect tensile stress – strain curves of SC4-25

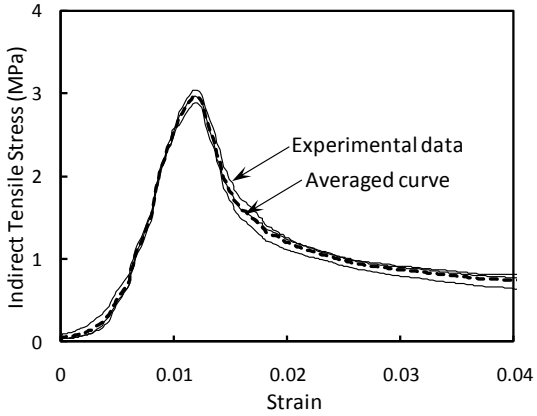

(a) SR3-30, V_f = 0.5%

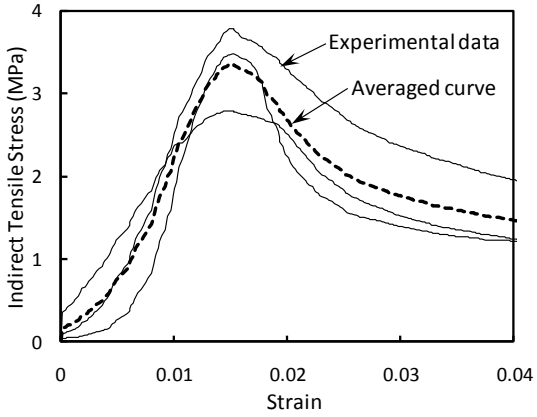

(b) SR3-30, V_f = 1.0%

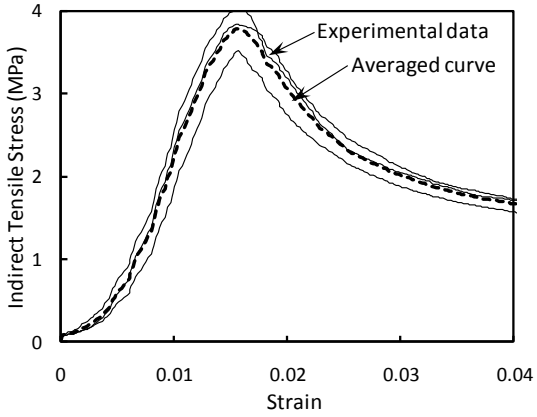

(c) SR3-30, V_f = 1.5%

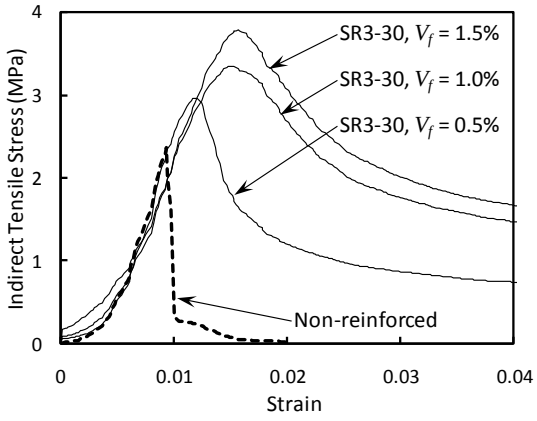

(d) the average curves compared to non-reinforced asphalt concrete

Fig. A.7 Indirect tensile stress – strain curves of SR3-30

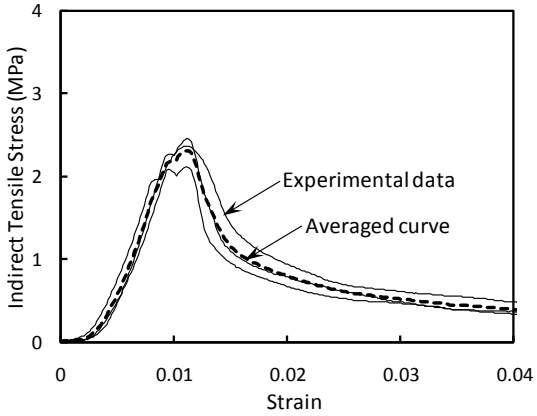

(a) TR3-18, V_f = 0.5%

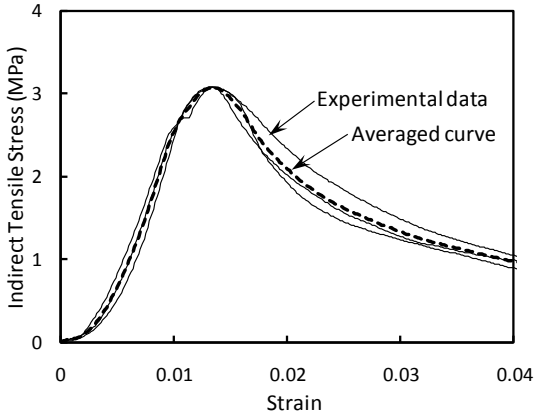

(b) TR3-18, V_f = 1.0%

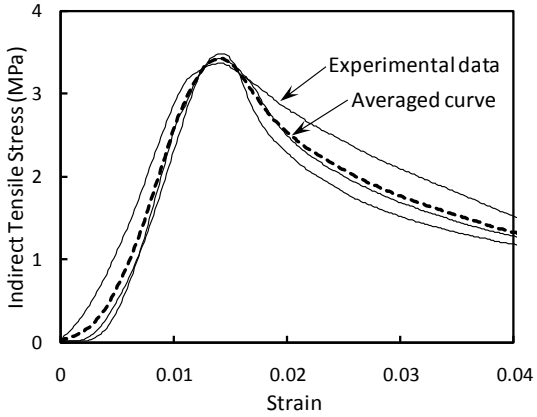

(c) TR3-18, V_f = 1.5%

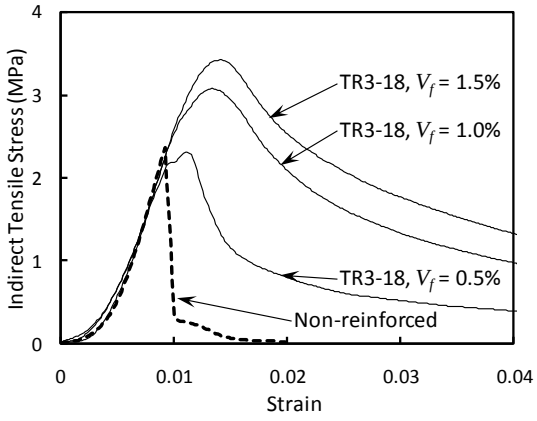

(d) the average curves compared to non-reinforced asphalt concrete

Fig. A.8 Indirect tensile stress – strain curves of TR3-18

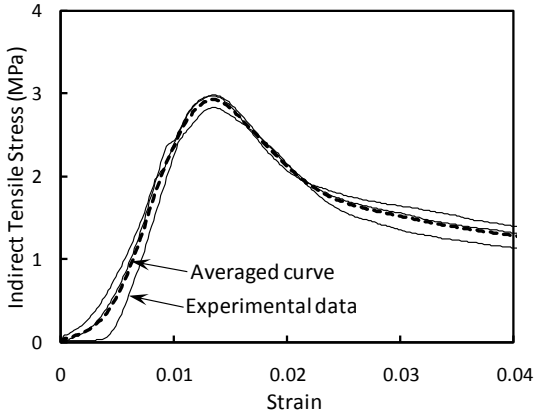

(a) TR3-30, V_f = 0.5%

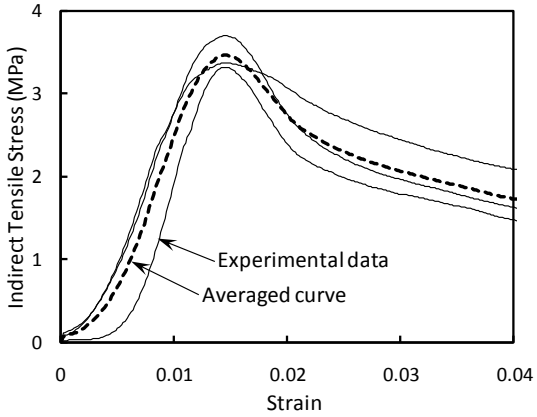

(b) TR3-30, V_f = 1.0%

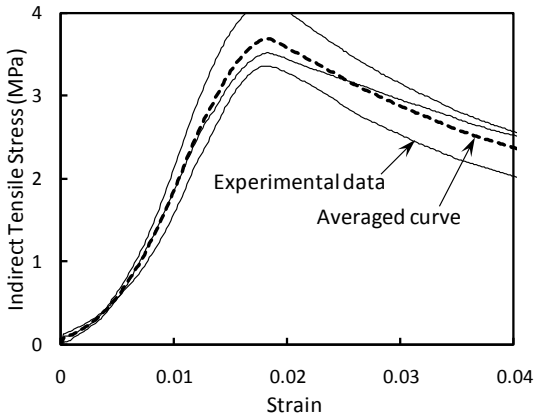

(c) TR3-30, V_f = 1.5%

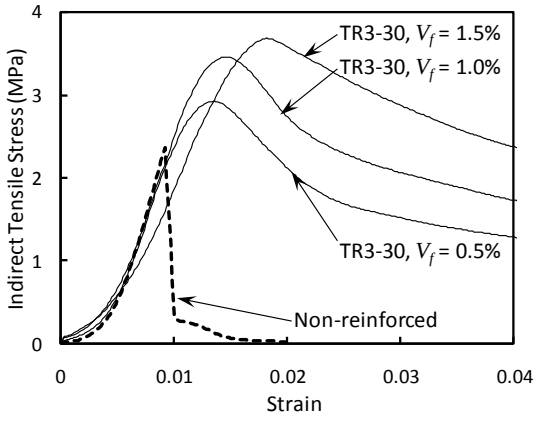

(d) the average curves compared to non-reinforced asphalt concrete

Fig. A.9 Indirect tensile stress – strain curves of TR3-30

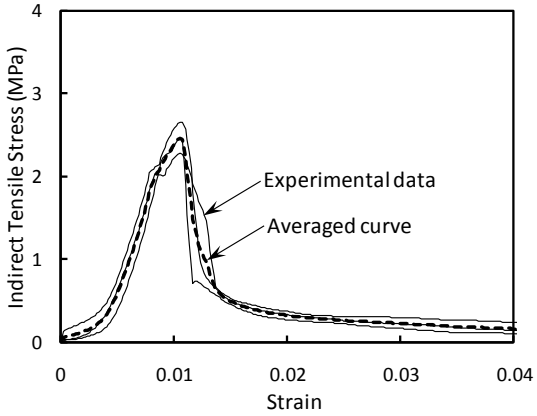

(a) SR5-25, V_f = 0.5%

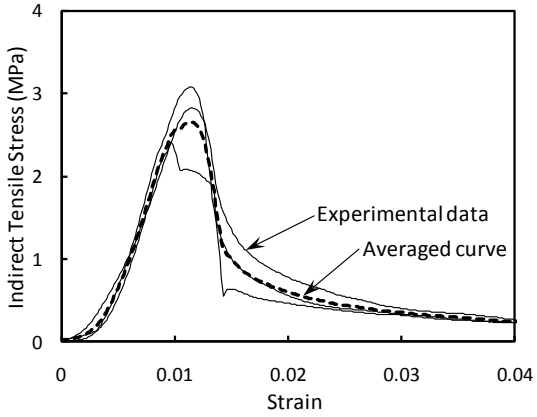

(b) SR5-25, V_f = 1.0%

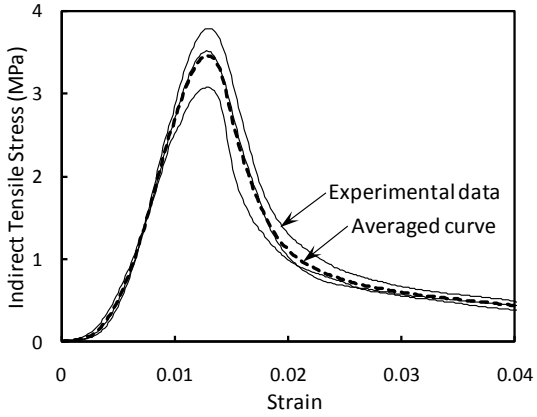

(c) SR5-25, V_f = 1.5%

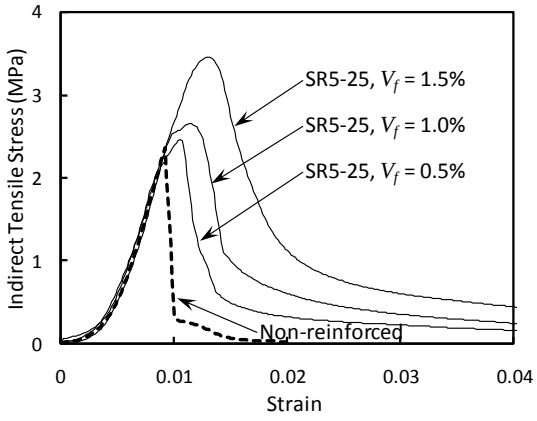

(d) the average curves compared to non-reinforced asphalt concrete

Fig. A.10 Indirect tensile stress – strain curves of SR5-25

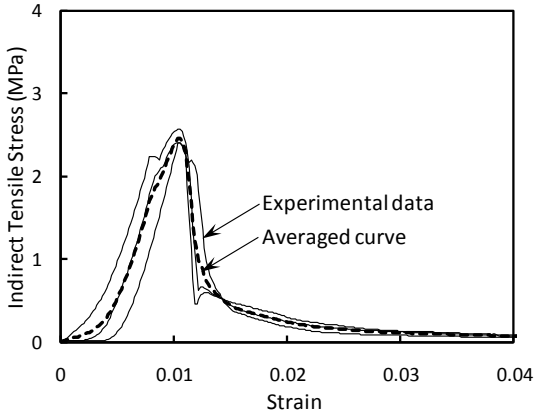

(a) CR5-25, V_f = 0.5%

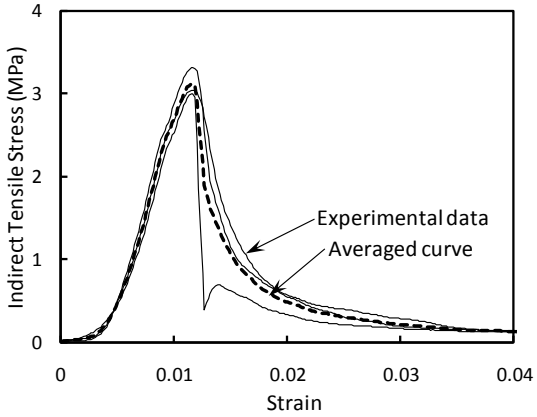

(b) CR5-25, V_f = 1.0%

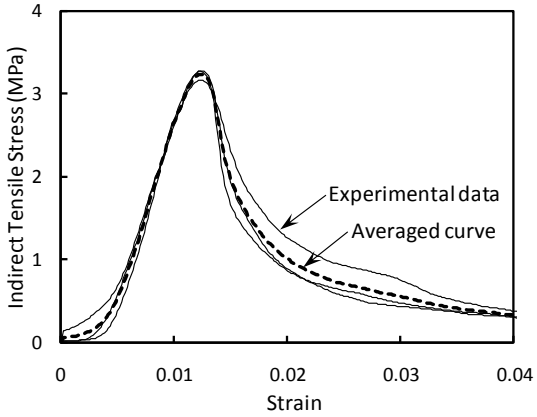

(c) CR5-25, V_f = 1.5%

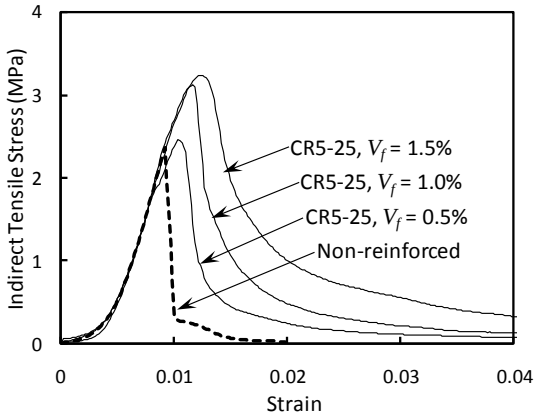

(d) the average curves compared to non-reinforced asphalt concrete

Fig. A.11 Indirect tensile stress – strain curves of CR5-25

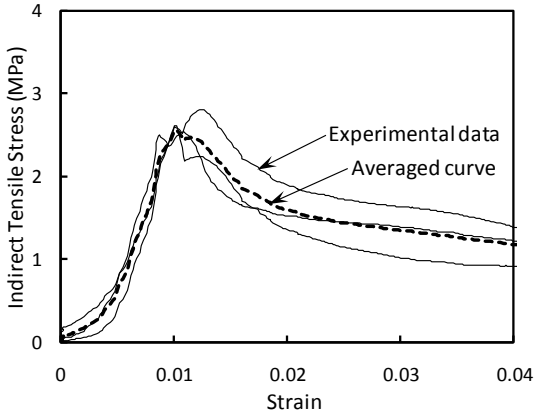

(a) HC4-30, V_f = 0.5%

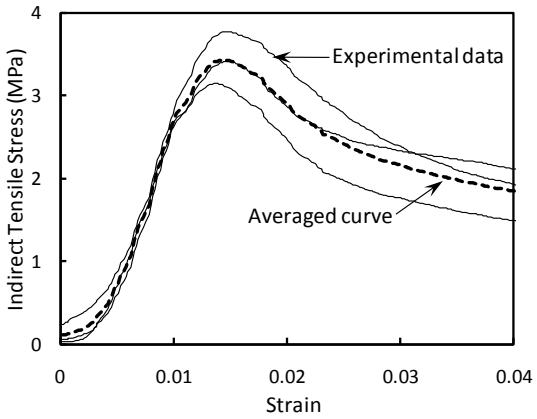

(b) HC4-30, V_f = 1.0%

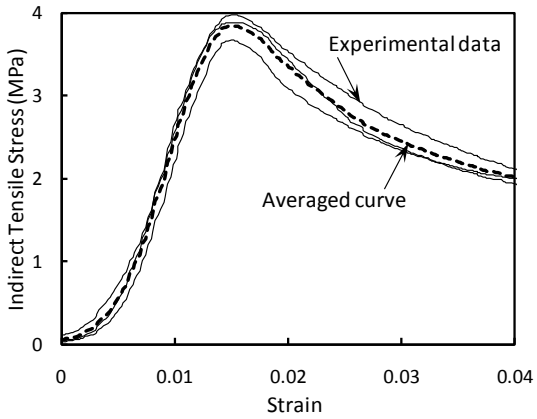

(c) HC4-30, V_f = 1.5%

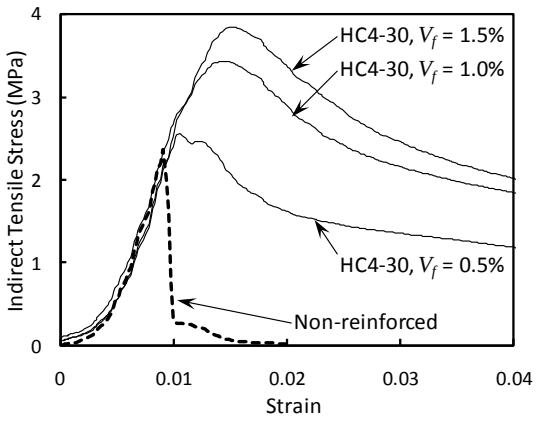

(d) the average curves compared to non-reinforced asphalt concrete

Fig. A.12 Indirect tensile stress – strain curves of HC4-30

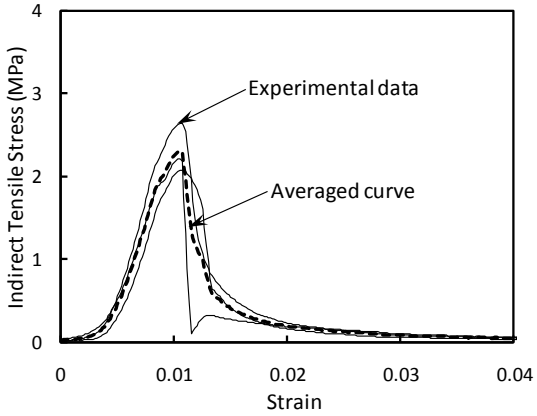

(a) CB-13, V_f = 0.5%

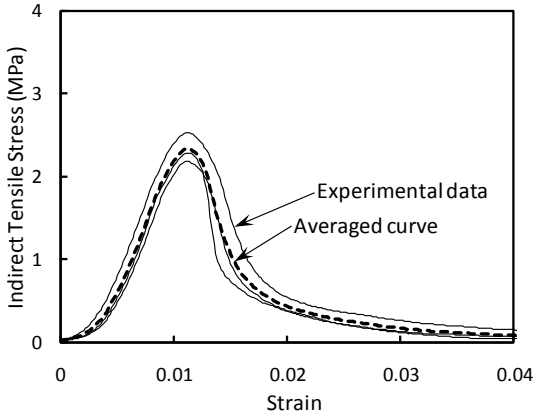

(b) CB-13, V_f = 1.0%

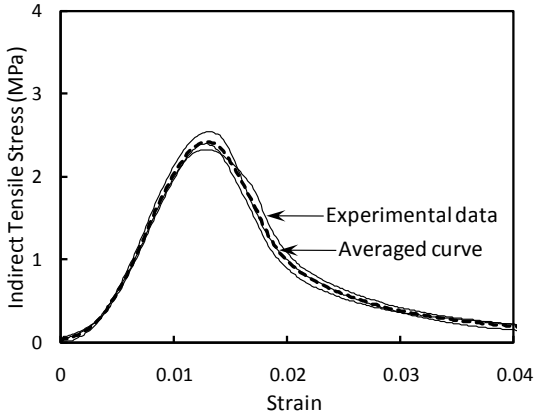

(c) CB-13, V_f = 1.5%

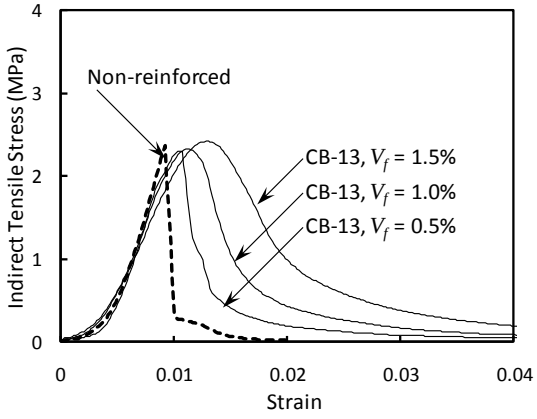

(d) the average curves compared to non-reinforced asphalt concrete

Fig. A.13 Indirect tensile stress – strain curves of CB-13

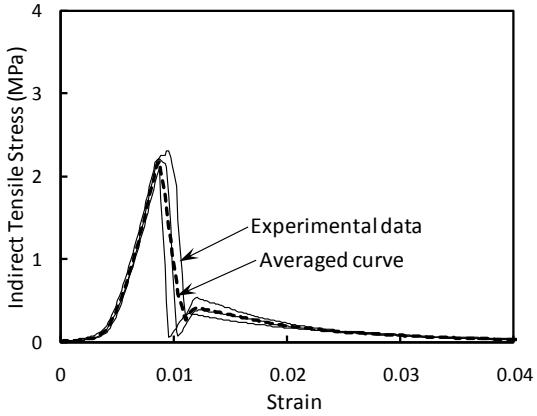

(a) PVA-13, V_f = 0.5%

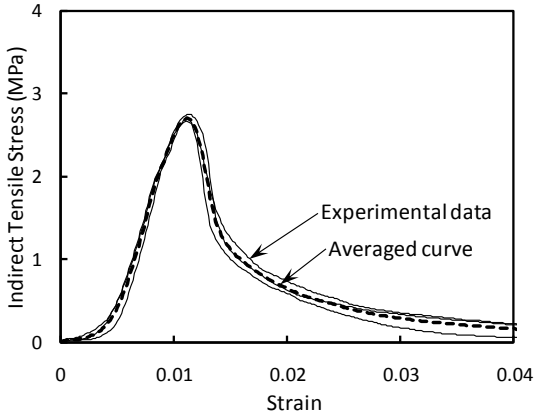

(b) PVA-13, V_f = 1.0%

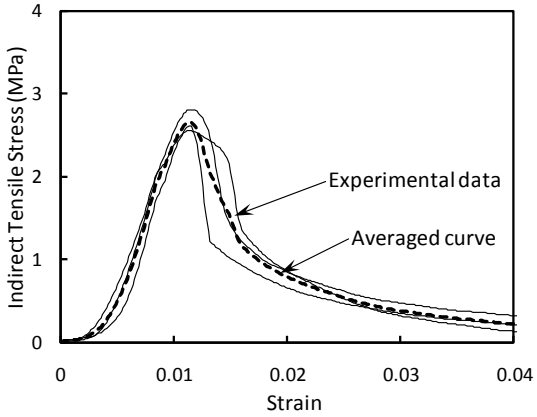

(c) PVA-13, V_f = 1.5%

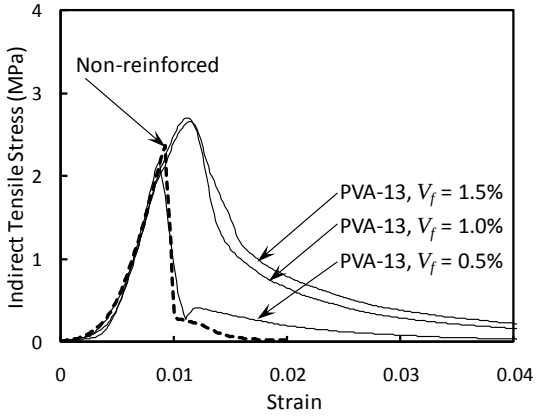

(d) the average curves compared to non-reinforced asphalt concrete

Fig. A.14 Indirect tensile stress – strain curves of PVA-13